Synthesis and Ultrafast Optical Characterization of Solid State and Functional Metal Nanocluster

by

Rosina Ho-Wu

A dissertation submitted in partial fulfillment
of the requirements for the degree of
Doctor of Philosophy
(Chemistry)
in the University of Michigan
2017

Doctoral Committee:

Professor Theodore Goodson III, Chair
Professor Stephen Maldonado
Professor Adam J. Matzger
Professor Richard E. Robertson

Rosina Ho-Wu

roshowu@umich.edu

ORCID iD: 0000-0002-6453-7961

Dedication

To Michael Kran, Jian Hong Wu, Chiu Kwan Ho and Wilson Ho

Acknowledgement

I would like to acknowledge several individuals who have helped this work become possible. First, I thank my advisor, professor Theodore Goodson III, for this research opportunity, for guidance and support. Similarly, to my undergraduate advisor, professor Marilyn Mackiewicz, who provided the foundation for this scientific journey. To my colleagues in the Goodson's research group, past and current members, for maintaining a fun, supportive and intellectual environment. I especially thank Dr. Sung Hei Yau, Dr. Neranga Abeyasinghe and Dr. Oleg Varnavski for providing the initial guidance to the present work. To my dissertation committee members: professor Maldonado, professor Matzger and professor Robertson, for helpful discussions about this work. To Dr. James Windak from the Department of Chemistry and Dr. Kai Sun from Material Science and Engineering, for collaborating in the characterization work. I would like to also thank Linda Van Blaircum for her support in managing and keeping the group together.

Table of Contents

List of Figures

List of Tables

Abstract

Metal nanoclusters have been extensively researched in the past few decades due to their unusual optical and physicochemical properties. Optical and theoretical investigations on these quantum metal nanoclusters allowed researchers to understand the origin of their properties and the evolution of optical properties with size. Optical characterizations of metal nanoclusters have revealed a lot about the electronic structures of metal nanoclusters. However, most of these investigations were conducted in the solution phase, while many applications will require solid state materials. This dissertation is aimed at the investigation of the effect of cluster-cluster and cluster-chromophore coupling on the optical properties of solid state and assemblies of metal nanoclusters.

Metal nanoclusters in the solid state were prepared by embedding the nanoclusters into a polymer matrix. The use of a polymer host allowed different nanocluster densities to be made, thus resulting in different inter-cluster distances. The nanocluster films were investigated by linear and non-linear optical spectroscopy. The fluorescence and two-photon absorption cross-sections of the nanocluster films are greatly enhanced compared to the solution phase nanoclusters. These results indicate that there is a strong dipole coupling between the nanoclusters due to the short inter-cluster distances, and possible energy transfer between the nanoclusters.

Similarly, metal nanocluster assemblies and architectures have been explored for practical applications due to the possibility of observing collective properties. On the fundamental science's point of view, the super-atom concept of metal nanoclusters means that they can add a third dimension to the periodic table, and used as building blocks for super-molecules. Presented in this dissertation is the optical characterization of a type of nanocluster assembly, metal nanoclusters linked with an organic linker. A chromophore was used as the linker to add functionality to the material. The correlation between the chromophore-Au_{25} nanocluster oligomer length and molecular geometry with their optical properties was analyzed. The chromophore-Au_{25} nanocluster oligomers showed larger transition dipole moment, which results in a two-photon absorption enhancement of up to 68 times. An analysis of the molecular geometry around the cluster-chromophore-cluster bonds reveals that the optical properties of the oligomers are very dependent on the molecular geometry. Therefore, solid state metal nanoclusters and nanocluster assembly materials are promising candidates for applications such as small molecular devices and protective coating for optical limiting.

Finally, this dissertation also aims to demonstrate the use of metal nanoclusters for photodynamic therapy application. Due to the strong quantum confinement effects of metal nanoclusters, the existence of triplet excited states and strong absorption, the nanoclusters are good candidates for singlet oxygen photosensitization. The rate of singlet oxygen generation is compared against three different metal nanoclusters and the electronic structure analysis of the metal nanoclusters indicate that high absorption-to-volume ratio nanoclusters are a select group of metal nanoclusters that will show high singlet oxygen formation efficiency. Furthermore, photodynamic therapy by two-photon

excitation (800 nm) is demonstrated to be more effective than one-photon excitation (400 nm) due to the large two-photon absorption cross sections of metal nanoclusters. Thus, metal nanoclusters can be used as a dual agent for effective photodynamic therapy treatment and high-resolution imaging.

The dissertation is closed by an analysis of the non-linear optical properties of the highly fluorescent bimetallic Au@Ag nanoclusters and future directions regarding the study of these bimetallic nanoclusters and the fabrication and optical characterization of solid state metal nanoclusters-conjugated polymer films.

Chapter 1
Introduction and Background

Figure 1.1. The Lycurgus Cup appears opaque green when it is lit from the outside (A) and translucent red when lit from the inside (B). (Source: https://www.nano.gov/timeline)

The use of metal nanomaterials dates back to ancient civilizations. Although they were not identified as nano-sized materials initially, gold and silver nanoparticles were produced for decorative purposes due to their interesting optical properties. The Lycurgus Cup is an example of using metal nanomaterials in the crafting of art (Figure 1.1). In 1857, Michael Faraday first reported the synthesis of red gold colloids and hypothesized that the colloids were smaller than the wavelength of light in the visible spectrum. Later, Gustav Mie successfully modeled the optical absorption of the gold nanoparticles by solving Maxwell's equations in 1908. The early period of metal nanoparticle research focused on colloidal nanoparticles in the size range of 1 – 100 nm.[1–8] With the advancement of technology related to mass spectrometry, it became possible for particles

smaller than 1 nm to be detected. This helped this area of research to gain great interest in science and technology.[9–13]

1.1 Size-dependent properties of metal nanomaterials

The electronic properties of metal nanoclusters and nanoparticles differ from those of atomic and bulk metals (Figure 1.2). The electronic properties of a system at different sizes can be explained by their density of states.[14,15] Three-dimensional objects such as bulk metals display a continuous distribution of density of states. Their sizes are larger than the wavelengths of the external electromagnetic field that interacts with them. As a result, the electronic levels in bulk metals are very closely packed, allowing the electrons to move freely between the electronic levels. In bulk metals, the conduction band, or unoccupied states (shaded in white), is very close in energy to the valence band (shaded in black), which allows the electrons to freely move from the occupied to the unoccupied states (Figure 1.2). This free movement of electrons is also called a "sea of electrons." The density of states scales down with decreasing particle size. Once it reaches a critical size, the highest occupied state and the lowest unoccupied state, also called the Kubo gap, will be equal to the thermal energy at room temperature (k_BT = 25 meV).[10,15] This is the size-induced metal-to-insulator transition. Particles which have an energy gap close to the Kubo gap can exhibit metallic or insulating properties, depending on the temperature of the system. When the energy gap increases with respect to the Kubo gap, a particle transitions from insulator to molecule.

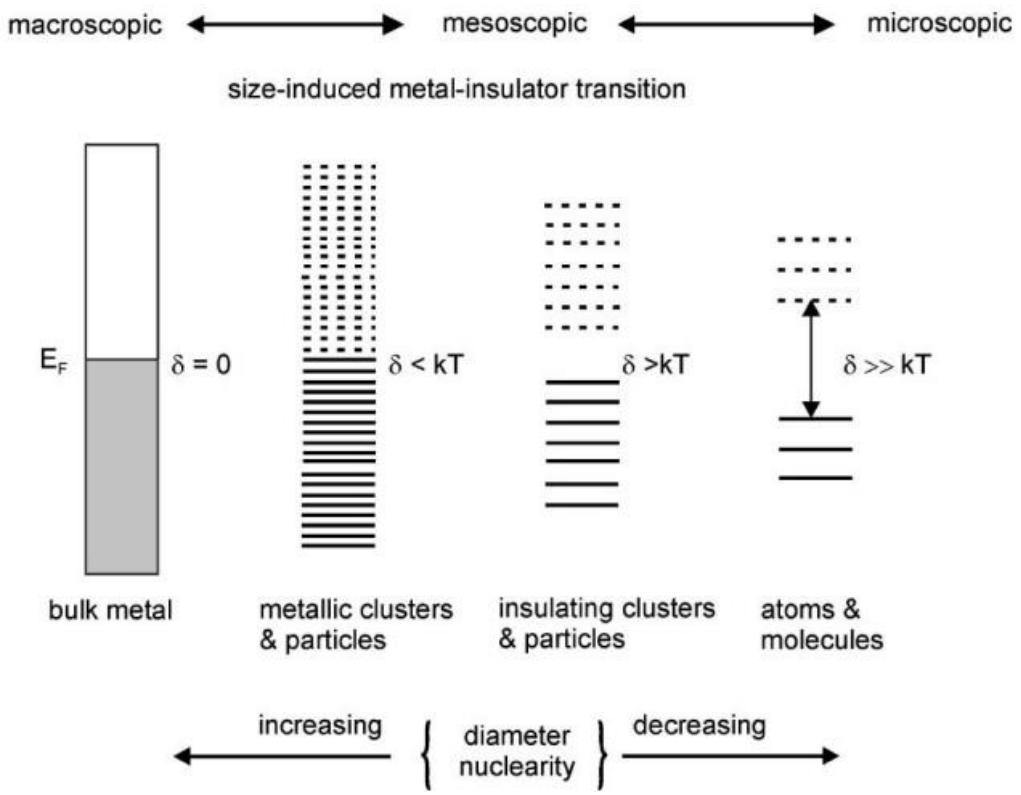

Figure 1.2. Size-dependent electronic properties of materials.[16]

Metal nanoparticles (~10 – 100 nm) are found in the metal-insulator regime. Metal nanoparticles are characterized by their surface plasmon resonance, which is the collective oscillation of electrons at the surface of the nanoparticle.[5,17,18] The surface plasmon resonance of metal nanoparticles have been theoretically described by Gustav Mie by solving the Maxwell equations.[17] In general, the surface plasmon resonance of metal nanoparticles red-shifts with increasing particle size, although the opposite trend has also been observed under specific conditions.[19] The energy levels become quantized as the particle size continue to decrease, thus, confining the electrons to discrete energy levels due to the increase in the energy gap between the levels. The particles in this size regime show molecular-like or insulator properties. From a basic science point of view, this size regime is the bridge between molecular systems and large particle systems.[20,21]

Particles in this size regime (1 – 2 nm) have been termed "metal nanoclusters" to distinguish them from plasmonic metal nanoparticles.

Different metal nanoparticles and nanoclusters have been synthesized over the decades, but gold has been the most studied type of metal nanoparticle and nanocluster due to their exceptional stability.[15,22–25] Gold nanoparticles and nanoclusters have been investigated for applications in catalysis, biomarkers, imaging, and molecular electronics; however, metal nanoclusters have been increasingly gaining research focus due to their molecular-like properties.[3,26–31]

1.2 Towards quantum confinement: "magic clusters"

The first observations of small metal nanoclusters were gas phase alkali, noble, group IIB and Al metal clusters.[9,12,32–37] These gas phase nanoclusters are produced by ionization sources in mass spectrometers at only certain sizes as determined by mass spectrometry.[9,33,34] Distinct periodic patterns in the mass spectra were observed for Na_N clusters of sizes N = 2, 8, 18, 20, 40, 58. Due to the preferential formation of certain cluster sizes, they were termed "magic number" clusters. The electronic structure of these nanoclusters resembles a spherical well potential which describes a spherical particle following an electron shell closing trend.[9,32–35] The existence of magic number clusters indicates that these particular cluster sizes are highly stable. Their stability was first explained by the jellium model which depicts the nanocluster as a uniform, positively-charged sphere surrounded by the valence electrons.[9,12,38,39] The theoretical treatment of the jellium model considers the valence electrons as free electrons and predict the electronic properties of the nanoclusters, including plasmon resonance, based on the number of atoms.[9,12,38,39] Metal nanoclusters have been referred to as "superatoms" due to

the similarities in the electronic shell closing between atoms and metal nanoclusters.[9,12,38,39]

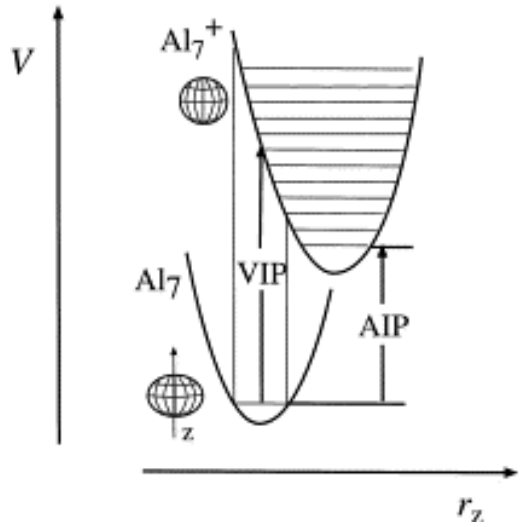

Figure 1.3. Potential curve of the ionization of Al_7 to Al_7^+.[43]

For further experimental characterization of metal nanoclusters, condensed phase metal nanoclusters must be synthesized. Noble metal nanoclusters were the best candidates, especially gold, due to their exceptional stability compared to alkali clusters in solution.[24,39,40] The jellium model has worked well in modeling the electronic structure of alkali metal nanoclusters, but it falls short in modelling other types of metal nanoclusters.[41] The close-shell model was then proposed to explain the stability of ligated noble metal nanoclusters.[24,41,42] This model can also be applied to symmetrical clusters. According to the close-shell model, the valence electrons in a cluster are independent from the metal atoms, but confined in a spherical potential well. Due to the symmetry of nanoclusters, the valence electrons fill the degenerate electronic levels in a systematic shell closing fashion which results in the cluster's stability.[24,41,42]

The aforementioned models work well for symmetrical and spherical systems. However, stable non-spherical nanoclusters have also been observed and a new model is

needed to describe their electronic structure and stability.[43–45] The Clemenger-Nilsson potential, also known as the ellipsoidal shell model, was developed for non-spherical clusters.[43–45] In this model, the valence electrons in the nanoclusters are treated as ellipses which adds up to a spherical shape in a single-particle Hamiltonian (Figure 1.3).[43,45] All these models provided the theoretical basis for both gas phase and condensed phase nanoclusters.

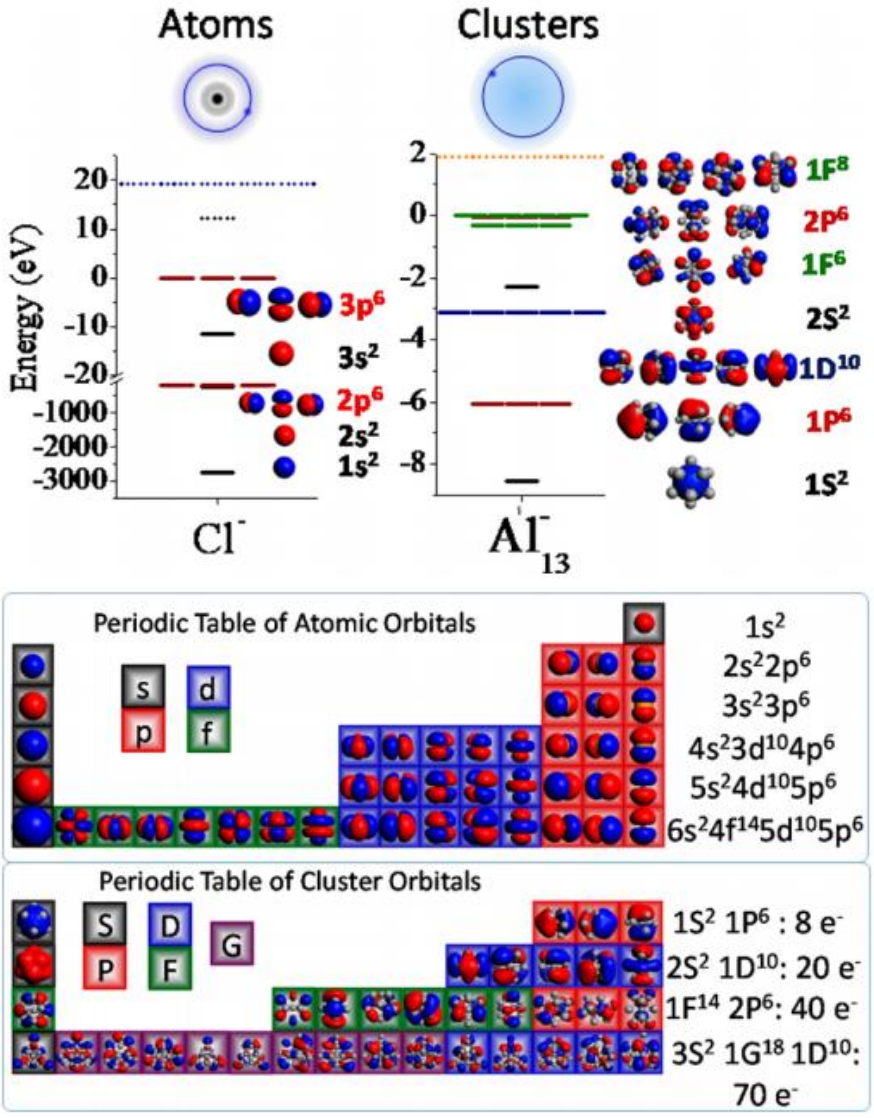

Figure 1.4. Atomic and molecular orbitals of Cl^- and Al_{13}^- exhibiting periodic pattern.[49]

Based on the superatom concept, metal nanoclusters are being considered as new materials that will add a third dimension to the element's periodic table.[46–49] According to the aforementioned models, the excellent stability of metal nanoclusters is due to the systematic filling of the degenerate electronic levels. The atomic and molecular orbitals of atoms and nanoclusters, respectively, are shown to be similar (Figure 1.4). For atoms, their periodicity follow a set of quantum mechanical rules, such as their principle, angular momentum, magnetic and electronic spin, and quantum numbers. For clusters, their periodicity is determined by the number of atoms, the number of valence electrons per atom and the net charge of the cluster.[49] The close-shell model describes quite well the periodicity of clusters by their valence electron count pattern.[49] However, this periodic pattern of clusters is only modeled after spherical clusters. Besides the variation in shapes (spherical vs ellipsoidal), the electronic structures of metal nanoclusters are largely dependent on the crystal structure, type of metal, and ligands. It is, therefore, a challenge to reconcile a unified view of metal nanoclusters. In this regard, Rongchao Jin and coworkers have recently discovered a magic series of gold nanoclusters, Au_{28}, Au_{36}, Au_{44}, Au_{52}, which show a periodic pattern in both their electronic properties and crystal structure evolution with increasing size.[50] Thus, it may be possible to fit other stable metal nanoclusters into a "magic series" of periodicity.

1.3. Metal nanoclusters in the condensed phase

Gas phase metal nanoclusters provided the foundation for understanding the quantum confinement effects of these ultra-small systems. However, the successful synthesis of metal nanoclusters in the solution phase expanded the characterization and the understanding of these systems. Unlike gas phase nanoclusters, the solution phase metal nanoclusters focused on noble metals such as Au and Ag, and other transition metals such

as Zn.[1,51,52] Of the different metal nanoclusters, gold nanocluster is the most extensively studied due to its better chemical stability in solution compared to other metal clusters.

Early synthesis of ligated small metal nanoclusters in solution phase was devised by Brust et al in 1994.[53] The Brust synthesis provided the basis for subsequent developments in the synthesis of solution phase metal nanoclusters.[54–57] The Brust synthesis consists of a redox reaction carried out in a two-phase system (water-toluene).[53] The precursor to the gold nanoparticles is a Au^{3+} ion (usually in the form $AuCl_4^-$) which is transferred from the aqueous phase to the organic phase by a phase-transfer agent, tetraoctylammonium bromide, and is reduced with $NaBH_4$ in the presence of an organic-soluble capping ligand. Initially, the Brust synthesis yielded particle sizes of 1 to 3 nm as determined by TEM and mass spectrometry.[53,58–62] One of the major challenges in the synthesis is achieving mono-dispersity. For nanoparticles (> 5 nm; >1,000 atoms), a small difference in the number of metal atoms does not affect their electronic properties, therefore, they can be identified by their size rather than number of metal atoms. On the other hand, the electronic levels of a metal nanocluster are quantized, which is dependent on its crystal structure and number of atoms. Therefore, achieving mono-dispersity with atomic precision is of paramount importance for structure-property investigations.

As the interest in the quantum confinement effects in small metal systems increased, efforts have been spent into synthesizing clusters that are smaller than 2 nm (< 250 atoms). Small clusters of 14 to 30 kDa core masses (~70-150 atoms) have been synthesized by controlling the cluster growth.[63,64] Hostetler and co-workers have synthesized a series of gold clusters of ~110 to 4,800 atoms by controlling the cluster growth at -78°C.[64] According to Schaaff and co-workers, smaller clusters are obtained by

reducing a pure Au(I)-ligand polymer sample with excess $NaBH_4$, the reducing agent, which is added in its entirety at once to the Au(I)-ligand polymer solution.[13] To obtain the smallest cluster, 8 kDa core mass, the reaction is terminated early (10^3 s vs 10^4 s). This reaction produces a mixture of cluster sizes which are separated by fractional crystallization. However, fractional crystallization can only resolve core masses of 14 kDa and higher. To isolate the smallest cluster, liquid gravity column chromatography was used.

Schaaff and co-workers later synthesized a water-soluble version of these clusters by using the glutathione (GSH) ligand.[65] The different sizes of Au-SG clusters are isolated by gel electrophoresis and characterized by MALDI which shows extensive fragmentation of the cluster core. The predominant cluster size from the synthesis was identified to be a $Au_{28}(SG)_{16}$. The optical absorption spectrum of this cluster shows step-like and discrete absorption peaks which indicates the homogeneity of the sample and the effectiveness of the electrophoresis separation. Additionally, the $Au_{28}(SG)_{16}$ nanocluster exhibits dual fluorescence in the visible and near-IR spectra.[66] It was found that the near-IR luminescence originates from the triplet excited states by fluorescence lifetime measurements.

With better structural characterizations of the gold clusters, specific cluster sizes are now referred to not by their diameter size, but by their exact chemical composition $Au_n(SR)_m$. Later, other small clusters were also isolated. Donkers et al have devised a synthesis to yield two cluster sizes with the phenylethanethiol ligand, the Au_{140} and Au_{38}.[67] Despite having the same ligand, the two clusters are soluble in different solvents which can be used as an advantage to separate the clusters.

In 2004, Negishi and coworkers were able to prepare a series of small Au:SG nanoclusters, Au_{18}, Au_{21}, Au_{25}, Au_{28}, Au_{32} and Au_{39}.[68] This series of clusters differ only by a few atoms, but they were able to be separated by polyacrylamide gel electrophoresis and their composition were determined by ESI mass spectrometry. This series of clusters showed a clear evolution of optical properties with increasing core size. Later in 2005, with improved separation and characterization techniques, the mixture of Au:SG clusters was separated into 9 fractions which were identified as $Au_{10}(SG)_{10}$, $Au_{15}(SG)_{13}$, $Au_{18}(SG)_{14}$, $Au_{22}(SG)_{16}$, $Au_{22}(SG)_{17}$, $Au_{25}(SG)_{18}$, $Au_{29}(SG)_{20}$, $Au_{33}(SG)_{22}$, and $Au_{39}(SG)_{24}$. Optical absorption spectra of these small clusters and of the polymeric Au(I)-SR clearly shows the evolution of Au(I)-SR complexes to Au nanoclusters.

Although metal nanocluster separation techniques were greatly improved to isolate atomically-precise nanoclusters (Au_nSR_m), the polydispersity in the product of a synthesis still in itself presents a drawback. For instance, certain sizes were produced in lower yield than others. The need for obtaining high-yield, mono-dispersed and atomically-precise nanoclusters become desirable. Professor Jin's group first reported a synthetic method for producing $Au_{25}(SR)_{18}$ nanoclusters in high yield by a kinetically-controlled reduction of the precursors Au(I)-SR polymers.[69,70] Later they discovered that $Au_{25}(SR)_{18}$ nanoclusters can be obtained exclusively through the size-focusing phenomenon.[71] During the size-focusing step in the synthesis, the mixture of nanoclusters is subjected to thermal etching with excess thiolate ligands to decompose less stable nanocluster sizes.[71] The product of the decomposition is the non-soluble Au(I)-SR polymer which can be filtered to recover pure $Au_{25}(SR)_{18}$ nanoclusters. The kinetic control of cluster growth and size-focusing

methodologies have formed the basis for synthesizing other cluster sizes in high purity such as Au_{38} and Au_{144}.[72–74]

The $Au_{25}(SR)_{18}$ nanocluster has been the golden child in nanocluster's investigations, as well as a good example of advances in nanocluster synthesis and characterization. The $Au_{25}(SR)_{18}$ nanocluster was initially determined as $Au_{28}(SG)_{16}$ and $Au_{38}(SCH_2CH_2Ph)_{24}$.[65,67] Later, by employing high resolution mass spectrometry, the identity of this nanocluster was finally unified to $Au_{25}(SR)_{18}$.[75–77] The $Au_{25}(SR)_{18}$ nanocluster has received much attention due to its ultra small size (strong quantum confinement effect), stability, and established synthetic method (tailored to produce monodisperse Au_{25}).[78–82]

The successful synthesis of monodisperse, atomically precise, Au_{25} nanocluster allowed for its structural determination and structure-property correlation. The structure of the Au_{25} nanocluster consists of a Au_{13} icosahedra core and six semirings of -S-Au-S-Au-S- (Figure 1.5).[83,84] The core-shell structure is found to be common for ligand-protected nanoclusters. In the same year, the crystal structure of a larger cluster, $Au_{102}(SR)_{44}$, was also determined to be a core-shell structure.[85] Due to this structure, solution phase metal nanoclusters are often called monolayer-protected metal nanoclusters (MPC). The core-shell structure is in accordance with earlier theoretical prediction that metal nanoclusters contain ring-like metalloorganic staples as protective units to a pure metal core.[86]

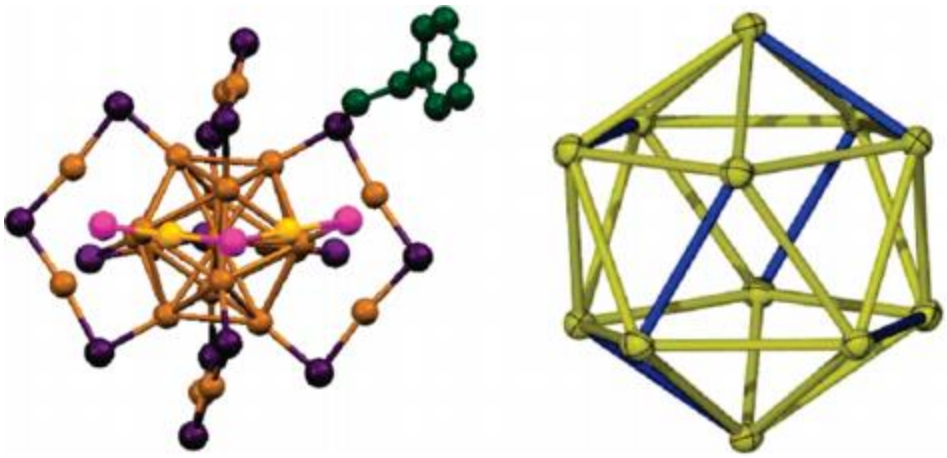

Figure 1.5. Crystal structure of a Au_{25} nanocluster showing one -SCH_2CH_2Ph ligand (left) and the structure of the Au_{13} isocahedra core (right) without the semirings.[83]

The versatility of producing solution phase metal nanoclusters is that they can be used for further reactions. For example, ligand exchange reaction has been employed to extend the variety of metal nanocluster systems.[87–89] Ligand exchange reaction can be used to add a desired ligand, such as a chromophore, to a metal nanocluster which is otherwise not accessible by direct synthesis with the desired ligand.[90–93] Another advantage to ligand exchange reaction is the accessibility to other cluster sizes and isomers which are not obtained by direct synthesis.[94,95] The basis for ligand-induced structural changes to the nanocluster is dependent on the steric hindrance of the new ligand, nanocluster's magic stability, and the degree of bond distortion during the ligand exchange process.[94,96–98]

1.4. Optical properties of metal nanoclusters

The production of solution phase metal nanoclusters allowed for further characterization of these materials. Metal nanoclusters show strong quantum confinement effects which result in molecular-like properties such as distinct absorption and emission

transitions. Due to these properties, metal nanoclusters can be used for fluorescence imaging, especially in biological samples, or for protective coatings for optics.

The Goodson group has researched metal nanoparticles and nanoclusters by investigating their optical properties using ultrafast spectroscopic techniques.[6,7,99–105] Optical spectroscopy on nanomaterials can reveal the photophysical properties which indicate quantum confinement effects. Metal nanoparticles are characterized by their surface plasmon resonance (SPR) which is absent in molecular-like metal nanoclusters due to the discrete energy level separation.[5,17–19] Plasmonic nanoparticles show a very fast fluorescence decay (50 fs) due to the Auger recombination. They also show large non-linear absorption due to non-linear scattering effects. On the other hand, metal nanoclusters are fluorescent.[106–108] The energy gap separation between the electronic levels reduces the number of non-radiative decay pathways, thus enhancing the fluorescence.

Gold and silver nanoclusters were the most studied type of noble metal nanoclusters.[109–114] One of the major breakthroughs in the characterization of metal nanoclusters is the total structural determination of a $[Au_{25}(SR)_{18}]^-$ nanocluster. The successful crystal structure determination allowed for structure-property correlation. Time-dependent density functional theory calculations show that the optical transitions of gold nanoclusters are due primarily from the inter-band (sp-d) and intra-band (sp-sp) transitions of the icosahedral Au_{13} core.[82] The theoretical calculations were reproduced experimentally for Au_{25}.[82,83] A clearly defined absorption peak is seen at 670 nm which is due to the HOMO-LUMO transition. The HOMO of the nanocluster show significant p-orbital character, and the LUMO shows d-orbital character.[81] The Au_{25} nanocluster,

therefore, can be considered a "superatom" with a total valence electron count of 8 ($1S^2$ $1P^6$) for the anion form. In low temperature experiments, the absorption spectra of metal nanoclusters show sharper features.[115,116] More importantly, spectral features were narrower at low temperatures, which reveal several optical transitions that would otherwise appear as "merged" broad peaks at room temperature. At low temperatures, the oscillator strength also increases. The appearance of new vibronic features and blue-shift of the optical transitions indicate that there is a strong electron-phonon interaction between the 13-atom Au core and the S-Au-S-Au-S staple motifs which constitute the shell of the nanocluster.[115,116]

Electronic structures and electron-phonon interactions of metal nanoclusters can be further investigated by ultrafast spectroscopic techniques such as time-resolved fluorescence up-conversion and transient absorption.[20,109,111,117–119] Metal nanoclusters show much longer fluorescence lifetime (ns to μs) than metal nanoparticles due to their discrete energy levels which are quantized.[66,106,113] On the other hand, metal nanoparticles exhibit a fast Auger recombination in 50 fs. The transient absorption of metal nanoclusters also gives evidence of the quantum size effect. Metal nanoclusters show broad excited state absorption over a wide range of the visible spectrum, and a ground state bleach from the HOMO-LUMO transition.[93,109,111,118] On the other hand, metal nanoparticles only show a ground state bleach due to the plasmon resonance. Additionally, electron dynamics of metal nanoclusters are independent of the excitation power, whereas metal nanoparticles show strong power-dependent electron-phonon coupling which is characteristic of metallic behavior.[93,109,111,118] Furthermore, the excited state dynamics of metal nanoclusters show that there is a fast core-to-shell energy transfer

within a nanocluster, followed by a long excited state lifetime.[111,120] This indicates the presence of a triplet excited state derived from the metal-ligand shell.

The fluorescence properties of metal nanoclusters has been a research attraction due to the potential applications of metal nanoclusters in bio-imaging, photodynamic therapy (Chapter 5), sensing, optoelectronics, etc.[29,113,121,122] The fluorescence of metal nanoclusters turns out to be sensitive to the structure of the nanocluster. In ligand-protected metal nanoclusters, the core-shell structure gives rise to two emission in the visible spectrum.[109,110,113] The emission which arises from the metal core is centered at ~500 nm, and the emission which arises from the organometallic Au-ligand shell is centered in the near-IR. Not surprisingly, the exact emission maximum, the emission quantum yield, and the fluorescence lifetime in the near-IR is very dependent on the type of ligand. This ligand-dependent emission has been demonstrated in steady state and time-resolved fluorescence of Au_{25} with different electron-donating and -withdrawing ligands.[106,110,113,123] It's been shown that electron-donating ligands, usually the water-soluble thiolates, enhance the near-IR fluorescence of the metal nanocluster by ligand-to-metal charge transfer (LMCT). The near-IR emission of the nanoclusters has been identified as the nanocluster's triplet states.[106,110,123]

The near-IR fluorescence of metal nanoclusters has a relatively higher quantum yield than the visible fluorescence.[106,110,113] Due to the nanoclusters' applications, many synthetic efforts have been placed into designing metal nanoclusters with improved fluorescence quantum yields.[124–129] Some of the approaches consist of doping the metal nanoclusters with a different metal atom, aggregation-induced emission, and rigidifying the metal-ligand shell. Of particular interest is the phenomenon of aggregation-induced

emission. Though studies have been conducted to gain insights into the origin of metal nanocluster's near-IR fluorescence, some questions remained unanswered.[106,109,110,113,130] The discovery of aggregation-induced emission of Au(I)-thiolate complexes shed some light into the origin of nanocluster's fluorescence. The Au(I)-thiolate complexes have shown to exhibit strong fluorescence when aggregated.[128] The fluorescence is very dependent on the degree of aggregation. Thus the near-IR emission of the nanoclusters is due to the aggregation-induced emission phenomenon.

The non-linear optical properties of a material are investigated by their two-photon absorption (TPA). TPA is a third-order non-linear optical process involving the simultaneous absorption of two photons of lower energy than the absorption transition in the linear process. In chapter 2, the TPA process as well as the spectroscopic techniques for measuring it will be elaborated further. The TPA cross sections of different metal nanocluster sizes have been investigated in our group.[131] The TPA cross section of a Au_{25} nanocluster is 2,700 GM (1 GM = 10^{-50} $cm^4 \cdot s \cdot photon^{-1}$) at 1290 nm, and it increases to 427,000 GM at 800 nm.[131] This shows that metal nanoclusters have a strong two-photon-absorbing core since the corresponding one-photon excitation (400 nm) is the optical transition from the core. The study shows that the TPA cross section increases with cluster's and particle's size. However, the study showed that the TPA cross section per atom increases with decreasing nanocluster size, indicating strong quantum confinement effects. Furthermore, the TPA cross section of isolated Au_{25} nanoclusters is enhanced in the absence of ensemble and aggregation effects.[114] The very high TPA cross section of metal nanoclusters (at least an order of magnitude higher than chromophores)[132] and the higher spatial resolution of the two-photon (or multiphoton) transition process make

metal nanoclusters useful for photodynamic therapy (Chapter 5), optical limiting and improved bio-imaging resolution applications.[29,122,131] Other non-linear optical effects that are observed in metal nanoclusters include second and third harmonic generation.[133]

Optical characterization techniques can also be used to understand the transition of quantum confinement effects and continuous energy levels. For example, by examining the excited state dynamics and TPA cross sections of different cluster sizes, it was found that the emergence of the optical gap occur at the critical size of 2.2 nm.[20] Other independent studies established that this critical size corresponds to the Au_{144} nanocluster which is ~1.8 nm in size and whose electronic structure show both quantum confinement effects and onset of metallic behavior.[21,134,119]

1.5. Metal nanoclusters in the solid state

Solution-phase metal nanoclusters have allowed researchers to conduct investigations to understand the properties of these materials. However, many applications will involve the use of solid state materials. It has already been reported that the properties of metal nanoclusters change in going from the solution phase to the solid phase. For instance, the Au_{25} nanocluster can form covalent bonds between each other when going from the solution phase to the solid state.[119] The caveat is that this effect is ligand-dependent. Besides practical applications, researchers have also employed metal nanocluster films for fundamental investigations, such as low temperature optical studies.[21,90,120] Mai et al have also acknowledged the need to study the properties of nanoclusters in the solid state, when they reported the synthesis of silver nanoclusters and nanoparticles in a glass host and their non-linear optical properties.[121]

Metal nanoclusters are considered super-atoms that can add a third dimension to the periodic table. Due to their unique properties, they have been considered as building

blocks for larger structural materials.[11,46,122–124] It is expected that the assembly of super-atoms would show new or enhanced properties. The clusters-assembled materials so far have been synthesized by fusing the nanoclusters' cores via metal-metal bond (Figure 1.6). The type of metal-metal bonding also affects the structure of the assembly and the resulting properties. For example, the vertex-sharing bonding assembly has tunable conductivity while the face-sharing assembly is metallic.[125] Cluster-assembled materials with an external linker has received less attention as these may be a different type of assemblies than the ones with fused clusters.[124] Akola et al have modeled the electronic structure of a simple Au_{25}-phenyldithiolate-Au_{25} dimer and showed that the dimer exhibit the collective properties of each individual cluster part.[126] By using an organic linker, the cluster-assembled materials can have additional functionality, such as a dye. One of the works in this thesis will be dedicated into the optical properties investigation of this materials.

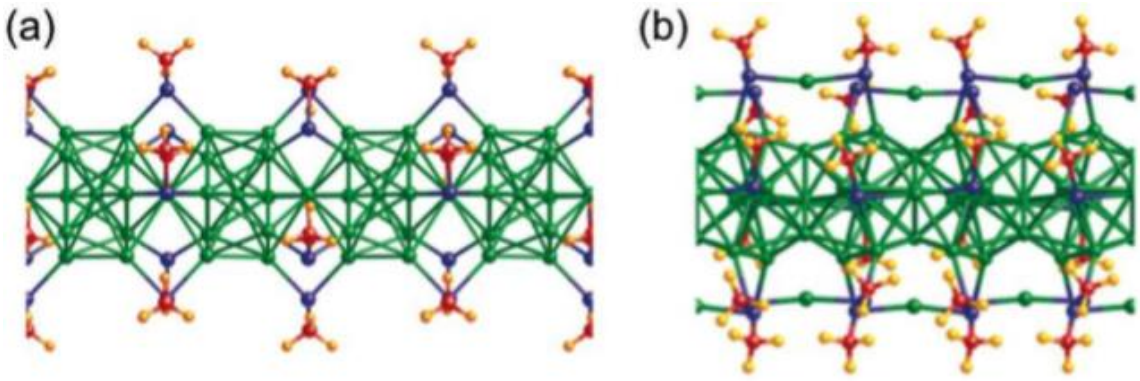

Figure 1.6. The icosahedra gold cluster as building blocks for supermolecules.[125]

1.6. Dissertation outline

In this dissertation, an emphasis is given to the optical properties of metal nanoclusters in the solid state. The spectroscopic techniques used in these works are detailed in chapter 2. Do the optical properties of metal nanoclusters in the solid state

differ from those in the solution phase? Are the optical properties of metal nanoclusters in the solid state sensitive to the inter-cluster distance? For this purpose, metal nanoclusters embedded into polymer matrixes were prepared and characterized by steady state and ultrafast non-linear spectroscopy (Chapter 3). Along the same line of inquiry, metal nanocluster oligomers were prepared and their optical properties were investigated (Chapter 4). By synthesizing metal nanocluster oligomers with an organic linker, the inter-cluster distance is fixed and the chain length can be varied. The aim of this inquiry is to understand metal nanoclusters assemblies. Do they exhibit enhanced collective properties as the result of cluster-to-cluster linkage? Furthermore, can the linker be used as a functional group to the nanoclusters and show energy transfer effects? Finally, metal nanoclusters were investigated for their application in photodynamic therapy (Chapter 5). The goal of this work is to elucidate the relationship between singlet oxygen generation rate and nanocluster size or type. It is also the aim of this work to demonstrate the effectiveness of using metal nanoclusters as photodynamic therapy agents in live cells by two-photon excitation. In chapter 6, a summary of the main results of these works will be outlined and future directions of research will be discussed.

1.7. References

(1) Chatterjee, A.; Chakravorty, D. Electrical Conductivity of Sol-Gel Derived Metal Nanoparticles. *J. Mater. Sci.* **1992**, *27*, 4115–4119.

(2) Gacoin, T.; Chaput, F.; Boilot, J. P. Metal, Semiconductor and Magnetic Nanoparticle Inclusions in Gels. *J. Sol-Gel Sci. Technol.* **1994**, *2*, 679–683.

(3) Murray, R. W. Nanoelectrochemistry: Metal Nanoparticles, Nanoelectrodes, and Nanopores. *Chem. Rev.* **2008**, *108*, 2688–2720.

(4) Ferrando, R.; Jellinek, J.; Johnston, R. L. Nanoalloys: From Theory to Applications of Alloy Clusters and Nanoparticles. *Chem. Rev.* **2008**, *108*, 845–910.

(5) Jain, P. K.; Huang, X.; El-Sayed, I. H.; El-Sayed, M. A. Noble Metals on the Nanoscale: Optical and Photothermal Properties and Some Applications in Imaging, Sensing, Biology, and Medicine. *Acc. Chem. Res.* **2008**, *41*, 1578–1586.

(6) Varnavski, O. P.; Ranasinghe, M.; Yan, X.; Bauer, C. A.; Chung, S.-J.; Perry, J. W.; Marder, S. R.; Goodson III, T. Ultrafast Energy Migration in Chromophore Shell-Metal Nanoparticle Assemblies. *J. Am. Chem. Soc.* **2006**, *128*, 10988–10989.

(7) Varnavski, O.; Goodson III, T.; Mohamed, M.; El-Sayed, M. Femtosecond Excitation Dynamics in Gold Nanospheres and Nanorods. *Phys. Rev. B* **2005**, *72*, 235405.

(8) Ramakrishna, G.; Dai, Q.; Zou, J.; Huo, Q.; Goodson III, T. Interparticle Electromagnetic Coupling in Assembled Gold-Necklace Nanoparticles. *J. Am. Chem. Soc.* **2007**, *129*, 1848–1849.

(9) Knight, W. D.; Clemenger, K.; de Heer, W. A.; Saunders, W. A.; Chou, M. Y.; Cohen, M. L. Electronic Shell Structure and Abundances of Sodium Clusters. *Phys. Rev. Lett.* **1984**, *52*, 2141–2143.

(10) Kubo, R.; Kawabata, A.; Kobayashi, S. Electronic Properties of Small Particles. *Annu. Rev. Mater. Sci.* **1984**, *14*, 49–66.

(11) Khanna, S. N.; Jena, P. Assembling Crystals from Clusters. *Phys. Rev. Lett.* **1992**, *69*, 1664–1667.

(12) de Heer, W. A. The Physics of Simple Metal Clusters: Experimental Aspects and Simple Models. *Rev. Mod. Phys.* **1993**, *65*, 611–676.

(13) Schaaff, T. G.; Shafigullin, M. N.; Khoury, J. T.; Vezmar, I.; Whetten, R. L.; Cullen, W. G.; First, P. N.; Gutiérrez-Wing, C.; Ascensio, J.; Jose-Yacamán, M. J. Isolation of Smaller Nanocrystal Au Molecules: Robust Quantum Effects in Optical Spectra. *J. Phys. Chem. B* **1997**, *101*, 7885–7891.

(14) *Nanoscale Materials in Chemistry*; Klabunde, K. J., Ed.; 1st ed.; John Wiley & Sons, Inc.: New York, N. Y., 2001.

(15) Roduner, E. Size Matters: Why Nanomaterials Are Different. *Chem. Soc. Rev.* **2006**, *35*, 583.

(16) Edwards, P. P.; Johnston, R. L.; Rao, C. N. R. On the Size-Induced Metal-Insulator Transition in Clusters and Small Particles. In *Metal Clusters in Chemistry*; Braunstein, P.; Oro, L. A.; Raithby, P. R., Eds.; Wiley-VCH Verlag GmbH: Weinheim, Germany, 1999; pp. 1454–1481.

(17) Peng, S.; McMahon, J. M.; Schatz, G. C.; Gray, S. K.; Sun, Y. Reversing the Size-

Dependence of Surface Plasmon Resonances. *Proc. Natl. Acad. Sci. U. S. A.* **2010**, *107*, 14530–14534.

(18) Maier, S. A.; Brongersma, M. L.; Kik, P. G.; Meltzer, S.; Requicha, A. A. G.; Atwater, H. A. Plasmonics-A Route to Nanoscale Optical Devices. *Adv. Mater.* **2001**, *13*, 1501–1505.

(19) Kreibig, U.; Genzel, L. Optical Absorption of Small Metallic Particles. *Surf. Sci.* **1985**, *156*, 678–700.

(20) Varnavski, O.; Ramakrishna, G.; Kim, J.; Lee, D.; Goodson III, T. Critical Size for the Observation of Quantum Confinement in Optically Excited Gold Clusters. *J. Am. Chem. Soc.* **2010**, *132*, 16–17.

(21) Negishi, Y.; Nakazaki, T.; Malola, S.; Takano, S.; Niihori, Y.; Kurashige, W.; Yamazoe, S.; Tsukuda, T.; Häkkinen, H. A Critical Size for Emergence of Nonbulk Electronic and Geometric Structures in Dodecanethiolate-Protected Au Clusters. *J. Am. Chem. Soc.* **2015**, *137*, 1206–1212.

(22) Jin, R. Quantum Sized, Thiolate-Protected Gold Nanoclusters. *Nanoscale* **2010**, *2*, 343–362.

(23) Whetten, R. L.; Price, R. C. Nano-Golden Order. *Science (80-.).* **2007**, *318*, 407–408.

(24) Walter, M.; Akola, J.; Lopez-Acevedo, O.; Jadzinsky, P. D.; Calero, G.; Ackerson, C. J.; Whetten, R. L.; Grönbeck, H.; Häkkinen, H. A Unified View of Ligand-Protected Gold Clusters as Superatom Complexes. *Proc. Natl. Acad. Sci. U. S. A.* **2008**, *105*, 9157–9162.

(25) Parker, J. F.; Fields-Zinna, C. A.; Murray, R. W. The Story of a Monodisperse Gold Nanoparticle: Au25L18. *Acc. Chem. Res.* **2010**, *43*, 1289–1296.

(26) Tan, Y.; Liu, X. Y.; Zhang, L.; Wang, A.; Li, L.; Pan, X.; Miao, S.; Haruta, M.; Wei, H.; Wang, H.; *et al.* ZnAl-Hydrotalcite-Supported Au 25 Nanoclusters as Precatalysts for Chemoselective Hydrogenation of 3-Nitrostyrene. *Angew. Chem. Int. Ed.* **2017**, *56*, 2709–2713.

(27) Turner, M.; Golovko, V.; Vaughan, owain P. H.; Abdulkin, P.; Berenguer-Murcia, A.; Tikhov, M.; Johnson, B. F. G.; Lambert, R. M. Selective Oxidation with Dioxygen by Gold Nanoparticle Catalysts Derived from 55-Atom Clusters. *Nature* **2008**, *454*, 981–983.

(28) Chen, S.; Ingram, R. S.; Hostetler, M. J.; Pietron, J. J.; Murray, R. W.; Schaaff, T. G.; Khoury, J. T.; Alvarez, M. M.; Whetten, R. L. Gold Nanoelectrodes of Varied Size: Transition to Molecule-like Charging. *Science* **1998**, *280*, 2098–2101.

(29) Polavarapu, L.; Manna, M.; Xu, Q.-H. Biocompatible Glutathione Capped Gold Clusters as One- and Two-Photon Excitation Fluorescence Contrast Agents for Live Cells Imaging. *Nanoscale* **2011**, *3*, 429–434.

(30) Yang, D.; Yang, G.; Gai, S.; He, F.; An, G.; Dai, Y.; Lv, R.; Yang, P.; Lin, J.; Shen, G.; *et al.* Au $_{25}$ Cluster Functionalized Metal–organic Nanostructures for Magnetically Targeted Photodynamic/photothermal Therapy Triggered by Single Wavelength 808 Nm near-Infrared Light. *Nanoscale* **2015**, *7*, 19568–19578.

(31) Nakaya, M.; Iwasa, T.; Tsunoyama, H.; Eguchi, T.; Nakajima, A. Formation and Control of Ultrasharp Metal/Molecule Interfaces by Controlled Immobilization of Size-Selected Metal Nanoclusters onto Organic Molecular Films. *Adv. Funct. Mater.* **2014**, *24*, 1202–1210.

(32) Häkkinen, H. Electronic Shell Structures in Bare and Protected Metal Nanoclusters. *Adv. Phys. X* **2016**, *1*, 467–491.

(33) Kappes, M. M.; Kunz, R. W.; Schumacher, E. Production of Large Sodium Clusters (Nax,.x⩽65) by Seeded Beam Expansions. *Chem. Phys. Lett.* **1982**, *91*, 413–418.

(34) Kappes, M. M.; Radi, P.; Schar, M.; Schumacher, E. Probes for Electronic and Geometrical Shell Structure Effects in Alkali-Metal Clusters. Photoionization Measurements on KxLi, KxMg and KxZn(x < 25). *Chem. Phys. Lett.* **1985**, *119*, 11–16.

(35) Tyo, E. C.; Vajda, S. Catalysis by Clusters with Precise Numbers of Atoms. *Nat. Nanotechnol.* **2015**, *10*, 577–588.

(36) Katakuse, I.; Ichihara, T.; Fujita, Y.; Matsuo, T.; Sakurai, T.; Matsuda, H. Mass Distributions of Copper, Silver and Gold Clusters and Electronic Shell Structure. *Int. J. Mass Spectrom. Ion Process.* **1985**, *67*, 229–236.

(37) Katakuse, I.; Ichihara, T.; Fujita, Y.; Matsuo, T.; Sakurai, T.; Matsuda, H. Correlation between Mass Distributions of Zinc, Cadmium Clusters and Electronic Shell Structure. *Int. J. Mass Spectrom. Ion Process.* **1986**, *69*, 109–114.

(38) de Heer, W. A.; Selby, K.; Kresin, V.; Masui, J.; Vollmer, M.; Chatelain, A.; Knight, W. D. Collective Dipole Oscillations in Small Sodium Clusters. *Phys. Rev. Lett.* **1987**, *59*, 1805–1808.

(39) Zheng, J.; Nicovich, P. R.; Dickson, R. M. Highly Fluorescent Noble-Metal Quantum Dots. *Annu. Rev. Phys. Chem.* **2007**, *58*, 409–431.

(40) Jin, R.; Zeng, C.; Zhou, M.; Chen, Y. Atomically Precise Colloidal Metal

Nanoclusters and Nanoparticles: Fundamentals and Opportunities. *Chem. Rev.* **2016**, *116*, 10346–10413.

(41) Lin, Z.; Kanters, R. P. F.; Mingos, D. M. P. Closed-Shell Electronic Requirements for Condensed Clusters of the Group 11 Elements. *Inorg. Chem.* **1991**, *30*, 91–95.

(42) Mingos, D. M. P. Structural and Bonding Patterns in Gold Clusters. *Dalt. Trans.* **2015**, *44*, 6680–6695.

(43) Ingólfssona, O.; Takeoab, H.; Nonosec, S. Electronic Shell Model Contemplation of the Dissociation Dynamics of Al8+: A Collision-Induced Dissociation Study. *Chem. Phys. Lett.* **1999**, *311*, 421–427.

(44) Becker, S.; Dietrich, G.; Hasse, H.-U.; Klisch, N.; Kluge, H.-J.; Kreisle, D.; Krückeberg, S.; Lindinger, M.; Lützenkirchen, K.; Schweikhard, L.; *et al.* Collision Induced Dissociation of Stored Gold Cluster Ions. *Zeitschrift für Phys. D Atoms, Mol. Clust.* **1994**, *30*, 341–348.

(45) Clemenger, K. Ellipsoidal Shell Structure in Free-Electron Metal Clusters. *Phys. Rev. B* **1985**, *32*, 1359–1362.

(46) Castleman, A. W.; Khanna, S. N. Clusters, Superatoms, and Building Blocks of New Materials. *J. Phys. Chem. C* **2009**, *113*, 2664–2675.

(47) Roy, X.; Lee, C.-H.; Crowther, A. C.; Schenck, C. L.; Besara, T.; Lalancette, R. A.; Siegrist, T.; Stephens, P. W.; Brus, L. E.; Kim, P.; *et al.* Nanoscale Atoms in Solid-State Chemistry. *Science (80-.).* **2013**, *341*, 157–160.

(48) Chauhan, V.; Reber, A. C.; Khanna, S. N. Metal Chalcogenide Clusters with Closed Electronic Shells and the Electronic Properties of Alkalis and Halogens. *J. Am. Chem. Soc.* **2017**, *139*, 1871–1877.

(49) Reber, A. C.; Khanna, S. N. Superatoms: Electronic and Geometric Effects on Reactivity. *Acc. Chem. Res.* **2017**, *50*, 255–263.

(50) Zeng, C.; Chen, Y.; Iida, K.; Nobusada, K.; Kirschbaum, K.; Lambright, K. J.; Jin, R. Gold Quantum Boxes: On the Periodicities and the Quantum Confinement in the Au_{28}, Au_{36}, Au_{44}, and Au_{52} Magic Series. *J. Am. Chem. Soc.* **2016**, *138*, 3950–3953.

(51) Khitrov, G. A.; Strouse, G. F. ZnS Nanomaterial Characterization by MALDI-TOF Mass Spectrometry. **2003**.

(52) Valden, M.; Lai, X.; Goodman, D. W. Onset of Catalytic Activity of Gold Clusters on Titania with the Appearance of Nonmetallic Properties. *Science* **1998**, *281*, 1647–1650.

(53) Brust, M.; Walker, M.; Bethell, D.; Schiffrin, D. J.; Whyman, R. Synthesis of Thiol-Derivatised Gold Nanoparticles in a Two-Phase Liquid-Liquid System. *J. Chem. Soc., Chem. Commun.* **1994**, 801–802.

(54) Chen, S.; Templeton, A. C.; Murray, R. W. Monolayer-Protected Cluster Growth Dynamics. *Langmuir* **2000**, *16*, 3543–3548.

(55) Roux, S.; Garcia, B.; Bridot, J.-L.; Salomé, M.; Marquette, C.; Lemelle, L.; Gillet, P.; Blum, L.; Pascal Perriat, A.; Tillement, O. Synthesis, Characterization of Dihydrolipoic Acid Capped Gold Nanoparticles, and Functionalization by the Electroluminescent Luminol. **2005**.

(56) Kim, J.; Lema, K.; Ukaigwe, M.; Lee, D. Facile Preparative Route to Alkanethiolate-Coated Au38 Nanoparticles: Postsynthesis Core Size Evolution. *Langmuir* **2007**, *23*, 7853–7858.

(57) Perala, S. R. K.; Kumar, S. On the Mechanism of Metal Nanoparticle Synthesis in the Brust-Schiffrin Method. *Langmuir* **2013**, *29*, 9863–9873.

(58) Whetten, R. L.; Khoury, J. T.; Alvarez, M. M.; Murthy, S.; Vezmar, I.; Wang, Z. L.; Stephens, P. W.; Cleveland, C. L.; Luedtke, W. D.; Landman, U. Nanocrystal Gold Molecules. *Adv. Mater.* **1996**, *8*, 428–433.

(59) Terrill, R. H.; Postlethwaite, T. A.; Chen, C.; Poon, C.-D.; Terzis, A.; Chen, A.; Hutchison, J. E.; Clark, M. R.; Wignall, G. Monolayers in Three Dimensions: NMR, SAXS, Thermal, and Electron Hopping Studies of Alkanethiol Stabilized Gold Clusters. *J. Am. Chem. Soc.* **1995**, *117*, 12537–12548.

(60) Brust, M.; Schiffrin, D. J.; Bethell, D.; Kiely, C. J. Novel Gold-Dithiol Nano-Networks with Non-Metallic Electronic Properties. *Adv. Mater.* **1995**, *7*, 795–797.

(61) Leff, D. V.; Ohara, P. C.; Heath, J. R.; Gelbart, W. M. Thermodynamic Control of Gold Nanocrystal Size: Experiment and Theory. *J. Phys. Chem.* **1995**, *99*, 7036–7041.

(62) Templeton, A. C.; Wuelfing, W. P.; Murray, R. W. Monolayer-Protected Cluster Molecules. *Acc. Chem. Res.* **2000**, *33*, 27–36.

(63) Alvarez, M. M.; Khoury, J. T.; Schaaff, T. G.; Shafigullin, M.; Vezmar, I.; Whetten, R. L. Critical Sizes in the Growth of Au Clusters. *Chem. Phys. Lett.* **1997**, *266*, 91–98.

(64) Hostetler, M. J.; Wingate, J. E.; Zhong, C.-J.; Harris, J. E.; Vachet, R. W.; Clark, M. R.; Londono, J. D.; Green, S. J.; Stokes, J. J.; Wignall, G. D.; *et al.* Alkanethiolate Gold Cluster Molecules with Core Diameters from 1.5 to 5.2 Nm:

Core and Monolayer Properties as a Function of Core Size. *Langmuir* **1998**, *14*, 17–30.

(65) Schaaff, T. G.; Knight, G.; Shafigullin, M. N.; Borkman, R. F.; Whetten, R. L. Isolation and Selected Properties of a 10.4 kDa Gold:Glutathione Cluster Compound. *J. Phys. Chem. B* **1998**, *102*, 10643–10646.

(66) Link, S.; Beeby, A.; FitzGerald, S.; El-Sayed, M. A.; Schaaff, T. G.; Whetten, R. Visible to Infrared Luminescence from a 28-Atom Gold Cluster. *J. Phys. Chem. B* **2002**, *106*, 3410–3415.

(67) Donkers, R. L.; Lee, D.; Murray, R. W. Synthesis and Isolation of the Molecule-like Cluster Au38(PhCH2CH2S)24. *Langmuir* **2004**, *20*, 1945–1952.

(68) Negishi, Y.; Takasugi, Y.; Sato, S.; Yao, H.; Keisaku Kimura, A.; Tatsuya Tsukuda. Magic-Numbered Aun Clusters Protected by Glutathione Monolayers (N = 18, 21, 25, 28, 32, 39): Isolation and Spectroscopic Characterization. **2004**.

(69) Zhu, M.; Lanni, E.; Garg, N.; Bier, M. E.; Jin, R. Kinetically Controlled, High-Yield Synthesis of Au25 Clusters. *J. Am. Chem. Soc.* **2008**, *130*, 1138–1139.

(70) Wu, Z.; Suhan, J.; Jin, R. One-Pot Synthesis of Atomically Monodisperse, Thiol-Functionalized Au 25 Nanoclusters. *J. Mater. Chem.* **2009**, *19*, 622–626.

(71) Jin, R.; Qian, H.; Wu, Z.; Zhu, Y.; Zhu, M.; Mohanty, A.; Garg, N. Size Focusing: A Methodology for Synthesizing Atomically Precise Gold Nanoclusters. *J. Phys. Chem. Lett.* **2010**, *1*, 2903–2910.

(72) Qian, H.; Zhu, M.; Andersen, U. N.; Jin, R. Facile, Large-Scale Synthesis of Dodecanethiol-Stabilized Au 38 Clusters. *J. Phys. Chem. A* **2009**, *113*, 4281–4284.

(73) Qian, H.; Zhu, Y.; Jin, R. Size-Focusing Synthesis, Optical and Electrochemical Properties of Monodisperse $Au_{38}(SC_2H_4Ph)_{24}$ Nanoclusters. *ACS Nano* **2009**, *3*, 3795–3803.

(74) Qian, H.; Jin, R. Controlling Nanoparticles with Atomic Precision: The Case of $Au_{144}(SCH_2CH_2Ph)_{60}$. *Nano Lett.* **2009**, *9*, 4083–4087.

(75) Negishi, Y.; Nobusada, K.; Tsukuda, T. Glutathione-Protected Gold Clusters Revisited: Bridging the Gap between gold(I)-Thiolate Complexes and Thiolate-Protected Gold Nanocrystals. *J. Am. Chem. Soc.* **2005**, *127*, 5261–5270.

(76) Tracy, J. B.; Crowe, M. C.; Parker, J. F.; Hampe, O.; Fields-Zinna, C. A.; Dass, A.; Murray, R. W. Electrospray Ionization Mass Spectrometry of Uniform and Mixed Monolayer Nanoparticles: Au 25 [S(CH 2) 2 Ph] 18 and Au 25 [S(CH 2) 2 Ph] 18 - X (SR) X. *J. Am. Chem. Soc.* **2007**, *129*, 16209–16215.

(77) Tracy, J. B.; Kalyuzhny, G.; Crowe, M. C.; Balasubramanian, R.; Choi, J.-P.; Murray, R. W. Poly(ethylene Glycol) Ligands for High-Resolution Nanoparticle Mass Spectrometry. *J. Am. Chem. Soc.* **2007**, *129*, 6706–6707.

(78) Shichibu, Y.; Negishi, Y.; Tsunoyama, H.; Kanehara, M.; Teranishi, T.; Tsukuda, T. Extremely High Stability of Glutathionate-Protected Au25 Clusters Against Core Etching. *Small* **2007**, *3*, 835–839.

(79) Negishi, Y.; Chaki, N. K.; Shichibu, Y.; Whetten, R. L.; Tsukuda, T. Origin of Magic Stability of Thiolated Gold Clusters: A Case Study on Au25(SC6H13)18. *J. Am. Chem. Soc.* **2007**, *129*, 11322–11323.

(80) Weerawardene, K. L. D. M.; Aikens, C. M. Theoretical Insights into the Origin of Photoluminescence of Au25(SR)18- Nanoparticles. *J. Am. Chem. Soc.* **2016**, *138*, 11202–11210.

(81) Akola, J.; Walter, M.; Whetten, R. L.; Häkkinen, H.; Grönbeck, H. On the Structure of Thiolate-Protected Au25. *J. Am. Chem. Soc.* **2008**, *130*, 3756–3757.

(82) Zhu, M.; Aikens, C. M.; Hollander, F. J.; Schatz, G. C.; Jin, R. Correlating the Crystal Structure of a Thiol-Protected Au25 Cluster and Optical Properties. *J. Am. Chem. Soc.* **2008**, *130*, 5883–5885.

(83) Heaven, M. W.; Dass, A.; White, P. S.; Holt, K. M.; Murray, R. W. Crystal Structure of the Gold Nanoparticle [N(C8H17)4][Au25(SCH2CH2Ph)18]. *J. Am. Chem. Soc.* **2008**, *130*, 3754–3755.

(84) Zhu, M.; Eckenhoff, W. T.; Pintauer, T.; Jin, R. Conversion of Anionic [$Au_{25}(SCH_2CH_2Ph)_{18}]^-$ Cluster to Charge Neutral Cluster via Air Oxidation. *J. Phys. Chem. C* **2008**, *112*, 14221–14224.

(85) Jadzinsky, P. D.; Calero, G.; Ackerson, C. J.; Bushnell, D. A.; Kornberg, R. D. Structure of a Thiol Monolayer-Protected Gold Nanoparticle at 1.1 A Resolution. *Science (80-.).* **2007**, *318*, 430–433.

(86) Häkkinen, H.; Walter, M.; Grönbeck, H. Divide and Protect: Capping Gold Nanoclusters with Molecular Gold−Thiolate Rings. *J. Phys. Chem. B* **2006**, *110*, 9927–9931.

(87) Parker, J. F.; Kacprzak, K. A.; Lopez-Acevedo, O.; Häkkinen, H.; Murray, R. W. Experimental and Density Functional Theory Analysis of Serial Introductions of Electron-Withdrawing Ligands into the Ligand Shell of a Thiolate-Protected Au 25 Nanoparticle. *J. Phys. Chem. C* **2010**, *114*, 8276–8281.

(88) Fernando, A.; Aikens, C. M. Ligand Exchange Mechanism on Thiolate Monolayer

Protected Au 25 (SR) 18 Nanoclusters. *J. Phys. Chem. C* **2015**, *119*, 20179–20187.

(89) Heinecke, C. L.; Ni, T. W.; Malola, S.; Mäkinen, V.; Wong, O. A.; Häkkinen, H.; Ackerson, C. J. Structural and Theoretical Basis for Ligand Exchange on Thiolate Monolayer Protected Gold Nanoclusters. *J. Am. Chem. Soc.* **2012**, *134*, 13316–13322.

(90) Shibu, E. S.; Muhammed, M. A. H.; Tsukuda, T.; Pradeep, T. Ligand Exchange of Au 25 SG 18 Leading to Functionalized Gold Clusters: Spectroscopy, Kinetics, and Luminescence. *J. Phys. Chem. C* **2008**, *112*, 12168–12176.

(91) Si, S.; Gautier, C.; Boudon, J.; Taras, R.; Gladiali, S.; Bürgi, T. Ligand Exchange on Au $_{25}$ Cluster with Chiral Thiols. *J. Phys. Chem. C* **2009**, *113*, 12966–12969.

(92) Varnholt, B.; Letrun, R.; Bergkamp, J. J.; Fu, Y.; Yushchenko, O.; Decurtins, S.; Vauthey, E.; Liu, S.-X.; Bürgi, T. Excited State Interactions between the Chiral Au38L24 Cluster and Covalently Attached Porphyrin. *Phys. Chem. Chem. Phys.* **2015**, *17*, 14788–14795.

(93) Devadas, M. S.; Kwak, K.; Park, J.-W.; Choi, J.-H.; Jun, C.-H.; Sinn, E.; Ramakrishna, G.; Lee, D. Directional Electron Transfer in Chromophore-Labeled Quantum-Sized Au 25 Clusters: Au 25 as an Electron Donor. *J. Phys. Chem. Lett.* **2010**, *1*, 1497–1503.

(94) Zeng, C.; Liu, C.; Pei, Y.; Jin, R. Thiol Ligand-Induced Transformation of Au $_{38}$ (SC $_{2}$ H $_{4}$ Ph) $_{24}$ to Au $_{36}$ (SPh- *T* -Bu) $_{24}$. *ACS Nano* **2013**, *7*, 6138–6145.

(95) Shichibu, Y.; Negishi, Y.; Tsukuda, T.; Teranishi, T. Large-Scale Synthesis of Thiolated Au25 Clusters via Ligand Exchange Reactions of Phosphine-Stabilized Au11 Clusters. *J. Am. Chem. Soc.* **2005**, *127*, 13464–13465.

(96) Chen, Y.; Liu, C.; Tang, Q.; Zeng, C.; Higaki, T.; Das, A.; Jiang, D.; Rosi, N. L.; Jin, R. Isomerism in Au $_{28}$ (SR) $_{20}$ Nanocluster and Stable Structures. *J. Am. Chem. Soc.* **2016**, *138*, 1482–1485.

(97) Tang, Q.; Ouyang, R.; Tian, Z.; Jiang, D. The Ligand Effect on the Isomer Stability of Au $_{24}$ (SR) $_{20}$ Clusters. *Nanoscale* **2015**, *7*, 2225–2229.

(98) Zeng, C.; Chen, Y.; Das, A.; Jin, R. Transformation Chemistry of Gold Nanoclusters: From One Stable Size to Another. *J. Phys. Chem. Lett.* **2015**, *6*, 2976–2986.

(99) Ispasoiu, R. G.; Jin, Y.; Lee, J.; Papadimitrakopoulos, F.; Goodson III, T. Two-Photon Absorption and Photon-Number Squeezing with CdSe Nanocrystals. *Nano Lett.* **2002**, *2*, 127–130.

(100) Ispasoiu, R. G.; Balogh, L.; Varnavski, O. P.; Tomalia, D. A.; Goodson III, T. Large Optical Limiting from Novel Metal−Dendrimer Nanocomposite Materials. *J. Am. Chem. Soc.* **2000**, *122*, 11005–11006.

(101) Varnavski, O.; Ispasoiu, R. G.; Balogh, L.; Tomalia, D.; Goodson III, T. Ultrafast Time-Resolved Photoluminescence from Novel Metal–dendrimer Nanocomposites. *J. Chem. Phys.* **2001**, *114*, 1962.

(102) Ispasoiu, R. G.; Lee, J.; Papadimitrakopoulos, F.; Goodson III, T. Surface Effects in the Fluorescence Ultra-Fast Dynamics from CdSe Nano-Crystals. *Chem. Phys. Lett.* **2001**, *340*, 7–12.

(103) Varnavski, O. P.; Mohamed, M. B.; El-Sayed, M. A.; Goodson III, T. Relative Enhancement of Ultrafast Emission in Gold Nanorods. *J. Phys. Chem. B* **2003**, *107*, 3101–3104.

(104) West, R.; Wang, Y.; Goodson III, T. Nonlinear Absorption Properties in Novel Gold Nanostructured Topologies. *J. Phys. Chem. B* **2003**, *107*, 3419–3426.

(105) Wang, Y.; Xie, X.; Goodson III, T. Enhanced Third-Order Nonlinear Optical Properties in Dendrimer-Metal Nanocomposites. *Nano Lett.* **2005**, *5*, 2379–2384.

(106) Wu, Z.; Jin, R. On the Ligand's Role in the Fluorescence of Gold Nanoclusters. *Nano Lett.* **2010**, *10*, 2568–2573.

(107) GoodsonIII, T.; Varnavski, O.; Wang, Y. Optical Properties and Applications of Dendrimer-Metal Nanocomposites. *Int. Rev. Phys. Chem.* **2004**, *23*, 109–150.

(108) Mooradian, A. Photoluminescence of Metals. *Phys. Rev. Lett.* **1969**, *22*, 185–187.

(109) Yau, S. H.; Varnavski, O.; Goodson III, T. An Ultrafast Look at Au Nanoclusters. *Acc. Chem. Res.* **2013**, *46*, 1506–1516.

(110) Devadas, M. S.; Kim, J.; Sinn, E.; Lee, D.; Goodson III, T.; Ramakrishna, G. Unique Ultrafast Visible Luminescence in Monolayer-Protected Au 25 Clusters. *J. Phys. Chem. C* **2010**, *114*, 22417–22423.

(111) Yau, S. H.; Ashenfelter, B.; Desireddy, A.; Ashwell, A. P.; Varnavski, O.; Schatz, G. C.; Bigioni, T.; Goodson III, T. Optical Properties and Structural Relationships of the Silver Nanoclusters Ag32(SG)19 and Ag15(SG)11. *J. Phys. Chem. C* **2017**, *121*, 1349–1361.

(112) Ashenfelter, B. A.; Desireddy, A.; Yau, S. H.; Goodson III, T.; Bigioni, T. P. Fluorescence from Molecular Silver Nanoparticles. *J. Phys. Chem. C* **2015**, *119*, 20728–20734.

(113) Yau, S. H.; Varnavski, O.; Gilbertson, J. D.; Chandler, B.; Ramakrishna, G.; Goodson III, T. Ultrafast Optical Study of Small Gold Monolayer Protected Clusters: A Closer Look at Emission. *J. Phys. Chem. C* **2010**, *114*, 15979–15985.

(114) Abeyasinghe, N.; Kumar, S.; Sun, K.; Mansfield, J. F.; Jin, R.; Goodson III, T. Enhanced Emission from Single Isolated Gold Quantum Dots Investigated Using Two-Photon-Excited Fluorescence Near-Field Scanning Optical Microscopy. *J. Am. Chem. Soc.* **2016**, *138*, 16299–16307.

(115) Devadas, M. S.; Thanthirige, V. D.; Bairu, S.; Sinn, E.; Ramakrishna, G. Temperature-Dependent Absorption and Ultrafast Luminescence Dynamics of Bi-Icosahedral Au 25 Clusters. *J. Phys. Chem. C* **2013**, *117*, 23155–23161.

(116) Devadas, M. S.; Bairu, S.; Qian, H.; Sinn, E.; Jin, R.; Ramakrishna, G. Temperature-Dependent Optical Absorption Properties of Monolayer-Protected Au 25 and Au 38 Clusters. *J. Phys. Chem. Lett.* **2011**, *2*, 2752–2758.

(117) Yau, S. H.; Abeyasinghe, N.; Orr, M.; Upton, L.; Varnavski, O.; Werner, J. H.; Yeh, H.-C.; Sharma, J.; Shreve, A. P.; Martinez, J. S.; *et al.* Bright Two-Photon Emission and Ultra-Fast Relaxation Dynamics in a DNA-Templated Nanocluster Investigated by Ultra-Fast Spectroscopy. *Nanoscale* **2012**, *4*, 4247–4254.

(118) Qian, H.; Sfeir, M. Y.; Jin, R. Ultrafast Relaxation Dynamics of [Au25(SR)18]q Nanoclusters: Effects of Charge State. *J. Phys. Chem. C* **2010**, *114*, 19935–19940.

(119) Yi, C.; Tofanelli, M. A.; Ackerson, C. J.; Knappenberger, K. L. Optical Properties and Electronic Energy Relaxation of Metallic Au $_{144}$ (SR) $_{60}$ Nanoclusters. *J. Am. Chem. Soc.* **2013**, *135*, 18222–18228.

(120) Miller, S. A.; Womick, J. M.; Parker, J. F.; Murray, R. W.; Moran, A. M. Femtosecond Relaxation Dynamics of Au 25 L 18 − Monolayer-Protected Clusters. *J. Phys. Chem. C* **2009**, *113*, 9440–9444.

(121) Biswas, A.; Banerjee, S.; Gart, E. V.; Nagaraja, A. T.; McShane, M. J. Gold Nanocluster Containing Polymeric Microcapsules for Intracellular Ratiometric Fluorescence Biosensing. *ACS Omega* **2017**, *2*, 2499–2506.

(122) Ho-Wu, R.; Yau, S. H.; Goodson III, T. Efficient Singlet Oxygen Generation by High Absorption-to-Volume Ratio Metal Nanoclusters. *J. Phys. Chem. B* **2017**, *Submitted*.

(123) Wang, S.; Zhu, X.; Cao, T.; Zhu, M. A Simple Model for Understanding the Fluorescence Behavior of Au25 Nanoclusters. *Nanoscale* **2014**, *6*, 5777–5781.

(124) Yang, X.; Hernandez-Martinez, P. L.; Dang, C.; Mutlugun, E.; Zhang, K.; Demir, H. V.; Sun, X. W. Electroluminescence Efficiency Enhancement in Quantum Dot

Light-Emitting Diodes by Embedding a Silver Nanoisland Layer. *Adv. Opt. Mater.* **2015**, *3*, 1439–1445.

(125) Pyo, K.; Thanthirige, V. D.; Kwak, K.; Pandurangan, P.; Ramakrishna, G.; Lee, D. Ultrabright Luminescence from Gold Nanoclusters: Rigidifying the Au(I)-Thiolate Shell. *J. Am. Chem. Soc.* **2015**, *137*, 8244–8250.

(126) Wang, S.; Meng, X.; Das, A.; Li, T.; Song, Y.; Cao, T.; Zhu, X.; Zhu, M.; Jin, R. A 200-Fold Quantum Yield Boost in the Photoluminescence of Silver-Doped Ag(x)Au(25-X) Nanoclusters: The 13th Silver Atom Matters. *Angew. Chem. Int. Ed. Engl.* **2014**, *53*, 2376–2380.

(127) Yu, Y.; Luo, Z.; Chevrier, D. M.; Leong, D. T.; Zhang, P.; Jiang, D.; Xie, J. Identification of a Highly Luminescent Au22(SG)18 Nanocluster. *J. Am. Chem. Soc.* **2014**, *136*, 1246–1249.

(128) Luo, Z.; Yuan, X.; Yu, Y.; Zhang, Q.; Leong, D. T.; Lee, J. Y.; Xie, J. From Aggregation-Induced Emission of Au(I)-Thiolate Complexes to Ultrabright Au(0)@Au(I)-Thiolate Core-Shell Nanoclusters. *J. Am. Chem. Soc.* **2012**, *134*, 16662–16670.

(129) Dou, X.; Yuan, X.; Yu, Y.; Luo, Z.; Yao, Q.; Leong, D. T.; Xie, J. Lighting up Thiolated Au@Ag Nanoclusters via Aggregation-Induced Emission. *Nanoscale* **2014**, *6*, 157–161.

(130) Green, T. D.; Yi, C.; Zeng, C.; Jin, R.; McGill, S.; Knappenberger Jr, K. L. Temperature-Dependent Photoluminescence of Structurally-Precise Quantum-Confined Au25(SC8H9)18 and Au38(SC12H25)24 Metal Nanoparticles. *J. Phys. Chem. A* **2014**, *118*, 10611–10621.

(131) Ramakrishna, G.; Varnavski, O.; Kim, J.; Lee, D.; Goodson III, T. Quantum-Sized Gold Clusters as Efficient Two-Photon Absorbers. *J. Am. Chem. Soc.* **2008**, *130*, 5032–5033.

(132) Pawlicki, M.; Collins, H. A.; Denning, R. G.; Anderson, H. L. Two-Photon Absorption and the Design of Two-Photon Dyes. *Angew. Chem. Int. Ed. Engl.* **2009**, *48*, 3244–3266.

(133) Knoppe, S.; Vanbel, M.; van Cleuvenbergen, S.; Vanpraet, L.; Bürgi, T.; Verbiest, T. Nonlinear Optical Properties of Thiolate-Protected Gold Clusters. *J. Phys. Chem. C* **2015**, *119*, 6221–6226.

(134) Philip, R.; Chantharasupawong, P.; Qian, H.; Jin, R.; Thomas, J. Evolution of Nonlinear Optical Properties: From Gold Atomic Clusters to Plasmonic Nanocrystals. *Nano Lett.* **2012**, *12*, 4661–4667.

(135) De Nardi, M.; Antonello, S.; Jiang, D.; Pan, F.; Rissanen, K.; Ruzzi, M.; Venzo, A.; Zoleo, A.; Maran, F. Gold Nanowired: A Linear (Au 25) N Polymer from Au 25 Molecular Clusters. *ACS Nano* **2014**, *8*, 8505–8512.

(136) Mai, H. H.; Kaydashev, V. E.; Tikhomirov, V. K.; Janssens, E.; Shestakov, M. V.; Meledina, M.; Turner, S.; Van Tendeloo, G.; Moshchalkov, V. V.; Lievens, P. Nonlinear Optical Properties of Ag Nanoclusters and Nanoparticles Dispersed in a Glass Host. *J. Phys. Chem. C* **2014**, *118*, 15995–16002.

(137) Khanna, S. N.; Jena, P. Atomic Clusters: Building Blocks for a Class of Solids. *Phys. Rev. B* **1995**, *51*, 13705–13716.

(138) Claridge, S. A.; Castleman, A. W.; Khanna, S. N.; Murray, C. B.; Sen, A.; Weiss, P. S. Cluster-Assembled Materials. *ACS Nano* **2009**, *3*, 244–255.

(139) Nishigaki, J.; Koyasu, K.; Tsukuda, T. Chemically Modified Gold Superatoms and Superatomic Molecules. *Chem. Rec.* **2014**, *14*, 897–909.

(140) Jiang, D.; Nobusada, K.; Luo, W.; Whetten, R. L. Thiolated Gold Nanowires: Metallic *versus* Semiconducting. *ACS Nano* **2009**, *3*, 2351–2357.

(141) Akola, J.; Kacprzak, K. A.; Lopez-Acevedo, O.; Walter, M.; Grönbeck, H.; Häkkinen, H. Thiolate-Protected Au 25 Superatoms as Building Blocks: Dimers and Crystals. *J. Phys. Chem. C* **2010**, *114*, 15986–15994.

Chapter 2

Experimental Techniques

General background information and operational details are presented in this chapter. These techniques are used in the publications which are presented in the later chapters. This chapter serves to aid the reader in familiarizing with the techniques and the type of information which can be extracted from them, allowing the reader to gain a better understanding on the materials that are being investigated in the subsequent chapters.

2.1. Synthesis of the $Au_{25}(SR)_{18}$ metal nanocluster

In the quest to finding a synthetic methodology to produce *monodisperse* metal nanoclusters, that is, metal nanoclusters which are uniform in size with atomic precision, scientists have scrutinized and revolutionized the original Brust's method of thiolate-protected gold nanoparticle synthesis in order to allow them greater control over the course of the synthesis to obtain metal nanoclusters of the desirable size. One successful outcome of the endeavor is the one-pot synthesis of monodisperse $Au_{25}(SR)_{18}$ nanocluster.

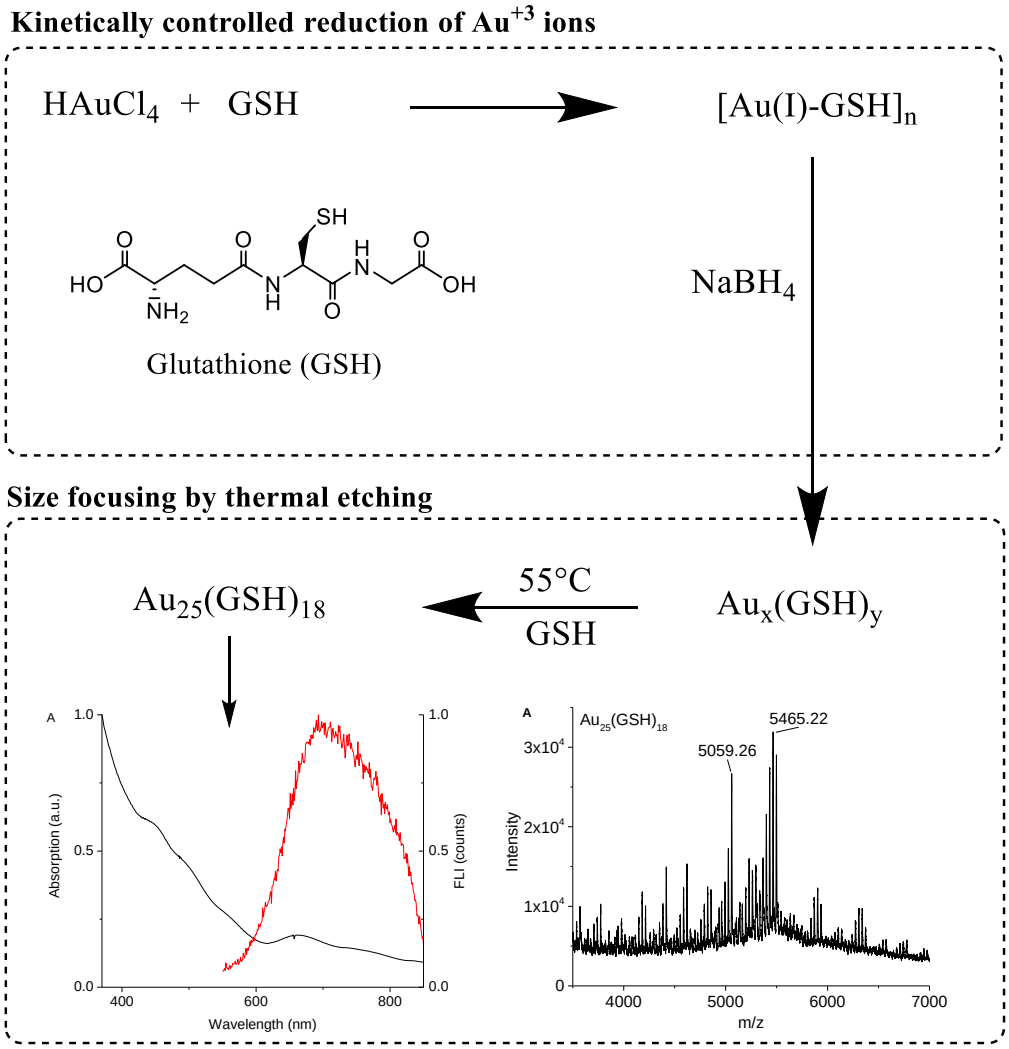

Figure 2.1. One-pot synthesis of the $Au_{25}(GSH)_{18}$ nanocluster.

Monodisperse $Au_{25}(SR)_{18}$ nanoclusters are synthesized by the size-focusing method which is first reported by professor Rongchao Jin's lab (Figure 2.1). This method consists of two reaction stages. The first stage is the kinetically controlled reduction of a Au^{3+} salt. A solution of $HAuCl_4 \cdot 3H_2O$ (170 mg, 0.5 mmol) is prepared in methanol (100 mL) and chilled in an ice bath for 15 min. A water-soluble capping ligand, glutathione ($C_{10}H_{17}N_3O_6S$; GSH) (614 mg, 2 mmol), is then added to the solution and stirred for 30 min. The solution turns from the initial yellow color to a white/clear solution which indicates the formation of Au(I)-GSH polymer. The Au(I)-GSH polymer is then further

reduced by a stronger reducing agent. A freshly prepared $NaBH_4$ (189 mg, 5 mmol) solution (25 mL H_2O) is added dropwise to the reaction mixture and is stirred for 1 h. The solution turns into a dark brown color, indicative of nanoclusters formation. These nanoclusters, however, consist of various sizes. Prior to the adaptation of the size-focusing method, these nanoclusters were usually separated by physical separation techniques such as gel electrophoresis.

The second stage of the reaction is the size-focusing method. During the size-focusing process, the nanoclusters are subjected to the thiol etching. This method, indeed, capitalizes on the concept of "magic clusters" which means that specific sizes of nanoclusters are highly stable. In the case of the reaction just described, incubating the nanoclusters with excess glutathione at 55°C for 3 h causes the decomposition of the less stable sizes. This process is termed by prof. Rongchao Jin as "the survival of the robustest." The result of this synthesis is a monodisperse solution of $Au_{25}(SR)_{18}$. This synthetic strategy is now well documented to yield $Au_{25}(SR)_{18}$ nanoclusters. This procedure is a breakthrough in nanocluster synthesis because it is time effective: one can now perform this procedure and obtain $Au_{25}(SR)_{18}$ nanoclusters without the need to perform separation or characterization. The $Au_{25}(SR)_{18}$ nanocluster has a distinct absorption spectrum which can be used to quickly evaluate the reaction product.

2.2. Ligand exchange reaction of metal nanoclusters

Ligand exchange reaction is a widely used method for functionalizing metal nanomaterials.[1–4] The ligand exchange process has been shown to follow an associative S_{N2} mechanism on the metal atom exposed to solvent molecules.[1,5,6] Typically, this is the atom at the vertexes of a –S-M-S- organometallic staple motif. Additionally, ligand exchange reaction has also been proved to induce structural changes to the nanocluster

itself, such as isomerization of the nanocluster's core and structural deformation.[7–10] The thermal etching step in the $Au_{25}(SR)_{18}$ synthesis is an example of structural deformation. Therefore, nanoclusters which can not be obtained by direct synthesis can be obtained by ligand exchange reaction. Predicting the outcome of a ligand exchange reaction is challenging without a systematic study, but the results from published work suggest that the type of outcome largely depends on the steric hindrance of incoming ligand, stability of the nanocluster's isomer, magnitude of bond distortion during the exchange reaction, and type of nanoclusters.

Focusing on the reaction of a simple ligand exchange (preserving the nanocluster's core integrity), there has been an interest in using dithiols as the new functional ligand for the exchange reaction.[11–16] This interest stems from the observed colloidal stability improvement of gold nanoparticles upon dithiol binding.[11] The reason for this stability is due to an entropy gain, specifically in the enhancement of the equilibrium binding constant, which is observed in metal complexes with multidentate ligands.[15] However, it was first thought that bulky dithiols cause decomposition of the nanoclusters in an attempt to do ligand exchange.[15–17] In later reports, after mass spectrometry characterization of the dithiol exchange product, it was shown that ligand exchange was successful and that the aromatic dithiol binding mode was inter-staple.[12,18] Moreover, density functional theory predictions indicate that the electronic levels are minimally affected, therefore the nanoclusters retain their structure.[12]

There is also an interest in understanding the surface binding and structure of monolayer-protected metal nanoclusters because changes in the surface structure affects the physicochemical and electronic properties of the nanoclusters.[13,14] For example, the

dithiol exchange of 2,3-dithiol dimercaptopropane sulfonate into the monolayer of a Au nanocluster quenches the near-IR emission of the nanocluster.[14]

Chapter 4 will be focused on covalently-linked nanocluster-dye-nanocluster systems. To synthesize these nanosystems, a dithiol exchange reaction with $Au_{25}(GSH)_{18}$ nanoclusters is employed. Although it was generally thought that bulky dithiols (as it is the case in organic dyes) in excess cause the nanocluster's decomposition, it was demonstrated by mass spectrometry analysis that even a very sterically hindered dithiol such as BINAS can be successfully exchanged into the nanocluster's monolayer.[12,18] The BINAS dithiol was shown to bind between two staple motifs on the Au_{25} nanocluster.[17,18] This was possible due to the positioning of the thiol groups which are on the same side of the binaphthyl unit. Inter-staple binding was also observed in short chains alkane dithiolates.[12] In that report, Dass et al also observed that the alkane dithiolates can form inter-cluster binding. For the purpose of this thesis, the same dithiolate exchange method was employed to form nanocluster oligomers that are linked by a chromophore. To prevent inter-staple binding, it was essential to choose a chromophore linker with terminal dithiols. Additionally, the chromophore linker must have some degree of structural rigidity to prevent coiling as in the case of the alkane dithiols.

Other parameters to consider for the ligand exchange reaction are number of ligands in solution, reaction time and temperature.[1,12] The excess of any one of these parameters can speed up the extent of the reaction and can also lead to the decomposition of the nanocluster.[12]

2.3. Steady state absorption and emission

The steady state spectroscopy provides the initial information on the optical properties of the system under study. This includes absorption and emission, in which the

excited state of a molecule exists as a constant over time. This initial information is then further expanded and elaborated by ultrafast time-resolved spectroscopy which gives the absorption and emission processes a time resolution. Non-linear optical properties are also based on this initial information.

The absorption of light by a material corresponds to specific atomic or molecular orbital transitions. During this transition, the electrons of an atom or molecule are promoted from the low energy ground state to a higher energy excited state. Therefore, the wavelength of light that is absorbed corresponds to the energy required to achieve this transition. This transition occurs in the 200-800 nm region, approximately, of the electromagnetic spectrum, which can be measured by commercially available ultraviolet-visible (UV-vis) spectrophotometers. The Beer-Lambert law describes UV-vis absorption spectroscopy analytically (equation 3.1). The absorption of light, *A*, is simply the ratio of the light intensity that is absorbed, *I*, over the initial intensity, I_0. More useful information can be obtained by the equation, such as the molar extinction coefficient, ε, which is a measure of the extent of light absorption, or the concentration, [C], with a known path length of *l*. Additionally, the UV-vis spectroscopy can also provide a qualitative analysis of a molecule, such as changes in the molecule's surrounding and molecule's degradation.

$$A = \log\left(\frac{I_0}{I}\right) = \epsilon[\mathrm{C}]l \qquad (2.1)$$

The spectrophotometer used for the projects in this thesis is an *Agilent model 8341* equipped with deuterium and tungsten lamps which provides a spectrum range of 200 - 1100 nm. Sample solutions are contained in quartz cuvettes manufactured by Starna Cells, with an optical path of 1 cm. For ultrafast spectroscopy experiments, the absorption

at the excitation wavelength is adjusted to prevent saturation on the PMT. The spectrophotometer is typically blanked with the cuvette with solvent or air to correct variation of the refractive index.

Steady state emission is the process of relaxation by a molecule in the excited state in which photons of specific wavelengths are emitted. A molecule is first excited (absorption) and some of the energy absorbed is lost by vibrational relaxation to a lower energy, then emission occurs. Therefore, emission usually occurs at lower energy wavelengths than the excitation. Additionally, energy can be dispersed through competitive relaxation mechanisms. Therefore, emission produces less photons than what is initially absorbed. The efficiency of an emission process can be expressed as emission quantum yield which is the ratio of photons emitted over photons absorbed. It can be calculated experimentally by equation 3.2.

$$\Phi_x = \Phi_{std} \frac{Grad_x}{Grad_{std}} \frac{\eta_x^2}{\eta_{std}^2} \tag{2.2}$$

A standard of a known quantum yield, Φ_{std}, is used for calculating the relative quantum yield of a sample, Φ_x. In a typical experiment, a series of solutions of different concentrations of the sample and the standard are prepared, and the emission of each is measured in a fluorimeter. The areas of fluorescence curves are integrated and plotted against the concentrations. This will yield a linear plot, with a slope of $Grad_x$ or $Grad_{std}$. The refractive indexes of the solvents are also taken into consideration to correct differences in the spectra, η.

The fluorimeter that is used in the projects of this thesis is a Fluoromax-2 by Horiba, equipped with a xenon lamp which produces the excitation wavelengths. The emission is

collected by a photomultiplier tube (PMT) with a diffraction grating that is positioned 90° from the excitation source. The solutions are contained in quartz cuvettes by Starna Cells. The fluorimeter is also used for measuring the excitation spectrum of a sample. Typically, the emission maximum is chosen to be monitored. The intensity of the emission maximum is recorded as the instrument scans through a range of excitation wavelengths. The maximum intensity of an excitation spectrum corresponds to the excitation wavelength which results in the strongest emission. Usually the excitation spectrum is the same as the absorption spectrum, but it need not be always the case; in other words, it does not necessarily mean the strongest absorption.

2.4. Time-resolved fluorescence upconversion

The fluorescence dynamics of a molecule can be investigated by time-resolved fluorescence upconversion. This technique allows one to monitor the emission *process* over time which yields information about the electronic processes at the excited state such as energy transfer or charge transfer. These processes occur on the time scale of femtosecond and picosecond.

The fluorescence upconversion set-up in our laboratory consists of multiple parts as illustrated in Figure 2.2. Our pump laser is a Millennia that produces a 532 nm beam which enters into a cavity, the Tsunami, manufactured by Spectra Physics. The gain medium is a Ti:sapphire crystal which produces a near IR beam. The system is made to mode-lock to produce pulsed laser. This is done by gently disturbing the prism and monitoring the laser spectrum with an Ocean Optics. A laser in the continuous wave mode (cw) is characterized by a very narrow emission peak, whereas a pulsed laser has a broader spectrum. In addition, the peak power of a pulsed laser is higher than a cw laser.

The peak power from our Tsunami is usually ~700 mW. The pulses are 120 fs in duration, and the repetition rate is 82 MHz. The optics set-up for fluorescence upconversion is contained by the FOG-100 system by CDP, Inc. A non-linear crystal (NC1 in the diagram), which is a β-barium borate (BBO), is positioned in the beam path and up-converts the laser beam to a 400 nm light by second harmonic generation. The upconverted beam and residual 800 nm arrive at a dichromic mirror which reflects the 400 nm beam and transmit the 800 nm beam.

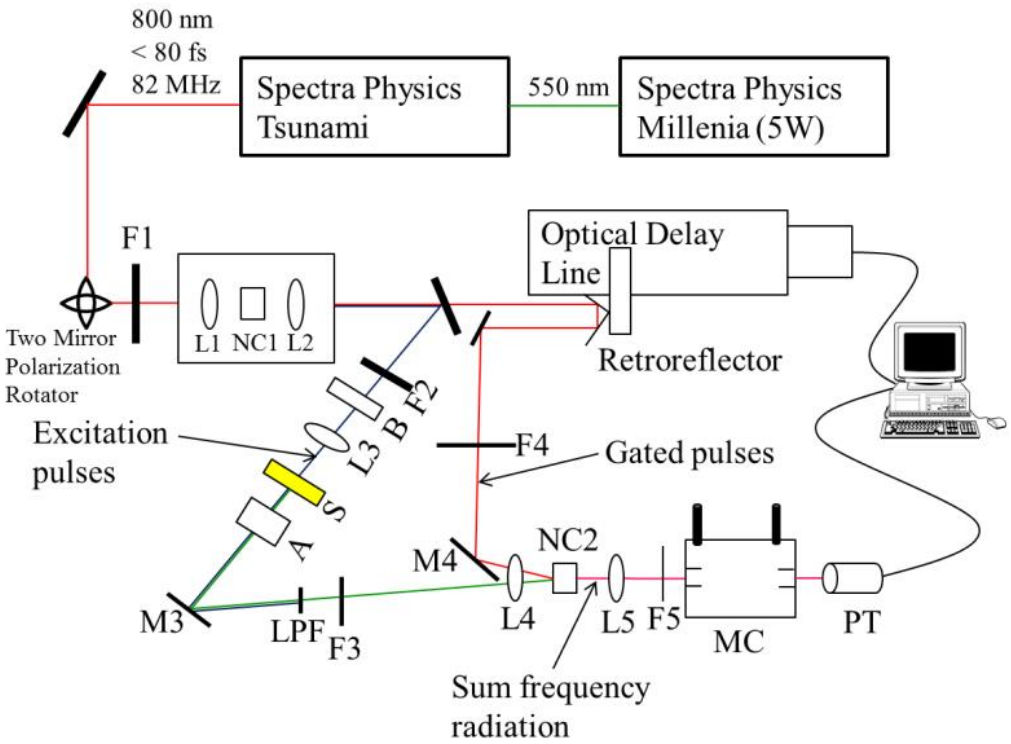

Figure 2.2. Time-resolved fluorescence upconversion set-up diagram.

The 400 nm is directed through a series of focusing lenses and filters to modulate the laser power, and focuses in the sample solution. The sample solution is contained in a rotating cell holder. The cell consists of 2 quartz windows spaced with a Teflon ring to give an optical path length of 1 mm. The rotating cell is fitted with a plastic belt which connects to a motor that gives a moderate rotation speed. This is done to prevent photo-

damage to the sample. Additionally, the absorption spectrum is measured before and after upconversion measurements to verify the sample stability. A Berek compensator, B, is position on the beam path to control the polarization of the beam. In this case, a perpendicular polarization is used.

The residual 800 nm beam enters into the optical delay line which produces a gated pulse that allows for time-resolved measurements. The position of the retroreflector in the delay line is controlled by the computer, and corresponds to the distance the beam travels. The distance the beam travels translates into the time it travels.

The fluorescence of the sample is mixed with the gated pulse on a second BBO (NC2) which spatially and temporally overlap. The result is a sum frequency radiation (300-400 nm). This up-converted signal is directed into a monochromator which selects a specific wavelength to monitor. The signal is finally directed into a PMT connected to the computer. The software that accompanies this set-up is Lumex which controls the delay line and collect the time-correlated emission signal.

The data collected has a step size resolution of 6.25 fs. However, the instrument's response function (IRF), which is the instrument's minimum capability to resolve the time duration of an emission process, is ~100 fs. The IRF of the instrument was obtained by collecting the raman scattering signal of water at 460 nm.

The fluorescence upconversion data is fitted by a multi-exponential function according to equation 3.3 and 3.4, where $F(t)$ is the fluorescence trace convoluted with the IRF, $g(t)$. Our lab has written a program in MATLAB based on these equations to allow fluorescence lifetime fitting of the data. Up to four exponential functions are used in the program but fewer may be used depending on the fit to the experimental data. The

amplitude, a_n, and lifetime, τ_n, of the fitting is manually changed to achieve the best fit. The exponentials used in our program are exponential decay, therefore the fitted lifetimes are the emission (relaxation) lifetimes. In cases where the emission rise time is larger than the IRF, it can be fitted by using a negative amplitude in the fit (the reverse of exponential decay – exponential growth).

$$F(t) = \int_{t0}^{tf} f(t) - t' g(t') \mathrm{d}t' \tag{2.3}$$

$$f(t) = \sum_{n=1}^{m} a_n \exp\left(\frac{-t}{\tau_n}\right) + a_{m+1} \tag{2.4}$$

2.5. Ultrafast transient absorption

The ultrafast transient absorption spectroscopy is another technique for measuring the excited state dynamics of a system. Unlike the time-resolved fluorescence up-conversion, transient absorption can also probe non-fluorescent excited states (dark states). Transient absorption spectroscopy is a pump-probe experiment.[19,20] The pump is a 120 fs monochromatic beam and the probe is a white light (450 – 750 nm). The probe beam is a white light generated by a 800 nm beam on a Ti:sapphire plate, which is time-delayed with respect to the pump beam. The differential absorption (ΔA) of the probe is measured and it's defined as the absorption in the excited state minus the absorption in the ground state.[20] The transient absorption is collected as a matrix which contains ΔA, wavelength and time.

Energy transfer processes occur in the timeframe of less than 100 femtoseconds to hundreds of picoseconds.[21,22] Ultrafast lasers now have the time resolution to investigate these processes. In a pump-probe experiment, a fraction of the molecules are excited by the pump beam from an initial state S_0 to an excited state S_1 (Figure 2.3). A delayed probe of weak intensity (to avoid multiphoton absorption) is absorbed by the excited

molecules from S_1 to higher excited states S_n. Different information can be displayed in a transient absorption spectrum.[19,20] A negative ΔA signal results in the wavelength region of ground state absorption, called a ground-state bleach. This results when there is strong steady state absorption, and the signal can be predicted by a steady state absorption spectrum. A negative ΔA signal also results when there is stimulated emission (Figure 2.3 C). This only occur for optically allowed transitions and occurs in the same wavelength region as that of the molecule's fluorescence spectrum. A positive ΔA signal is indicative of excited state absorption (Figure 2.3 A). This is also limited to optically allowed transitions from an excited state to higher excited states. Finally, a positive ΔA signal can also indicate a product absorption which is the result of a reaction in the excited state which leads to triplet states, charge-separated states or isomerized states.[20] This signal usually has a large stoke shift with respect to the ground state bleach signal. Based on these signals and their lifetimes, it is possible to observe processes such as inter-system crossing (singlet to triplet), vibrational cooling and thermalization.

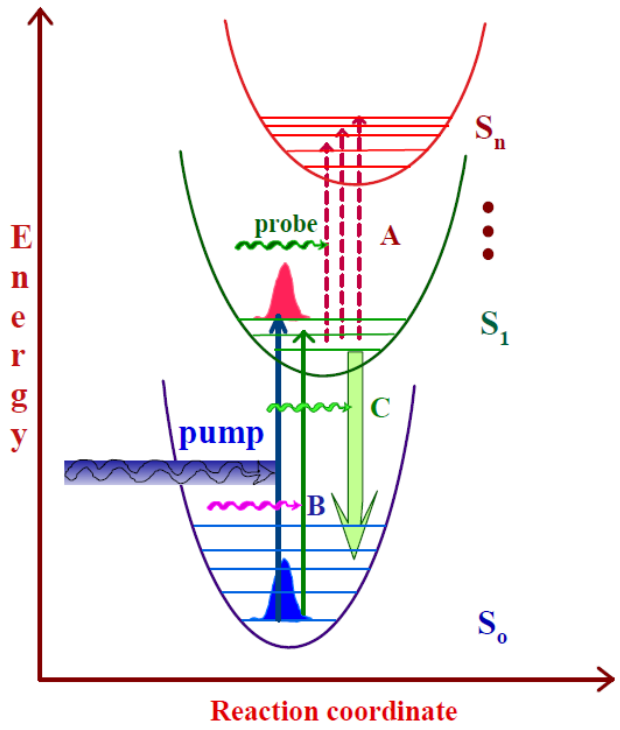

Figure 2.3. Principle of transient absorption. A sample is excited by a pump beam which promotes a fraction of the molecules from the ground state to the excited state (B). The probe beam is absorbed by the excited state molecules (A), or cause stimulated emission (C).

The transient absorption instrumental set-up in the Goodson lab consists of several parts (Figure 2.4). The part where the transient absorption measurements take place is a Helios system by Ultrafast Systems Inc (Figure 2.5). The Helios receives ~20% of the output of an amplified laser and directs the beam into a variable optical delay line (RR). This beam is then focused on a Ti:sapphire plate (SP) to generate a white light between 450 nm and 750 nm. This becomes the probe beam. The other 80% of the amplified beam is directed into the OPA which generates a tunable monochromatic beam that enters the Helios. This becomes the pump beam. The pump and the probe beams are focused and overlapped in a sample that is contained in a 2 mm quartz cell. The probe light is directed

to a CCD detector (Ocean Optics 2000) which is connected to a collection software by Ultrafast Systems Inc.

The amplifier system (Spitfire Spectra Physics) produces femtosecond pulses with high power. During the regenerative amplification process, the Spitfire uses the chirped pulse amplification (CPA) technique to temporary stretch out the seed pulse (800 nm) and combines it with a 7.5 W beam from Empower (532 nm) in a Ti:sapphire crystal. The stretched, amplified pulse is then compressed back to 120 fs at 1 kHz and ~800-1,000 mW. The seed pulse is produced in a separate cavity, the Tsunami, which is pumped by a Millennia Pro and generate 800 nm, 100 fs pulses of ~270 mW.

The amplified beam (80%) is directed to the Optical Parametric Amplifier (OPA, Spectra Physics) which allows for a large tunable wavelength range from 350 nm to 2,000 nm. The output from the OPA is used as the pump/excitation beam in the transient absorption experiments. To achieve this range of wavelengths, the optics inside the OPA are set up to manipulate non-linear frequency conversion processes (up- and down-conversion). For the purpose of this thesis, a 400 nm pump beam was used for the excitation of the nanocluster's core states. Therefore, the optics inside the OPA were set up to only double the frequency of the amplifier's output (800 nm) using a BBO crystal. This process is called second harmonic generation.

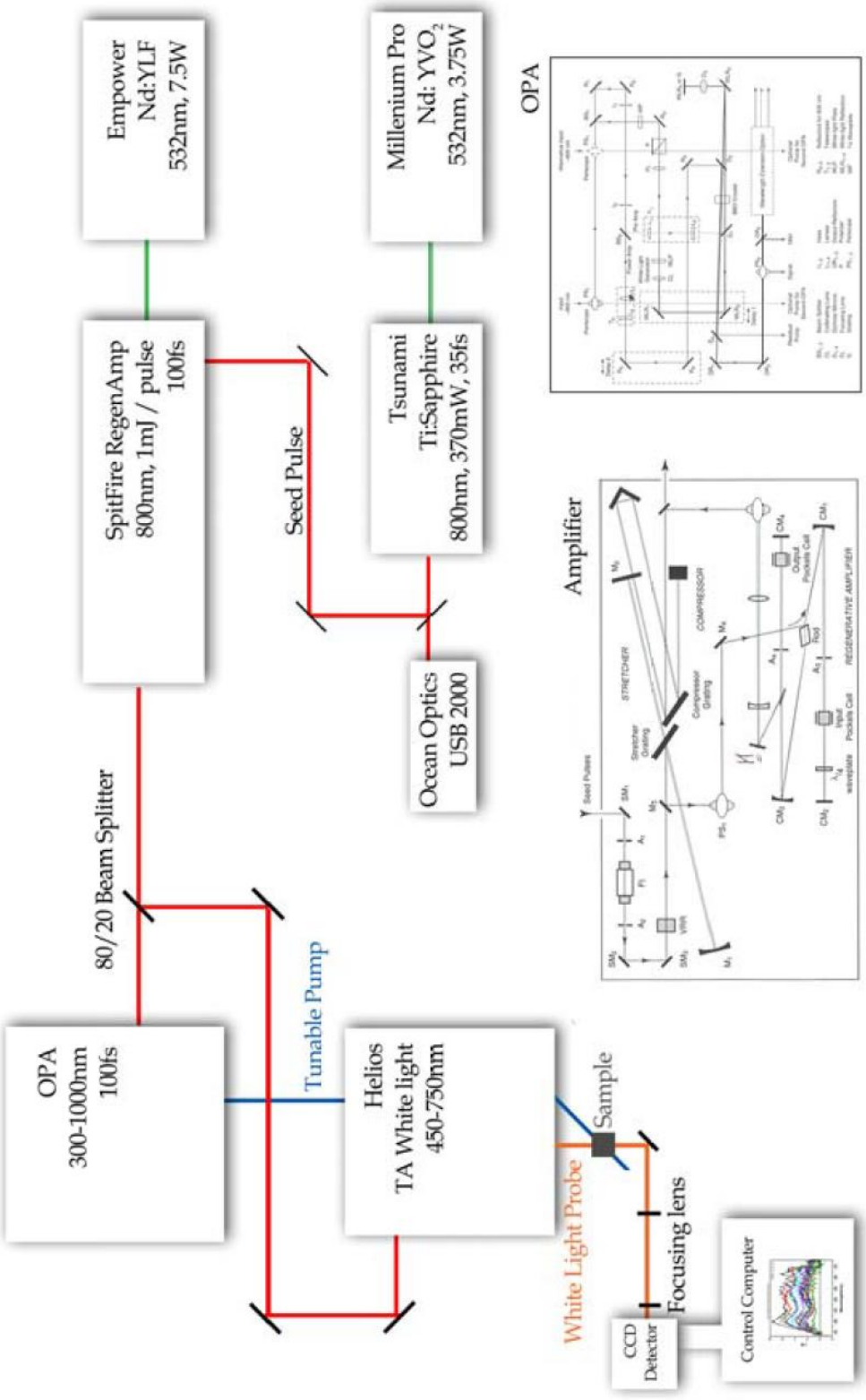

Figure 2.4. Transient absorption instrumental set-up.

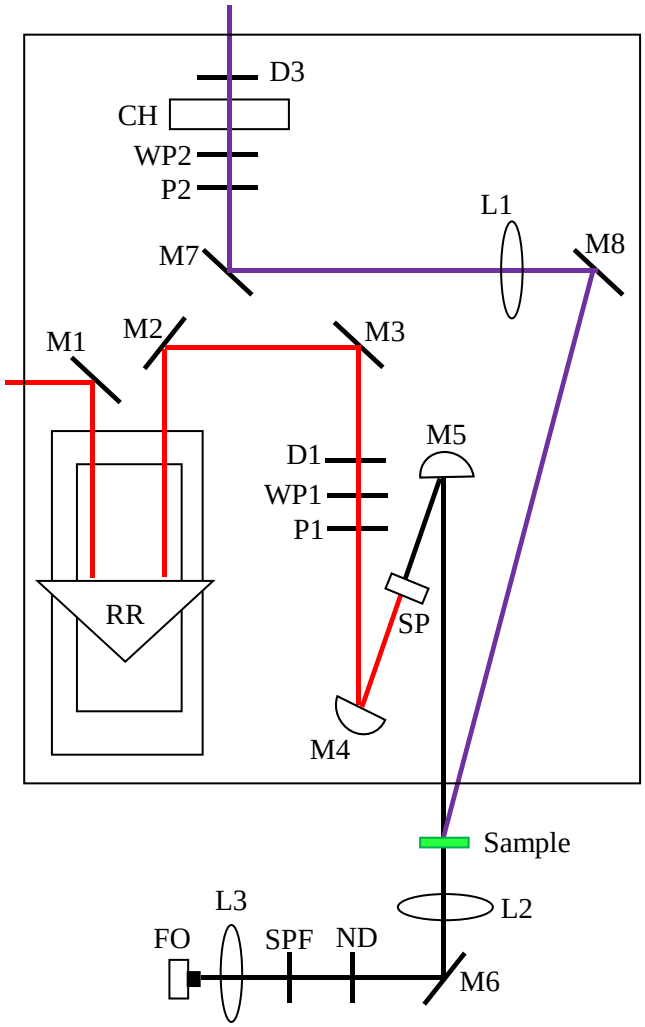

Figure 2.5. The Helios set-up for transient absorption measurements. A pump-probe experiment.

2.6. Two-photon absorption

Two-photon absorption is a non-linear process in which two photons of half the energy of a single photon used for one-photon excitation are absorbed simultaneously. The two-photon absorption process was first theoretically described by Maria Göppert-Mayer in 1931. Decades later, with the invention of pulsed lasers, this phenomenon was experimentally demonstrated. The two-photon absorption process requires a very high density of photons to allow the simultaneous absorption of two photons. Such high density and power of photons can be delivered by pulsed lasers. The two-photon absorption process results in the same excited state as that obtained by one-photon

absorption process. For example, a molecule that can be excited at 800 nm by two-photon absorption, has an absorption at 400 nm. Therefore, the resulting relaxation process, radiative or non-radiative, is the same in both absorption processes (Figure 2.6).

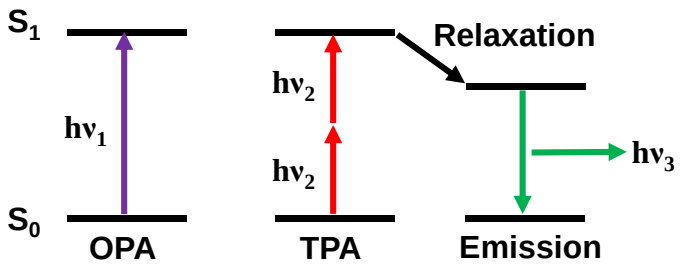

Figure 2.6. Jablonski diagram of one-photon absorption, two-photon absorption, and emission processes.

Two-photon absorption (TPA) has been used to gain insight into the structure-function relationship of a molecule, such as charge-transfer strength and changes in dipole moment. The TPA of a molecule can be quantitatively analyzed by determining its TPA cross section (σ). The TPA cross section describes the simultaneous absorption of two photons in a given area and time. Therefore, its unit is in $cm^4 \cdot s \cdot photon^{-1}$. Since the TPA process is weaker in strength compared to one-photon absorption, the cross sections are very small and are thus conveniently reported in units of GM (Göppert-Mayer; 1 GM = 10^{-50} $cm^4 \cdot s \cdot photon^{-1}$). There are two techniques for determining the TPA cross sections: two-photon excited fluorescence and z-scan.

2.6.1. Two-photon excited fluorescence

In two-photon excited fluorescence (TPEF), the fluorescence of a sample after TPA is monitored. Since the TPA process is intensity-dependent, specifically square intensity-dependent, adjusting the laser power and monitoring the fluorescence will allow for the determination of the TPA cross sections.

Our laboratory has two set-ups which allows for TPEF measurements. The difference between the two systems is the excitation source. The one described here has a fixed excitation of ~800 nm (Figure 2.7). This system consists of a diode pump laser head, the Millennia by Spectra Physics, which produces a 532 nm beam that enters the cavity of a Kapteyn-Murnane (KM) Laboratories set-up which contains a Ti:sapphire crystal. The output beam is ~800 nm and is mode-locked by gently disturbing one of the prisms in the KM set-up and monitoring the output beam using an Ocean Optics. The typical output power from the cavity is 200-250 mW, with a pulse duration of 30 fs, and a repetition rate of 87 MHz. The beam quality and peak wavelength are adjusted by the two prisms inside the cavity.

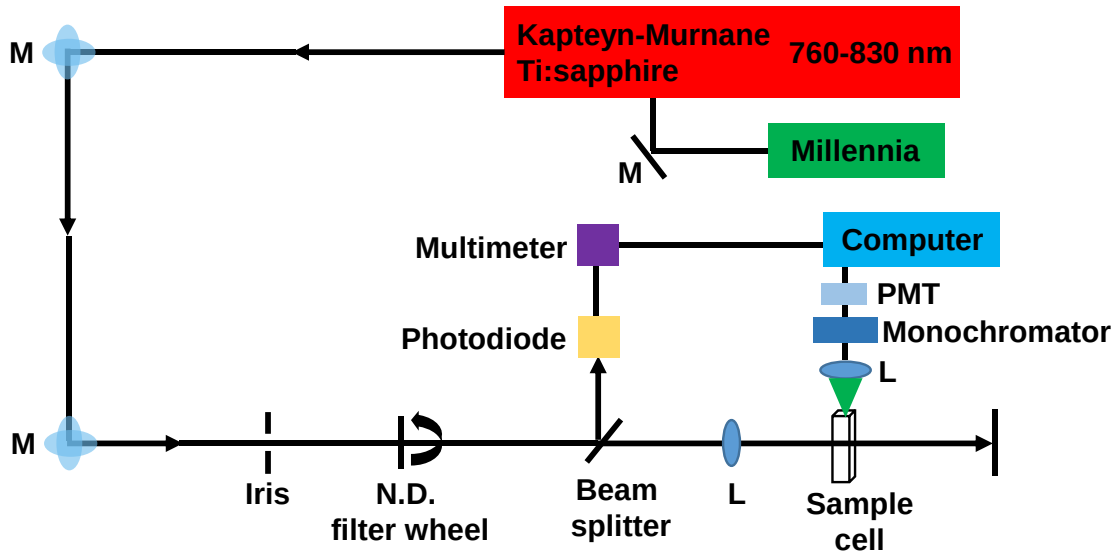

Figure 2.7. TPEF set-up in our laboratory.

The complete experimental set-up of TPEF includes a circular neutral density (N.D.) filter, a beam splitter which reflects a percentage of the beam into a photodiode/multimeter device, a focusing lens, L, which increases the photon density in the sample, and a fluorescence collection unit of monochromator coupled to a PMT.

Different excitation powers are obtained by varying the N.D. filter and the resulting emission at different excitation powers is recorded. The log of the emission intensity against the log of the laser power results in a linear plot with a slope of 2 if a molecule is TPA active. In a lot of cases, small variations in the laser and fluorescence alignment to the devices and optics will result in a slope of less than 2. Other factors such as the stability of the beam power and stray light can also affect the TPEF measurement. Typically, a coumarin 307 dye (σ = 15 GM; emission 480 nm) or a rhodamine B dye (σ = 150 GM; emission 570 nm) are used for improving the alignment of the system by monitoring changes in their fluorescence intensity. They are also used as standards for calculating the relative TPA cross section of a sample.

The different excitation powers are recorded by the multimeter which is connected to the computer. The multimeter allows for the simultaneous measurement of the laser power while the PMT measures the fluorescence. A calibration plot, called the Keithley plot, is obtained separately by measuring the laser power using the multimeter and a power meter positioned after the beam splitter. The Keithley plot allows for the conversion of the input power from mV (multimeter) to mW.

The TPA cross section that is determined from TPEF experiments follows the mathematical equation 2.5. $F(t)$ is the TPEF photons collected per second, η is the refractive index of the solvent, σ is the TPA cross section, [C] is the sample's concentration, Φ is the fluorescence quantum yield, g_p is the shape factor of the pulsed laser (0.664 for Gaussian shape), f is the laser frequency (75 MHz), λ is the excitation wavelength, τ is the pulse duration, φ is the collection efficiency, and $P(t)$ is the input

intensity. Since a standard dye is used for determining the relative TPA cross section of a sample, the laser parameters can be eliminated from the calculation.

$$F(t) = \frac{1}{2}\eta\sigma[C]\Phi\frac{g_p}{\pi f\lambda\tau}\varphi\langle P(t)\rangle^2 \tag{2.5}$$

The logarithm of equation 2.5 results in a linear equation (2.6). Therefore, a log-log plot of fluorescence intensity against laser intensity results in a slope of 2 in a two-photon absorbing molecule. The third log term, which contains the molecule and laser parameters, is the y-intercept, b, of the linear plot.

$$\log[F(t)] = 2\log[\langle P(t)\rangle] + \log\left[\frac{1}{2}\eta\sigma[C]\Phi\frac{g_p}{\pi f\lambda\tau}\varphi\right] \tag{2.6}$$

When comparing a sample (x) against a standard (std), the following equalities can be established:

$$2\log[\langle P(t)\rangle]_x = 2\log[\langle P(t)\rangle]_{std} \tag{2.7}$$

$$\log[F(t)]_x - b_x = \log[F(t)]_{std} - b_{std} \tag{2.8}$$

Equation 2.8 can be simplified to equation 2.9.

$$\frac{[F(t)]_x}{[F(t)]_{std}} = 10^{(b_x - b_{std})} \tag{2.9}$$

When the logarithm of the power is zero, the *F(t)* term is equal to b. Therefore, it can be substituted into equation 2.9 to yield an expression for calculating the TPA cross section of a sample (equation 2.12).

$$\frac{\frac{1}{2}\eta_x\sigma_x[C]_x\Phi_x\frac{g_p}{\pi f\lambda\tau}\varphi}{\frac{1}{2}\eta_{std}\sigma_{std}[C]_{std}\Phi_{std}\frac{g_p}{\pi f\lambda\tau}\varphi} = 10^{(b_x - b_{std})} \tag{2.10}$$

$$\frac{\eta_x\sigma_x[C]_x\Phi_x}{\eta_{std}\sigma_{std}[C]_{std}\Phi_{std}} = 10^{(b_x - b_{std})} \tag{2.11}$$

$$\sigma_x = 10^{(b_x - b_{std})}\frac{\eta_{std}\sigma_{std}[C]_{std}\Phi_{std}}{\eta_x[C]_x\Phi_x} \tag{2.12}$$

In using equation 2.12, the TPA cross section of a sample can be calculated by knowing the emission quantum yield, concentration, refractive index of the solvent, and the y-intercept of the log-log plot. At times the slope of the log-log plot may not yield a slope of 2 due to artifacts of the instrument and variables such as residual light which is beyond an experimenter's control. With careful alignment, however, an acceptable slope between 1.8 and 2 can be obtained. In which case the slope is corrected by manually subtracting fluorescence counts until it yields a slope of 2. Typically, the correction is less than 5% of the smallest fluorescence count.

2.6.2. Z-scan technique

Another method for that was used in this thesis for TPA measurements is the z-scan technique which is a non-linear transmission measurement. Unlike the TPEF method, this method measures the transmitted beam after it passes through the sample where TPA occurs.

The general optical set-up for the z-scan technique that is used in this work is illustrated in Figure 2.8. The laser system that is used for TPEF was also used for z-scan. The beam power is controlled by a circular variable neutral density filter (CVNDF) and the intensity of the beam is varied by the focusing lens (f = 10 cm). The sample is mounted on a translational stage along the beam path. The non-linear transmission is monitored by an open aperture detector as the excitation input intensity is varied by translating the sample along the beam path.

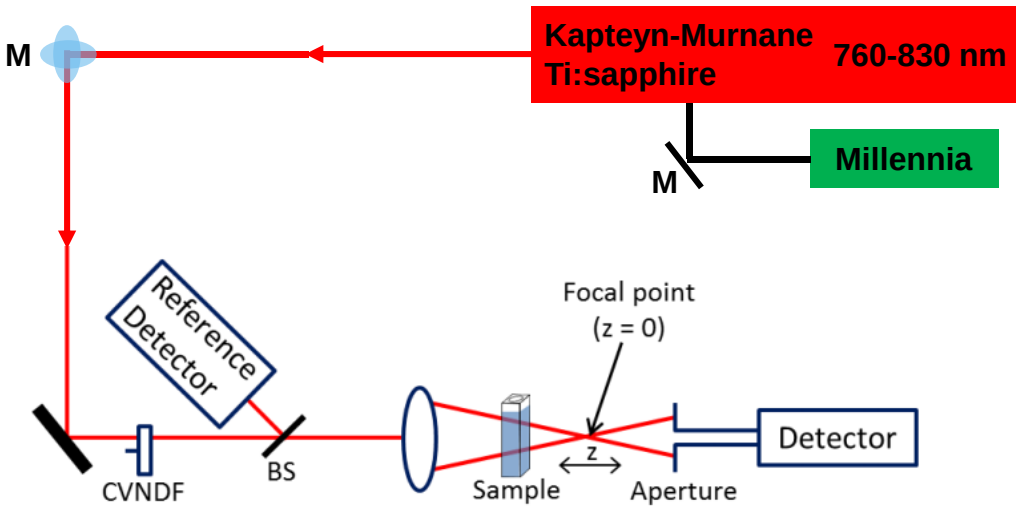

Figure 2.8. Optical set-up for non-linear transmission measurement (z-scan).

The intensity-dependent non-linear transmission is plotted against the z-axis of the beam to generate a z-scan curve. In an open aperture configuration, the z-scan curve shows a drop in transmission near the focus of the beam, where the intensity is highest. Typically, the focus point is chosen to be the zero position. This configuration provides information about the two-photon absorption process and can be used to calculate the TPA cross section. Another configuration, the close aperture configuration, provides information about changes in the non-linear refractive index. The open aperture configuration was used in this work.

The change in transmission in the z-scan method can be described by equation 2.13, where q_0 is defined by equation 2.14; P_i is the input power in the sample and is defined by equation 2.15; β is the two-photon absorption coefficient; $I_0(t)$ is the intensity at the focus; L_{eff} is the effective sample's length and is defined by equation 2.16; α is the linear absorption coefficient; L is the sample's thickness; z_0 is the diffraction length and is defined by equation 2.17; w_0 is the beam radius at the focus; and λ is the laser's wavelength.[23]

$$P(z,t) = P_i(t)e^{-\alpha L}\frac{\ln[1+q_0(z,t)]}{q_0(z,t)} \quad (2.13)$$

$$q_0(z,t) = \frac{\beta I_0(t) L_{eff}}{1+\frac{z^2}{z_0^2}} \quad (2.14)$$

$$P_i(t) = \frac{\pi w_0^2 I_o(t)}{2} \quad (2.15)$$

$$L_{eff} = \frac{1-e^{-\alpha L}}{\alpha} \quad (2.16)$$

$$z_0 = \frac{\pi w_0^2}{\lambda} \quad (2.17)$$

The z-scan profile can be modeled by equation 2.18 when $|q_0| < 1$. It can be simplified to equation 2.20 if $\alpha << 1$, in which case L_{eff} can be replaced by L. This is usually the case for thin samples and when the linear absorption at the two-photon excitation wavelength is negligible. The β is related to the TPA cross section σ by equation 2.21, where h is the Planck's constant, v is the laser's frequency, N is the Avogadro's number, and c is the sample's concentration.

$$T(z) = \sum_{m=0}^{\infty} \frac{[-q_0(z,0)]^m}{(m+1)^{\frac{3}{2}}} \quad (2.18)$$

$$T(z) = 1 - \frac{\beta I_0 L_{eff}}{2^{\frac{3}{2}}\left(1+\frac{z^2}{z_0^2}\right)} + \text{higher terms} \quad (2.19)$$

$$T(z) = 1 - \frac{\beta I_0 L}{2^{\frac{3}{2}}\left(1+\frac{z^2}{z_0^2}\right)} \quad (2.20)$$

$$\sigma = \frac{\beta h v 10^3}{Nc} \quad (2.21)$$

Alternatively, the z-scan transmission profile can be converted to a linear plot by taking the difference in transmission, ΔT (equation 2.22).[24]

$$\Delta T = -\beta I L_{eff} \quad (2.22)$$

Comparing between the two techniques for TPA cross section determination, the TPEF technique is usually more accurate than the z-scan technique. Fluorescence detection is usually a more sensitive technique than measuring absorption, but is limited by a molecule's fluorescence quantum yield. The TPEF is also superior to z-scan because the thermal lensing effect of the laser beam can cause an apparent drop in the intensity transmission.[25] However, the z-scan technique is useful for two-photon absorption cross section determination in cases where the fluorescence quantum yield is very low for TPEF.

2.7. Matrix-assisted laser desorption ionization mass spectrometry (MALDI-MS)

Mass spectrometry is a widely used analytical tool for small molecules, polymers, and proteins. It is used for identifying the chemical formula of a sample, or its molecular mass. Mass spectrometry is a very sensitive technique – a small amount of analyte in a matrix or solution is enough for detection.

Mass spectrometry is a versatile technique as it has various configurations.[26] It consists of four parts: an inlet system which introduces the sample, an ion source to produce analyte ions, a mass analyzer which detects the molecular ions by their mass-to-charge ratio, and a detector. A mass spectrum displays the relative abundance of molecular ions, in mass-to-charge ratios. The molecular ions are produced by an ion source which can be classified into different types. For metal nanocluster analysis, the popular types of ion sources that have been used are electrospray ionization (ESI), which employs a high electrical field, and matrix-assisted desorption-ionization (MALDI), which uses a laser beam. In this work, the MALDI-MS was employed.

The ionization process in MALDI-MS is depicted in Figure 2.9.[26] A small concentration of analyte (approximately micromolar) is first mixed with a UV-absorbing

matrix. The mixture is then drop casted and allowed to crystallize on a metal plate. The plate is introduced into the MALDI-MS instrument under vacuum and a laser is focused on the analyte-matrix mixture. During the desorption process, the matrix absorbs the energy of the laser and transfer it to the analyte to form ions which then enters to a mass analyzer. The MALDI-MS that was used for the work in this thesis is a Bruker Autoflex MALDI (Figure 2.9) which employs a nitrogen laser (337 nm) as the ionization source with an adjustable laser repetition rate of up to 2,000 Hz. The MALDI-MS is equipped with a time-of-flight (TOF) mass analyzer. The instrument has a range of 100 – 100,000 m/z. The matrix used in this work is *trans*-2-[3-(4-tert-butylphenyl)-2-methyl-2-propenylidene] malononitrile (DCTB) for organic-soluble nanoclusters, and 2,5-dihydroxybenzoic acid (DHB) for water-soluble nanoclusters. The instrument is paired with a FlexControl software which collects the mass spectrum. Analysis of the mass spectra is performed with the FlexAnalysis software.

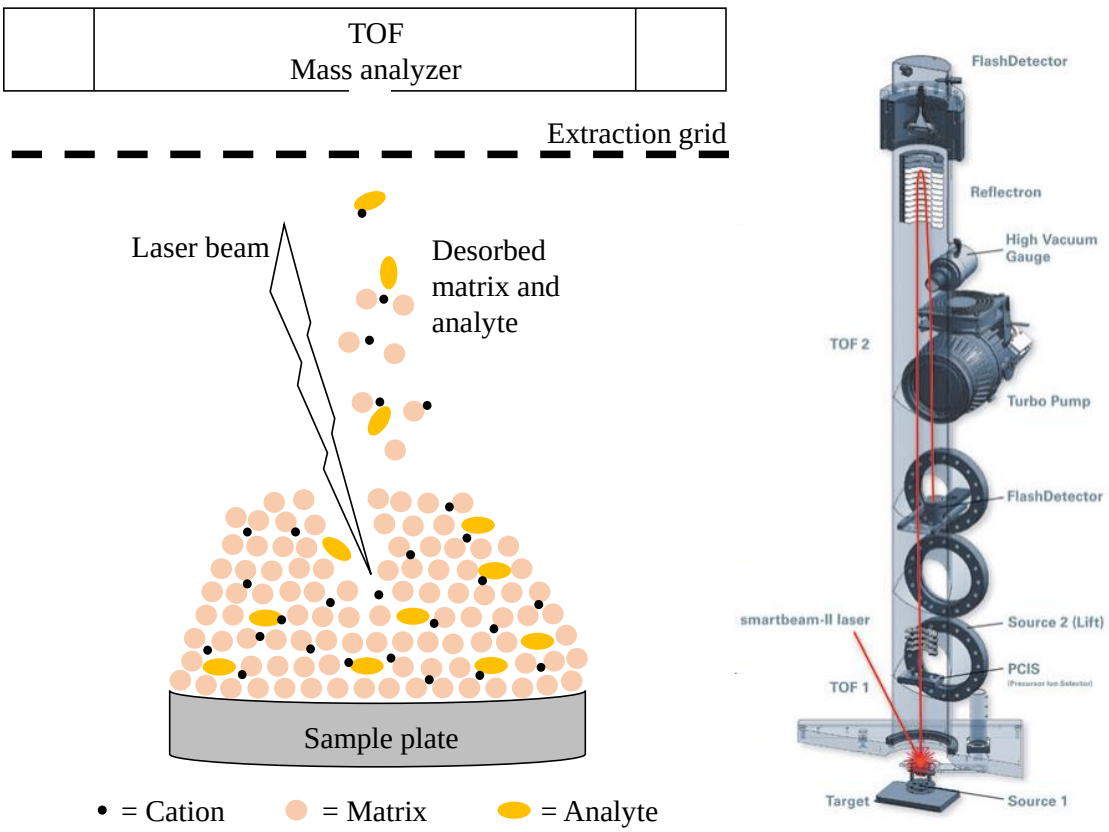

Figure 2.9. The matrix-assisted laser desorption-ionization process and diagram of the Bruker Autoflex MALDI-MS.

In the context of this thesis, mass spectrometry has been used for characterizing metal nanoclusters for more than a decade. Mass spectrometry was initially used for determining the molecular mass of a metal nanocluster.[27–30] Although mass spectrometry has been used for a long time for nanoclusters characterization, the exact composition of the nanoclusters did not come to light until later. This was partly due to the lack of a method for obtaining pure, monodisperse nanoclusters, which hindered the exact determination of their chemical formula.[31] Another reason was that past techniques used hard ionization sources, such has laser desorption ionization mass spectrometry (LDI-MS), which results in the fragmentation of the nanoclusters.[32] The Whetten group has identified a series of 1.5 – 3.5 nm Au-thiolate nanoparticles by LDI-MS in 1996, but

these were big nanoparticles in comparison to what are synthesized and isolated later.[27] The first identification of quantum-sized metal nanoclusters by mass spectrometry was by LDI-MS as well, where the 8kDa species was identified as a Au_{38} nanocluster with step-like optical absorption.[28] The improvement of mass spectrometry to characterize the chemical formula of nanoclusters continued in this direction.[29,33,34]

The exact structure and formula solution of metal nanoclusters came later with the improvement in the mass spectrometry characterization of metal nanoclusters in conjunction with the improvement in the size separation to produce monodisperse samples. The Tsukuda group improved the polyacrylamide gel electrophoresis separation of the water-soluble $Au_n(GSH)_m$ nanoclusters and by using a soft ionization (ESI-MS) to suppress fragmentation, they were able to obtain clean mass spectra.[35] It should be noted that the Tsukuda group's ESI-MS was a custom-built instrument with a resolution ($M/\Delta M$) of 400.[35,36] With the improvement of mass spectrometry characterization of metal nanoclusters, the subsequent years saw the successful chemical formula determination of metal nanoclusters.[37–44] The pinnacle of this success is the re-assignment of the $Au_{25}(SR)_{18}$ nanocluster which was previously determined to be $Au_{38}(PET)_{24}$ and $Au_{28}(GSH)_{16}$.[35,37]

The ESI and MALDI have been the two popular methods for nanocluster characterization. The use of ESI and MALDI is often complementary.[41,45] In MALDI-MS, high molecular species lead to the formation of singly charged ions and offer a wider mass range, while in ESI-MS, it leads to the formation of multiply charged species.[46,47] It should be noted that it is now relatively easier to obtain the mass spectrum of an organic-soluble nanoclusters by either method compared to the water-soluble nanocluster. It is

more challenging to characterize metal nanoclusters by ESI-MS, but it allows intact nanoclusters measurement and a greater precision which allows the observation of isotope patterns.[48] Although efforts have been put into obtaining intact nanoclusters in the mass spectrometry, it should be noted that obtaining a mass spectrum of fragmented nanoclusters can provide insights into their structure.[41]

2.8. Polyacrylamide gel electrophoresis (PAGE)

Polyacrylamide gel electrophoresis is a widely used technique in biochemistry for the separation proteins for analysis and purification. The molecules in an electrophoresis gel respond to an applied electric field by movement towards the electrodes (Figure 2.10). The migration rate of the molecules depend on several factors: the strength of the electric field, the temperature, the pH, the ion type, the buffer concentration, the gel composition, the molecule's size, shape, mass and charge.[49]

The polyacrylamide gel acts as a sieve through which the molecules migrate. The pore sizes are controlled by the percent composition of the monomers and the weight percent of the cross-linker. Both the molecular mass and size of proteins are large, therefore a low gel density (larger pore sizes) of 4 – 15% is used for separating the proteins. Metal nanoclusters, however, have large molecular mass and small sizes because they are composed of heavy transition metals in far fewer numbers of atoms compared to proteins. Therefore, to achieve a good resolution in the separation, smaller pore sizes should be used. Increasing the monomers concentration can achieve this. Furthermore, a discontinuous buffer system is used to achieve a good separation. In a discontinuous buffer system, two gels of different percent compositions are used. The stacking gel is usually larger in pore size. Molecules do not all enter the gel at the same

time; once they reach the bottom end of the stacking gel, they are more tightly packed. The molecules then enter the second gel called the resolving gel which has smaller pore sizes. Additionally, the buffer concentration used in the polymerization of the gel and the buffer concentration used as the electrode solution are different.

In addition to increasing the percent composition of the gel, sodium dodecyl sulfate (SDS) is removed from the gel-making recipe. SDS-PAGE is very popular for protein separation because it allows for a better protein separation by imparting an overall negative charge on all proteins, by denaturing the complex conformation of the protein and by imparting a similar charge-to-mass ratio to the proteins. In short, the SDS standardizes the proteins properties and the basis for their separation is their size. Since the nanoclusters are negatively charged, SDS is not necessary. The nanoclusters separate on the basis of their molecular mass. Finally, a staining agent is not necessary in the PAGE of nanoclusters because they are colored.

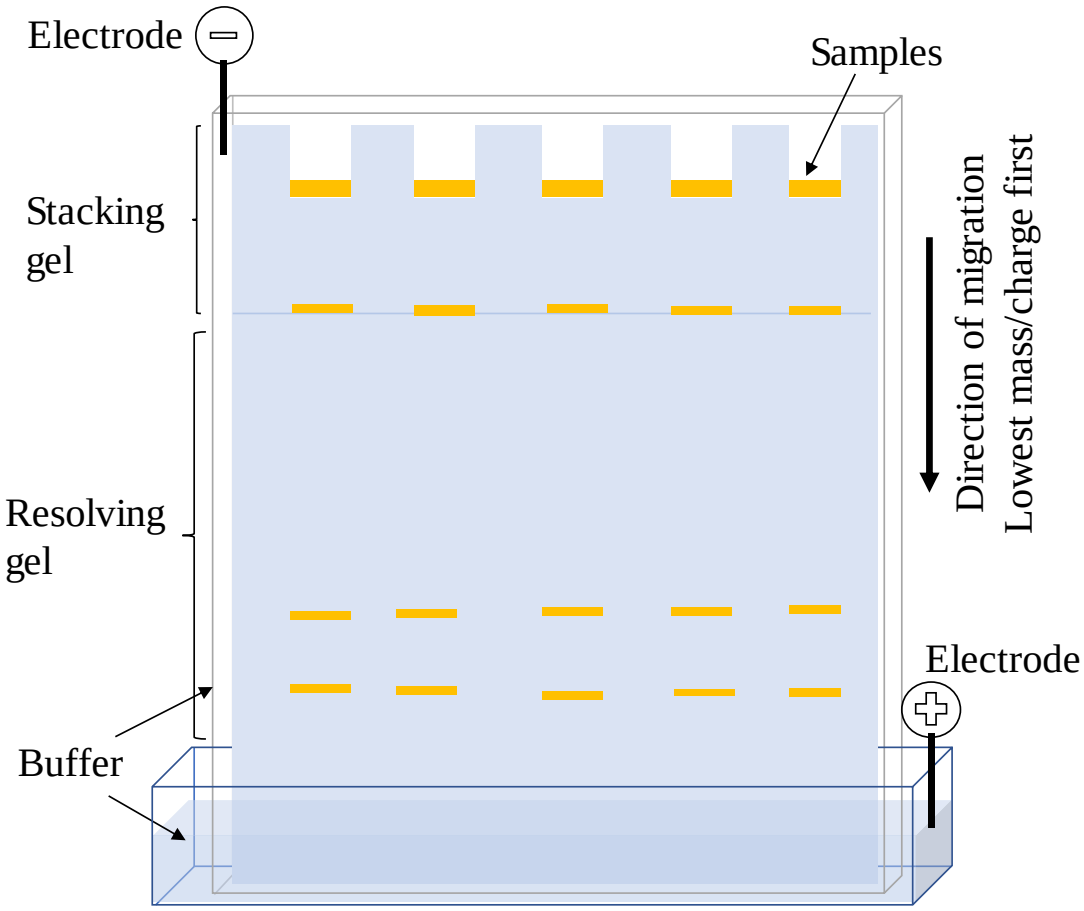

Figure 2.10. Gel electrophoresis components.

2.9. References

(1) Hostetler, M. J.; Templeton, A. C.; Murray, R. W. Dynamics of Place-Exchange Reactions on Monolayer-Protected Gold Cluster Molecules. *Langmuir* **1999**, *15*, 3782–3789.

(2) Shibu, E. S.; Muhammed, M. A. H.; Tsukuda, T.; Pradeep, T. Ligand Exchange of Au 25 SG 18 Leading to Functionalized Gold Clusters: Spectroscopy, Kinetics, and Luminescence. *J. Phys. Chem. C* **2008**, *112*, 12168–12176.

(3) Parker, J. F.; Kacprzak, K. A.; Lopez-Acevedo, O.; Häkkinen, H.; Murray, R. W. Experimental and Density Functional Theory Analysis of Serial Introductions of Electron-Withdrawing Ligands into the Ligand Shell of a Thiolate-Protected Au 25 Nanoparticle. *J. Phys. Chem. C* **2010**, *114*, 8276–8281.

(4) Malicki, M.; Hales, J. M.; Rumi, M.; Barlow, S.; McClary, L.; Marder, S. R.; Perry, J. W. Excited-State Dynamics and Dye-Dye Interactions in Dye-Coated Gold Nanoparticles with Varying Alkyl Spacer Lengths. *Phys. Chem. Chem. Phys.* **2010**, *12*, 6267–6277.

(5) Heinecke, C. L.; Ni, T. W.; Malola, S.; Mäkinen, V.; Wong, O. A.; Häkkinen, H.; Ackerson, C. J. Structural and Theoretical Basis for Ligand Exchange on Thiolate Monolayer Protected Gold Nanoclusters. *J. Am. Chem. Soc.* **2012**, *134*, 13316–13322.

(6) Fernando, A.; Aikens, C. M. Ligand Exchange Mechanism on Thiolate Monolayer Protected Au 25 (SR) 18 Nanoclusters. *J. Phys. Chem. C* **2015**, *119*, 20179–20187.

(7) Chen, Y.; Liu, C.; Tang, Q.; Zeng, C.; Higaki, T.; Das, A.; Jiang, D.; Rosi, N. L.; Jin, R. Isomerism in Au $_{28}$ (SR) $_{20}$ Nanocluster and Stable Structures. *J. Am. Chem. Soc.* **2016**, *138*, 1482–1485.

(8) Tang, Q.; Ouyang, R.; Tian, Z.; Jiang, D. The Ligand Effect on the Isomer Stability of Au $_{24}$ (SR) $_{20}$ Clusters. *Nanoscale* **2015**, *7*, 2225–2229.

(9) Zeng, C.; Liu, C.; Pei, Y.; Jin, R. Thiol Ligand-Induced Transformation of Au $_{38}$ (SC $_{2}$ H $_{4}$ Ph) $_{24}$ to Au $_{36}$ (SPh- *T* -Bu) $_{24}$. *ACS Nano* **2013**, *7*, 6138–6145.

(10) Zeng, C.; Chen, Y.; Das, A.; Jin, R. Transformation Chemistry of Gold Nanoclusters: From One Stable Size to Another. *J. Phys. Chem. Lett.* **2015**, *6*, 2976–2986.

(11) Roux, S.; Garcia, B.; Bridot, J.-L.; Salomé, M.; Marquette, C.; Lemelle, L.; Gillet, P.; Blum, L.; Pascal Perriat, A.; Tillement, O. Synthesis, Characterization of Dihydrolipoic Acid Capped Gold Nanoparticles, and Functionalization by the Electroluminescent Luminol. **2005**.

(12) Jupally, V. R.; Kota, R.; Dornshuld, E. Van; Mattern, D. L.; Tschumper, G. S.; Jiang, D.; Dass, A. Interstaple Dithiol Cross-Linking in Au 25 (SR) 18 Nanomolecules: A Combined Mass Spectrometric and Computational Study. *J. Am. Chem. Soc.* **2011**, *133*, 20258–20266.

(13) Tang, Z.; Xu, B.; Wu, B.; Germann, M. W.; Wang, G. Synthesis and Structural Determination of Multidentate 2,3-Dithiol-Stabilized Au Clusters. *J. Am. Chem. Soc.* **2010**, *132*, 3367–3374.

(14) Tang, Z.; Xu, B.; Wu, B.; Robinson, D. A.; Bokossa, N.; Wang, G. Monolayer Reactions of Protected Au Nanoclusters with Monothiol Tiopronin and 2,3-Dithiol Dimercaptopropanesulfonate. *Langmuir* **2011**, *27*, 2989–2996.

(15) Fields-Zinna, C. A.; Parker, J. F.; Murray, R. W. Mass Spectrometry of Ligand Exchange Chelation of the Nanoparticle [Au25(SCH2CH2C6H5)18]1- by CH3C6H3(SH)2. *J. Am. Chem. Soc.* **2010**, *132*, 17193–17198.

(16) Knoppe, S.; Dharmaratne, A. C.; Schreiner, E.; Dass, A.; Bürgi, T. Ligand

Exchange Reactions on Au $_{38}$ and Au $_{40}$ Clusters: A Combined Circular Dichroism and Mass Spectrometry Study. *J. Am. Chem. Soc.* **2010**, *132*, 16783–16789.

(17) Si, S.; Gautier, C.; Boudon, J.; Taras, R.; Gladiali, S.; Bürgi, T. Ligand Exchange on Au $_{25}$ Cluster with Chiral Thiols. *J. Phys. Chem. C* **2009**, *113*, 12966–12969.

(18) Knoppe, S.; Bürgi, T. The Fate of Au25(SR)18 Clusters upon Ligand Exchange with Binaphthyl-Dithiol: Interstaple Binding vs. Decomposition. *Phys. Chem. Chem. Phys.* **2013**, *15*, 15816–15820.

(19) Ohkita, H.; Tamai, Y.; Benten, H.; Ito, S. Transient Absorption Spectroscopy for Polymer Solar Cells. *IEEE J. Sel. Top. Quantum Electron.* **2016**, *22*, 100–111.

(20) Berera, R.; van Grondelle, R.; Kennis, J. T. M. Ultrafast Transient Absorption Spectroscopy: Principles and Application to Photosynthetic Systems. *Photosynth. Res.* **2009**, *101*, 105–118.

(21) Sundström, V.; Pullerits, T.; Van Grondelle, R. Photosynthetic Light-Harvesting: Reconciling Dynamics and Structure of Purple Bacterial LH2 Reveals Function of Photosynthetic Unit. *J. Phys. Chem. B* **1999**, *103*, 2327–2346.

(22) van Amerongen, H.; van Grondelle, R. Understanding the Energy Transfer Function of LHCII, the Major Light-Harvesting Complex of Green Plants. *J. Phys. Chem. B* **2001**, *105*, 604–617.

(23) Sheik-Bahae, M.; Said, A. A.; Wei, T.-H.; Hagan, D. J.; Van Stryland, E. W. Sensitive Measurement of Optical Nonlinearities Using a Single Beam. *IEEE J. Quantum Electron.* **1990**, *26*, 760–769.

(24) Mansour, K.; Soileau, M. J.; Stryland, E. W. Van. Nonlinear Optical Properties of Carbon-Black Suspensions (Ink). *J. Opt. Soc. Am. B* **1992**, *9*, 1100.

(25) Pawlicki, M.; Collins, H. A.; Denning, R. G.; Anderson, H. L. Two-Photon Absorption and the Design of Two-Photon Dyes. *Angew. Chem. Int. Ed. Engl.* **2009**, *48*, 3244–3266.

(26) Skoog, D.; Holler, F. J.; Crouch, S. R. *Instrumental Analysis*; Cengage Learning, 2007.

(27) Whetten, R. L.; Khoury, J. T.; Alvarez, M. M.; Murthy, S.; Vezmar, I.; Wang, Z. L.; Stephens, P. W.; Cleveland, C. L.; Luedtke, W. D.; Landman, U. Nanocrystal Gold Molecules. *Adv. Mater.* **1996**, *8*, 428–433.

(28) Schaaff, T. G.; Shafigullin, M. N.; Khoury, J. T.; Vezmar, I.; Whetten, R. L.; Cullen, W. G.; First, P. N.; Gutiérrez-Wing, C.; Ascensio, J.; Jose-Yacamán, M. J. Isolation of Smaller Nanocrystal Au Molecules: Robust Quantum Effects in

Optical Spectra. *J. Phys. Chem. B* **1997**, *101*, 7885–7891.

(29) Schaaff, T. G.; Knight, G.; Shafigullin, M. N.; Borkman, R. F.; Whetten, R. L. Isolation and Selected Properties of a 10.4 kDa Gold:Glutathione Cluster Compound. *J. Phys. Chem. B* **1998**, *102*, 10643–10646.

(30) Khitrov, G. A.; Strouse, G. F. ZnS Nanomaterial Characterization by MALDI-TOF Mass Spectrometry. **2003**.

(31) Jin, R.; Zeng, C.; Zhou, M.; Chen, Y. Atomically Precise Colloidal Metal Nanoclusters and Nanoparticles: Fundamentals and Opportunities. *Chem. Rev.* **2016**, *116*, 10346–10413.

(32) Templeton, A. C.; Wuelfing, W. P.; Murray, R. W. Monolayer-Protected Cluster Molecules. *Acc. Chem. Res.* **2000**, *33*, 27–36.

(33) Donkers, R. L.; Lee, D.; Murray, R. W. Synthesis and Isolation of the Molecule-like Cluster Au38(PhCH2CH2S)24. *Langmuir* **2004**, *20*, 1945–1952.

(34) Schaaff, T. G.; Marat N. Shafigullin; Khoury, J. T.; Igor Vezmar, A.; Robert L. Whetten. Properties of a Ubiquitous 29 kDa Au:SR Cluster Compound. **2001**.

(35) Negishi, Y.; Nobusada, K.; Tsukuda, T. Glutathione-Protected Gold Clusters Revisited: Bridging the Gap between gold(I)-Thiolate Complexes and Thiolate-Protected Gold Nanocrystals. *J. Am. Chem. Soc.* **2005**, *127*, 5261–5270.

(36) Negishi, Y.; Takasugi, Y.; Sato, S.; Yao, H.; Keisaku Kimura, A.; Tatsuya Tsukuda. Magic-Numbered Aun Clusters Protected by Glutathione Monolayers (N = 18, 21, 25, 28, 32, 39): Isolation and Spectroscopic Characterization. **2004**.

(37) Tracy, J. B.; Crowe, M. C.; Parker, J. F.; Hampe, O.; Fields-Zinna, C. A.; Dass, A.; Murray, R. W. Electrospray Ionization Mass Spectrometry of Uniform and Mixed Monolayer Nanoparticles: Au 25 [S(CH 2) 2 Ph] 18 and Au 25 [S(CH 2) 2 Ph] 18 - X (SR) X. *J. Am. Chem. Soc.* **2007**, *129*, 16209–16215.

(38) Chaki, N. K.; Negishi, Y.; Tsunoyama, H.; Shichibu, Y.; Tsukuda, T. Ubiquitous 8 and 29 kDa Gold:alkanethiolate Cluster Compounds: Mass-Spectrometric Determination of Molecular Formulas and Structural Implications. *J. Am. Chem. Soc.* **2008**, *130*, 8608–8610.

(39) Qian, H.; Zhu, Y.; Jin, R. Size-Focusing Synthesis, Optical and Electrochemical Properties of Monodisperse Au $_{38}$ (SC $_{2}$ H $_{4}$ Ph) $_{24}$ Nanoclusters. *ACS Nano* **2009**, *3*, 3795–3803.

(40) Guo, J.; Kumar, S.; Bolan, M.; Desireddy, A.; Bigioni, T. P.; Griffith, W. P. Mass Spectrometric Identification of Silver Nanoparticles: The Case of Ag $_{32}$ (SG) $_{19}$.

Anal. Chem. **2012**, *84*, 5304–5308.

(41) Wu, Z.; Gayathri, C.; Gil, R. R.; Jin, R. Probing the Structure and Charge State of Glutathione-Capped Au 25 (SG) 18 Clusters by NMR and Mass Spectrometry. *J. Am. Chem. Soc.* **2009**, *131*, 6535–6542.

(42) Das, A.; Li, T.; Nobusada, K.; Zeng, Q.; Rosi, N. L.; Jin, R. Total Structure and Optical Properties of a Phosphine/thiolate-Protected Au24 Nanocluster. *J. Am. Chem. Soc.* **2012**, *134*, 20286–20289.

(43) Zeng, C.; Chen, Y.; Iida, K.; Nobusada, K.; Kirschbaum, K.; Lambright, K. J.; Jin, R. Gold Quantum Boxes: On the Periodicities and the Quantum Confinement in the Au_{28}, Au_{36}, Au_{44}, and Au_{52} Magic Series. *J. Am. Chem. Soc.* **2016**, *138*, 3950–3953.

(44) Negishi, Y.; Chaki, N. K.; Shichibu, Y.; Whetten, R. L.; Tsukuda, T. Origin of Magic Stability of Thiolated Gold Clusters: A Case Study on Au25(SC6H13)18. *J. Am. Chem. Soc.* **2007**, *129*, 11322–11323.

(45) Wu, Z.; Suhan, J.; Jin, R. One-Pot Synthesis of Atomically Monodisperse, Thiol-Functionalized Au 25 Nanoclusters. *J. Mater. Chem.* **2009**, *19*, 622–626.

(46) Dass, A. Faradaurate Nanomolecules: A Superstable Plasmonic 76.3 kDa Cluster. *J. Am. Chem. Soc.* **2011**, *133*, 19259–19261.

(47) Qian, H.; Zhu, Y.; Jin, R. Atomically Precise Gold Nanocrystal Molecules with Surface Plasmon Resonance. *Proc. Natl. Acad. Sci. U. S. A.* **2012**, *109*, 696–700.

(48) Harkness, K. M.; Tang, Y.; Dass, A.; Pan, J.; Kothalawala, N.; Reddy, V. J.; Cliffel, D. E.; Demeler, B.; Stellacci, F.; Bakr, O. M.; *et al.* Ag44(SR)304−: A Silver–thiolate Superatom Complex. *Nanoscale* **2012**, *4*, 4269.

(49) Garfin, D. E. One-Dimensional Gel Electrophoresis. *Methods Enzymol.* **1990**, *182*, 425–441.

Chapter 3

Linear and Nonlinear Optical Properties of Monolayer-Protected Gold Nanocluster Films

3.1 Original Publication Information

This chapter was published as the following document:

Ho-Wu, R; Yau, S. H.; Goodson III, T. "Linear and Nonlinear Optical Properties of Monolayer-Protected Gold Nanocluster Films" *ACS Nano* **2016**, *10*, 562.

3.2 Abstract

Gold nanoclusters have been extensively studied in solution for their unique optical properties. However, many applications of nanoclusters involve the use of the material in the solid state such as films. $Au_{25}(SR)_{18}$ in polymeric hosts was used as the model for studying the optical properties of nanocluster films. Different film processing conditions as well as types of polymers were explored to produce a good quality film that is suitable for optical measurements. The best optical film was made using $Au_{25}(C_6S)_{18}$ and polystyrene. The formation of nanocluster films drastically reduces the inter-cluster distances to a few nanometers, which were estimated and characterized by optical absorption. The steady state absorption and emission properties of the nanocluster film maintained their molecular characteristic. The emissions from the nanocluster films are

found to be strongly enhanced at 730 nm with a smaller enhancement at 820 nm when the inter-cluster distance is below 8 nm. The emission enhancement can be attributed to the energy transfer between clusters due to the small inter-cluster distance. Two-photon z scan revealed that the two-photon absorption cross sections are in the order of 10^6 GM, which is an order of magnitude higher than it is in solution. The TPA enhancement is correlated with strong dipole coupling. These results show that metal nanoclusters can be made into optical quality films, which increase the interaction between clusters and enhances their linear and non-linear optical responses.

3.3 Introduction

Monolayer-protected clusters (MPCs) are metal nanosystems less than 2 nm in size, covered by a layer of organic ligands, allowing them to be studied in the condensed phase.[1–5] Some MPCs are found at certain sizes and configurations which earn them the name "magic clusters," while other MPCs do not follow this empirical rule.[6,7] The idea behind magic clusters is that there is a stable electron shell closing of the metal core and ligands, which is detailed in the super atom theory.[6] However, this theory is developed with spherical clusters. MPCs have also been found to be non-spherical and they have been studied theoretically and experimentally.[8–10] MPCs are different than typical metal nanoparticles because they exhibit molecular characteristics due to quantum confinement effects, which give them unique optical and physical properties.[2,11–15] In particular, the fluorescence[2,12,16–22] and high two-photon absorption (TPA) cross section of these systems are of great interest.[3,5,23–28] These unique optical properties are useful for applications such as biological imaging and optical limiting.[11,24,29]

Of the different MPCs that have been discovered, gold nanoclusters have been extensively studied.[15,19,30,31] The realization of a one-pot synthesis of atomically precise, mono-dispersed gold nanoclusters has been achieved by kinetically controlling the experimental conditions.[13,32–35] One-pot synthesis is now a fairly standard synthetic method.[2,4,5,35–39] Gold nanoclusters are, therefore, well characterized by various techniques. X-ray crystallography is the most powerful characterization technique for their structural identification.[40] Mass spectrometry is a faster characterization method and has been used more commonly.[13,32,38,41–47] The advancement in producing atomically precise nanoclusters allowed for the understanding of the relationship between structure and optical properties.[1,2,4,16,17,36,39,41,48] $Au_{25}(SR)_{18}$ nanoclusters, the most studied MPC, exhibits a core-shell motif that is also found for other sizes of nanoclusters.[15,41–43,49,50]

The unique optical properties of nanoclusters are strongly correlated to their structure; specifically, the core and the cluster's shell each have their own contribution.[1,3,4,16,18,51,52] Previously, we have investigated the origin of the optical properties of metal nanoclusters in solution.[1,4,5,16,17] We demonstrated that the emission of small metal clusters has higher quantum yield and longer lifetime than larger plasmonic particles or bulk metals.[1,3,4] Moreover, the visible emission of metal nanoclusters can be assigned to the MPC's core, which is short-lived, and the NIR emission to the surface-related state, which is long-lived.[1,3,4,16] While research on the optical properties of MPCs is extensive, most investigations are conducted in the solution phase. However, many applications of MPCs will be in the solid state. In the solid state, the removal of solvent can bring clusters closer to each other and it may be possible to observe cluster-cluster interaction.

Previous studies have used MPC films for optical measurements, but they were done at very low temperatures. Green *et al*. have prepared gold nanoclusters dispersed in polystyrene for low temperature photoluminescence study of $Au_{25}(SR)_{18}$, and required the samples to be desolvated.[53] Similarly, Negishi *et al*. have prepared gold nanocluster films for low temperature optical absorption study to understand the intrinsic optical properties of the nanoclusters.[48,53,54] They found that the linear optical absorption and emission of Au nanoclusters are more defined and blue-shifted at lower temperatures in contrast to large Au nanoparticles which showed temperature-independent optical properties.[48,53] However, this is a low temperature effect and it is not a good comparison between solution-phase nanoclusters versus solid-state nanoclusters. Various aspects of silver nanoclusters and nanoparticles in the solid state have been studied previously. Mai *et al*. have studied the nonlinear optical properties of silver nanoclusters and nanoparticles dispersed in glass hosts and found that the TPA cross section of Ag nanoclusters is comparable to that of Au nanoclusters in solution (~ 10^5 GM).[55] However, the Ag nanoclusters were directly synthesized inside the glass host without the monolayer ligand shell and the results were not compared against the same type of cluster in solution. Miyamura *et al*. have also prepared gold nanoclusters in a polymer matrix by direct synthesis of the clusters mixed with polystyrene.[56] The purpose of their study was to achieve high catalytic activity by controlling the preparation method of the polymer-incarcerated gold nanoclusters. So far, the optical properties of solid state MPCs at room temperature have not been explored. We show in this report a method for preparing optical quality $Au_{25}(SR)_{18}$ films in a polymer host. Taking into consideration the solubility of the nanoclusters, a few polymers were selected to investigate their effect on

the quality of the film. We also report the linear and non-linear optical properties of solid state nanoclusters as a function of inter-cluster distance and compare the results with those in solution. Based on our previous observations on fast inter-particle charge transfer that increases the nonlinear optical response,[3,21,57] we suggest that the nanocluster films would show higher TPA cross sections and a different photoluminescence response compared to those in solution. This is the first contribution that explores the optical properties of MPCs in the solid state with direct comparison with those in solution and provides new information regarding the effect of inter-cluster interaction on the photoluminescence and TPA cross sections of metal nanoclusters.

3.4 Experimental

$Au_{25}(GSH)_{18}$ nanoclusters. $Au_{25}(GSH)_{18}$ nanoclusters were synthesized following published procedure.[36] Briefly, $HAuCl_4 \cdot 3H_2O$ (170 mg, 0.5 mmol) was dissolved in 100 mL methanol and was cooled in an ice bath for 15 min. 614 mg (2 mmol) of glutathione ($C_{10}H_{17}N_3O_6S$) was added to the cooled solution and stirred for 30 min. The solution turned from yellow white, which indicates the formation of Au(I)-SG polymer.[32,33,35] A freshly prepared $NaBH_4$ (189 mg, 5 mmol) aqueous solution (25 mL) was then added to the mixture and allowed to stir for 1 h. The final solution turned dark brown, which indicates the formation of nanoclusters.[34] The crude clusters were collected by centrifuging the solution at 4700 rpm for 3 min, and washed with methanol to remove excess reagents. The precipitate was then redissolved in H_2O and incubated with excess GSH at 55°C for 3 h. The reaction mixture was centrifuged and the supernatant was collected and subsequently washed with ethanol ten times. The procedure used is optimized for the synthesis of atomically precise $Au_{25}(SR)_{18}$ and has been employed in

different publications.[18,35,49] The UV-vis absorption spectra are used to identify $Au_{25}(SG)_{18}$ and the spectrum is associated with the purity of the sample.

$Au_{25}(C_6S)_{18}$ nanoclusters. $Au_{25}(C_6S)_{18}$ nanoclusters were synthesized following a published procedure similar to that of $Au_{25}(GSH)_{18}$.[16] $HAuCl_4$ (0.5 g) was dissolved in 10 mL H_2O and mixed with TOABr (0.9 g) dissolved in 40 mL toluene. The toluene quickly turned red indicating the phase transfer of $HAuCl_4$.[30,31] The solution was placed in an ice bath. 1-hexanethiol (0.9 mL) was added to the solution and stirred until it became white. A freshly prepared $NaBH_4$ solution (0.485 g, 10 mL H_2O) was quickly added. The solution turned black and the reaction was allowed to stir for 30 min. The aqueous phase was removed and the toluene solution was washed with copious amount of water. The toluene solvent was rotary evaporated and the product was washed with DMSO. $Au_{25}(C_6S)_{18}$ nanoclusters were extracted multiple times with acetone. The acetone was evaporated and the $Au_{25}(C_6S)_{18}$ nanoclusters were washed with ethanol and acetonitrile. Similarly, the purity of the nanoclusters was verified by its UV-vis absorption spectrum.

Preparation of $Au_{25}(SR)_{18}$/polymer films. Polymers were used as a host for making nanoclusters free standing films. Different polymers were explored such as polyvinylpyrrolidone (PVP), polyvinyl alcohol (PVA), poly(methyl methacrylate) (PMMA), polystyrene (PS), polyethylene oxide (PEO, M_w = 900kDa), and polyethylene glycol (PEG, M_w = 3.9kDa). Final experimental condition for making the $Au_{25}(SR)_{18}$ film is chosen based on film clarity and film uniformity. The experimental conditions were also optimized with respect to the drying conditions. First, the polymer solution concentration was investigated. As an example, PVP films were prepared as follow: the

polymer was dissolved in water and sonicated for 1 h until the solution is clear. Four different concentrations were prepared: 133.3 g/L, 233.3 g/L, 333.3 g/L, and 400 g/L. The polymer solutions were drop-cast on clean glass slides and dried at room temperature overnight. Second, to investigate the effect of different drying conditions on the quality of the film, a drop-cast solution on a clean glass slide was allowed to dry at 40° C in the oven for a few hours. Finally, different types of polymers were investigated. PVA, PMMA, PS, PEO, and PEG films were prepared in the same manner as described for the PVP films. PEO and PEG were dissolved in water; PS, in toluene; PVA, in ethanol; and PMMA, in THF. They were dried at room temperature.

The optimized film-making condition was chosen for making $Au_{25}(SR)_{18}$ nanoclusters films (see the next section for detailed discussion). For $Au_{25}(GSH)_{18}$ film, PVP was used at a concentration of 145 mg/mL. For $Au_{25}(C_6S)_{18}$, PS was used at a concentration of 72.5 mg/mL. A general procedure for making the nanoclusters films is as follows. After the polymer is dissolved in the appropriate solvent, the nanoclusters were added to the polymer solution and briefly stirred. The amount of added nanoclusters is adjusted depending on the desired cluster concentration in the film. For example, for a 1.8 wt% $Au_{25}(GSH)_{18}$ in PVP, 2.7 mg of the clusters is added to a 1 mL solution of PVP (145 mg/mL). The $Au_{25}(SR)_{18}$/polymer solutions were drop-cast on a clean quartz coverslip and dried at room temperature overnight. To ensure a slow drying process, a cover was placed over the films.

Steady-state absorption and fluorescence measurements. The absorption spectra of $Au_{25}(GSH)_{18}$ and $Au_{25}(C_6S)_{18}$ were recorded with an Agilent 8453 spectrophotometer over 200-1200 nm. Solutions of nanoclusters were prepared in H_2O for $Au_{25}(GSH)_{18}$ and

in toluene for $Au_{25}(C_6S)_{18}$ in a 1-cm cuvette cell. The films thicknesses were estimated using a profilometer. Fluorescence measurements were recorded with Fluoromax-2 spectrophotometer (Horiba group) for the aqueous solutions and films. The films were oriented parallel to the detector at a slightly tilted angle.

Open-aperture Z-scan measurement. Non-linear optical measurements were recorded using the z-scan method.[63] A Nd:YVO_4 pump (Spectra Physics Millenia-Pro) was used to generate a cw 532 nm laser which then enters into a cavity of Ti:sapphire (Kapteyn-Murnane Laboratories Inc.) to produce 30 fs at 800 nm laser with a frequency of 90 MHz. The pulsed 800 nm laser was passed through a 10-cm focusing lens which was placed before the sample to focus the incident beam. The sample was translated along the z-axis and the transmitted beam power was measured with a power meter. To minimize the effect of beam distortion in the far field, the samples have been attached to the power meter. Measurements were taken at different spots of the films.

3.5 Results

Linear optical properties of $Au_{25}(SR)_{18}$ nanoclusters in solution. The synthesis reported here follows a published procedure to yield atomically precise mono-dispersed $Au_{25}(SR)_{18}$ nanoclusters.[34,36] Briefly, this synthetic method consists of the kinetically controlled reduction of Au(III) to Au(0), and core etching of the product to convert less stable species into the most stable $Au_{25}(SR)_{18}$ or Au(I)-SR which can be removed during the purification process.[16,35,36,38,58] The final product consists of $Au_{25}(SR)_{18}$ as the major product.[35] Distinct absorption features in the UV-Vis spectrum are seen for $Au_{25}(GSH)_{18}$ and $Au_{25}(C_6S)_{18}$ clusters (Figure). Electronic transitions at 449 and 500 nm correspond to the inter-bands and inter/intra-bands transitions of $Au_{25}(SR)_{18}$ nanoclusters.[2,16,35,41,48] The

electronic transitions at 657 nm for $Au_{25}(GSH)_{18}$ and 670 nm for $Au_{25}(C_6S)_{18}$ correspond to the HOMO-LUMO transition.[1,16,41,42] The well-defined absorption features of these clusters distinguish them from the larger plasmonic particles which show a broad surface plasmon resonance (SPR) at 520 nm.[1,2,4,21,59] Similar absorption spectra are reported in the literature for $Au_{25}(SR)_{18}$ nanoclusters, indicating that pure $Au_{25}(SR)_{18}$ nanoclusters were obtained from the synthesis.[2,4,16,35]

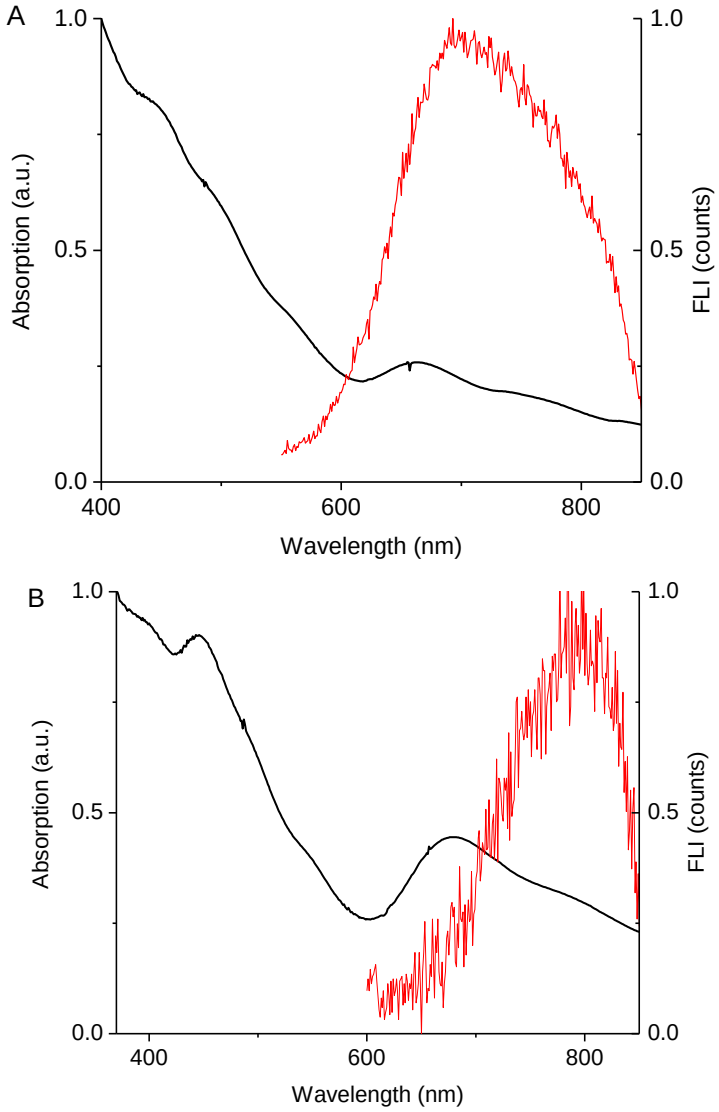

Figure 3.1. Normalized absorption spectra (black) and fluorescence emission (red) of $Au_{25}(GSH)_{18}$ (A) and $Au_{25}(C_6S)_{18}$ (B) nanoclusters in solution. (Excitation at 450 nm).

$Au_{25}(GSH)_{18}$ and $Au_{25}(C_6S)_{18}$ nanoclusters in solution exhibit a NIR fluorescence emission at 700 nm and 820 nm, respectively, upon excitation at 450 nm (Figure). NIR emission of these clusters has been observed previously by our group and elsewhere.[1,4,16] The 700 nm emission of $Au_{25}(GSH)_{18}$ is stronger than the 820 nm emission of $Au_{25}(C_6S)_{18}$.[18,52] The NIR emission of these gold clusters has been attributed to the ligand-Au motifs on the surface of the nanoclusters.[1,4,16,18,52] The ligands glutathione and hexanethiol contribute to the different emission wavelengths and quantum yield.[16,18] Glutathione is a tripeptide containing –COOH and $–NH_2$ functional groups, whereas 1-hexanethiol is an alkyl chain. It has been observed that ligands containing electron-rich groups, such as gluthathione, enhance the fluorescence emission of the nanoclusters.[18,52] Although it is not clear how the different ligands affect the emission wavelength, it has been proposed that the electron-rich ligands donate their delocalized electrons to the gold core in the cluster, which is one possible explanation why the quantum yield of $Au_{25}(GSH)_{18}$ is higher than $Au_{25}(C_6S)_{18}$.[18,52]

Film-making optimization and fabrication of $Au_{25}(SR)_{18}$ films. Different experimental conditions were explored to make optical quality films, in which the polymer is transparent between 300 nm to 800 nm so that the optical absorption of the nanoclusters could be seen in this region. In particular, the effect of polymer solution concentration, drying condition, and type of polymer were explored. First, the effect of polymer solution concentration on the quality of the film was investigated. It was found that optical quality films were obtained (dried over several hours at room temperature) from the polymer concentration range of 130 – 400 g/L (Figure 3.2).

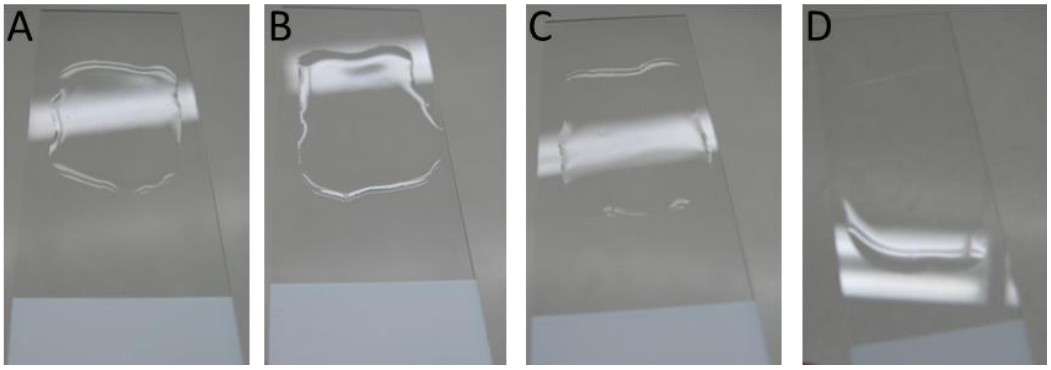

Figure 3.2. PVP films dried from 133.3 (A), 233.3 (B), 333.3 (C), 400 (D) g/L solutions at room temperature.

Secondly, different drying conditions were investigated. For slow drying conditions, the solutions were dropcast on a clean glass slide and allowed to dry at room temperature. A cover was placed on top of the films to ensure a slow drying process. For a faster drying process, the films were dried at 40° C in vacuum. Films that were dried at room temperature were of optical quality. On the other hand, films that were dried faster were not uniform and clear. From these tests, it is concluded that a good quality film is obtained by controlling the drying process. Finally, the quality of the film also depends on the polymer that was used. Various polymers were tested in order to find one that dissolves in the same solvent as the nanoclusters and does not aggregate the nanoclusters. We limited our polymer choices by taking into account that $Au_{25}(GSH)_{18}$ is only soluble in water, whereas $Au_{25}(C_6S)_{18}$ is soluble in toluene, hexane, and dichloromethane. For $Au_{25}(C_6S)_{18}$, toluene was chosen because it dries slower (boiling point 110.6 ° C). The following polymers were selected because they contained polar functional groups: polyvinylpyrrolidone (PVP), polyvinyl alcohol (PVA), poly(methyl methacrylate) (PMMA), polyethylene oxide (PEO), and polyethylene glycol (PEG). Very brittle and non-uniform films were obtained from PVA, PMMA, PEO, and PEG when they were

dried at room temperature. On the other hand, polystyrene (PS) films were very uniform and clear, comparable to PVP films. A summary of the results is shown in Table 3.1. The optical quality of the films was assessed as follows: first, the film must be transparent in the 300 – 800 nm wavelength region with respect to the polymer so that the optical properties of the nanoclusters can be observed. Second, the film must be uniform, a quality defined as free of surface irregularities in our case, to ensure minimal beam distortion or scattering when performing optical measurements.

Table 3.1. Films quality prepared by different drying conditions.

Polymer solutions	Solubility [a]	Dried at R.T.	Dried at 40 ° C	$Au_{25}(SR)_{18}$ films
PVA (in H_2O)	NS	NU, NT	NU, NT	NU, NT
PMMA (in H_2O)	NS	NU, NT	NU, NT	NU, NT
PEO (in H_2O)	S	NU, NT	NU, NT	NU, NT
PEG (in H_2O)	NS	NU, NT	NU, NT	NU, NT
PVP (in H_2O)	S	U, T	NU, NT	U, NT
PS (in toluene)	S	U, T	NU, NT	U, T

[a] Solubility of the nanoclusters in the presence of the polymer, without significant change in the absorption spectrum of the clusters. NS = not soluble; S = soluble; T = transparent; NT = non transparent; U = uniform; NU = non uniform.

Of the polymers that were tested, only PVP and PS resulted in optical quality films when slowly dried at room temperature (Table 3.1, third column). These polymeric hosts were used to prepare nanocluster films in two steps. First, the polymer was dissolved in the appropriate solvent and the nanoclusters were added. Second, the clusters/polymer solution was dropcast on a clean quartz coverslip and dried. Although we were able to produce optical quality films with PVP and PS, upon the addition of $Au_{25}(SR)_{18}$ nanoclusters, the quality of the films could change. As seen on Figure 3.3, $Au_{25}(C_6S)_{18}$/PS not only dried into a uniform film, but the film is also clear. This is an important factor when performing optical measurements, which will be discussed below.

$Au_{25}(GSH)_{18}$/PVP film, in contrast, is not as clear as $Au_{25}(C_6S)_{18}$/PS, especially when the amount of nanoclusters in the film is increased. Moreover, the $Au_{25}(GSH)_{18}$/PVP films were very brittle and degrades easily by moisture in the air. Therefore, a series of $Au_{25}(C_6S)_{18}$/PS films of different densities were prepared for density (or inter-cluster distance) dependent studies.

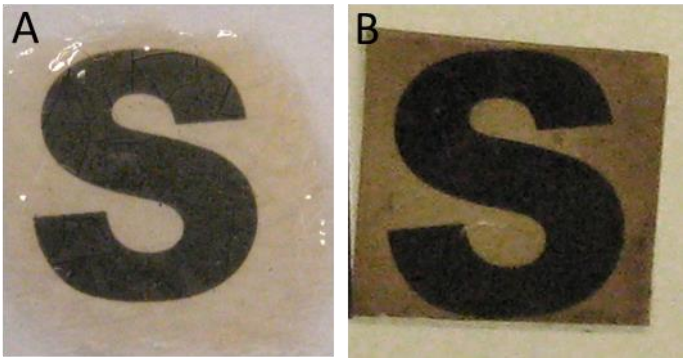

Figure 3.3. Samples of $Au_{25}(GSH)_{18}$/PVP films (A) and $Au_{25}(C_6S)_{18}$/PS films (B) at different nanoclusters loading.

Scheme 3.1. Typical nanoclusters densities in solution and in film for this study.

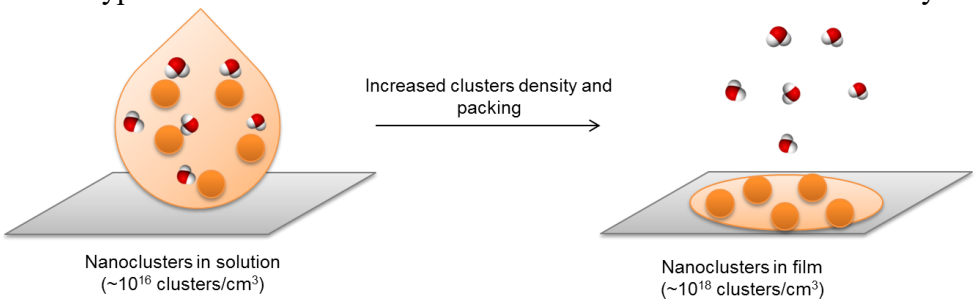

Average density and inter-cluster distance in nanocluster films. The densities of the nanoclusters are significantly increased in the film. The polymers that were used as hosts for the nanocluster films can be seen as new environments for dispersing the nanoclusters, but at a much smaller volume (Scheme 3.1). We estimated the *average* nanocluster density and inter-cluster distance in the film and in solution based on their film thickness and optical density at 670 nm (ε = 8000 M^{-1} cm^{-1}).[38]

Using the estimated densities, we calculated the average inter-cluster distance using dimensional analysis (equation 3.1 and figure 3.4). In equation 1, r is the inter-cluster distance; *l* is the length of the cube; N is the number of clusters along that length; $d_{cluster}$ is the diameter of the cluster taken to be 1.1 nm.[17] In this estimation, we assumed that the cluster films are uniform and that the clusters are spherical. The optical density, which was used for this estimation, was measured at the center of each film where the nanoclusters appear to be most uniform. A series of nanocluster films of varying densities were prepared and their inter-cluster distances were calculated (Table 3.2). The inter-cluster distance, r, becomes relevant when comparing the optical properties of the films and solution because one might expect cluster-cluster interactions as the inter-cluster distance becomes very short.

$$r = (l - Nd_{cluster}) / (N - 1) \qquad (3.1)$$

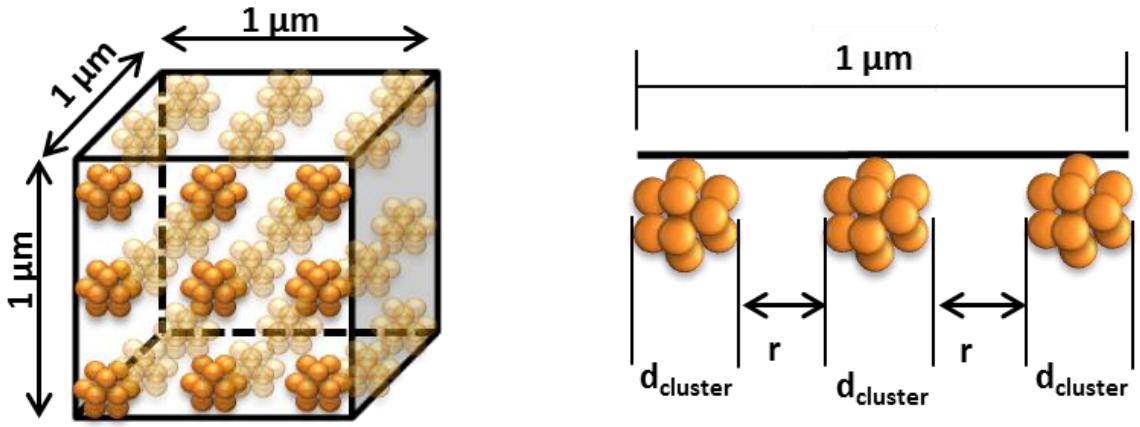

Figure 3.4. Inter-cluster distance derived from the nanoclusters density in a cubic volume, taken to be 1 μm^3.

Table 3.2. Average densities and inter-cluster distances of $Au_{25}(C_6S)_{18}$ films compared to solutions, estimated by their optical densities at 670 nm.

ρ ($x10^{18}$ cluster/cm^3)		$< r >$ (nm)	
solution	film	solution	film
0.24	8.80	15.2	3.76
0.12	3.44	19.5	5.56
0.06	2.41	25	6.40
0.02	1.72	38.7	7.30
0.006	1.39	57.4	7.90
0.002	1.16	85.5	8.51

Linear optical properties of $Au_{25}(SR)_{18}$ films. $Au_{25}(SR)_{18}$ in solution show pronounced absorption features due to the strong quantum confinement effects and its highly ordered core.[1,41] Upon the addition of polymers to the nanocluster solutions, a slight decrease in absorption between 400 nm and 800 nm is observed for both $Au_{25}(GSH)_{18}$ and $Au_{25}(C_6S)_{18}$. The decrease in absorption is indicative of the interdiffusion of the polymer in the nanocluster solutions. A comparison between the absorption spectra of the $Au_{25}(SR)_{18}$ nanoclusters in solution and in film is shown in Figure 3.5. Although PVP films are optically transparent, the $Au_{25}(GSH)_{18}$/PVP films are not as clear compared to $Au_{25}(C_6S)_{18}$/PS films (Figure 3.3 and Figure 3.5). The presence of PVA, PMMA, or PEG in a solution of $Au_{25}(GSH)_{18}$ nanocluster drastically changes the absorption spectrum of the nanoclusters and the resulting films were not uniform or transparent. Thus, we limited our choice to PVP. For $Au_{25}(GSH)_{18}$/PVP film, the absorption features of the nanoclusters are overshadowed by the high extinction of the film, due to the poor incorporation of the nanoclusters in the polymer host or formation of crystals. On the other hand, the presence of PEO does not change the absorption spectrum of $Au_{25}(GSH)_{18}$ solution significantly but the dried film was not uniform or transparent. $Au_{25}(C_6S)_{18}$/PS film is the best film produced. It remains optically transparent, allowing

the absorption features at 400 nm and 670 nm to be seen (Figure 3.5B). However, the absorption features are less pronounced than those in solution because the densities of the nanocluster films are at least one order of magnitude higher than that in solutions. Here we show that the nanocluster's absorption spectrum provides a way to assess the optical quality of the films.

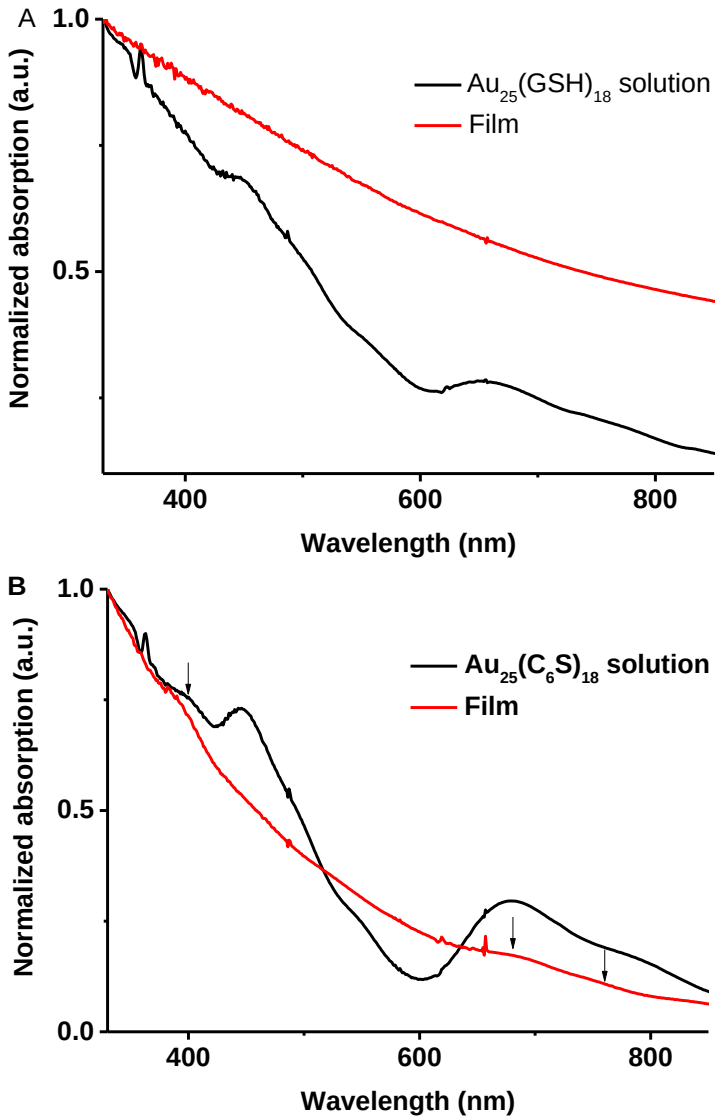

Figure 3.5. Normalized absorption spectra of $Au_{25}(GSH)_{18}$ (A) and $Au_{25}(C_6S)_{18}$ (B) nanoclusters in solution, and in film. A 1-cm cell was used for the solutions. The thickness of the films is ~60 μm.

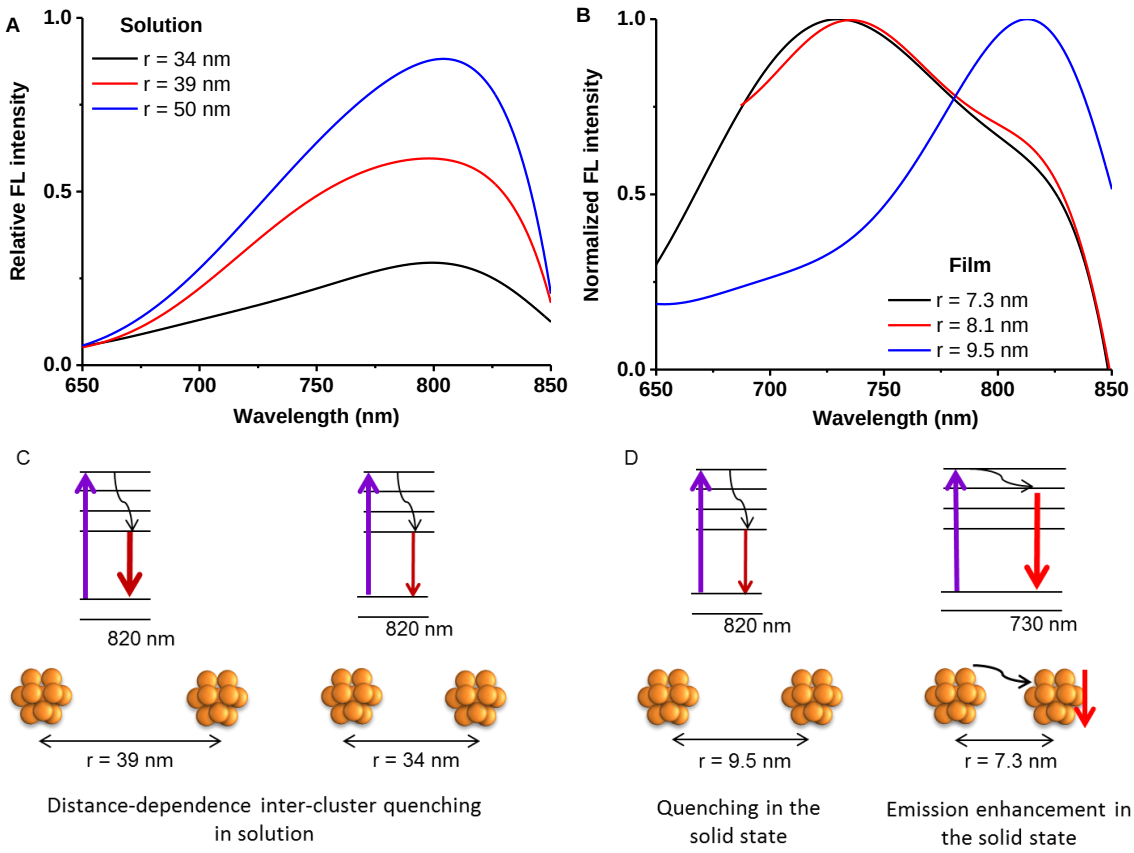

Figure 3.6. Photoluminescence of $Au_{25}(C_6S)_{18}$ solutions (A) and films (B) excited at 400 nm and 450 nm respectively. The 800 nm peak due to excitation has been cut off in the spectra of the solutions. Energy level diagrams depicting the photoluminescence behaviors of $Au_{25}(C_6S)_{18}$ in solutions (C) and solid state (D).

The photoluminescence of $Au_{25}(C_6S)_{18}$ is shown in Figure 3.6. The photoluminescence of $Au_{25}(C_6S)_{18}$ solutions show a maximum at ~820 nm (Figure 3.6A).[18,53] Photoluminescence enhancement was observed in a dilute solution of $Au_{25}(C_6S)_{18}$ because the interaction between neighboring clusters are minimized (Figure 3.6A). There are two deactivation processes to consider: coupling to vibrations of the surface ligand and energy transfer between surface ligands of neighboring clusters. In solution, $Au_{25}(C_6S)_{18}$ emits at 820 nm independent of concentration. This would indicate that the total excited state energy lost to non-radiative pathways is the same at all concentrations: the dilute concentration is expected to have less interaction between

neighboring clusters, therefore inter-cluster quenching is minimized. Emission enhancement at 820 nm in the dilute concentration can be seen as minimal loss of emitted photons for other processes such as absorption by a nearby cluster (Figure 3.6C). Under the same experimental conditions, $Au_{25}(C_6S)_{18}$ films show photoluminescence at around 820 nm (Figure 3.6B). Interestingly, for $Au_{25}(C_6S)_{18}$ films of r = 7.3 – 8.1 nm, we observe an additional emission peak at 730 nm (Figure 3.6B).

It is possible that the 730 nm emission is always present, but too weak to be detected in solution. This emission at 730 nm has been reported in low-temperature experiments.[53] To better understand this emission, the emission spectra of r = 7.3 and 9.5 nm films and r = 34 nm solution are modeled with two Gaussian peaks at 730 nm and 820 nm (Figure 3.7). It was interesting to see that the 730 nm emission is present even in the solution, which was usually not reported for room temperature experiments.[1,18,60] When the inter-cluster distance is decreased in the film, the emission observed was probably due to the enhancement of both 730 nm and 820 nm emissions (Figure 3.7 A and B). In order to quantify the emission enhancement, relative quantum yields were calculated by dividing the fluorescence counts with the absorption of the film (optical density), since all excitation and emission collection parameters are the same. The relative quantum yields (corrected fluorescence intensity) of the films and the solution (Figure 3.7D) show that there is an emission enhancement at 730 nm as well as 820 nm, when the inter-cluster distance is less than 8 nm. The photoluminescence of the film r = 8.1 nm was similar to that of the film r = 7.3 nm and were fitted with the same parameters. Interestingly, when the film r = 9.5 nm is compared to solution, both emissions at 730 nm and 820 nm are quenched (Figure 3.7D). These results suggest that emission enhancement and quenching

happen at different inter-cluster distance regimes separated at about 9 nm. Possible explanation for this observation can be found in the discussion section (see below).

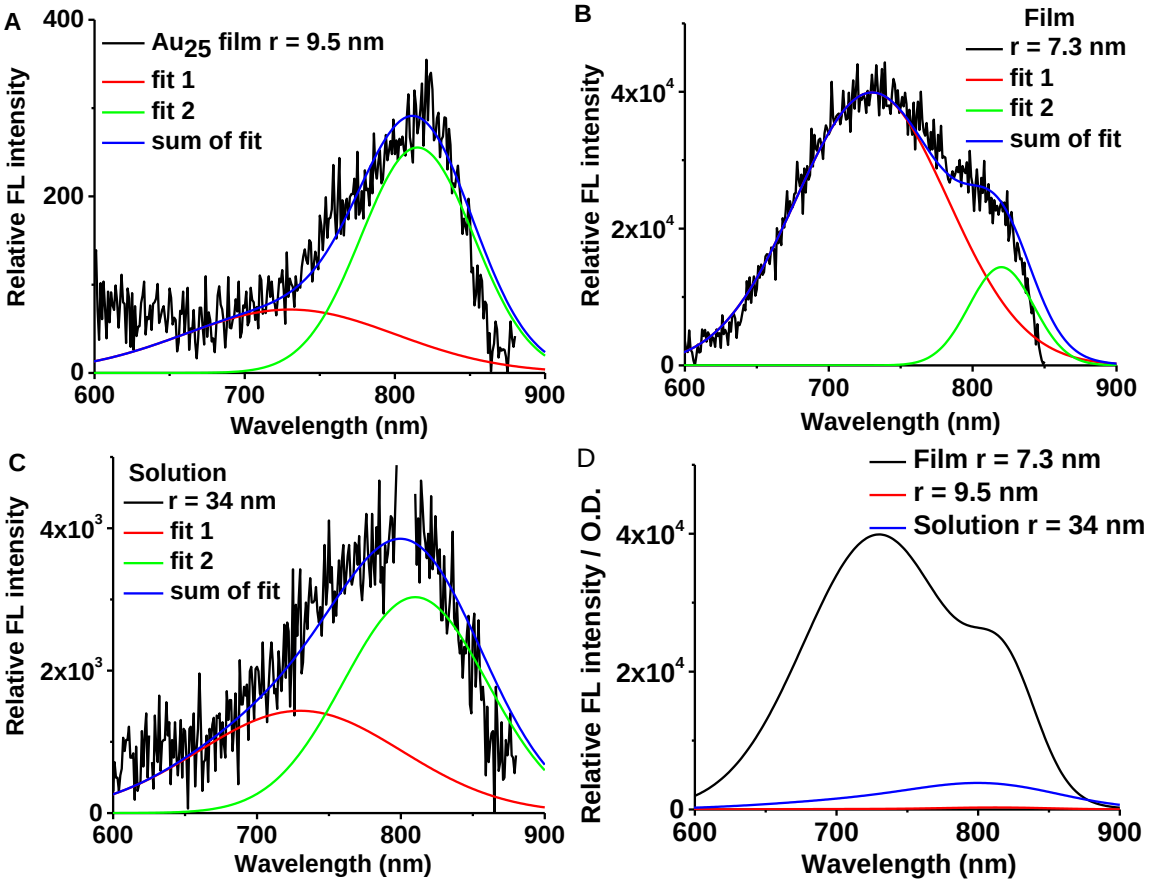

Figure 3.7. Photoluminescence of $Au_{25}(C_6S)_{18}$ films with r = 9.5 nm (A) and r = 7.3 nm (B), and solution with r = 34 nm fit to two Gaussian peaks at 730 nm and 820 nm. Photoluminescence of $Au_{25}(C_6S)_{18}$ films and solution with normalized optical density (D).

Non-linear transmission of $Au_{25}(SR)_{18}$ nanocluster films. The non-linear optical properties of $Au_{25}(SR)_{18}$ nanocluster films were investigated using the z-scan method. The z-scan data can be plotted as an intensity-dependent transmission curve because the laser intensity increases when it is being focused. For this set-up, the intensity of the monochromatic Gaussian beam can be calculated along the z direction with radius *w*:

$$w(z) = w_0\sqrt{1 + \left(\frac{z}{z_R}\right)^2} \qquad (3.2)$$

where w_0 is the beam waist radius; z is the distance from the focus; and z_R is the Rayleigh range. The decrease in transmission as the film is brought closer to the laser focus, z = 0, (highest intensity) indicates a non-linear absorption process.[5,23,24] This behavior is consistent with $Au_{25}(SR)_{18}$ nanoclusters in solution as reported in the literature.[5,23,24] The decrease in transmission is characteristic of molecular-like behavior and differs from plasmonic particles.[23] In larger plasmonic particles, the z-scan profile shows an increase in transmission near the focus, indicative of saturable absorption behavior.[23] The transmission decrease is also observed in thiol-functionalized gold nanodots (~1.33 nm diameter), indicating that nonlinear absorption occurs in quantum sized systems.[61]

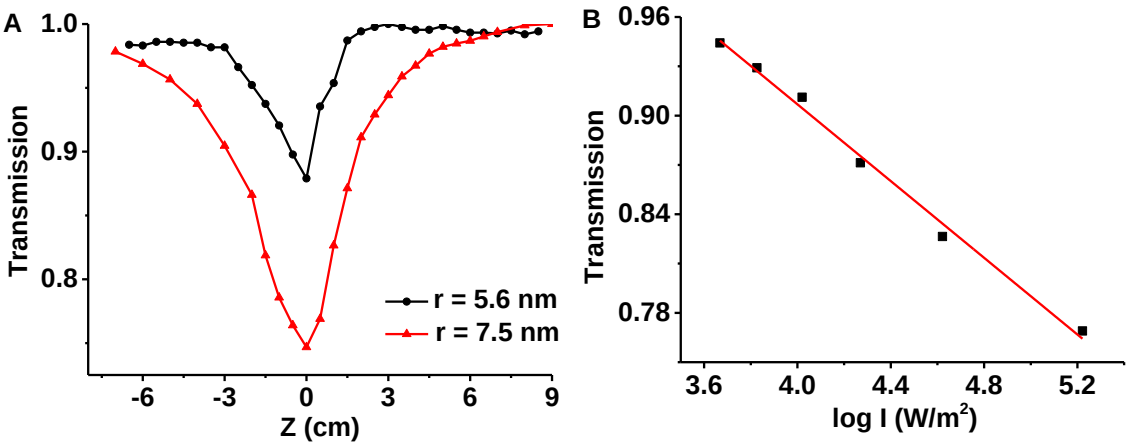

Figure 3.8. Z-scan profile of $Au_{25}(C_6S)_{18}$ films (A) and intensity-dependent transmission of the r = 7.5 nm film (B).

The z-scan data can be plotted as an intensity-dependent transmission curve (Figure 3.8B). The intensity-dependent transmission of the $Au_{25}(SR)_{18}$ films was fitted by equation 3.3,[62] where β is the TPA coefficient; I, intensity of the laser along the focus, which is defined as power (W) over the beam area (m^2); L_{eff}, the effective interaction length. The effective interaction length takes into account the linear absorption coefficient and the length of the sample.[63] For thin samples and negligible linear

absorption at 800 nm, the L_{eff} can be assumed to be the nanoclusters film thickness. The TPA coefficient, β, is related to the TPA cross section, σ, by equation 4;[63] where N is the Avogadro's number; c, concentration; h, Planck constant; υ, laser frequency. By fitting the transmission curves of the $Au_{25}(SR)_{18}$ films with these equations, the TPA coefficients and cross sections were obtained. Note that in Figure 3.8B, the intensity is expressed in $\log_{10}$ to adjust the scale for visual purpose. The TPA cross sections for $Au_{25}(C_6S)_{18}$ films show an order of magnitude increase compared to that reported for $Au_{25}(C_6S)_{18}$ in solution (Table 3.3).[5,24] For $Au_{25}(GSH)_{18}$ film, a TPA cross section of $1.6x10^8$ GM was calculated.

$$\Delta T = -\beta I L_{eff} \qquad (3.3)$$

$$\sigma = \frac{\beta h \upsilon 10^3}{Nc} \qquad (3.4)$$

Table 3.3. $Au_{25}(C_6S)_{18}$ films of varying densities and average TPA cross section.

ρ ($x10^{18}$ cluster/cm^3)	r (nm)	σ ($x10^6$ GM)
~0.0006	~133	0.19[a], 0.43[b]
7.50	4.0	1.53 ± 0.71
3.43	5.6	3.45 ± 1.47
1.83	7.1	3.54 ± 1.82
1.59	7.5	4.39 ± 0.73
1.19	8.4	4.83 ± 1.59
0.80	9.8	10.5 ± 0.84

[a]$Au_{25}(GSH)_{18}$ solution in water, calculated from z-scan measurement.[24] [b]$Au_{25}(C_6S)_{18}$ solution in toluene, calculated from TPE fluorescence.[5]

3.6 Discussion

The optical properties of $Au_{25}(SR)_{18}$ nanoclusters are closely related to their structure. Specifically, the core and the surface ligand shell each have their own contributions. The absorption in the visible region is primarily due to the optical properties of the nanocluster's core and mixed metal-ligand states.[1,3,4,41] The linear absorption of the nanocluster films is comparable to that in solution and suggests that the molecular

properties of the nanoclusters are maintained, and no large aggregates or plasmonic nanoparticles were formed. However, one would expect that the absorption features of the nanoclusters in the solid state to become more pronounced, which was not observed. Sharper absorption features have been seen in the solid state and solution phase $Au_{25}(SR)_{18}$ nanoclusters at low temperatures (90 – 25 K).[48,64] Film quality, thickness (~60 μm), and high density might contribute to the less pronounced optical features in the film. We report that it is possible to have very short inter-cluster distances in films without the formation of nanocluster aggregates.

NIR photoluminescence has been reported for $Au_{25}(SR)_{18}$ nanoclusters.[4,16,18,52] Photoluminescence enhancement is observed in $Au_{25}(C_6S)_{18}$ solutions at 820 nm as the inter-cluster distance is increased which suggests that there is some inter-cluster quenching. However, in the solid state, strong emission enhancement was observed for decreasing inter-distance distances. Our careful analysis discovered that the emission of the film is enhanced at 730 nm as well as 820 nm. Both emissions are present in the solution, identified by our Gaussian fitting (Figure 3.7), with the 820 nm emission being much stronger than the 730 nm emission. When the inter-cluster distance is at 8.1 and 7.3 nm, both emissions are enhanced. Similar nanoparticle-dye systems at defined distances have been studied previously where energy transfer has been observed.[65–67] At a separation of 9 nm, emissions at both 730 and 820 nm were quenched compared to the solution. One possible explanation for this is that Förster Resonance Energy Transfer (FRET) can occur in the separation regime of 4-8 nm.[65–67] At distances larger than 8 nm, fluorescence quenching occurs which is typical of dyes near plasmonic gold nanoparticles.[65] For a dye near a 1.5 nm gold cluster, it is more common that the

quenching mechanism occurs by Nanosurface Energy Transfer (NSET), which follows a $1/d^4$ distance dependence.[65,68–70] In our system, however, we do not have a dye-particle pair. We have two identical molecules within 7.3, 8.1, and 9.5 nm of each other, which could be coupled by their dipoles or electric fields. It is evident by our experiment that the dipole coupling of two identical nanocluster actually enhances the emission at 730 nm and 820 nm. Based on this result, we suggest that FRET could occur below 8.1 nm separation while above 9 nm, quenching occurs possibly by the NSET mechanism (Figure 3.9).[65,68,69]

Another possible explanation for the 730 nm emission enhancement may be due to the presence of highly emissive nanocluster dimers. If dimers are present, a very short inter-cluster distance can be assumed to be less than 2 nm.[71] Based on the nearest neighbor distribution model, using an average inter-cluster distance of 8 nm, the model suggests that 1% of the separation distances are less than 2 nm. Possible dimers of Au_{25} nanoclusters would be similar to Au_{38} nanoclusters which consist of a core fused together by two Au_{13} icosahedrons.[72,73] Au_{38} emits at 920 nm, which is different than the 730 nm observed, ruling out the possibility of Au_{38} nanoclusters in the films studied. Another example of dimer-like system is bi-icosahedral Au_{25} clusters ("Au_{25}-rods") capped with 2-phenylethanethiol which have emissions at 770 nm and 830 nm, and are also different than what we observed.[74] If the 730 nm emission is caused by the "dimers" which is 1% of the modeled inter-cluster distance distribution, the relative quantum yield would be 5 orders of magnitude higher than that in solution, which is higher than dimer-like nanoclusters. Combined with the lack of aggregation peaks in the absorption spectrum, the dimer model is possible but unlikely.

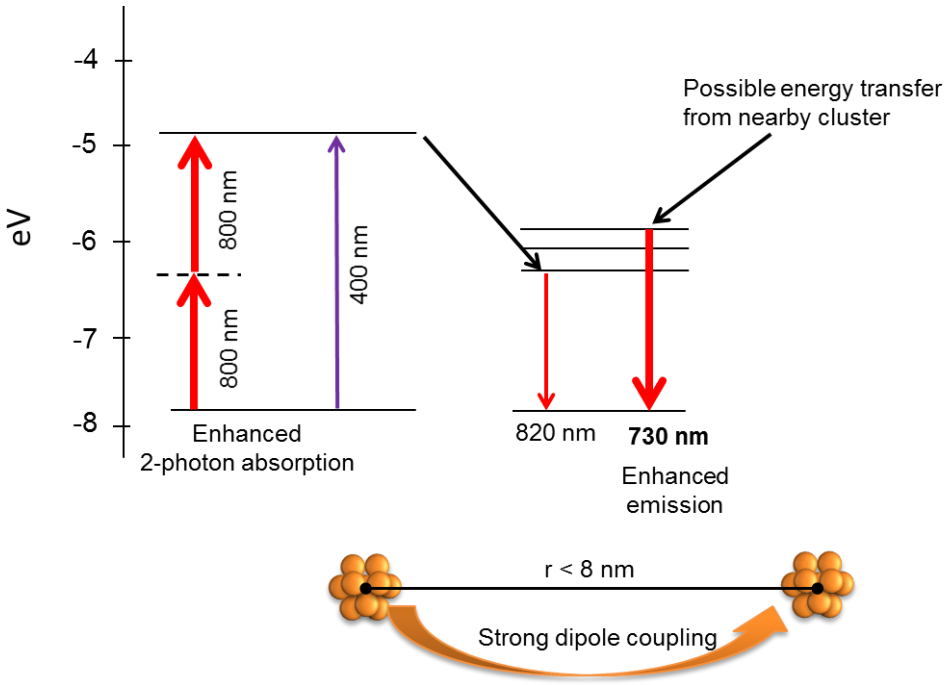

Figure 3.9. Energy diagram depicting the linear[41] and non-linear absorptions and emission of $Au_{25}(SR)_{18}$ nanoclusters in solid state. Interaction of the ligand-shell motif and vibrational lock at small inter-cluster distances gives rise to the higher energy emission, while strong dipole coupling between nanoclusters enhance TPA cross-sections.

The TPA cross sections of the $Au_{25}(C_6S)_{18}$ films are ten times higher than the cross section (obtained by TPE fluorescence) of the nanoclusters in solution. Note that the z-scan method is known for overestimating the TPA cross-section because of the self-defocusing behavior of the incident light or light scattering, compared to TPE fluorescence.[75] Despite this, a TPA cross section of 1.9×10^5 GM has been reported for $Au_{25}(GSH)_{18}$ in solution using the z-scan method.[24] This cross section is in the same order of magnitude as the cross section of $Au_{25}(C_6S)_{18}$ solution measured by TPE fluorescence.[1,5,76] The enhanced TPA cross section is likely due to the strong dipole coupling of nearby nanoclusters. A similar comparison between the nonlinear optical properties of nanoclusters in the solid state and in solution has been reported by Mai *et al.*[55] For small (1.2 nm) Ag nanoclusters dispersed in a glass host, TPA cross sections of

0.06-0.8 x 10^6 GM have been calculated, which are in the same order of magnitude as that of Au nanoclusters in solution.[1,5,55] This comparison demonstrates that Ag nanoclusters in the solid state can have a TPA cross section as high as Au nanoclusters in solution. However, Mai's work does not compare between the same type of metal nanocluster and a definitive conclusion cannot be drawn on how the nonlinear optical response changes for a metal nanocluster going from solution to solid. Another possible explanation for the high TPA cross sections of the nanocluster films is the increased rigidity of the nanocluster in the film. In organic chromophores, one of the criteria for a high TPA cross section in solution is ensuring an extended π conjugation which increases the rigidity of the molecule (locked-conformation).[75] For $Au_{25}(C_6S)_{18}$, the small *r* suggests the possibility of effective dipole coupling between clusters, similar to extending a molecule's π conjugation (Figure 3.9). Similar observation has been reported where NLO response is larger in dendrimer-metal nanocomposites in films compared to solutions.[77,78] It is interesting to note that the TPA cross sections of the films increases with *r*. A similar trend has been observed in chromophores attached to gold nanorods at distances between 6 – 15 nm, excited at off resonance from the plasmon.[79] It was proposed that the trend observed was due to the constructive and destructive interference between the excitation and the electric field from the nanorod.[79,80]

3.7 Conclusion

$Au_{25}(SR)_{18}$ nanoclusters films with excellent optical quality can be made by using a polymer host. Nanocluster films can be made with controllable inter-cluster distances, much smaller than solution, without aggregation. The inter-cluster distances can be estimated using the film thickness and the optical density of the films. We demonstrated

that the production of optical quality nanocluster films with $Au_{25}(SR)_{18}$ relies on the drying condition and solvent/polymer choice. This is the first report on the relationship between optical properties and inter-cluster distance in the solid state. The steady state absorption properties of nanocluster films show that the nanoclusters retain the same molecular-like properties and it is clear that no larger aggregates or plasmonic particles were formed using this method. The TPA and photoluminescence properties of the nanoclusters can be enhanced, due to the strong dipole coupling between nanoclusters. The enhancement of the emission is strongest at a separation of smaller than 8 nm, with strong enhancement to the emission at 730 nm and a moderate enhancement to the emission at 820 nm. This emission enhancement distance is similar to the FRET distance observed for nanoparticle-dye systems. TPA cross section of the nanocluster films are an order of magnitude higher than in solution, which suggest strong dipole coupling between clusters. Metal nanoclusters films are a new way to produce nanoclusters in the solid state, and these results suggest that their linear and non-linear optical properties can be enhanced.

3.8 References

(1) Yau, S. H.; Varnavski, O.; Goodson, T. An Ultrafast Look at Au Nanoclusters. *Acc. Chem. Res.* **2013**, *46*, 1506–1516.

(2) Varnavski, O.; Ramakrishna, G.; Kim, J.; Lee, D.; Goodson, T. Critical Size for the Observation of Quantum Confinement in Optically Excited Gold Clusters. *J. Am. Chem. Soc.* **2010**, *132*, 16–17.

(3) Yau, S. H.; Abeyasinghe, N.; Orr, M.; Upton, L.; Varnavski, O.; Werner, J. H.; Yeh, H.-C.; Sharma, J.; Shreve, A. P.; Martinez, J. S.; Goodson, T. Bright Two-Photon Emission and Ultra-Fast Relaxation Dynamics in a DNA-Templated Nanocluster Investigated by Ultra-Fast Spectroscopy. *Nanoscale* **2012**, *4*, 4247–4254.

(4) Yau, S. H.; Varnavski, O.; Gilbertson, J. D.; Chandler, B.; Ramakrishna, G.;

Goodson, T. Ultrafast Optical Study of Small Gold Monolayer Protected Clusters: A Closer Look at Emission. *J. Phys. Chem. C* **2010**, *114*, 15979–15985.

(5) Ramakrishna, G.; Varnavski, O.; Kim, J.; Lee, D.; Goodson, T. Quantum-Sized Gold Clusters as Efficient Two-Photon Absorbers. *J. Am. Chem. Soc.* **2008**, *130*, 5032–5033.

(6) Walter, M.; Akola, J.; Lopez-Acevedo, O.; Jadzinsky, P. D.; Calero, G.; Ackerson, C. J.; Whetten, R. L.; Grönbeck, H.; Häkkinen, H. A Unified View of Ligand-Protected Gold Clusters as Superatom Complexes. *Proc. Natl. Acad. Sci. U. S. A.* **2008**, *105*, 9157–9162.

(7) Kreibig, U.; Genzel, L. Optical Absorption of Small Metallic Particles. *Surf. Sci.* **1985**, *156*, 678–700.

(8) Das, A.; Li, T.; Nobusada, K.; Zeng, Q.; Rosi, N. L.; Jin, R. Total Structure and Optical Properties of a Phosphine/Thiolate-Protected Au_{24} Nanocluster. *J. Am. Chem. Soc.* **2012**, *134*, 20286–20289.

(9) Chen, J.; Zhang, Q.-F.; Bonaccorso, T. A.; Williard, P. G.; Wang, L.-S. Controlling Gold Nanoclusters by Diphospine Ligands. *J. Am. Chem. Soc.* **2014**, *136*, 92–95.

(10) Muniz-Miranda, F.; Menziani, M. C.; Pedone, A. Assessment of Exchange-Correlation Functionals in Reproducing the Structure and Optical Gap of Organic-Protected Gold Nanoclusters. *J. Phys. Chem. C* **2014**, *118*, 7532–7544.

(11) Daniel, M.-C.; Astruc, D. Gold Nanoparticles: Assembly, Supramolecular Chemistry, Quantum-Size-Related Properties, and Applications toward Biology, Catalysis, and Nanotechnology. *Chem. Rev.* **2004**, *104*, 293–346.

(12) Varnavski, O. P.; Mohamed, M. B.; El-Sayed, M. A.; Goodson, T. Relative Enhancement of Ultrafast Emission in Gold Nanorods. *J. Phys. Chem. B* **2003**, *107*, 3101–3104.

(13) Schaaff, T. G.; Shafigullin, M. N.; Khoury, J. T.; Vezmar, I.; Whetten, R. L.; Cullen, W. G.; First, P. N.; Gutiérrez-Wing, C.; Ascensio, J.; Jose-Yacamán, M. J. Isolation of Smaller Nanocrystal Au Molecules: Robust Quantum Effects in Optical Spectra. *J. Phys. Chem. B* **1997**, *101*, 7885–7891.

(14) Kubo, R.; Kawabata, A.; Kobayashi, S. Electronic Properties of Small Particles. *Annu. Rev. Mater. Sci.* **1984**, *14*, 49–66.

(15) Jin, R. Atomically Precise Metal Nanoclusters: Stable Sizes and Optical Properties. *Nanoscale* **2015**, *7*, 1549–1565.

(16) Devadas, M. S.; Kim, J.; Sinn, E.; Lee, D.; Goodson, T.; Ramakrishna, G. Unique Ultrafast Visible Luminescence in Monolayer-Protected Au_{25} Clusters. *J. Phys. Chem. C* **2010**, *114*, 22417–22423.

(17) Varnavski, O.; Ramakrishna, G.; Kim, J.; Lee, D.; Goodson, T. Optically Excited Acoustic Vibrations in Quantum-Sized Monolayer-Protected Gold Clusters. *ACS Nano* **2010**, *4*, 3406–3412.

(18) Wu, Z.; Jin, R. On the Ligand's Role in the Fluorescence of Gold Nanoclusters. *Nano Lett.* **2010**, *10*, 2568–2573.

(19) Jin, R. Quantum Sized, Thiolate-Protected Gold Nanoclusters. *Nanoscale* **2010**, *2*, 343–362.

(20) Wu, Z.; Wang, M.; Yang, J.; Zheng, X.; Cai, W.; Meng, G.; Qian, H.; Wang, H.; Jin, R. Well-Defined Nanoclusters as Fluorescent Nanosensors: A Case Study on $Au_{25}(SG)_{18}$. *small* **2012**, *8*, 2028–2035.

(21) Varnavski, O. P.; Ranasinghe, M.; Yan, X.; Bauer, C. A.; Chung, S.-J.; Perry, J. W.; Marder, S. R.; Goodson, T. Ultrafast Energy Migration in Chromophore Shell-Metal Nanoparticle Assemblies. *J. Am. Chem. Soc.* **2006**, *128*, 10988–10989.

(22) Varnavski, O.; Ispasoiu, R. G.; Balogh, L.; Tomalia, D.; Goodson, T. Ultrafast Time-Resolved Photoluminescence from Novel Metal–Dendrimer Nanocomposites. *J. Chem. Phys.* **2001**, *114*, 1962-1965.

(23) Philip, R.; Chantharasupawong, P.; Qian, H.; Jin, R.; Thomas, J. Evolution of Nonlinear Optical Properties: From Gold Atomic Clusters to Plasmonic Nanocrystals. *Nano Lett.* **2012**, *12*, 4661–4667.

(24) Polavarapu, L.; Manna, M.; Xu, Q.-H. Biocompatible Glutathione Capped Gold Clusters as One- and Two-Photon Excitation Fluorescence Contrast Agents for Live Cells Imaging. *Nanoscale* **2011**, *3*, 429–434.

(25) Smith, D. D.; Yoon, Y.; Boyd, R. W.; Campbell, J. K.; Baker, L. A.; Crooks, R. M.; George, M. Z-Scan Measurement of the Nonlinear Absorption of a Thin Gold Film. *J. Appl. Phys.* **1999**, *86*, 6200–6205.

(26) West, R.; Wang, Y.; Goodson, T. Nonlinear Absorption Properties in Novel Gold Nanostructured Topologies. *J. Phys. Chem. B* **2003**, *107*, 3419–3426.

(27) Ispasoiu, R. G.; Jin, Y.; Lee, J.; Papadimitrakopoulos, F.; Goodson, T. Two-Photon Absorption and Photon-Number Squeezing with CdSe Nanocrystals. *Nano Lett.* **2002**, *2*, 127–130.

(28) Ispasoiu, R. G.; Balogh, L.; Varnavski, O. P.; Tomalia, D. A. Large Optical

Limiting from Novel Metal−Dendrimer Nanocomposite Materials. *J. Am. Chem. Soc.* **2000**, *122*, 11005–11006.

(29) Ding, C.; Tian, Y. Gold Nanocluster-Based Fluorescence Biosensor for Targeted Imaging in Cancer Cells and Ratiometric Determination of Intracellular pH. *Biosens. Bioelectron.* **2015**, *65*, 183–190.

(30) Brust, M.; Walker, M.; Bethell, D.; Schiffrin, D. J.; Whyman, R. Synthesis of Thiol-Derivatised Gold Nanoparticles in a Two-Phase Liquid-Liquid System. *J. Chem. Soc., Chem. Commun.* **1994**, 801–802.

(31) Perala, S. R. K.; Kumar, S. On the Mechanism of Metal Nanoparticle Synthesis in the Brust-Schiffrin Method. *Langmuir* **2013**, *29*, 9863–9873.

(32) Hostetler, M. J.; Wingate, J. E.; Zhong, C.-J.; Harris, J. E.; Vachet, R. W.; Clark, M. R.; Londono, J. D.; Green, S. J.; Stokes, J. J.; Wignall, G. D.; Glish, G. L.; Porter, M. D.; Evans, N. D.; Murray, R. W. Alkanethiolate Gold Cluster Molecules with Core Diameters from 1.5 to 5.2 nm: Core and Monolayer Properties as a Function of Core Size. *Langmuir* **1998**, *14*, 17–30.

(33) Chen, S.; Templeton, A. C.; Murray, R. W. Monolayer-Protected Cluster Growth Dynamics. *Langmuir* **2000**, *16*, 3543–3548.

(34) Kim, J.; Lema, K.; Ukaigwe, M.; Lee, D. Facile Preparative Route to Alkanethiolate-Coated Au_{38} Nanoparticles: Postsynthesis Core Size Evolution. *Langmuir* **2007**, *23*, 7853–7858.

(35) Zhu, M.; Lanni, E.; Garg, N.; Bier, M. E.; Jin, R. Kinetically Controlled, High-Yield Synthesis of Au_{25} Clusters. *J. Am. Chem. Soc.* **2008**, *130*, 1138–1139.

(36) Li, G.; Jiang, D.; Kumar, S.; Chen, Y.; Jin, R. Size Dependence of Atomically Precise Gold Nanoclusters in Chemoselective Hydrogenation and Active Site Structure. *ACS Catal.* **2014**, *4*, 2463–2469.

(37) Yuan, X.; Zhang, B.; Luo, Z.; Yao, Q.; Leong, D. T.; Yan, N.; Xie, J. Balancing the Rate of Cluster Growth and Etching for Gram-Scale Synthesis of Thiolate-Protected Au_{25} Nanoclusters with Atomic Precision. *Angew. Chem. Int. Ed. Engl.* **2014**, *53*, 4623–4627.

(38) Negishi, Y.; Nobusada, K.; Tsukuda, T. Glutathione-Protected Gold Clusters Revisited: Bridging the Gap Between Gold(I)-Thiolate Complexes and Thiolate-Protected Gold Nanocrystals. *J. Am. Chem. Soc.* **2005**, *127*, 5261–5270.

(39) Chaki, N. K.; Negishi, Y.; Tsunoyama, H.; Shichibu, Y.; Tsukuda, T. Ubiquitous 8 and 29 kDa Gold:Alkanethiolate Cluster Compounds: Mass-Spectrometric Determination of Molecular Formulas and Structural Implications. *J. Am. Chem.*

Soc. **2008**, *130*, 8608–8610.

(40) Jadzinsky, P. D.; Calero, G.; Ackerson, C. J.; Bushnell, D. A.; Kornberg, R. D. Structure of a Thiol Monolayer-Protected Gold Nanoparticle at 1.1 Å Resolution. *Science* **2007**, *318*, 430–433.

(41) Zhu, M.; Aikens, C. M.; Hollander, F. J.; Schatz, G. C.; Jin, R. Correlating the Crystal Structure of a Thiol-Protected Au_{25} Cluster and Optical Properties. *J. Am. Chem. Soc.* **2008**, *130*, 5883–5885.

(42) Akola, J.; Walter, M.; Whetten, R. L.; Häkkinen, H.; Grönbeck, H. On the Structure of Thiolate-Protected Au_{25}. *J. Am. Chem. Soc.* **2008**, *130*, 3756–3757.

(43) Heaven, M. W.; Dass, A.; White, P. S.; Holt, K. M.; Murray, R. W. Crystal Structure of the Gold Nanoparticle $[N(C_8H_{17})_4][Au_{25}(SCH_2CH_2Ph)_{18}]$. *J. Am. Chem. Soc.* **2008**, *130*, 3754–3755.

(44) Zeng, C.; Liu, C.; Chen, Y.; Rosi, N. L.; Jin, R. Gold-Thiolate Ring as a Protecting Motif in the $Au_{20}(SR)_{16}$ Nanocluster and Implications. *J. Am. Chem. Soc.* **2014**, *136*, 11922–11925.

(45) Das, A.; Li, T.; Li, G.; Nobusada, K.; Zeng, C.; Rosi, N. L.; Jin, R. Crystal Structure and Electronic Properties of a Thiolate-Protected Au_{24} Nanocluster. *Nanoscale* **2014**, *6*, 6458–6462.

(46) Schaaff, T. G.; Knight, G.; Shafigullin, M. N.; Borkman, R. F.; Whetten, R. L. Isolation and Selected Properties of a 10.4 kDa Gold:Glutathione Cluster Compound. *J. Phys. Chem. B* **1998**, *102*, 10643–10646.

(47) Tracy, J.; Crowe, M.; Parker, J. F.; Hampe, O.; Fields-Zinna, C.; Dass, A.; Murray, R. W. Electrospray Ionization Mass Spectrometry of Uniform and Mixed Monolayer Nanoparticles: $Au_{25}[S(CH_2)_2Ph]_{18}$ and $Au_{25}[S(CH_2)_2Ph]_{18-x}(SR)_x$. *J. Am. Chem. Soc.* **2007**, *129*, 16209–16215.

(48) Negishi, Y.; Nakazaki, T.; Malola, S.; Takano, S.; Niihori, Y.; Kurashige, W.; Yamazoe, S.; Tsukuda, T.; Häkkinen, H. A Critical Size for Emergence of Nonbulk Electronic and Geometric Structures in Dodecanethiolate-Protected Au Clusters. *J. Am. Chem. Soc.* **2015**, *137*, 1206–1212.

(49) Chevrier, D.; MacDonald, M.; Chatt, A.; Zhang, P.; Wu, Z.; Jin, R. Sensitivity of Structural and Electronic Properties of Gold–Thiolate Nanoclusters to the Atomic Composition: A Comparative X-Ray Study of $Au_{19}(SR)_{13}$ and $Au_{25}(SR)_{18}$. *J. Phys. Chem. C* **2012**, *116*, 25137–25142.

(50) Kurashige, W.; Niihori, Y.; Sharma, S.; Negishi, Y. Recent Progress in the Functionalization Methods of Thiolate-Protected Gold Clusters. *J. Phys. Chem.*

Lett. **2014**, *5*, 4134–4142.

(51) Ashenfelter, B. A.; Desireddy, A.; Yau, S. H.; Goodson, T.; Bigioni, T. P. Fluorescence from Molecular Silver Nanoparticles. *J. Phys. Chem. C* **2015**, *119*, 20728–20734.

(52) Wang, S.; Zhu, X.; Cao, T.; Zhu, M. A Simple Model for Understanding the Fluorescence Behavior of Au_{25} Nanoclusters. *Nanoscale* **2014**, *6*, 5777–5781.

(53) Green, T. D.; Yi, C.; Zeng, C.; Jin, R.; McGill, S.; Knappenberger Jr, K. L. Temperature-Dependent Photoluminescence of Structurally-Precise Quantum-Confined $Au_{25}(SC_8H_9)_{18}$ and $Au_{38}(SC_{12}H_{25})_{24}$ Metal Nanoparticles. *J. Phys. Chem. A* **2014**, *118*, 10611–10621.

(54) Shibu, E. S.; Muhammed, M. A. H.; Tsukuda, T.; Pradeep, T. Ligand Exchange of $Au_{25}(SG)_{18}$ Leading to Functionalized Gold Clusters: Spectroscopy, Kinetics, and Luminescence. *J. Phys. Chem. C* **2008**, *112*, 12168–12176.

(55) Mai, H. H.; Kaydashev, V. E.; Tikhomirov, V. K.; Janssens, E.; Shestakov, M. V.; Meledina, M.; Turner, S.; Van Tendeloo, G.; Moshchalkov, V. V.; Lievens, P. Nonlinear Optical Properties of Ag Nanoclusters and Nanoparticles Dispersed in a Glass Host. *J. Phys. Chem. C* **2014**, *118*, 15995–16002.

(56) Miyamura, H.; Yasukawa, T.; Kobayashi, S. Preparation of Polymer Incarcerated Gold Nanocluster Catalysts (PI-Au) and Their Application to Aerobic Oxidation Reactions of Boronic Acids, Alcohols, and Silyl Enol Ethers. *Tetrahedron* **2014**, *70*, 6039–6049.

(57) Ramakrishna, G.; Dai, Q.; Zou, J.; Huo, Q.; Goodson, T. Interparticle Electromagnetic Coupling in Assembled Gold-Necklace Nanoparticles. *J. Am. Chem. Soc.* **2007**, *129*, 1848–1849.

(58) Jin, R.; Qian, H.; Wu, Z.; Zhu, Y.; Zhu, M.; Mohanty, A.; Garg, N. Size Focusing: A Methodology for Synthesizing Atomically Precise Gold Nanoclusters. *J. Phys. Chem. Lett.* **2010**, *1*, 2903–2910.

(59) Lance Kelly, K.; Coronado, E.; Zhao, L. L.; Schatz, George, C. The Optical Properties of Metal Nanoparticles: The Influence of Size, Shape, and Dielectric Environment. *J. Phys. Chem. B* **2003**, *107*, 668–677.

(60) Devadas, M. S.; Kim, J.; Sinn, E.; Lee, D.; Goodson, T.; Ramakrishna, G. Unique Ultrafast Visible Luminescence in Monolayer-Protected Au_{25} Clusters. *J. Phys. Chem. C* **2010**, *114*, 22417–22423.

(61) Liu, C.-L.; Ho, M.-L.; Chen, Y.-C.; Hsieh, C.-C.; Lin, Y.-C.; Wang, Y.-H.; Yang, M.-J.; Duan, H.-S.; Chen, B.-S.; Lee, J.-F.; Hsiao, J.-K.; Chou, P.-T. Thiol-

Functionalized Gold Nanodots: Two-Photon Absorption Property and Imaging *In Vitro*. *J. Phys. Chem. C* **2009**, *113*, 21082–21089.

(62) Mansour, K.; Soileau, M. J.; Stryland, E. W. Van. Nonlinear Optical Properties of Carbon-Black Suspensions (ink). *J. Opt. Soc. Am. B* **1992**, *9*, 1100-1109.

(63) Sheik-Bahae, M.; Said, A. A.; Wei, T.-H.; Hagan, D. J.; Van Stryland, E. W. Sensitive Measurement of Optical Nonlinearities Using a Single Beam. *IEEE J. Quantum Electron.* **1990**, *26*, 760–769.

(64) Devadas, M. S.; Bairu, S.; Qian, H.; Sinn, E.; Jin, R.; Ramakrishna, G. Temperature-Dependent Optical Absorption Properties of Monolayer-Protected Au_{25} and Au_{38} Clusters. *J. Phys. Chem. Lett.* **2011**, *2*, 2752–2758.

(65) Acuna, G. P.; Bucher, M.; Stein, I. H.; Steinhauer, C.; Kuzyk, A.; Holzmeister, P.; Schreiber, R.; Moroz, A.; Stefani, F. D.; Liedl, T.; Simmel, F. C.; Tinnefeld, P. Distance Dependence of Single-Fluorophore Quenching by Gold Nanoparticles Studied on DNA Origami. *ACS Nano* **2012**, *6*, 3189–3195.

(66) Stein, I. H.; Steinhauer, C.; Tinnefeld, P. Single-Molecule Four-Color FRET Visualizes Energy-Transfer Paths on DNA Origami. *J. Am. Chem. Soc.* **2011**, *133*, 4193–4195.

(67) Clapp, A. R.; Medintz, I. L.; Mauro, J. M.; Fisher, B. R.; Bawendi, M. G.; Mattoussi, H. Fluorescence Resonance Energy Transfer Between Quantum Dot Donors and Dye-Labeled Protein Acceptors. *J. Am. Chem. Soc.* **2004**, *126*, 301–310.

(68) Yun, C. S.; Javier, A.; Jennings, T.; Fisher, M.; Hira, S.; Peterson, S.; Hopkins, B.; Reich, N. O.; Strouse, G. F. Nanometal Surface Energy Transfer in Optical Rulers, Breaking the FRET Barrier. *J. Am. Chem. Soc.* **2005**, *127*, 3115–3119.

(69) Jennings, T. L.; Singh, M. P.; Strouse, G. F. Fluorescent Lifetime Quenching near D = 1.5 nm Gold Nanoparticles: Probing NSET Validity. *J. Am. Chem. Soc.* **2006**, *128*, 5462–5467.

(70) Persson, B. N. J.; Lang, N. D. Electron-Hole-Pair Quenching of Excited States Near a Metal. *Phys. Rev. B* **1982**, *26*, 5409–5415.

(71) Akola, J.; Kacprzak, K. A.; Lopez-Acevedo, O.; Walter, M.; Grönbeck, H.; Häkkinen, H. Thiolate-Protected Au_{25} Superatoms as Building Blocks: Dimers and Crystals. *J. Phys. Chem. C* **2010**, *114*, 15986–15994.

(72) Qian, H.; Eckenhoff, W. T.; Zhu, Y.; Pintauer, T.; Jin, R. Total Structure Determination of Thiolate-Protected Au_{38} Nanoparticles. *J. Am. Chem. Soc.* **2010**, *132*, 8280–8281.

(73) Wijngaarden, J. T. van; Toikkanen, O.; Liljeroth, P.; Quinn, B. M.; Meijerink, A. Temperature-Dependent Emission of Monolayer-Protected Au_{38} Clusters. *J. Phys. Chem. C* **2010**, *114*, 16025–16028.

(74) Park, S.; Lee, D. Synthesis and Electrochemical and Spectroscopic Characterization of Biicosahedral Au_{25} Clusters. *Langmuir* **2012**, *28*, 7049–7054.

(75) Pawlicki, M.; Collins, H. A.; Denning, R. G.; Anderson, H. L. Two-Photon Absorption and the Design of Two-Photon Dyes. *Angew. Chem. Int. Ed. Engl.* **2009**, *48*, 3244–3266.

(76) Russier-Antoine, I.; Bertorelle, F.; Vojkovic, M.; Rayane, D.; Salmon, E.; Jonin, C.; Dugourd, P.; Antoine, R.; Brevet, P.-F. Non-Linear Optical Properties of Gold Quantum Clusters: The Smaller the Better. *Nanoscale* **2014**, *6*, 13572–13578.

(77) Wang, Y.; Xie, X.; Goodson, T. Enhanced Third-Order Nonlinear Optical Properties in Dendrimer-Metal Nanocomposites. *Nano Lett.* **2005**, *5*, 2379–2384.

(78) III, T. G.; Varnavski, O.; Wang, Y. Optical Properties and Applications of Dendrimer–Metal Nanocomposites. *Int. Rev. Phys. Chem.* **2007**, *23*, 109-150.

(79) Sivapalan, S. T.; Vella, J. H.; Yang, T. K.; Dalton, M. J.; Haley, J. E.; Cooper, T. M.; Urbas, A. M.; Tan, L.-S.; Murphy, C. J. Off-Resonant Two-Photon Absorption Cross-Section Enhancement of an Organic Chromophore on Gold Nanorods. *J. Phys. Chem. Lett.* **2013**, *4*, 749–752.

(80) Baida, H.; Mongin, D.; Christofilos, D.; Bachelier, G.; Crut, A.; Maioli, P.; Del Fatti, N.; Vallée, F. Ultrafast Nonlinear Optical Response of a Single Gold Nanorod Near Its Surface Plasmon Resonance. *Phys. Rev. Lett.* **2011**, *107*, 057402.

Chapter 4

Synthesis and Enhanced Linear and Nonlinear Optical Properties of Chromophore-Au Metal Cluster Oligomers

4.1 Original Publication Information

This chapter was published as the following document:

Ho-Wu, R.; Sun, K.; Goodson III, T. "Synthesis and Enhanced Linear and Nonlinear Optical Properties of Chromophore-Au Metal Cluster Oligomers" *J. Phys. Chem. C*, **2017**, submitted.

4.2 Abstract

Using nanoclusters as building blocks for supracrystals has sparked research interest due to the unique optical and electronic properties that nanoclusters can incorporate in large crystals. The advantage of building nanocluster crystals through molecular linkers is that the linker can be used as a functional group for the nanoclusters (e.g. dye-nanocluster systems). In this study, we employed the ligand exchange reaction to synthesize chromophore-Au_{25} nanocluster oligomers and investigated their linear and nonlinear optical properties. The chromophore-Au_{25} nanocluster oligomers product mixture was separated into four bands by polyacrylamide gel electrophoresis and characterized by matrix assisted laser desorption ionization mass spectrometry and scanning transmission

electron microscopy imaging. The linear optical properties of the systems were investigated by steady state UV-vis absorption and fluorescence spectroscopy. The chromophore-Au_{25} nanocluster oligomers showed increased oscillator strength and transition dipole moment compared to single Au_{25} nanoclusters. Energy transfer from the chromophore 4,4'-thiodibenzenethiol (TBT) to the metal cluster was observed in the chromophore-Au_{25} nanocluster dimer system. The excited state and fluorescence dynamics were investigated by transient absorption spectroscopy, time-resolved fluorescence up-conversion and time-correlated single photon counting. The chromophore-Au_{25} nanocluster oligomers have a long-lived surface state, due to the contribution of energy transfer by two nanocluster cores. The two-photon absorption cross sections of the chromophore-Au_{25} nanocluster oligomers showed an increasing enhancement trend with increasing oligomer length. An enhancement factor of up to 68 times was found compared to single Au_{25} nanoclusters. Finally, we performed a structure-property correlation analysis to explain the observed optical properties of these systems.

4.3 Introduction

The synthesis and optical characterization of metal particles has led to applications of their use in many optical and electronic devices.[1–3] In the case of metal nanoparticles (> 2 nm), applications have exploited their surface plasmon resonance for imaging, sensing, and electronic and magnetic devices.[4–10] For example, metal nanoparticles have been coupled to organic chromophores, which results in the nonlinear optical enhancement of the chromophore-nanoparticle assembly.[11–14] Theoretical and experimental results of organic molecules with metal nanoparticles show strong distance dependence of the electronic coupling which makes the design and fabrication of a device's topology very

challenging.[5,155,15] It has been suggested that it would be more feasible if one could couple to specific transitions in the metal as opposed to the surface plasmon band.[16,17]

Monolayer-protected metal nanoclusters (MPCs) are smaller than 2 nm and exhibit discrete energy levels due to the quantum confinement effect.[18–26] The molecular characteristics of metal nanoclusters give rise to unique physical and optical properties, such as bright fluorescence and large two-photon absorption cross sections.[22,27–29] One particular area of interest of metal nanoclusters is their tunable electronic and optical properties by surface ligand modification, metal atom doping, and size control.[29–33] Surface ligand modification with a chromophore has been accomplished with nanoparticles and nanoclusters.[11,34–41] A group of chromophores, for example, on a plasmonic metal nanoparticle shows much faster energy transfer compared to a group of free, concentrated chromophores.[11,42] The ultrafast energy transfer between the chromophores on the nanoparticle's surface was found to be related to a specific geometrical configuration of the chromophores on the nanoparticle's surface as opposed to random rotational diffusion of free dyes.[11] Ding and coworkers have recently shown through theoretical calculations that the rate of energy transfer between a donor and an acceptor attached to a plasmonic gold nanoparticle can be reduced or enhanced based on the relative orientation of the donor-acceptor pair; but the enhancement factor, up to 10^6 times, greatly outweighs any quenching effects.[43] Certain fluorescent dyes attached to a gold nanocluster show significant fluorescence quenching of the dye due to static quenching from the nanocluster, which forms a non-fluorescent ground state complex.[44] For example, a pyrene attached to a Au_{25} nanocluster shows electron transfer from the nanocluster to the dye, which forms a low fluorescence quantum yield pyrene anion.[40]

Therefore, there is high motivation in designing network of functionalized metal nanocluster systems that exhibit enhanced energy transfer properties for a wide range of applications.

Beyond dye-nanocluster or dye-nanoparticle systems, there has been an interest in nanocluster-nanocluster systems in which well-defined metal nanoclusters can be used as molecular building block units to form "metal nanocluster oligomer" materials.[45–48] A network of metal nanoclusters may present a huge advantage compared to conventional crystals based on atoms of the same metal. For example, a nanocrystal composed of nanoclusters would incorporate the optical properties contributed by the nanoclusters, such as fluorescence, whereas a nanoparticle of the same size composed of metal atoms does not exhibit fluorescence. The coupling of the metal nanoclusters could also lead to enhanced nonlinear optical effects.[27] So far, only theoretical studies on the optical properties of "metal nanocluster oligomers" have been reported.[45,48–50] For example, in a theoretical study of the Au_{25}-benzenedithiolate-Au_{25} dimer system, it was shown that the basic electronic structure of the Au_{25} nanocluster is not disturbed compared to single Au_{25} nanoclusters.[45] There are also reports that show that metal nanocluster oligomers can be synthesized.[51,52] Baksi and coworkers have demonstrated experimentally the formation of $[Au_{25}]_2$ dimers and $[Au_{25}]_3$ trimers in the gas phase inside an ion mobility mass spectrometer. The dimers and the trimers are found to be covalently linked together by the aurophilic bonding between the Au_2S_3 staples of adjacent nanoclusters.[51] Aurophilic interactions between Au-SR staples are also observed in the polymeric $Au_{25}(SCH_2CH_2CH_3)_{18}$ nanocluster "wire", where the Au_{25} nanoclusters are linked together by inter-cluster Au-Au bonds.[52]

In this report, we show the first systematic study of the optical properties of chromophore-Au_{25} nanocluster oligomers. We demonstrate that the chromophore-Au_{25} nanocluster oligomers can be synthesized by ligand exchange with a dithiol linker, and the resulting mixture of oligomers can be separated by gel electrophoresis. This type of metal nanocluster oligomer consists of linkers between the nanoclusters instead of direct nanocluster linking through their surface gold atoms. The linear and nonlinear optical absorption of the chromophore-Au_{25} nanocluster oligomers were studied by steady state absorption and fluorescence spectroscopy and two-photon absorption spectroscopy. The excited state dynamics of the nanocluster oligomers were analyzed by transient absorption spectroscopy, time-resolved fluorescence up-conversion and time-correlated single photon counting. The basic questions posed here are, how chromophore-Au_{25} nanocluster oligomers differ from the single Au_{25} nanocluster in their optical properties, and how energy transfer occurs between the chromophore and the Au_{25}, and between the linked Au_{25} nanoclusters.

4.4 Experimental

Chemicals. All reagents are commercially available and were used without further purification. $HAuCl_4 \cdot 3H_2O$, glutathione (GSH), 4,4'-thiodibenzenethiol (TBT) are from Sigma Aldrich. Sodium borohydride ($NaBH_4$) is from Merck Millipore. Polyacrylamide/bis-acrylamide solution and tetramethylethylenediamine (TEMED) are from Bio-Rad Laboratories. Ammonium persulfate (APS) and TBE buffer are from IBI Scientific. Nanopure H_2O was used throughout the experiments.

Synthesis of $Au_{25}(GSH)_{18}$ nanoclusters. Water soluble $Au_{25}(GSH)_{18}$ nanoclusters were synthesized following the one-pot synthesis method.[53] A solution of $HAuCl_4 \cdot 3H_2O$

(170 mg, 0.5 mmol) was prepared in methanol (100 mL) and chilled in an ice bath for 15 min. The capping ligand, glutathione ($C_{10}H_{17}N_3O_6S$; GSH) (614 mg, 2 mmol), was added to the solution and stirred for 30 min. The solution turned from the initial yellow color to a white/clear solution, indicating the formation of Au(I)-GSH polymer.[54,55] Freshly prepared $NaBH_4$ (189 mg, 5 mmol) solution (25 mL H_2O) was added dropwise and the mixture was stirred for 1 h. The solution turned into a dark brown color, indicative of nanoclusters formation.[56] The crude product was washed with methanol to remove excess reagents, then re-dissolved in H_2O and incubated with excess GSH at 55°C for 3 h. The precipitate of the reaction was discarded. The supernatant containing $Au_{25}(GSH)_{18}$ was collected and washed with methanol.[57] The purity of the sample was assessed by UV-vis absorption spectroscopy which shows the distinct absorption bands of $Au_{25}(GSH)_{18}$ at 450, 500, and 670 nm, and by electrophoresis which showed a single band.

Synthesis of chromophore-Au_{25} nanocluster oligomers. Nanocluster oligomers were prepared by ligand exchange reaction with a dithiol ligand. A representative procedure is as follows. An aqueous solution of $Au_{25}(GSH)_{18}$ was prepared at a concentration of 8.1 x 10^{-5} M (0.2 μmol). 4,4'-thiodibenzenethiol (TBT) (1.6 mg) was dissolved in basic water (2 mL) to yield a clear solution. For a 1:2 cluster-to-TBT ratio, 100 μL of the TBT solution was added to the $Au_{25}(GSH)_{18}$ solution and stirred at room temperature overnight.

Polyacrylamide gel electrophoresis (PAGE). The nanoclusters oligomers were purified by PAGE. The resolving gel was prepared with 30% polyacrylamide (29:1 acrylamide/bis-acrylamide) and the stacking gel was prepared with 10% polyacrylamide.

The formulation of the gels is modified from the traditional gels that are used for biological samples.[58] The main modification is the elimination of the denaturing agent, sodium dodecyl sulphate. Different concentrations of the initiators (APS and TEMED) and gel were experimented to optimize separation. PAGE was run in a TBE 1x buffer (in MeOH:water solvent mixture) at constant 270 V for 2 h. A coolant pack was placed inside the electrophoresis tank to prevent the gel from heating up. The electrophoresis was performed in a Mini-PROTEAN Tetra Cell from Bio-Rad Laboratories. The individual bands were retrieved, crushed, and soaked in water to extract the nanocluster oligomers. For the 4th band, we extracted the nanocluster oligomers that were found near the running and stacking gel interface as shown in Figure 1. The extracted nanocluster oligomer solutions were filtered to remove traces of gel.

Steady state absorption and emission. UV-vis absorption spectra were recorded with Agilent 8453 spectrophotometer over 200 – 1200 nm. Fluorescence emission spectra were recorded with Fluoromax-2 spectrophotometer. The samples were loaded in quartz cuvettes and the excitation path length was 1 cm. The emission quantum yields of the chromophore-nanocluster oligomers were calculated using tetraphenylporphyrin zinc as the standard, excited at 400 nm.

Matrix-assisted laser desorption ionization (MALDI) mass spectrometry characterization. Mass spectrometry was performed by matrix-assisted laser desorption ionization with a Bruker Autoflex MALDI, using a 2,5-dihydroxybenzoic acid matrix (approximately 400:1 molar ratio of matrix to sample). Mass spectra were recorded in negative, linear mode. The MALDI was calibrated with different proteins between 5.7 – 66kDa. The laser beam size was “medium” and the intensity was adjusted to ~62% for

$Au_{25}(GSH)_{18}$, band 1, and band 2, and adjusted to ~85% for band 3. The detector voltage was adjusted to 2.924 kV. The spectra were the average of 2,000 scans and has a mass range/resolution of 2.50 GS/s. The data were collected with the FlexControl software and analysis was performed with FlexAnalysis software.

Femtosecond time-resolved fluorescence up-conversion. The fluorescence up-conversion system is described elsewhere.[20] The aqueous solution samples were placed in a 0.1 cm thick rotating cell and excited with a frequency-doubled light (~400 nm) from a mode-locked Ti:sapphire laser (Tsunami, Spectra Physics) which produces a 100 fs 800 nm beam. The emission of the sample is up-converted at a β-barium borate (BBO) crystal using 800 nm light which was passed through a delay line prior. The instrument response function (IRF) was measured using the raman scattering of water and is found to be 94 fs. The system was calibrated with standard laser dyes. The up-converted light is directed to a monochromator and detected with a photomultiplier tube (R1527P, Hamamatsu). The lifetimes of the fluorescence decay were calculated by fitting the experimental data with a multi-exponential decay function convoluted with the IRF.

Two-photon excited fluorescence. Two-photon excited fluorescence (TPEF) was performed as follows. The ~820 nm excitation was produced from a mode-locked Ti:sapphire laser (Kapteyn-Murnane Laboratories, Inc.) with ~30 fs pulses. A Nd:YVO_4 pump (Millenia-Pro, Spectra Physics) was used to generate a cw 532 nm laser that enters the cavity of the Ti:sapphire. The excitation beam power was varied with a neutral density filter and focused on the sample cell with an 11.5 cm focusing lens. A monochromator, placed perpendicular to the excitation beam, was used to collect the fluorescence and is coupled to a photomultiplier tube.

Femtosecond transient absorption. An amplified laser (Spectra Physics Spitfire) with pulse duration of ~100 fs, repetition rate of 1 kHz, and power of 800 mW was directed at a beam splitter to generate the pump (85%) and the probe beams (15%). The pump beam (~66 μJ per pulse) was generated from the second harmonic of the amplifier's output (~800 nm) using a BBO crystal and was focused onto the sample cell (l = 1 mm). The probe beam was passed through a computer-controlled delay line and focused onto a 2 mm sapphire plate to generate the white light continuum (Helios by Ultrafast Systems Inc.). The white light was focused onto the sample and overlapped with the pump beam. The absorption difference (ΔA) of the signal was collected by a CCD detector (Ocean Optics). Data acquisition was performed with the software Helios by Ultrafast Systems Inc. The IRF was measured by the raman scattering of water at 466 nm and is found to be 110 fs. Data analysis was performed with Surface Xplorer Pro software.

Scanning transmission electron microscopy (STEM) imaging. $Au_{25}(GSH)_{18}$ nanocluster and band 2 solutions were prepared at pH 7.2. The solutions were sonicated for 40 min and filtered through 220 nm pore PTFE filters. The solutions were diluted to 120 nM concentration. The solutions were drop-cast on 200-mesh holey carbon copper grids and air dried. The holey carbon copper grids were purchased from SPI Supplies. Both STEM bright-field (BF) and high angle annular dark-field (HAADF) images were collected with a JEM-2100F electron microscope with CEOS probe corrector. The size and inter-cluster distribution were analyzed with Digital Micrograph software by Gatan Inc.

4.5 Results and discussion

Synthesis and separation of chromophore-Au_{25} nanocluster oligomers. Chromophore-Au_{25} nanocluster oligomers were synthesized by the ligand exchange reaction with 4,4'-thiodibenzenethiol (TBT) (Scheme 4.1). Previous reports on dithiol ligand exchange with Au_{25} nanoclusters showed that inter-staple cross-linking of $Au_{25}(SCH_2CH_2Ph)_{18}$ nanoclusters was achieved using binaphthyl-dithiol and short alkanes dithiols.[59,60] The inter-staple cross-linking, however, happened within the same nanoclusters, where the dithiols cross-link two of the -Au-S-Au- staples on the nanocluster's surface. Inter-staple cross-linking was possible due to the close positioning of the two thiol functional groups in the molecule. For instance, the binaphthyl-dithiol has two thiols positioned on the same side of the binaphthyl molecule. To achieve inter-staple cross-linking between two nanoclusters, a dithiol was chosen that contains –SH groups at opposite "ends" of the molecule, such as 4,4'-thiodibenzenethiol.

Scheme 4.1. Ligand exchange reaction of $Au_{25}(GSH)_{18}$ nanocluster[18] with TBT to form chromophore-Au_{25} nanocluster oligomers.

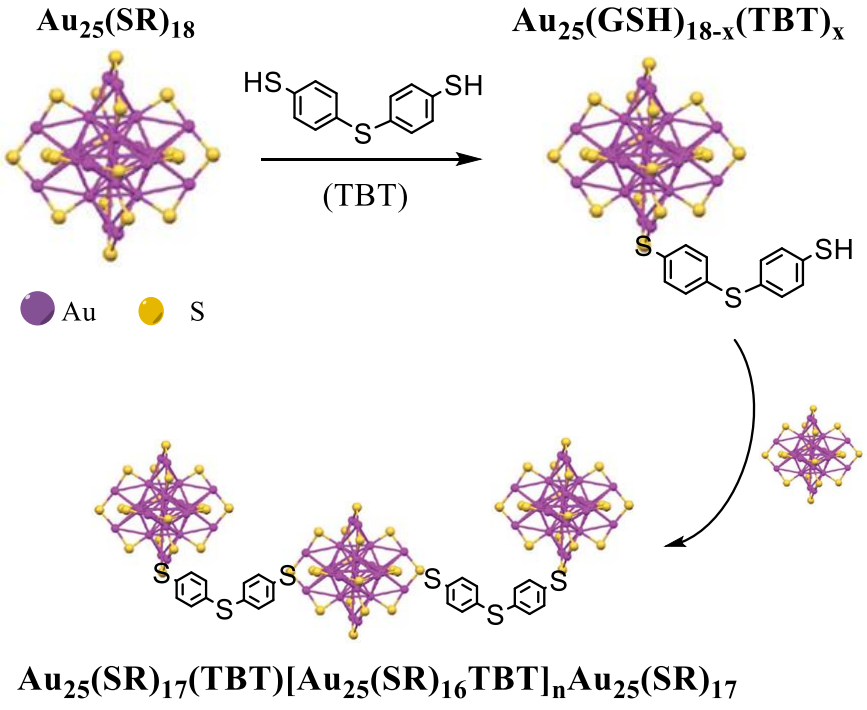

The separation of the as-synthesized chromophore-Au_{25} nanocluster oligomer product was performed by polyacrylamide gel electrophoresis (PAGE). Different experimental conditions were investigated to achieve a good separation. For the best separation, a 30% resolving and 10% stacking gel were used (Figure 4.1). The nanocluster oligomers separated into 4 bands. The species with the smallest mass and charge migrates faster towards the bottom of the gel. It is evident that band 2 is the major chromophore-Au_{25} nanocluster oligomer product. In general, the probability of obtaining dimers is higher than longer oligomers: a nanocluster functionalized with TBT, must come together with another $Au_{25}(GSH)_{18}$ nanocluster to form $Au_{25}(GSH)_{17}$-TBT-$Au_{25}(GSH)_{17}$. On the other hand, the probability to obtain a trimer is lower because a nanocluster dimer and a single nanocluster must come together for the ligand exchange reaction to take place. The probability of this encounter is low compared to the encounter of two single nanoclusters to form a dimer due to the higher number of single nanoclusters at the early stage of ligand exchange and the slower mobility of a dimer compared to a single cluster. Ligand exchange reaction has been proven to be a versatile strategy for deliberately functionalizing metal nanoclusters with the desired ligands.[59–61] Based on the clear separation of the reaction products in the gel electrophoresis (Figure 4.1), we are confident that the exchange reaction between Au_{25} nanoclusters and the dithiol chromophore TBT yielded chromophore-Au_{25} nanocluster oligomers. The chromophore-Au_{25} nanocluster oligomers were further characterized by MALDI mass spectrometry and scanning transmission electron microscopy.

MALDI-MS characterization of chromophore-Au_{25} nanocluster oligomers. The results from the gel electrophoresis separation show that the ligand exchange reaction of

$Au_{25}(GSH)_{18}$ with the dithiol TBT chromophore yielded products that have higher molecular masses than the $Au_{25}(GSH)_{18}$ nanocluster itself.

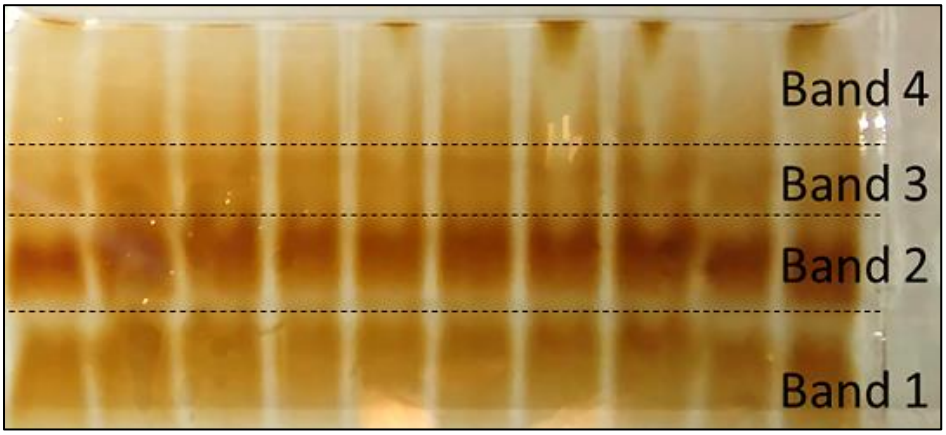

Figure 4.1. PAGE separation of chromophore-Au25 nanocluster oligomers.

Since the chromophore-Au_{25} nanocluster oligomers contain a combination of polar (glutathione) and non-polar (TBT) ligands, the fragmentation pattern for each type of ligand must be taken into consideration in the analysis of the chromophore-Au_{25} nanocluster oligomers mass spectra. It has been shown that the MALDI mass spectrum of the Au_{25} nanocluster with the non-polar ligand, 2-phenylethanethiol (PET), displays a single peak centered at 7,394 m/z which corresponds to the molecular mass of the $[Au_{25}(PET)_{18}]^-$ nanocluster species.[53] This intact mass was obtained with minimal laser intensity. On the other hand, the LDI mass spectra of the $Au_{25}(GSH)_{18}$ and $Au_{25}(PET)_{18}$ nanoclusters showed the same cluster fragmentations between 3,000 m/z and 6,000 m/z.[62] Shown in the first panel of Figure 4.2 is the MALDI mass spectrum of the $Au_{25}(GSH)_{18}$ nanocluster. According to Wu and coworkers, the fragmentation of a $Au_{25}(SR)_{18}$ nanocluster occurs in the following manner: $[Au_{25}(SR)_{18}]^- \rightarrow [Au_{25}S_{12}]^- + 6S + 18R$.[62] Relatively high laser intensity must be used (~62%) to obtain the MALDI mass spectrum of the $Au_{25}(GSH)_{18}$. Though the MALDI mass spectrum of $Au_{25}(PET)_{18}$ nanocluster

could be obtained with low laser intensity (~20%), at 62% laser intensity, the mass spectrum also showed the same fragmentation. Therefore, the Au_{25} nanocluster shows the same fragmentation pattern regardless of the type of ligand at high laser intensity. A comparison between band 1 and $Au_{25}(GSH)_{18}$ shows that the identity of band 1 is the single $[Au_{25}(GSH)_{18}]^-$ nanocluster. The fragmented ion species are $Au_xS_y^-$ clusters, showing complete loss of ligands, therefore the isotope mass distribution depends on the sulfur atom since gold is a mono-isotopic atom.[62] The difference of 2 mass units in the high resolution spectrum is due to the difference between the ^{32}S and ^{34}S isotopes. Therefore, band 1 are the unreacted Au_{25} nanoclusters that did not form chromophore-Au_{25} nanocluster oligomers.

The mass spectrum of band 2 shows similar fragmentation ion peaks in the 3,500 – 7,000 m/z range as the mass spectrum of single $Au_{25}(GSH)_{18}$ nanoclusters. Additionally, a peak centered at ~9,147 m/z is observed in the mass spectrum of band 2 (Figure 4.2). In consideration of the facts that a) ligand substitution can result in a distribution of substituted ligands, b) that the isotope mass distribution increases with oligomer size and c) that high laser intensity was used, it is expected that the mass spectra of the chromophore-Au_{25} nanocluster oligomers would have a relatively broad band due to the higher number of masses and fragmented ions. Since the m/z of this broad peak is roughly twice that of single nanoclusters, the initial suggestion is that band 2 is a dimer. The general formula of a chromophore-Au_{25} nanocluster dimer is $Au_{25}(SR)_{17}(TBT)Au_{25}(SR)_{17}$, where SR represents the distribution of –GSH and –TBT. We estimated the lowest and highest molecular mass limits for a chromophore-Au_{25} nanocluster dimer based on full TBT (248.403 g/mol) and full GSH (306.32 g/mol)

substitution, respectively. Additionally, for the lowest and the highest molecular mass of the dimer, we also calculated the isotopic mass distribution based on the two most abundant isotopes of S, C, H, N, and O (Figure 4.3). A relatively high laser intensity (~62%) was necessary to obtain the mass spectrum of band 2, which explains the presence of the fragmented ion peaks at ~6,000 m/z and below. The mass distribution of the dimer is 18,530 – 22,058 Da. Since each nanocluster bears a -1 charge, it is expected that the dimer would have an overall -2 charge. Therefore, the z = 2 and the dimer's peaks would appear between 9,265 – 11,029 m/z (Figure 4.3). The lowest and highest estimated m/z of a chromophore-Au_{25} nanocluster dimer match with the high m/z of the broad peak on the mass spectrum of band 2. The low m/z part of the broad peak is due to the fragmentation of the dimer to various extent. Therefore, we have synthesized chromophore-Au_{25} nanocluster dimers which are the major product from the synthesis.

The mass spectrum of band 3 did not show any ion peaks between 3,000 – 15,000 m/z, but it shows a broad peak at higher m/z, centered at 22,787 m/z (Figure 4.2 last panel). The mass in this range is, by estimation, suggested to be of a nanocluster trimer. The general formula of a chromophore-Au_{25} nanocluster trimer is $Au_{25}(SR)_{17}(TBT)[Au_{25}(SR)_{16}TBT]Au_{25}(SR)_{17}$, where SR represents the distribution of –GSH and –TBT. Using the same analysis in the mass spectrum of band 2, the lowest and highest molecular masses of a trimer (taking into consideration the two most abundant isotopes as well) were calculated. It was suggested initially that the trimer would bear a -3 charge due to the contribution of each nanocluster. Therefore, it was expected that the trimer would have peaks at 9,223 – 10,776 m/z, but these are not observed. The broad peak centered at 22,787 m/z corresponds to the mass distribution of the chromophore-

Au_{25} nanocluster trimers with a single charge. The mass distribution of the trimer matches with the high m/z of the broad peak (Figure 4.3). Due to the high laser intensity, the low m/z of the broad peak corresponds to the fragmentation of the trimer to various extent. However, it is not a complete fragmentation of the nanocluster oligomer where all ligands are lost. The mass spectrum of band 3 confirms that we also synthesized and separated chromophore-Au_{25} nanoclusters trimers.

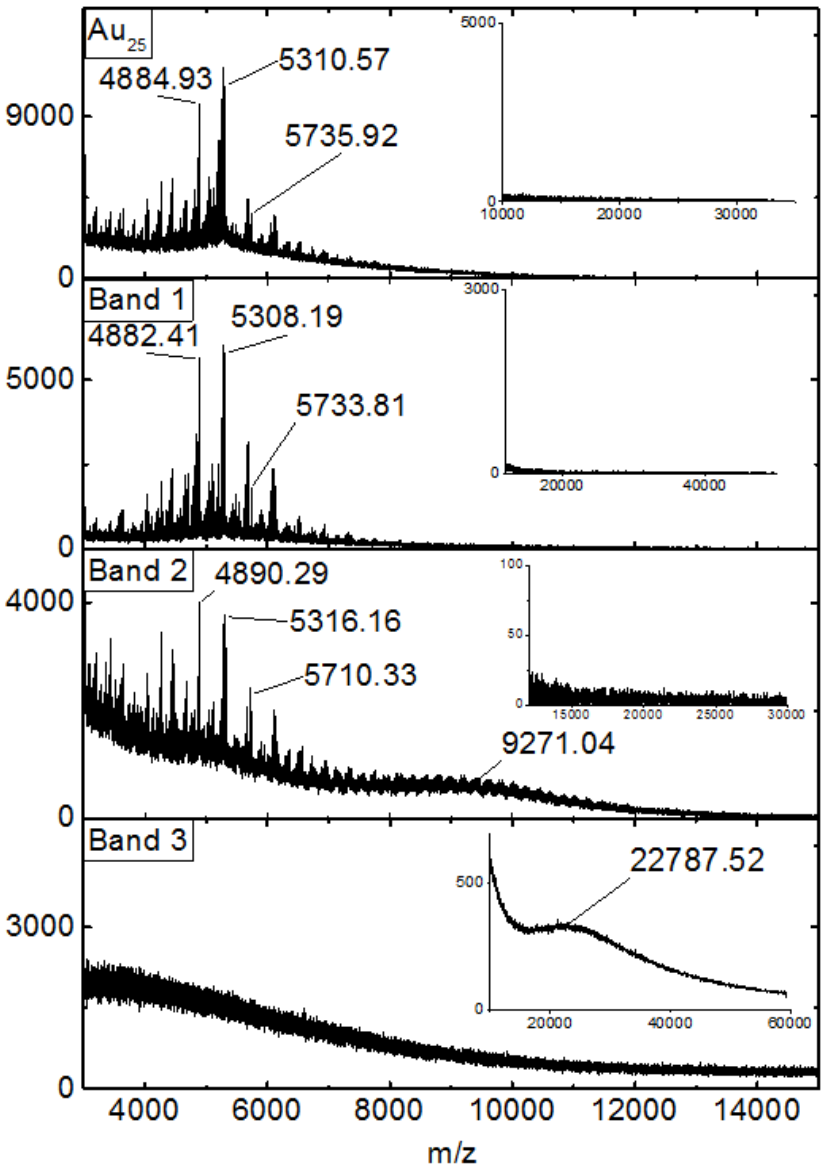

Figure 4.2. Negative ion mode MALDI spectra of the $Au_{25}(GSH)_{18}$ nanocluster and bands 1-3 from the PAGE separation. Insets show the medium mass range.

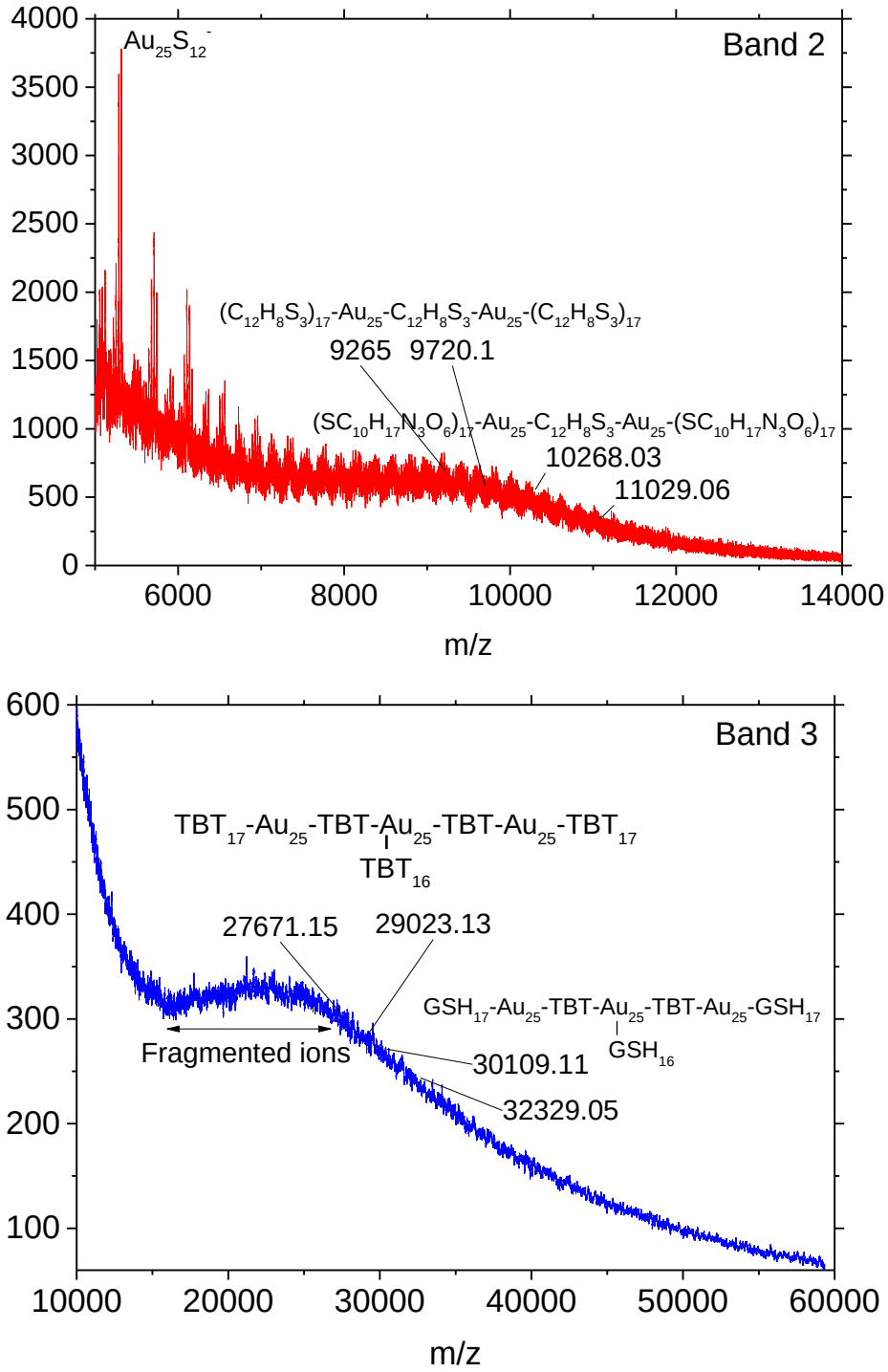

Figure 4.3. MALDI spectra of band 2 and band 3, suggesting a dimer and a trimer, respectively. A distribution of molecular masses was calculated for the dimer and trimer, which matches with the high m/z of the broad peaks. The low m/z of the broad peaks are due to fragmented ions as high laser intensity was used to obtain the spectra.

We have considered the possibility of observing fragmentations for band 2 and 3, similar to the that of the single nanocluster. However, since the fragmented species is a bare Au_{25} cluster, it would be impossible to trace it back to an oligomer if band 2 and 3 displayed such fragmentation. This was not the case in the spectrum of band 2 and 3. A peak appears at higher m/z than the single nanocluster's spectrum. We also considered, like in the case of the dimer, the possibility of no fragmentation and an overall 3- charge contributed by each cluster in the case of a trimer. If this was the case, the m/z of the trimer would show up in the same m/z as that of band 2 and would complicate the assignment of the oligomer sizes. But this was not the case because a higher charge state is even rarer in MALDI. We know that oxidation of the nanoclusters can occur with a thiolate, as in the case of thiol etching in the synthesis of Au_{25}. However, the extent of the thiol etching in the synthesis of Au_{25} is far: the result is the decomposition of unstable cluster sizes by oxidation to Au^{1+} ions. To achieve this, either high temperature or long period of time (days) is needed. The ligand exchange reaction was allowed to elapse overnight, therefore it may be possible to have achieved oxidation of the $Au_{25}(SR)_{18}^{1-}$ nanoclusters into the neutral charged cluster.

Band 4 is a heterogeneous mixture of large chromophore-Au_{25} nanocluster oligomers due to the low band resolution from the PAGE separation (Figure 4.1). Based on the coloration of the gel, the yield of these large oligomers is low compared to the other bands. A rough estimate of the size of these oligomers is made using the semi-log plot method which is commonly used for the estimation of proteins and nucleic acid's molecular masses in gel electrophoresis.[63] A linear plot is generated based on the log of the molecular masses of band 1, 2 and 3 as a function of the distance travelled by each

bands (Figure 4.4). We have taken our point of measurement the center of each band as indicated in Figure 4.4. Due to the low resolution of band 4, we estimated the lowest and highest possible masses by measuring the furthest point travelled (d) and the shortest point travelled (e) in the gel, respectively (Figure 4.4). The lowest estimated mass in this band is a trimer with full GSH substitution, $Au_{25}(GSH)_{17}(TBT)[Au_{25}(GSH)_{16}TBT]Au_{25}(GSH)_{17}$. It is no surprise that band 4 would contain the highest possible mass of a trimer given that this band is not well resolved from band 3. The highest estimated mass in band 4 is a chromophore-Au_{25} nanocluster hexamer (~6-mer).

From the mass spectrometry analysis of the chromophore-Au_{25} nanocluster oligomers, we demonstrate that we were able to synthesize chromophore-Au_{25} nanocluster dimers and trimers. The major product of the reaction is the chromophore-Au_{25} nanocluster dimer, $Au_{25}(SR)_{17}(TBT)Au_{25}(SR)_{17}$. We were able to also separate chromophore-Au_{25} nanocluster trimers, ~6-mers, and unreacted single Au_{25} nanoclusters from the reaction by polyacrylamide gel electrophoresis.

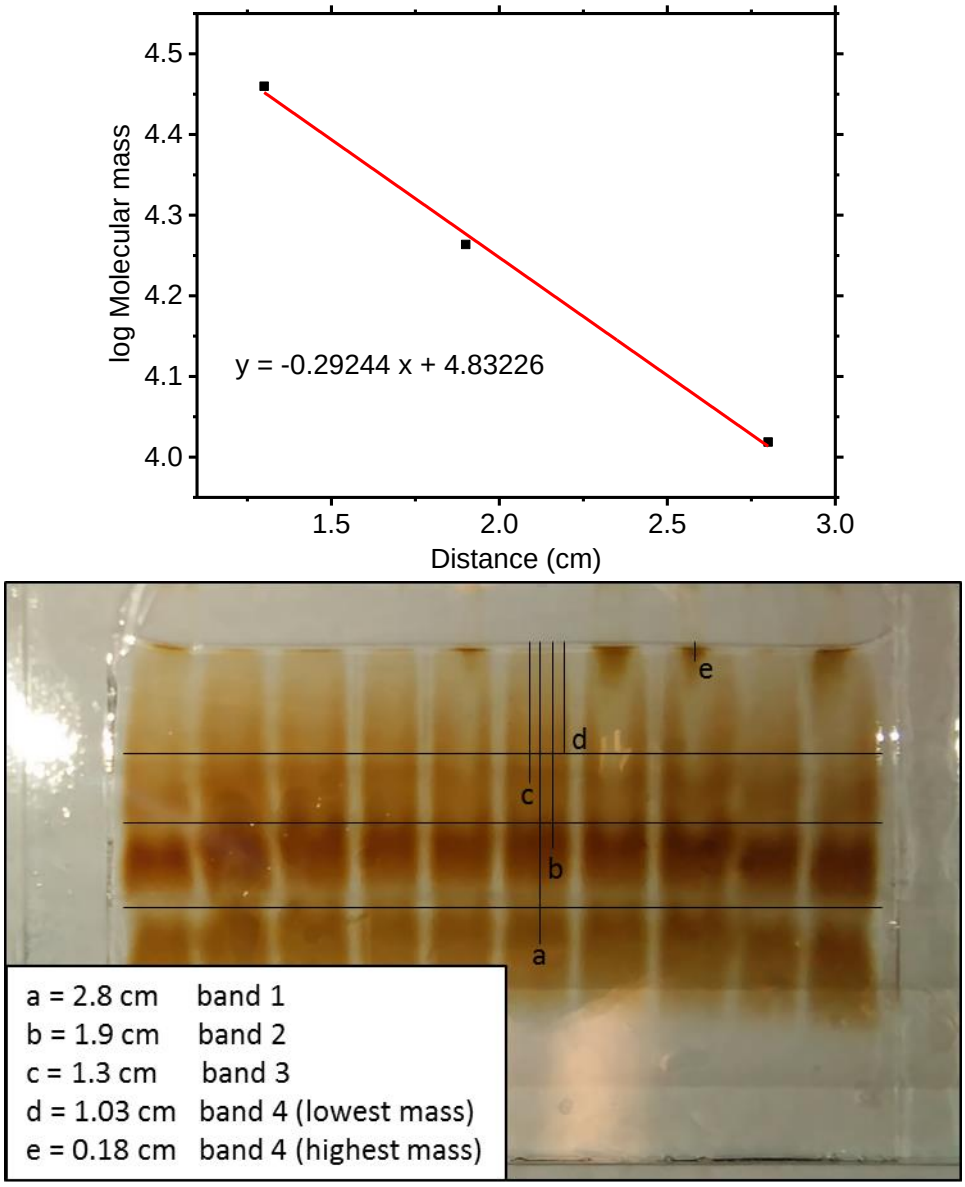

Figure 4.4. Semi-log plot for the estimation of the molecular masses of band 4. Due to the low band resolution in the PAGE separation, band 4 is a heterogeneous mixture of chromophore-Au_{25} nanocluster oligomers larger than band 1, 2 and 3. The distances travelled by each band were measured on the gel, and the molecular masses used for the semi-log plot were determined in MALDI mass spectrometry for band 1, 2 and 3.

Scanning transmission electron microscopy imaging of the chromophore-Au_{25} nanocluster dimer. To further characterize the chromophore-Au_{25} nanocluster dimers, scanning transmission electron microscopy (STEM) imaging was performed on the chromophore-Au_{25} nanocluster dimer and on the single $Au_{25}(GSH)_{18}$ nanocluster. To

carry out this process, the pH of the samples' solutions was adjusted to 7.2 to prevent nanocluster aggregation and to rule out dimers based on aggregation.[64] Additionally, the solutions were sonicated and filtered prior to drop-casting on holey carbon copper grids. Finally, the solutions concentrations were diluted to 120 nM to minimize aggregation.

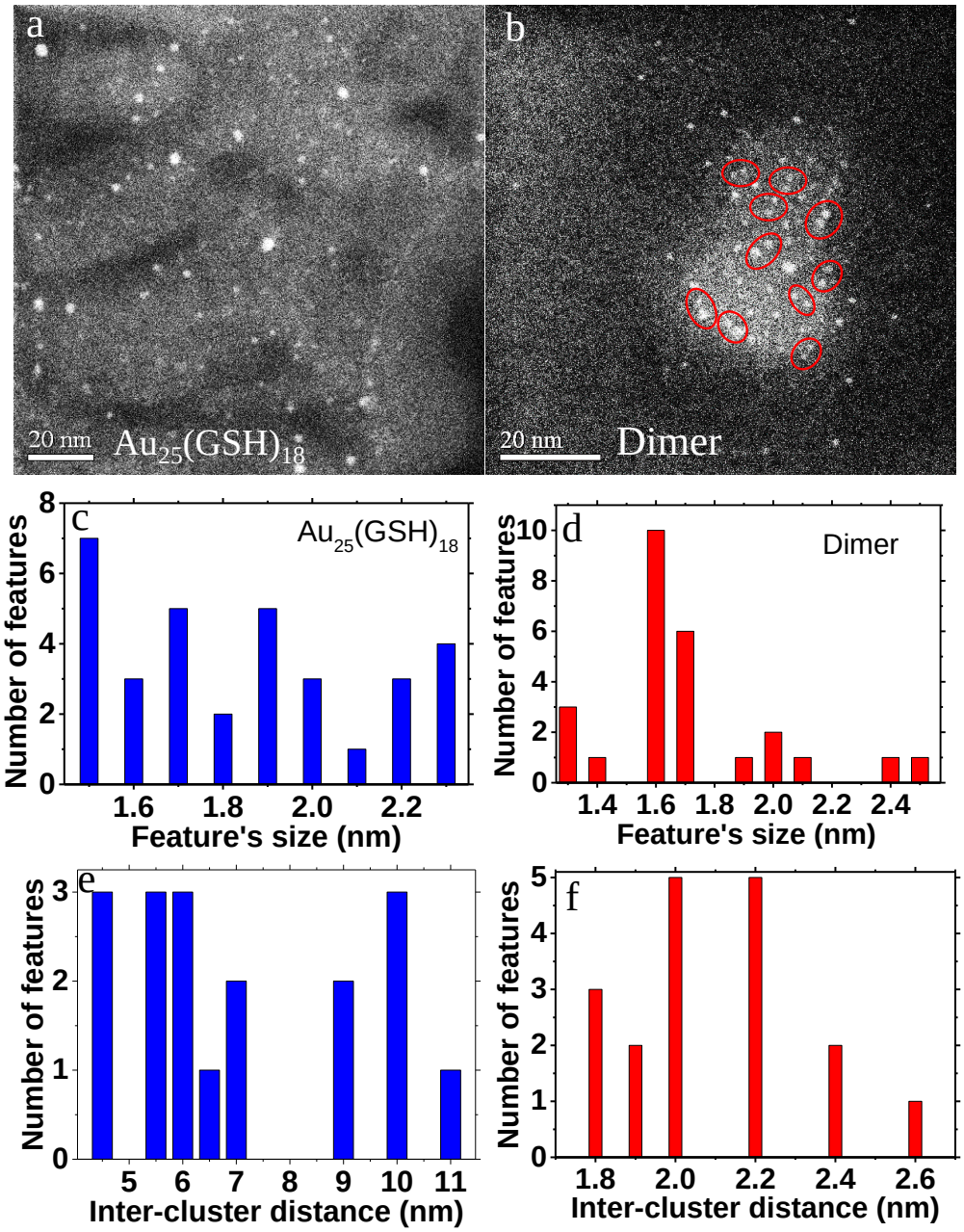

Figure 4.5. STEM dark field images of single Au_{25} nanoclusters and of chromophore-Au_{25} nanocluster dimers. Size distribution analysis shows features of approximately ~2

nm. Inter-cluster distance distribution was performed only on features that appear to be in close proximity.

Shown in Figure 4.5 is the dark field STEM images of single Au_{25} nanoclusters (a) and of chromophore-Au_{25} nanocluster dimers (b). The size distribution analysis of the individual bright features showed that they are approximately 2 nm in size in both the single cluster and the chromophore-Au_{25} nanocluster dimer images (Figure 4.5c, d). Au_{25} nanoclusters have been reported to be <2 nm in diameter, in accordance to our observation.[24,64] The dimensions of a Au_{25} nanocluster's triclinic unit cell are a = 16.2 Å, b = 17.4 Å, c = 18.7 Å, which take into account the nanocluster's surface ligands and the counter-ion.[23] These dimensions are in good agreement with the features' size distribution in both STEM images. The variation of the features' sizes is likely due to the varying resolution of the features in the images. For example, features that are less bright will account for the underestimation of the features' size, and features that are brighter will account for the overestimation of the features' size. We were able to confirm that these features are $Au_{25}(GSH)_{18}$ nanoclusters based on MALDI mass spectrometry analysis of $Au_{25}(GSH)_{18}$ which shows the characteristic fragmented ion peaks of this nanocluster, and based on the distinct absorption profile of Au_{25} nanoclusters. The STEM images further confirm that the Au_{25} nanoclusters did not undergo structural change to form large particles in the synthesis of the chromophore-Au_{25} nanocluster oligomers.

To properly identify the chromophore-Au_{25} nanocluster dimers in the STEM images, careful sample preparation was performed to disperse both the nanoclusters and the dimers. This is to ensure that the observed dimers are not due to aggregation of two nanoclusters when deposited on the holey carbon films. A distribution of the inter-cluster distances was analyzed for single Au_{25} nanoclusters to confirm that aggregation was

prevented. The inter-cluster distance distribution for the single Au_{25} STEM image was obtained only for the features that appear to be in close proximity to one another (Figure 4.3e). The shortest inter-cluster distance found in the single Au_{25} nanocluster STEM image was 4.5 nm. The core-to-core distance of the chromophore-Au_{25} nanocluster dimer was estimated to be ~1.88 nm (Figure 4.6). The shortest inter-cluster distance observed in the single Au_{25} image is almost twice as large as the estimated core-to-core distance of the Au_{25} nanoclusters in the dimer. If we take into account small distortions in bond angles and lengths, the change of the core-to-core distance would be very small. The maximum inter-cluster distance is ~2.5 nm, when the geometric conformation of the dimer is planar which is unlikely. Therefore, the result of the inter-cluster distance analysis for the single Au_{25} STEM image confirms that the samples are dispersed well enough to avoid aggregation, and that the observation of inter-cluster distance smaller than 2 nm would be an indication of the presence of chromophore-Au_{25} nanocluster dimers.

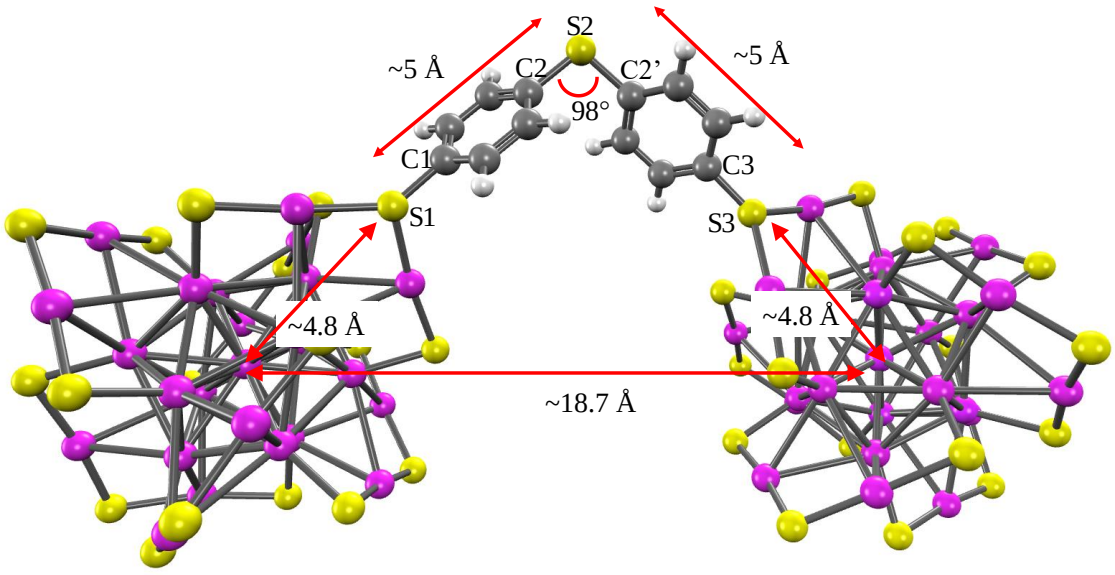

Figure 4.6. MM2 energy minimized structure at the Au-TBT-Au bridging site. The estimated distance between two Au_{25} nanoclusters (core-to-core) is 1.87 nm. Approximately half of the Au_{25} unit cell was taken into consideration. The atoms are

labeled as follows: magenta – Au; yellow – S; grey – C; white – H. The ligands around the nanocluster are omitted for clarity.

The STEM image of chromophore-Au_{25} nanocluster dimers is shown in Figure 4.5b. Highlighted in circles are some of the chromophore-Au_{25} nanocluster dimers that are observed across the deposited holy carbon film. The inter-cluster distance distribution was also obtained only for the features that appear to be in close proximity (Figure 4.5f). Inter-cluster distances between 1.8 and 2.6 nm are observed. Taking into consideration small bond angle and length distortions, the orientation of the dimer when deposited on the holey carbon film, and the features' pixel resolution, the variation of the inter-cluster distances seem acceptable. As mentioned earlier, the largest inter-cluster distance would be 2.5 nm. The average inter-cluster distance observed in the chromophore-Au_{25} nanocluster dimer image is about 2 times smaller than the smallest observed inter-cluster distance in the single Au_{25} nanocluster image, which is 4.5 nm. Therefore, the STEM images confirm that we have synthesized chromophore-Au_{25} nanocluster dimers because the inter-cluster distance is significantly smaller than that observed in single Au_{25} nanoclusters, and is in good agreement with the calculated inter-cluster distance based on the molecular geometry of the dimer (Figure 4.6).

Steady state absorption of chromophore-nanocluster oligomers. The absorption spectra of the chromophore-Au_{25} nanocluster oligomers are significantly different than the single Au_{25} nanocluster's spectrum. Distinct absorption features of $Au_{25}(GSH)_{18}$ are observed at 400, 450, 500 and 670 nm due to a quantum confinement effect (Figure 4.7).[21,22,64] Note that surface plasmon resonance bands are not observed in the optical absorption spectra of the chromophore-Au_{25} nanocluster oligomers, which means that the

oligomers did not form large particles. When the different chromophore-Au_{25} nanocluster oligomers are separated from the mixture, band 1 shows the same absorption peaks at 450, 500, 550, 670 and 770 nm as the Au_{25} nanocluster, indicating the presence of single Au_{25} nanocluster in the reaction product which are unreacted. This observation is in accordance with the conclusion drawn from the mass spectrum analysis. The absorption peaks at 450 and 500 nm are present in moving from single Au_{25} nanocluster to the chromophore-Au_{25} dimer (Figure 4.7). The larger oligomers, chromophore-Au_{25} nanocluster trimer and band 4, show absorption in the same broad area but the peaks are less defined. Changing the plot to a photon energy scale (Figure 4.8) allows us to better visualize the two broad peaks of the nanocluster oligomers. The optical absorption of Au_{25} nanoclusters is primarily due to intra-band and inter-band transitions from the atomic orbitals of the nanocluster's icosahedral Au_{13} core and the six Au_2S_3 motifs.[19,23,65]

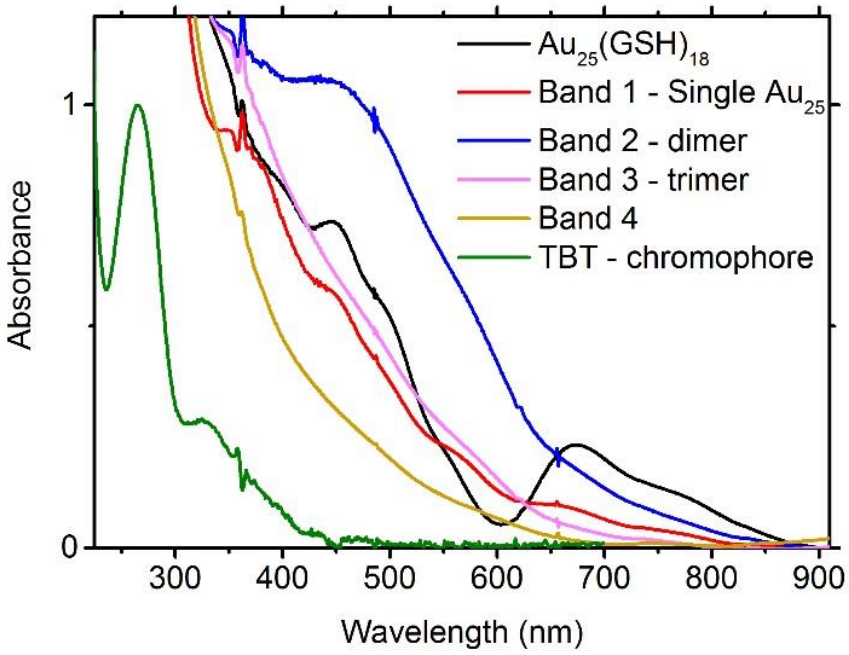

Figure 4.7. Steady state absorption of $Au_{25}(GSH)_{18}$ and chromophore-nanocluster oligomers.

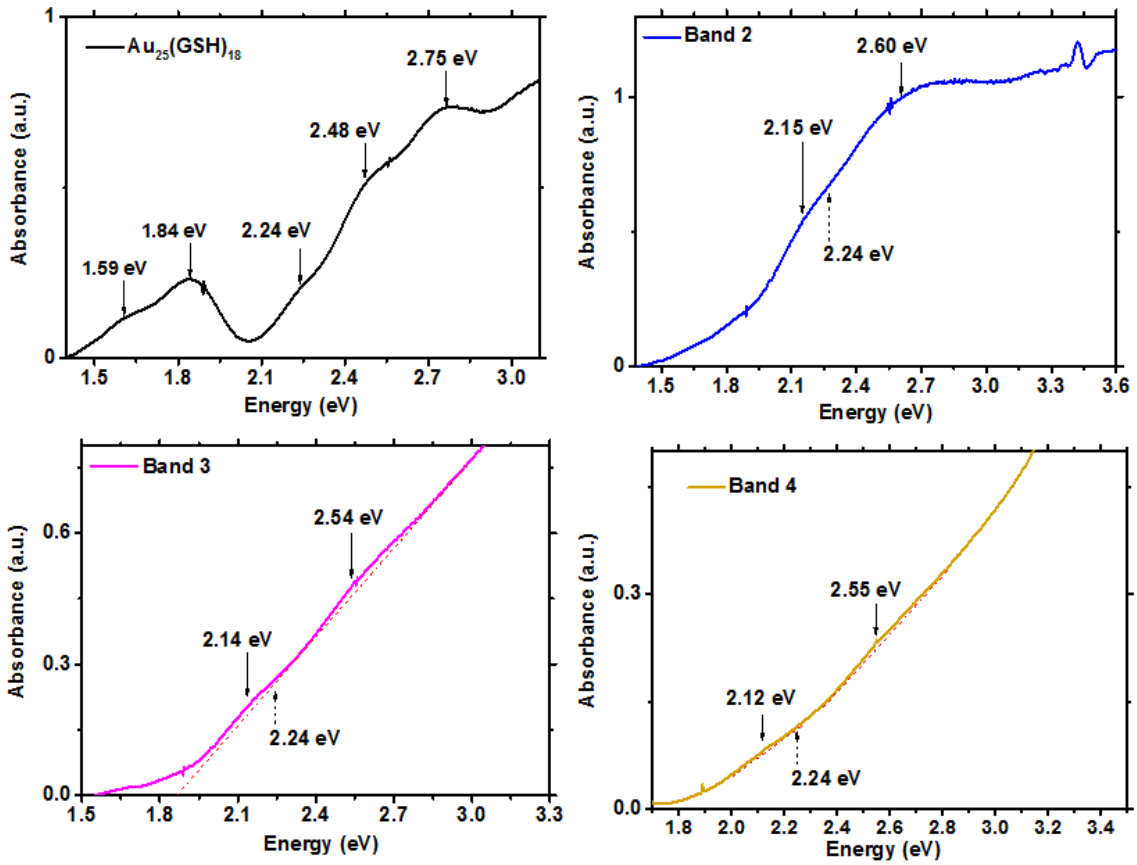

Figure 4.8. Absorption spectra of the $Au_{25}(GSH)_{18}$ nanocluster and of the nanocluster oligomers in the photon energy scale. Two broad absorption features are observed in the nanocluster oligomers.

In a theoretical study of Au_{25}-benzenedithiol-Au_{25} dimer, it was shown that the two linked Au_{25} nanoclusters do not disturb the electronic shell structure of each other.[45] The calculated energy gaps of a gas phase $Au_{25}(SMe)_{18}$ species and a gas phase Au_{25}-benzenedithiol-Au_{25} species remain the same in both species (1.24 eV and 1.25 eV respectively).[45] The density of states are increased, according to the calculations, arising from the individual contribution of the two nanoclusters. For example, the single Au_{25} nanocluster has 4 single-particle states in the LUMO and 6 states in the LUMO+1, whereas the Au_{25}-benzenedithiolate-Au_{25} has 8 and 12 states in the LUMO and LUMO+1 respectively.[45] Thus, the observed absorption broadening of the ~450 nm peak of the

chromophore-Au_{25} nanocluster dimers compared to the narrower peak of the single cluster is due to the increased density of states of the dimer. The disappearance of the 1.84 eV (670 nm) peak might be due to the broadening and red shift of the 2.24 eV peak. The contribution of each nanocluster's unit to the increasing of density of states is also predicted in $[Al_{13}M_3O]_n$ superatom assemblies (the icosahedron Al_{13} nanoclusters are linked by the alkali M_3O motif).[49] Although the energy levels of the $[Al_{13}M_3O]_n$ superatom assemblies are shifted, the energy gap also remained the same as in the case of the Au_{25}-benzenedithiol-Au_{25} system.[49] According to this pattern, the chromophore-Au_{25} nanocluster trimer and band 4 are expected to have higher density of states compared to the dimer. This might account for their absorption peaks being less defined. Future theoretical work on larger chromophore-Au_{25} nanocluster oligomers are needed to understand the optical properties of larger systems. Although metal nanoclusters are considered to be molecular-like in behavior, they are also considered superatom complexes due to their exceptional stability, precise composition and discrete energy levels that are analogous to noble-gas superatoms.[18] The idea of $Au_{25}(GSH)_{18}$ nanoclusters as superatoms aptly explains the absorption coupling of chromophore-Au_{25} nanocluster oligomers. The formation of the chromophore-Au_{25} nanocluster oligomers is similar to the formation of molecules from atoms. Molecules exhibit broad spectral bands compared to atoms which exhibit narrow spectral lines. The narrower absorption bands of Au_{25} compared to the broader absorption bands of chromophore-Au_{25} dimer mirror the transition between atoms and molecules. Thus, the chromophore-Au_{25} nanocluster oligomers can be considered as supermolecules.

One major difference between the modeled Au_{25}-benzenedithiol-Au_{25} dimer[45] and our Au_{25}-thiodibenzenethiol-Au_{25} dimer is the molecular geometry of the linker. The benzenedithiolate has a planar geometry. The calculated structure of the Au_{25}-benzenedithiol-Au_{25} dimer shows an overall linear geometry.[45] On the other hand, our system Au_{25}-thiodibenzenethiol-Au_{25} dimer has an overall bent geometry due to the central sulfur atom connecting the two benzene units (Figure 4.6). The bent geometry of our dimer system, and the fact that the central sulfur atom is electronegative, results in a net dipole moment that is larger than single Au_{25} nanoclusters. Therefore, we expect that our dimer system would exhibit different electronic properties compared to the modeled linear Au_{25}-benzenedithiol-Au_{25} dimer system[45] and single Au_{25} nanoclusters. The transition dipole moment of a molecule is proportional to the molecule's oscillator strength (probability of electronic transition) by equation 4.1:[66]

$$f_{pq} = \frac{2}{3}\Delta E\left|\mathrm{d}_{pq}\right|^2 \qquad (4.1)$$

where f_{pq} is the oscillator strength transition between two states, ΔE is the energy gap, and d_{pq} is the transition dipole moment. As mentioned earlier, theoretical calculations showed that the energy gap of linked nanocluster assemblies remain the same as the single nanocluster.[45,49] The absorption spectrum of the chromophore-Au_{25} nanocluster dimer show the same energy gaps as those of single Au_{25} nanoclusters, therefore we can assume that the ΔE term remains unchanged. In transitioning from the single Au_{25} to the chromophore-Au_{25} dimer, it is expected that the oscillator strength of the dimer would be greatly enhanced due to the dimer's increase in dipole moment as a virtue of its bent molecular geometry. Indeed, we have estimated that the absorption coefficients of these oligomers increases with oligomer size, which indicates stronger electronic transition

(Figure 4.9). As mentioned earlier, the observed absorption peak broadening is related to the increase of the density of states in the chromophore-Au_{25} nanocluster dimer. This is related to the dimer's dielectric constant (ϵ), which is influenced by the molecular geometry, by equation 2:[67]

$$\epsilon\,(\Delta E) = \frac{2\pi^2}{\Delta E} f_{pq} N_d(\Delta E) \qquad (4.2)$$

where N_d is the number of density of states. These relationships suggest that by controlling the chromophore-Au_{25} nanocluster oligomer's geometry through the linker, and by achieving larger nanocluster superatom assemblies, it is expected that larger oscillator strength and polarizability can be achieved with linked metal-chromophore nanoclusters systems.

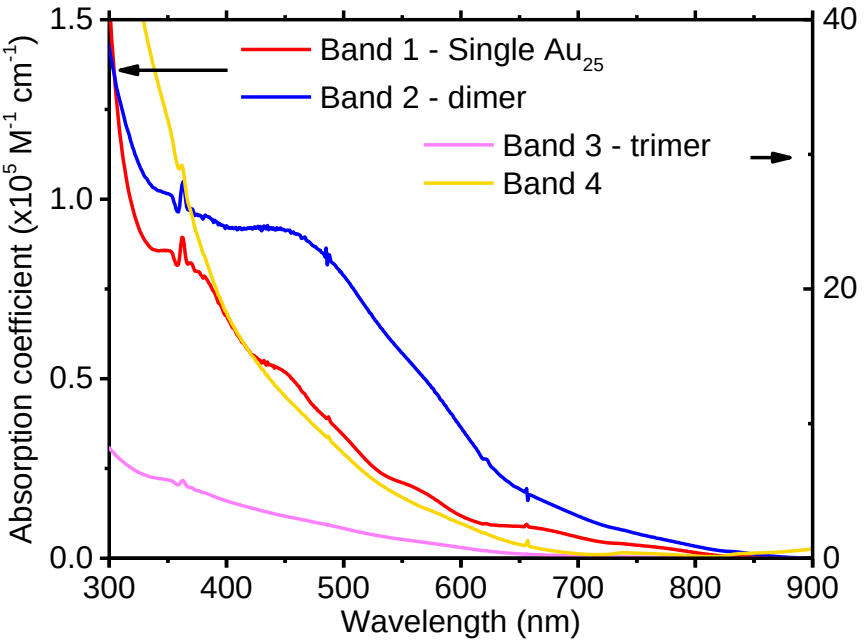

Figure 4.9. Estimated absorption coefficients of the chromophore-Au_{25} nanocluster oligomers.

Steady state emission. $Au_{25}(GSH)_{18}$ nanoclusters and chromophore-Au_{25} nanocluster oligomers show emission bands at 685 and 713 nm, respectively (Figure 4.10A). This emission arises from the surface states of the nanoclusters and it is influenced by the type

of ligand used in the nanocluster's synthesis.[29,68–70] The emission of the chromophore-Au_{25} nanocluster oligomers is ~27 nm red-shifted from that of the $Au_{25}(GSH)_{18}$ nanoclusters. The origin of the near-IR emission is likely the collective response of each nanocluster in the oligomer since this emission arises from the core-to-surface energy transfer.[68,71] However, this emission is significantly affected by different factors. It has been shown that the emission of Au_{25} nanoclusters with non-polar organic ligands is red-shifted from the emission of Au_{25} with polar organic ligands such as glutathione.[29] Therefore, the covalent linking of the non-polar organic chromophore TBT contributed to the emission red-shift of the chromophore-Au_{25} nanoclusters oligomers systems. In addition, the phenomenon aggregation-induced emission could also affect the emission of the nanocluster oligomers due to the close proximity between the nanocluster's surfaces.[72,73]

Based on theoretical calculations of other linked metal nanoclusters systems, the density of states of the metal nanoclusters increases with the subsequent addition of repeating units into the linked metal nanoclusters system.[45,50] Because of the additional states per energy level, the lowest vibrational level in the excited S1 state lies lower in energy for the chromophore-Au_{25} nanocluster oligomers than for the single Au_{25} nanoclusters, which contributes to the observed emission red-shift. This observation is also analogous to conjugated polymers with increasing repeating units, where the energy levels are lowered by the increasing delocalization of the π electrons.[74] The emission wavelength red-shift between single Au_{25} and chromophore-Au_{25} oligomers suggests that the emission wavelength is tunable by strategically designing the chromophore-nanocluster oligomer architecture. Additionally, the excitation spectra show a blue-shift

with increasing oligomer length (Figure 4.10B). As will be demonstrated shortly, higher energy excitation of the Au_{25} nanocluster does not result in emission. Therefore, the excitation spectra indicate that the contribution from the chromophore TBT becomes increasingly significant with increasing oligomer length, which suggests an energy transfer process from the chromophore to the nanocluster.

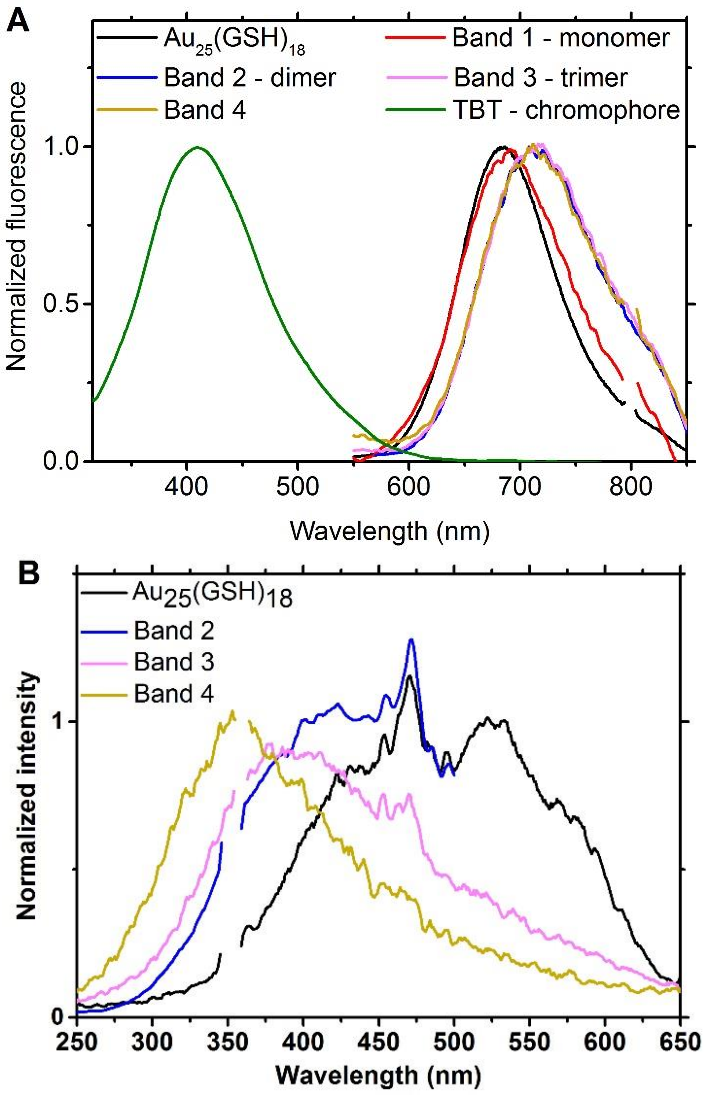

Figure 4.10. (A) Steady state emission of $Au_{25}(GSH)_{18}$ and chromophore-nanocluster oligomers excited at 400 nm, and emission of TBT chromophore excited at 265 nm. (B) Excitation spectra of $Au_{25}(GSH)_{18}$ and chromophore-nanocluster oligomers, obtained from emission λ_{max}.

The quantum yield of $Au_{25}(GSH)_{18}$ was calculated to be $1.8x10^{-3}$. The nanocluster's core is directly excited at 400 nm, which then undergoes two competing relaxation pathways, the radiative relaxation to the ground state and non-radiative relaxation to the semi-ring surface states which results in the red emission.[68] Although the Au_{25} nanoclusters are covalently attached through the chromophore TBT, direct excitation of the nanocluster's core can be safely assumed to be independent between the two nanoclusters. Due to the shared chromophore between the Au_{25} nanoclusters in the dimer, the relaxation from both the nanocluster's core states to a surface state, with characteristics of the shared chromophore, is expected to increase the near-IR emission quantum yield of the dimer system. Therefore, an emission quenching mechanism must be present in the system to decrease the emission quantum yield. One emission quenching mechanism is the Förster resonance energy transfer (FRET) which occurs when the inter-molecular distance is less than ~8 nm.[75,76] The core-to-core distance between the two Au_{25} nanoclusters in the chromophore-Au_{25} dimer was estimated to be 1.88 nm which is well within the FRET distance (Figure 4.6). The core-to-core separation is only slightly larger than the length of a single Au_{25} nanocluster, which means that the surfaces of the two nanoclusters are close enough for energy transfer to occur.[77,78] Energy transfer between the two Au_{25} nanoclusters is also possible due to the spectral overlap between the near-IR emission and the lowest energy absorption transition at ~670 nm. The combined effects of enhanced emission by contribution from two nanoclusters' core states to the surface state, and of emission quenching by energy transfer between the nanoclusters resulted in a net emission quantum yield close to the quantum yield for single Au_{25} nanoclusters. This suggests that by controlling the bridging chromophore's

length and geometry, the quenching mechanism by energy transfer between the nanoclusters can be minimized while enhancing the fluorescence of the chromophore-Au_{25} nanocluster oligomer system.

Both the chromophore TBT and the Au_{25} nanocluster have high energy absorption transitions as seen previously in Figure 4.7, the Au_{25} nanocluster also shows lower energy absorptions. Upon excitation with a high energy wavelength, at 265 nm, the chromophore TBT shows an emission at 400 nm, but the Au_{25} nanocluster does not show emission (Figure 4.11A). However, when excited at 400 nm, the nanocluster shows an emission at 700 nm. Therefore, it is possible for energy transfer to occur from the chromophore to the nanocluster in the chromophore-nanocluster oligomers. Indeed, when the chromophore-nanocluster dimer is excited at 265 nm, two emissions can be observed (Figure 4.11B). The emission band at ~400 nm is due to the TBT in the nanocluster dimer system, and the emission band at ~700 nm is due to the nanoclusters. The result of the 700 nm emission of the dimer suggests an energy transfer process from the chromophore TBT to the nanocluster. This opens the possibility of achieving greater near-IR fluorescence enhancement if both the nanocluster's core states and the chromophore can transfer energy to the nanocluster's surface states. To rule out the possibility that the 700 nm emission in the dimer is caused by the excitation of the second harmonic of 265 nm (530 nm), we performed excitation scans with and without a filter to cut off the 530 nm (Figure 4.12). The excitation scans show a maximum at 400 nm, and the intensity decreases towards 265 nm. Therefore, the emission of the nanocluster at 700 nm is due to the energy transfer from TBT which has an emission maximum at 400 nm.

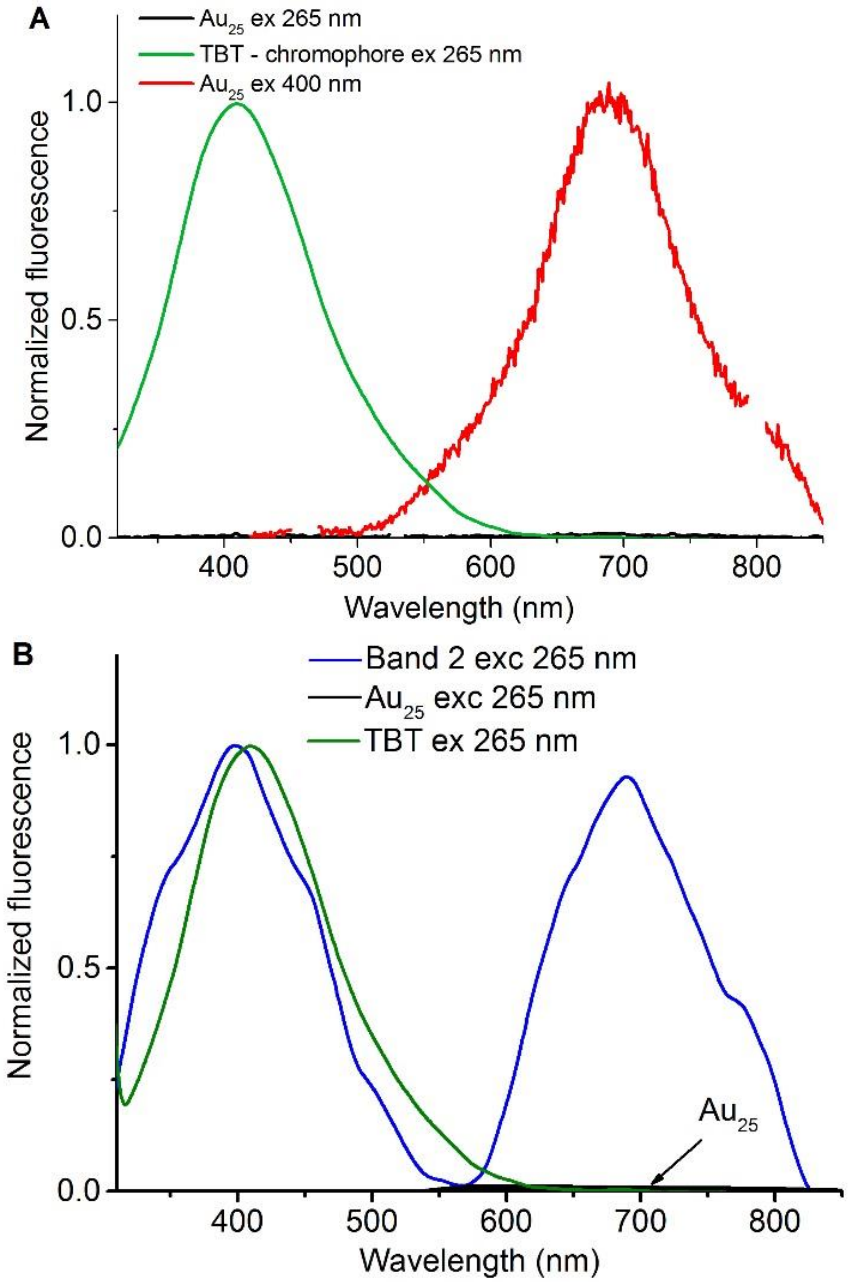

Figure 4.11. Emission of Au_{25} nanocluster excited at 265 and 400 nm (A), and emission of chromophore-nanocluster dimer excited at 265 nm (B).

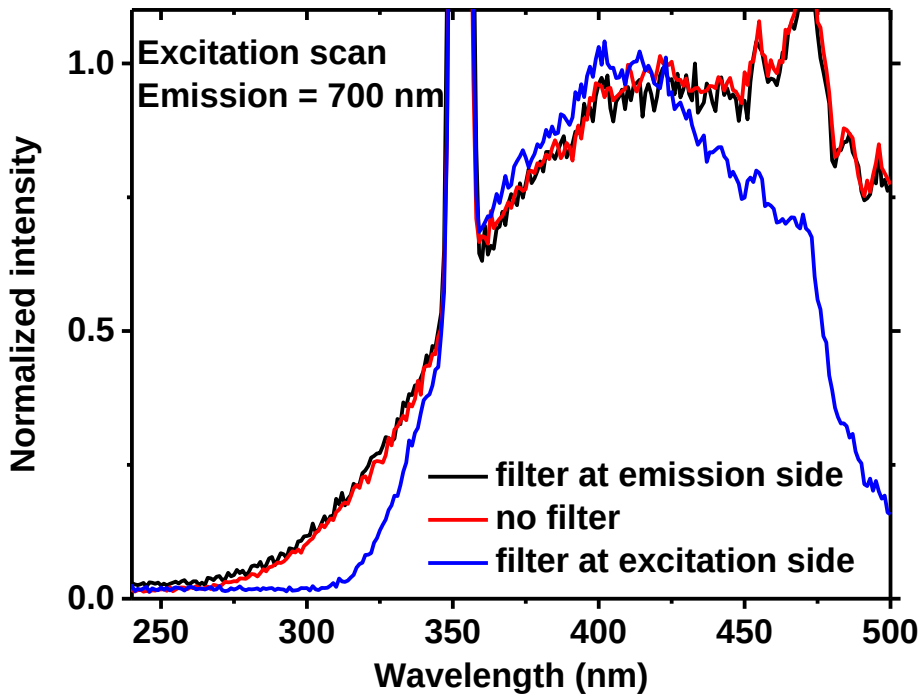

Figure 4.12. Excitation scan of the chromophore-Au_{25} nanocluster dimer performed with and without a filter (~500-600 nm).

Two-photon excited emission. Two-photon excited (TPE) emissions of the chromophore-nanocluster oligomers were measured using a mode-locked Ti:sapphire laser with 50 fs pulses. The emissions were recorded with 800 nm excitation. TPE emission further reveals the nanocluster's core emission at 500 nm which is not seen in one-photon excited emission (Figure 4.13). The 500 nm emission has a very short lifetime and quantum yield but can be detected by ultrafast spectroscopic techniques.[19,22] The core emission is the same for all systems, which suggests that the core electronic structure is affected minimally by the linking between nanoclusters. An emission red-shift of ~25 nm is observed in the near-IR of the TPE fluorescence of the chromophore-Au_{25} nanoclusters oligomers, consistent with the red-shift observed in the steady state fluorescence. The intensity-dependence of the emission bands at 500 nm and 681 nm is

linear with a slope of ~2 which indicates that they are indeed two-photon excited emissions (Figure 4.14).

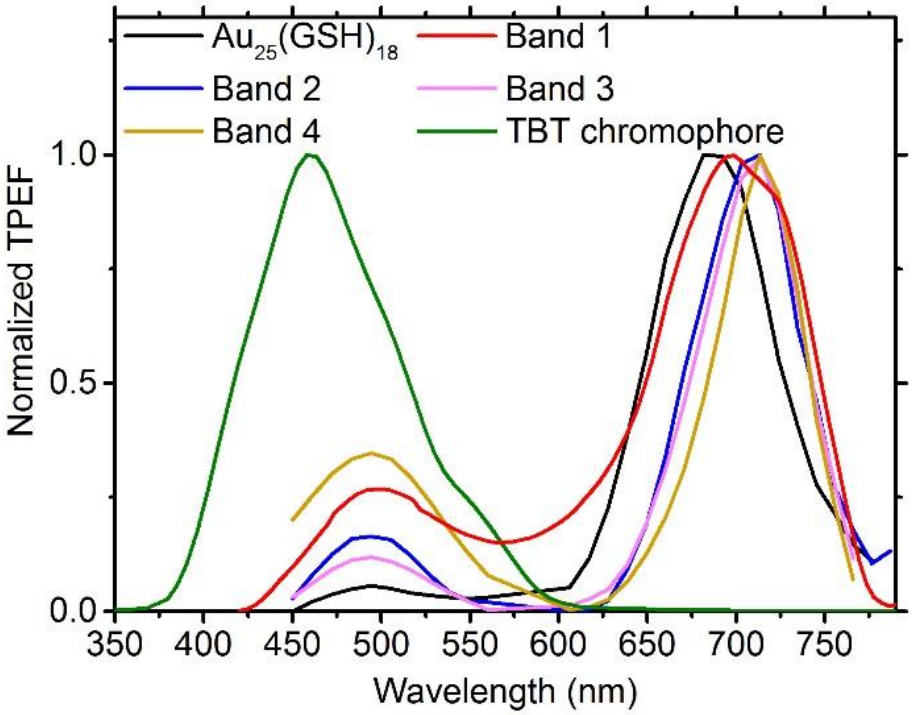

Figure 4.13. Two-photon excited emission of $Au_{25}(GSH)_{18}$ and chromophore-Au_{25} oligomers, excited at 800 nm, and TBT chromophore excited at 600 nm.

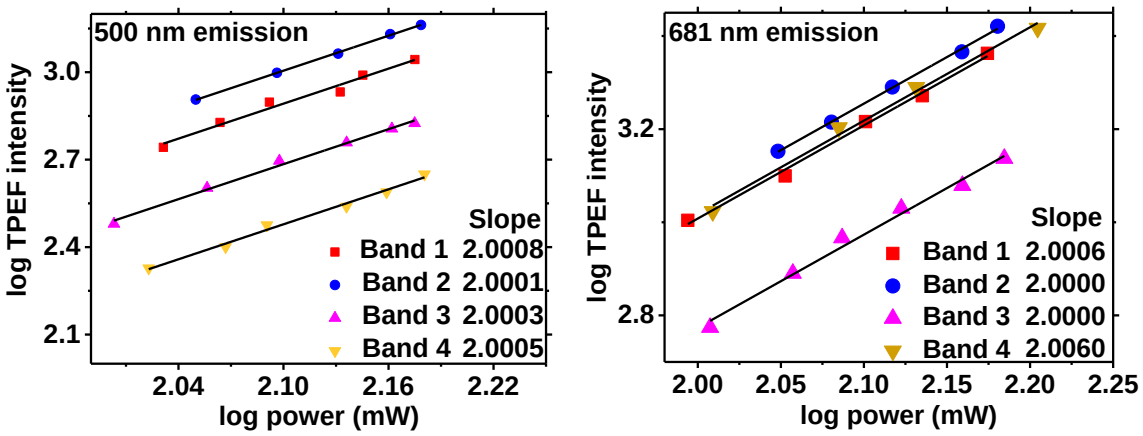

Figure 4.14. Intensity-dependence plot of chromophore-Au_{25} nanoclusters oligomers at 500 nm and 681 nm emission.

The TPA cross sections of the chromophore-Au_{25} nanocluster oligomers were calculated based on the intensity-dependence at 681 nm emission and referenced to

rhodamine B (σ = 150 GM at 800 nm).[79] The TPA cross sections of the chromophore-Au_{25} nanocluster oligomers were compared to the cross section of single Au_{25} nanoclusters which has a value of 427,000 GM at 800 nm excitation (Table 4.1).[22,80] The TPA cross section shows a steady enhancement in transitioning from Au_{25} to ~6-mer, up to 68 times. The enhancement of TPA cross sections in larger chromophore-Au_{25} nanocluster oligomers could indicate that there is a local field enhancement around the Au_{25} nanocluster since the core-to-core distance between the nanoclusters are about 1.88 nm which is approximately the length of one nanocluster. The two-photon absorption process is a third order non-linear effect which is affected by the third order polarizability (equation 4.3), where μ_{nm} is the transition dipole between states n and m, E_{i0} is the energy difference between the excited state and ground state, and Γ_{i0} is a damping constant when the photon energy reaches zero frequency.[81]

$$\gamma \alpha \frac{\mu_{02}^2 \mu_{12}^2}{(E_{20} - \hbar\omega - i\Gamma_{20})^2 (E_{10} - 2\hbar\omega - i\Gamma_{10})} \qquad (4.3)$$

Table 4.1. Two-photon absorption cross sections and action cross sections of chromophore-Au_{25} nanocluster oligomers.

Samples	Relative σ to Au_{25} x(427,000 GM)	λ_{max} TPEF (nm)	ϕ
Au_{25}	1	700	1.8×10^{-3}
Dimer	4	713	2.2×10^{-3}
Trimer	26	713	4.1×10^{-5}
Band 4	68.5	724	3.2×10^{-5}

The 1.88 nm core-to-core separation between the nanoclusters corresponds to the size of one nanocluster, approximately, which means that at the *surface* of the nanoclusters, the ligands are close enough to exert Van der Waals and dipole (through the GSH's polar functional groups) interactions between the two nanoclusters. The Au_{25} nanocluster is a negatively charged species (-1), with the charge localized at the core.[82] Therefore, to

account for the TPA cross section enhancement, the dipole interaction at the surface of the nanocluster must induce a local field enhancement. The local field enhancement around the Au_{25} nanoclusters is the enhancement of the nanocluster's dipole μ_{nm}, thus increasing the polarizability of the nanocluster. Note that the chromophore TBT has a bent molecular geometry and an electronegative sulfur atom, thus it is expected that the net dipole of TBT also enhances the polarizability of the covalently bonded nanoclusters compared to the single Au_{25} nanocluster in the ground state. This change between the dipole moment in the ground state and the excited state increases the transition dipole moment. In transitioning from the single Au_{25} nanocluster to the chromophore-Au_{25} ~6-mer, the enhanced two photon absorption suggests that there is a collective contribution from each repeating unit to the large dipole of the chromophore-Au_{25} oligomer system. We have observed similar TPA enhancement in Au_{25} nanoclusters films compared to solution, and in single isolated Au_{25} nanoclusters on a glass substrate compared to solution.[27,64] A ten-fold enhancement was observed in solid state Au_{25} nanoclusters and a 64% enhancement was observed in single isolated Au_{25} nanoclusters. The highest enhancement observed in the chromophore-Au_{25} nanocluster oligomer is ~68 times. From these results, it is expected that by synthesizing larger chromophore-Au_{25} nanocluster oligomers, larger TPA enhancement can be achieved. Our results also suggest that the chromophore's dipole can also be tailored (such as incorporating more electronegative atoms) to achieve larger TPA enhancement.

Time-resolved fluorescence of chromophore-Au_{25} nanocluster oligomers. The fluorescence dynamics of the nanocluster's core excited state in the chromophore-nanocluster dimer was investigated by the femtosecond fluorescence up-conversion

technique. The fluorescence decay traces were fitted with a function, $F(t)$, of one exponential component, convoluted with the instrument's response function, $g(t)$, or IRF (equation 4.4 and 4.5).[68] In these equations, τ_n is the decay lifetime, a_n is the amplitude, and a_m is the infinitely long lifetime amplitude background.

$$F(t) = \int_{t0}^{tf} f(t) - t' g(t') \mathrm{d}t' \qquad (4.4)$$

$$f(t) = \sum_{n=1}^{m} a_n \exp\left(\frac{-t}{\tau_n}\right) + a_{m+1} \qquad (4.5)$$

The 800 nm output was frequency-doubled to 400 nm to directly excite the Au_{25} core. The lifetimes of the core states emission at 510 nm were fitted with a single exponential decay convoluted with the IRF. The $Au_{25}(SR)_{18}$ nanocluster is known to have two emissions, one in the visible spectrum (500 nm) and one in the near-IR spectrum (~700-900 nm).[21,29,68] The fluorescence decay lifetime at 500 nm for single Au_{25} nanoclusters is 250 fs and for the chromophore-Au_{25} nanocluster dimer is 180 fs (Figure 4.15). The same fluorescence decay lifetime from the core states has been observed in Au_{25} nanoclusters previously.[21,68] In contrast to Au_{25} nanoclusters, large plasmonic nanoparticles decay lifetime is ~50 fs due to the fast Auger recombination.[83,84] Therefore, the chromophore-nanocluster dimer still maintains the properties of nanoclusters and not that of large nanoparticles. The shorter core emissive state lifetime indicates a faster non-radiative relaxation to the surface states, and that the Au_{25} nanocluster has a larger transition dipole in the chromophore-Au_{25} oligomers than as single Au_{25}.

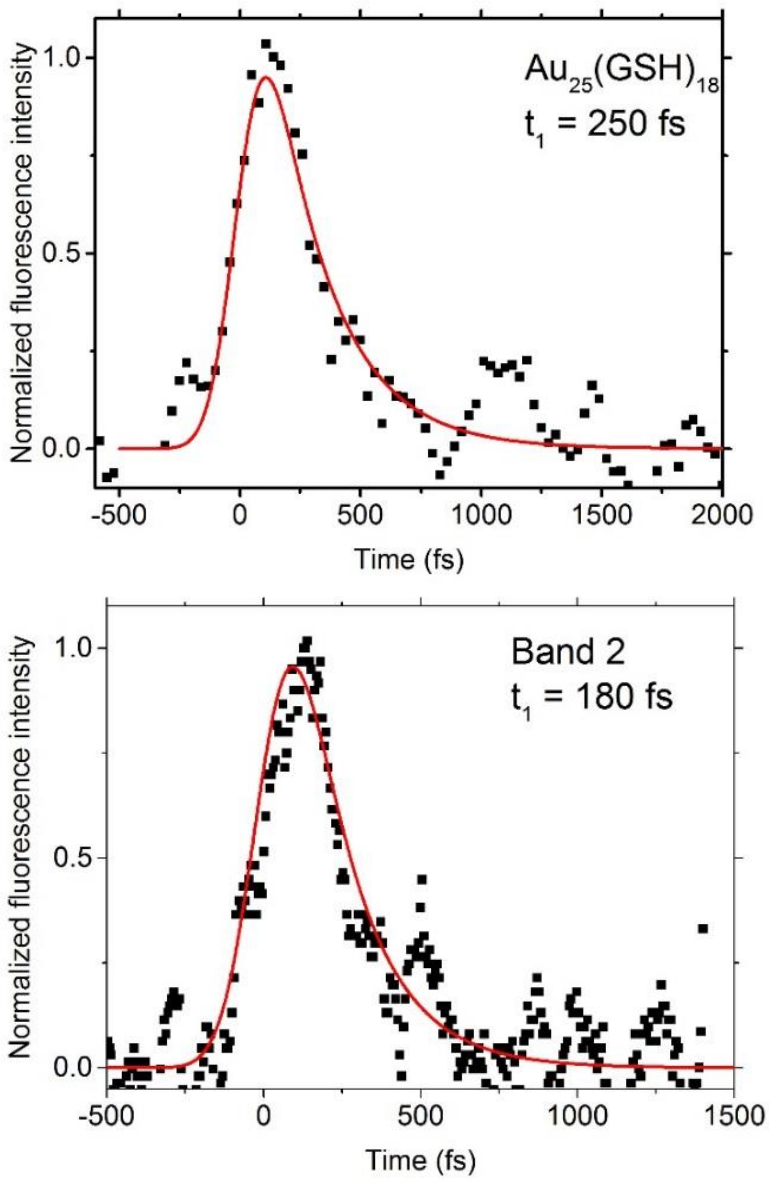

Figure 4.15. Time-resolved fluorescence at 500 nm of $Au_{25}(GSH)_{18}$ and chromophore-Au_{25} nanocluster dimer.

The presence of TBT may have increased the non-radiative relaxation rate from the core states to the surface states, which is the competitive deactivation mechanism to the core's radiative relaxation. A look at the molecular picture of the chromophore-Au_{25} nanocluster dimer system in Figure 4.6 reveals that the covalent bonds between the atoms C1-S1, C2-S2-C2, and C3-S3 are σ bonds that can be rotated. However, the rotation may

be restricted to some degree due to the "bulky" Au_{25} nanocluster and the ligands (which are omitted for clarity) to minimize steric hindrance. Due to the fixed conformation of the chromophore between the two nanoclusters, vibronic relaxation becomes more significant in the dimer system than in the single nanocluster system. Therefore, it is most likely that the excited nanocluster's core relaxes through the vibrations along the σ bonds of the attached chromophore TBT. The shortening in the core's excited state lifetime indicates that the rate of vibronic relaxation is faster than radiative relaxation when compared to single Au_{25} nanoclusters. In the single nanocluster system, the ligand's backbone and the Au-SR bonds can rotate freely. The only restriction to their bond rotation would be to minimize static repulsion between adjacent ligands on the nanocluster's surface. The competitive deactivation mechanism through vibration to the surface states would allow the dimer's surface states to have longer excited state lifetime compared to single Au_{25} nanoclusters. However, as mentioned in a previous section, a quenching mechanism is present that competes with the surface states emission, which accounts for the decrease in the emission quantum yield. As discussed in the next section, the transient absorption experiment reveals that the surface states indeed are long-lived in the dimer system compared to single Au_{25} nanoclusters.

Another factor contributing to the shortening of the nanocluster's core excited state lifetime is the change in the nanocluster's transition dipole moment. The fluorescence lifetime τ_f is a measure of the duration of a molecule in the excited state, and is inversely proportional to the radiative and non-radiative rate constants, k_r and k_{nr}, respectively.[85] In accordance with the Strickler-Berg equation, the radiative rate constant is proportional to

the oscillator strength of a molecule.[86,87] Therefore, the radiative lifetime of a molecule is inversely proportional to the transition dipole moment.

Based on the TPA enhancement, we have suggested that the transition dipole moment of Au_{25} in chromophore-Au_{25} nanocluster dimer is larger than that of single Au_{25} nanocluster. Therefore, the shortening of the excited state lifetime is due to the increase in the transition dipole moment of the chromophore-Au_{25} nanocluster dimers compared to the single Au_{25} nanoclusters. Similar correlation between transition dipole and fluorescence lifetime has been observed in naphthylmethylene malononitriles and certain fluorophores[85,87,88] Another example is the shortening of emission lifetime of attached fluorophores due to energy transfer to a plasmonic metal nanoparticle with large dipole moment, generating a non-fluorescent state, the "dark states".[89,90]

The increase of transition dipole moment combined with the competitive non-radiative relaxation from the core to the surface states contributed to the shortening of the nanocluster's core excited state lifetime. However the change is rather small considering that large TPA enhancement can be achieved in the chromophore-Au_{25} nanocluster oligomer systems. Additionally, enhancing the relaxation from the core states to the surface states may be potentially beneficial because the surface state emission has proven to be useful in sensing and imaging applications.[80,91]

Femtosecond transient absorption of the chromophore-Au_{25} dimer system. In addition to time-resolved fluorescence dynamic measurements, transient absorption analysis was performed to investigate excited states which are not seen in fluorescence dynamic measurements. A global analysis of the transient absorption spectra of $Au_{25}(GSH)_{18}$ and of the chromophore-Au_{25} nanocluster dimer shows two distinct kinetic

components (Figure 4.16). The global analysis allows us to observe the wavelength-dependence of the decay components (equation 4.6).[82] The lifetimes, τ_n, are wavelength-independent, while the amplitude, c_n, is wavelength-dependent. The transient absorption spectra for both systems evolve into a long-lived excited state absorption (ESA) which is more dominant at approximately 600 nm. Similar global kinetic has been observed in $Au_{25}(SR)_{18}$ nanoclusters.[82,92] Upon direct excitation of the nanocluster's core, the $Au_{25}(SR)_{18}$ nanocluster is shown to relax in 1.2 ps from the core states to the surface states.[92] A comparison between the single Au_{25} nanocluster and the dimer system shows that the dimer system has longer core and surface excited state lifetimes (Figure 4.16). Additionally, the long-lived state is strongly dominated by photoinduced absorption in the dimer system centered at ~600 nm. With excitation in excess of the HOMO-LUMO, the 600 nm probe is found to monitor the surface excited states.[26,82,92] Therefore, the chromophore-Au_{25} nanocluster dimer has a long-lived surface state.

$$\Delta A\ (\lambda) = \sum_n c_n(\lambda)\exp[-\frac{t}{\tau_n}] \qquad (4.6)$$

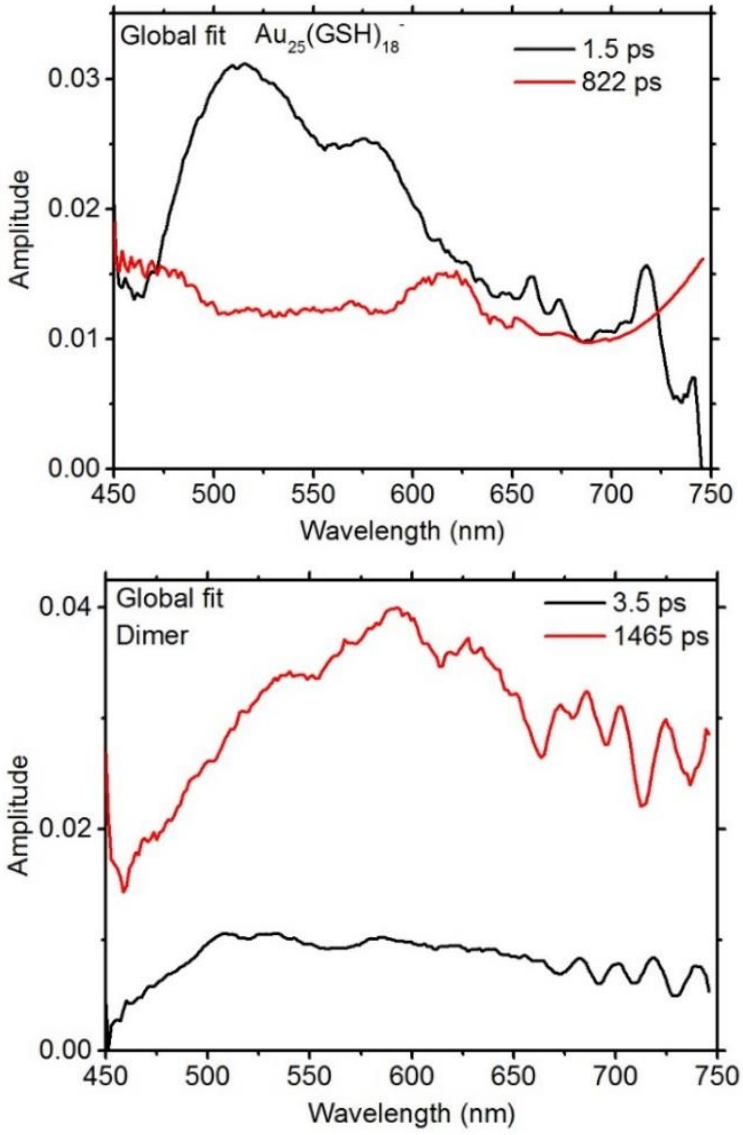

Figure 4.16. Global analysis of the $Au_{25}(GSH)_{18}$ nanocluster and of the chromophore-Au_{25} nanocluster dimer, excited at 410 nm.

The representative transient kinetics of $Au_{25}(GSH)_{18}$ and of the chromophore-nanocluster dimer are shown in Figure 4.17. Direct excitation of the core states at 410 nm allows us to observe the excited state dynamics of the core and its subsequent relaxation to the ligand-surface states.[26,82,92] The chromophore-nanocluster dimer has excited states that do not decay within the measurement window of the instrument (1 ns). Since the chromophore TBT is shared by two nanoclusters, we suggest that the energy transfer

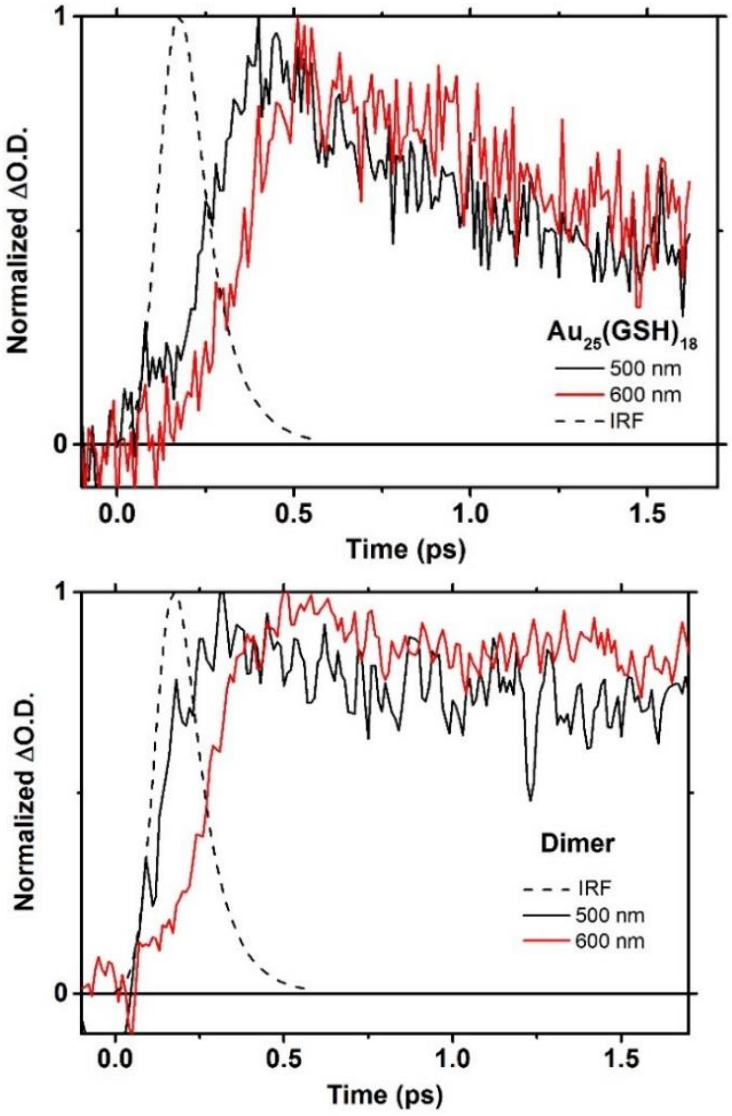

Figure 4.17. Representative transient absorption kinetics of $Au_{25}(GSH)_{18}^-$ and the dimer system at 500 nm and 600 nm, excited at 410 nm.

contributions from two nanoclusters' excited core states to the surface states extend the surface state lifetime. As mentioned in a previous section, the emission quantum yield is lowered compared to single Au_{25} nanoclusters. This means that by controlling the inter-cluster distance through the linker, it will be possible to minimize re-absorption of the fluorescence of the nanoclusters. The long excited state lifetime of the chromophore-Au_{25}

nanocluster dimer system indicates that networks of metal nanoclusters can be useful in light-harvesting and photodynamic therapy applications, where avoiding electron-hole recombination is important so that it may be converted to useful energy or used to generate reactive oxygen species.

4.6 Conclusion

We were able to synthesize chromophore-Au_{25} nanocluster oligomers by ligand exchange with the dithiol ligand 4,4'-thiodibenzenedithiol (TBT). Dimers, trimers, ~6-mers, and unreacted single Au_{25} nanoclusters were separated from the reaction mixture by gel electrophoresis and characterized by MALDI mass spectrometry and STEM imaging. Based on the characterization results, we have synthesized a chromophore-Au_{25} nanocluster dimer as the major product. These chromophore-Au_{25} nanocluster oligomers exhibited increased transition dipole moments, oscillator strength and polarizability compared to the single Au_{25} nanoclusters. The two-photon absorption cross sections were enhanced with increasing oligomer length. Up to 68 times enhancement was found compared to the cross section of single Au_{25} nanoclusters. The increased dipole moment and polarizability of these systems compared to single Au_{25} nanoclusters is due to the bent molecular geometry around the central electronegative sulfur atom of the chromophore connecting the nanoclusters. Due to the functionalization of the TBT to the nanoclusters, the chromophore-Au_{25} nanocluster dimer showed energy transfer from the excited states of TBT to the surface states of the nanocluster (Figure 4.18). Excitation at 265 nm did not show emission from the single Au_{25} nanoclusters due to the high density of the Au's *sp* bands at higher energy levels, through which the excited state can decay by a non-radiative pathway. This shows that specific energy transitions of the

chromophore and the nanocluster can be coupled. For example, one can instead design a system where both the chromophore and the nanocluster's core states can transfer energy to the surface state, thus enhancing the near-IR fluorescence emission.

Since the surface states of the nanoclusters in the dimer system has the shared chromophore's orbital character from the sulfur atom, excitation to the lower energy of the Au's *sp* bands showed energy transfer to the surface states which have a long excited state lifetime. The long lifetime is due to the contribution by two nanocluster cores, as the Au_{25}-chromophore-Au_{25} are covalently connected. This again suggests that the near-IR fluorescence efficiency of the dimer system is enhanced. In short, the energy transfer from the chromophore and from the cluster's core states enhance the near-IR emission of the chromophore-Au_{25} nanocluster oligomers. However, fluorescence quenching is observed in the systems studied because of the dipole interaction at the surface of the nanoclusters which are within the FRET distance. Enhancing the energy transfer and emission while minimizing quenching is important for applications involving light-harvesting, sensing and photodynamic therapy.[15,93,94] The fluorescence quenching event happens after the radiative decay of the surface states by FRET, as the surface states' lifetime is significantly longer than that of single Au_{25} nanoclusters. Therefore, we suggest that in designing large networks based on metal nanoclusters and chromophores, controlling the linker's size, molecular geometry, composition (e.g. extended π conjugation), and the type of metal nanocluster can achieve the desired optical properties for specific applications. Moreover, the collective properties of the metal nanoclusters and chromophores in a large network would be enhanced compared to the individual constituents. Additionally, this enhancement is proportional to the size of the network.

Therefore, networks of metal nanoclusters will find use in a wide range of applications, such as improved environmental sensing, photodynamic therapy, imaging, optics and light-harvesting, to name a few.

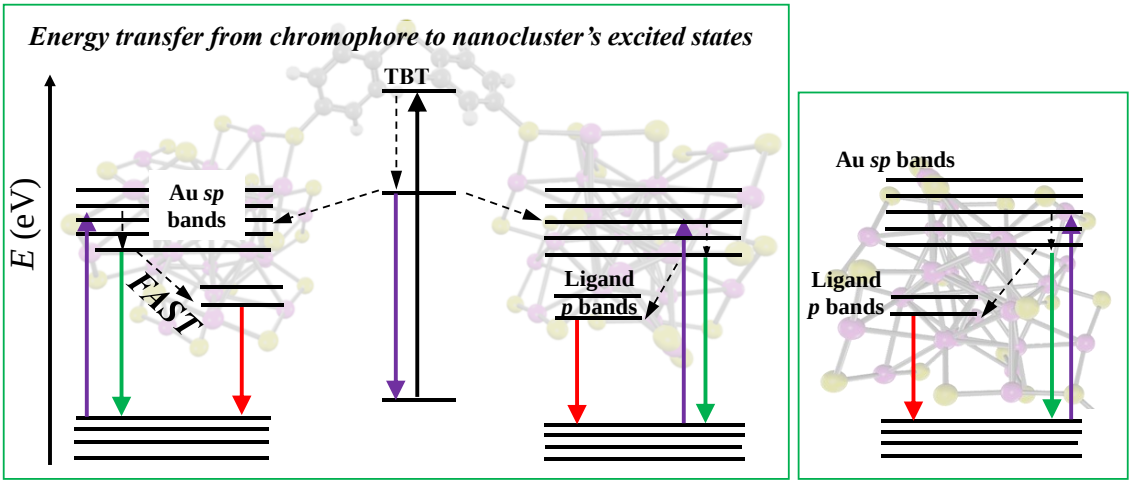

A. Chromophore-Au_{25} dimer system **B.** Single Au_{25} nanocluster

Figure 4.18. Transition energies of single Au_{25} nanoclusters and of chromophore-Au_{25} nanocluster dimers.

4.7 References

(1) Petridis, C.; Savva, K.; Kymakis, E.; Stratakis, E. Laser Generated Nanoparticles Based Photovoltaics. *J. Colloid Interface Sci.* **2017**, 489, 28–37.

(2) Tran, V.-H.; Ambade, R. B.; Ambade, S. B.; Lee, S.-H.; Lee, I.-H. Low-Temperature Solution-Processed SnO_2 Nanoparticles as a Cathode Buffer Layer for Inverted Organic Solar Cells. *ACS Appl. Mater. Interfaces* **2017**, 9, 1645–1653.

(3) Valenti, M.; Jonsson, M. P.; Biskos, G.; Schmidt-Ott, A.; Smith, W. A.; Liu, H.; Zhang, H.; Chang, K.; Meng, X.; Kako, T.; *et al.* Plasmonic Nanoparticle-Semiconductor Composites for Efficient Solar Water Splitting. *J. Mater. Chem. A* **2016**, 4, 17891–17912.

(4) Zou, Y.; Steinvurzel, P.; Yang, T.; Crozier, K. B. Surface Plasmon Resonances of Optical Antenna Atomic Force Microscope Tips. *Appl. Phys. Lett.* **2009**, 94, 171107.

(5) Colas des Francs, G.; Girard, C.; Laroche, T.; Lévèque, G.; Martin, O. J. F. Theory of Molecular Excitation and Relaxation near a Plasmonic Device. *J. Chem. Phys.* **2007**, 127, 34701.

(6) Zhang, R.; Wang, Z.; Song, C.; Yang, J.; Sadaf, A.; Cui, Y. Immunoassays Based on Surface-Enhanced Fluorescence Using Gap-Plasmon-Tunable Ag Bilayer Nanoparticle Films. *J. Fluoresc.* **2013**, 23, 71–77.

(7) Conklin, D.; Nanayakkara, S.; Park, T.-H.; Lagadec, M. F.; Stecher, J. T.; Chen, X.; Therien, M. J.; Bonnell, D. A. Exploiting Plasmon-Induced Hot Electrons in Molecular Electronic Devices. *ACS Nano* **2013**, 7, 4479–4486.

(8) Liu, R.; Liao, B.; Guo, X.; Hu, D.; Hu, H.; Du, L.; Yu, H.; Zhang, G.; Yang, X.; Dai, Q.; *et al.* Study of Graphene Plasmons in graphene–MoS_2 Heterostructures for Optoelectronic Integrated Devices. *Nanoscale* **2017**, 9, 208–215.

(9) Ramakrishna, G.; Dai, Q.; Zou, J.; Huo, Q.; Goodson III, T. Interparticle Electromagnetic Coupling in Assembled Gold-Necklace Nanoparticles. *J. Am. Chem. Soc.* **2007**, 129, 1848–1849.

(10) West, R.; Wang, Y.; Goodson III, T. Nonlinear Absorption Properties in Novel Gold Nanostructured Topologies. *J. Phys. Chem. B* **2003**, 107, 3419–3426.

(11) Varnavski, O. P.; Ranasinghe, M.; Yan, X.; Bauer, C. A.; Chung, S.-J.; Perry, J. W.; Marder, S. R.; Goodson III, T. Ultrafast Energy Migration in Chromophore Shell-Metal Nanoparticle Assemblies. *J. Am. Chem. Soc.* **2006**, 128, 10988–10989.

(12) Kühn, S.; Håkanson, U.; Rogobete, L.; Sandoghdar, V. Enhancement of Single-Molecule Fluorescence Using a Gold Nanoparticle as an Optical Nanoantenna. *Phys. Rev. Lett.* **2006**, 97, 17402.

(13) Harrington, W. N.; Haji, M. R.; Galanzha, E. I.; Nedosekin, D. A.; Nima, Z. A.; Watanabe, F.; Ghosh, A.; Biris, A. S.; Zharov, V. P. Photoswitchable Non-Fluorescent Thermochromic Dye-Nanoparticle Hybrid Probes. *Sci. Rep.* **2016**, 6, 36417.

(14) Varnavski, O. P.; Mohamed, M. B.; El-Sayed, M. A.; Goodson III, T. Relative Enhancement of Ultrafast Emission in Gold Nanorods. *J. Phys. Chem. B* **2003**, 107, 3101–3104.

(15) Andreussi, O.; Caprasecca, S.; Cupellini, L.; Guarnetti-Prandi, I.; Guido, C. A.; Jurinovich, S.; Viani, L.; Mennucci, B. Plasmon Enhanced Light Harvesting: Multiscale Modeling of the FMO Protein Coupled with Gold Nanoparticles. *J. Phys. Chem. A* **2015**, 119, 5197–5206.

(16) Tang, Q.; Jiang, D. Computational Insight into the Covalent Organic–Inorganic Interface. *Chem. Mater.* **2016**, 28, 5976–5988.

(17) Muniz-Miranda, F.; Menziani, M. C.; Pedone, A. DFT and TD-DFT Assessment of the Structural and Optoelectronic Properties of an Organic–Ag 14 Nanocluster.

J. Phys. Chem. A **2015**, 119, 5088–5098.

(18) Walter, M.; Akola, J.; Lopez-Acevedo, O.; Jadzinsky, P. D.; Calero, G.; Ackerson, C. J.; Whetten, R. L.; Grönbeck, H.; Häkkinen, H. A Unified View of Ligand-Protected Gold Clusters as Superatom Complexes. *Proc. Natl. Acad. Sci. U. S. A.* **2008**, 105, 9157–9162.

(19) Yau, S. H.; Varnavski, O.; Goodson III, T. An Ultrafast Look at Au Nanoclusters. *Acc. Chem. Res.* **2013**, 46, 1506–1516.

(20) Yau, S. H.; Abeyasinghe, N.; Orr, M.; Upton, L.; Varnavski, O.; Werner, J. H.; Yeh, H.-C.; Sharma, J.; Shreve, A. P.; Martinez, J. S.; *et al.* Bright Two-Photon Emission and Ultra-Fast Relaxation Dynamics in a DNA-Templated Nanocluster Investigated by Ultra-Fast Spectroscopy. *Nanoscale* **2012**, 4, 4247–4254.

(21) Yau, S. H.; Varnavski, O.; Gilbertson, J. D.; Chandler, B.; Ramakrishna, G.; Goodson III, T. Ultrafast Optical Study of Small Gold Monolayer Protected Clusters: A Closer Look at Emission. *J. Phys. Chem. C* **2010**, 114, 15979–15985.

(22) Ramakrishna, G.; Varnavski, O.; Kim, J.; Lee, D.; Goodson III, T. Quantum-Sized Gold Clusters as Efficient Two-Photon Absorbers. *J. Am. Chem. Soc.* **2008**, 130, 5032–5033.

(23) Zhu, M.; Aikens, C. M.; Hollander, F. J.; Schatz, G. C.; Jin, R. Correlating the Crystal Structure of a Thiol-Protected Au25 Cluster and Optical Properties. *J. Am. Chem. Soc.* **2008**, 130, 5883–5885.

(24) Varnavski, O.; Ramakrishna, G.; Kim, J.; Lee, D.; Goodson III, T. Critical Size for the Observation of Quantum Confinement in Optically Excited Gold Clusters. *J. Am. Chem. Soc.* **2010**, 132, 16–17.

(25) Varnavski, O.; Ramakrishna, G.; Kim, J.; Lee, D.; Goodson III, T. Optically Excited Acoustic Vibrations in Quantum-Sized Monolayer-Protected Gold Clusters. *ACS Nano* **2010**, 4, 3406–3412.

(26) Yau, S. H.; Ashenfelter, B.; Desireddy, A.; Ashwell, A. P.; Varnavski, O.; Schatz, G. C.; Bigioni, T.; Goodson III, T. Optical Properties and Structural Relationships of the Silver Nanoclusters Ag32(SG)19 and Ag15(SG)11. *J. Phys. Chem. C* **2017**, 121, 1349–1361.

(27) Ho-Wu, R.; Yau, S. H.; Goodson III, T. Linear and Nonlinear Optical Properties of Monolayer-Protected Gold Nanocluster Films. *ACS Nano* **2016**, 10, 562–572.

(28) Ashenfelter, B. A.; Desireddy, A.; Yau, S. H.; Goodson III, T.; Bigioni, T. P. Fluorescence from Molecular Silver Nanoparticles. *J. Phys. Chem. C* **2015**, 119, 20728–20734.

(29) Wu, Z.; Jin, R. On the Ligand's Role in the Fluorescence of Gold Nanoclusters. *Nano Lett.* **2010**, 10, 2568–2573.

(30) Shibu, E. S.; Muhammed, M. A. H.; Tsukuda, T.; Pradeep, T. Ligand Exchange of Au 25 SG 18 Leading to Functionalized Gold Clusters: Spectroscopy, Kinetics, and Luminescence. *J. Phys. Chem. C* **2008**, 112, 12168–12176.

(31) Wang, S.; Meng, X.; Das, A.; Li, T.; Song, Y.; Cao, T.; Zhu, X.; Zhu, M.; Jin, R. A 200-Fold Quantum Yield Boost in the Photoluminescence of Silver-Doped Ag(x)Au(25-X) Nanoclusters: The 13th Silver Atom Matters. *Angew. Chem. Int. Ed. Engl.* **2014**, 53, 2376–2380.

(32) Guidez, E. B.; Makinen, V.; Hakkinen, H.; Aikens, C. M. Effects of Silver Doping on the Geometric and Electronic Structure and Optical Absorption Spectra of the Au25−nAgn(SH)18− (N = 1, 2, 4, 6, 8, 10, 12) Bimetallic Nanoclusters. *J. Phys. Chem. C* **2012**, 116, 20617–20624.

(33) Parker, J. F.; Kacprzak, K. A.; Lopez-Acevedo, O.; Häkkinen, H.; Murray, R. W. Experimental and Density Functional Theory Analysis of Serial Introductions of Electron-Withdrawing Ligands into the Ligand Shell of a Thiolate-Protected Au 25 Nanoparticle. *J. Phys. Chem. C* **2010**, 114, 8276–8281.

(34) Varnavski, O.; Ispasoiu, R. G.; Balogh, L.; Tomalia, D.; Goodson III, T. Ultrafast Time-Resolved Photoluminescence from Novel Metal–dendrimer Nanocomposites. *J. Chem. Phys.* **2001**, 114, 1962.

(35) Ispasoiu, R. G.; Jin, Y.; Lee, J.; Papadimitrakopoulos, F.; Goodson III, T. Two-Photon Absorption and Photon-Number Squeezing with CdSe Nanocrystals. *Nano Lett.* **2002**, 2, 127–130.

(36) Ispasoiu, R. G.; Balogh, L.; Varnavski, O. P.; Tomalia, D. A.; Goodson III, T. Large Optical Limiting from Novel Metal-Dendrimer Nanocomposite Materials. *J. Am. Chem. Soc.* **2000**, 122, 11005–11006.

(37) Carminati, R.; Greffet, J.-J.; Henkel, C.; Vigoureux, J. M. Radiative and Non-Radiative Decay of a Single Molecule close to a Metallic Nanoparticle. *Opt. Commun.* **2006**, 261, 368–375.

(38) Wang, Y.; Xie, X.; Goodson III, T. Enhanced Third-Order Nonlinear Optical Properties in Dendrimer-Metal Nanocomposites. *Nano Lett.* **2005**, 5, 2379–2384.

(39) Goodson III, T.; Varnavski, O.; Wang, Y. Optical Properties and Applications of Dendrimer–metal Nanocomposites. *Int. Rev. Phys. Chem.* **2004**, 23, 109–150.

(40) Devadas, M. S.; Kwak, K.; Park, J.-W.; Choi, J.-H.; Jun, C.-H.; Sinn, E.;

Ramakrishna, G.; Lee, D. Directional Electron Transfer in Chromophore-Labeled Quantum-Sized Au 25 Clusters: Au 25 as an Electron Donor. *J. Phys. Chem. Lett.* **2010**, 1, 1497–1503.

(41) Ispasoiu, R. G.; Lee, J.; Papadimitrakopoulos, F.; Goodson III, T. Surface Effects in the Fluorescence Ultra-Fast Dynamics from CdSe Nano-Crystals. *Chem. Phys. Lett.* **2001**, 340, 7–12.

(42) Malicki, M.; Hales, J. M.; Rumi, M.; Barlow, S.; McClary, L.; Marder, S. R.; Perry, J. W. Excited-State Dynamics and Dye-Dye Interactions in Dye-Coated Gold Nanoparticles with Varying Alkyl Spacer Lengths. *Phys. Chem. Chem. Phys.* **2010**, 12, 6267–6277.

(43) Ding, W.; Hsu, L.-Y.; Schatz, G. C. Plasmon-Coupled Resonance Energy Transfer: A Real-Time Electrodynamics Approach. *J. Chem. Phys.* **2017**, 146, 64109.

(44) Liu, X.; Wu, Y.; Li, S.; Zhao, Y.; Yuan, C.; Jia, M.; Luo, Z.; Fu, H.; Yao, J. Quantum-Size-Effect Accommodation of Gold Clusters with Altered Fluorescence of Dyes. *RSC Adv.* **2015**, 5, 30610–30616.

(45) Akola, J.; Kacprzak, K. A.; Lopez-Acevedo, O.; Walter, M.; Grönbeck, H.; Häkkinen, H. Thiolate-Protected Au 25 Superatoms as Building Blocks: Dimers and Crystals †. *J. Phys. Chem. C* **2010**, 114, 15986–15994.

(46) Khanna, S. N.; Jena, P. Assembling Crystals from Clusters. *Phys. Rev. Lett.* **1992**, 69, 1664–1667.

(47) Khanna, S. N.; Jena, P. Atomic Clusters: Building Blocks for a Class of Solids. *Phys. Rev. B* **1995**, 51, 13705–13716.

(48) Nishigaki, J.; Koyasu, K.; Tsukuda, T. Chemically Modified Gold Superatoms and Superatomic Molecules. *Chem. Rec.* **2014**, 14, 897–909.

(49) Reber, A. C.; Khanna, S. N.; Castleman, A. W. Superatom Compounds, Clusters, and Assemblies: Ultra Alkali Motifs and Architectures. *J. Phys. Chem. C* **2009**, 113, 2664–2675.

(50) Castleman, A. W.; Khanna, S. N. Clusters, Superatoms, and Building Blocks of New Materials. *J. Phys. Chem. C* **2009**, 113, 2664–2675.

(51) Baksi, A.; Chakraborty, P.; Bhat, S.; Natarajan, G.; Pradeep, T. [Au 25 (SR) 18] 2 2− : A Noble Metal Cluster Dimer in the Gas Phase. *Chem. Commun.* **2016**, 52, 8397–8400.

(52) De Nardi, M.; Antonello, S.; Jiang, D.; Pan, F.; Rissanen, K.; Ruzzi, M.; Venzo,

A.; Zoleo, A.; Maran, F. Gold Nanowired: A Linear (Au 25) N Polymer from Au 25 Molecular Clusters. *ACS Nano* **2014**, 8, 8505–8512.

(53) Wu, Z.; Suhan, J.; Jin, R. One-Pot Synthesis of Atomically Monodisperse, Thiol-Functionalized Au 25 Nanoclusters. *J. Mater. Chem.* **2009**, 19, 622–626.

(54) Hostetler, M. J.; Wingate, J. E.; Zhong, C.-J.; Harris, J. E.; Vachet, R. W.; Clark, M. R.; Londono, J. D.; Green, S. J.; Stokes, J. J.; Wignall, G. D.; *et al.* Alkanethiolate Gold Cluster Molecules with Core Diameters from 1.5 to 5.2 Nm: Core and Monolayer Properties as a Function of Core Size. *Langmuir* **1998**, 14, 17–30.

(55) Chen, S.; Templeton, A. C.; Murray, R. W. Monolayer-Protected Cluster Growth Dynamics. *Langmuir* **2000**, 16, 3543–3548.

(56) Kim, J.; Lema, K.; Ukaigwe, M.; Lee, D. Facile Preparative Route to Alkanethiolate-Coated Au38 Nanoparticles: Postsynthesis Core Size Evolution. *Langmuir* **2007**, 23, 7853–7858.

(57) Zhu, M.; Lanni, E.; Garg, N.; Bier, M. E.; Jin, R. Kinetically Controlled, High-Yield Synthesis of Au25 Clusters. *J. Am. Chem. Soc.* **2008**, 130, 1138–1139.

(58) Kumar, S.; Bolan, M. D.; Bigioni, T. P. Glutathione-Stabilized Magic-Number Silver Cluster Compounds. *J. Am. Chem. Soc.* **2010**, 132, 13141–13143.

(59) Jupally, V. R.; Kota, R.; Dornshuld, E. Van; Mattern, D. L.; Tschumper, G. S.; Jiang, D.; Dass, A. Interstaple Dithiol Cross-Linking in Au25(SR)18 Nanomolecules: A Combined Mass Spectrometric and Computational Study. *J. Am. Chem. Soc.* **2011**, 133, 20258–20266.

(60) Knoppe, S.; Bürgi, T. The Fate of Au25(SR)18 Clusters upon Ligand Exchange with Binaphthyl-Dithiol: Interstaple Binding vs. Decomposition. *Phys. Chem. Chem. Phys.* **2013**, 15, 15816–15820.

(61) Hostetler, M. J.; Templeton, A. C.; Murray, R. W. Dynamics of Place-Exchange Reactions on Monolayer-Protected Gold Cluster Molecules. *Langmuir* **1999**, 15, 3782–3789.

(62) Wu, Z.; Gayathri, C.; Gil, R. R.; Jin, R. Probing the Structure and Charge State of Glutathione-Capped Au25(SG)18 Clusters by NMR and Mass Spectrometry. *J. Am. Chem. Soc.* **2009**, 131, 6535–6542.

(63) Slater, G. W.; Guo, H. L. Ogston Gel Electrophoretic Sieving: How Is the Fractional Volume Available to a Particle Related to Its Mobility and Diffusion Coefficient(s)? *Electrophoresis* **1995**, 16, 11–15.

(64) Abeyasinghe, N.; Kumar, S.; Sun, K.; Mansfield, J. F.; Jin, R.; Goodson III, T. Enhanced Emission from Single Isolated Gold Quantum Dots Investigated Using Two-Photon-Excited Fluorescence Near-Field Scanning Optical Microscopy. *J. Am. Chem. Soc.* **2016**, 138, 16299–16307.

(65) Akola, J.; Walter, M.; Whetten, R. L.; Häkkinen, H.; Grönbeck, H. On the Structure of Thiolate-Protected Au25. *J. Am. Chem. Soc.* **2008**, 130, 3756–3757.

(66) Bhattacharya, D.; Vaval, N.; Pal, S. Electronic Transition Dipole Moments and Dipole Oscillator Strengths within Fock-Space Multi-Reference Coupled Cluster Framework: An Efficient and Novel Approach. *J. Chem. Phys.* **2013**, 138, 94108.

(67) Cardona, M. Optical Properties and Electronic Density of States. *J. Res. Natl. Bur. Stand. (1934).* **1970**, 74A, 253–265.

(68) Devadas, M. S.; Kim, J.; Sinn, E.; Lee, D.; Goodson III, T.; Ramakrishna, G. Unique Ultrafast Visible Luminescence in Monolayer-Protected Au 25 Clusters. *J. Phys. Chem. C* **2010**, 114, 22417–22423.

(69) Green, T. D.; Yi, C.; Zeng, C.; Jin, R.; McGill, S.; Knappenberger Jr, K. L. Temperature-Dependent Photoluminescence of Structurally-Precise Quantum-Confined Au25(SC8H9)18 and Au38(SC12H25)24 Metal Nanoparticles. *J. Phys. Chem. A* **2014**, 118, 10611–10621.

(70) Devadas, M. S.; Thanthirige, V. D.; Bairu, S.; Sinn, E.; Ramakrishna, G. Temperature-Dependent Absorption and Ultrafast Luminescence Dynamics of Bi-Icosahedral Au 25 Clusters. *J. Phys. Chem. C* **2013**, 117, 23155–23161.

(71) Link, S.; Beeby, A.; FitzGerald, S.; El-Sayed, M. A.; Schaaff, T. G.; Whetten, R. Visible to Infrared Luminescence from a 28-Atom Gold Cluster. *J. Phys. Chem. B* **2002**, 106, 3410–3415.

(72) Dou, X.; Yuan, X.; Yu, Y.; Luo, Z.; Yao, Q.; Leong, D. T.; Xie, J. Lighting up Thiolated Au@Ag Nanoclusters via Aggregation-Induced Emission. *Nanoscale* **2014**, 6, 157–161.

(73) Luo, Z.; Yuan, X.; Yu, Y.; Zhang, Q.; Leong, D. T.; Lee, J. Y.; Xie, J. From Aggregation-Induced Emission of Au(I)-Thiolate Complexes to Ultrabright Au(0)@Au(I)-Thiolate Core-Shell Nanoclusters. *J. Am. Chem. Soc.* **2012**, 134, 16662–16670.

(74) Zheng, T.; Cai, Z.; Ho-Wu, R.; Yau, S. H.; Shaparov, V.; Goodson III, T.; Yu, L. Synthesis of Ladder-Type Thienoacenes and Their Electronic and Optical Properties. *J. Am. Chem. Soc.* **2016**, 138, 868–875.

(75) Stryer, L. Fluorescence Energy Transfer as a Spectroscopic Ruler. *Annu. Rev.*

Biochem. **1978**, 47, 819–846.

(76) Schaufele, F.; Demarco, I.; Day, R. N. In *Molecular Imaging*; Periasamy, A., Day, R., Eds; Elsevier: New York, NY, 2005; Chapter 4, pp 72–94.

(77) Yue, M.; Li, Y.; Hou, Y.; Cao, W.; Zhu, J.; Han, J.; Lu, Z.; Yang, M. Hydrogen Bonding Stabilized Self-Assembly of Inorganic Nanoparticles: Mechanism and Collective Properties. *ACS Nano* **2015**, 9, 5807–5817.

(78) Wu, Q.; Chen, L.; Huang, L.; Wang, J.; Liu, J.; Hu, C.; Han, H. Quantum Dots Decorated Gold Nanorod as Fluorescent-Plasmonic Dual-Modal Contrasts Agent for Cancer Imaging. *Biosens. Bioelectron.* **2015**, 74, 16–23.

(79) Xu, C.; Webb, W. W. Measurement of Two-Photon Excitation Cross Sections of Molecular Fluorophores with Data from 690 to 1050 Nm. *J. Opt. Soc. Am. B* **1996**, 13, 481.

(80) Polavarapu, L.; Manna, M.; Xu, Q.-H. Biocompatible Glutathione Capped Gold Clusters as One- and Two-Photon Excitation Fluorescence Contrast Agents for Live Cells Imaging. *Nanoscale* **2011**, 3, 429–434.

(81) Beels, M. T.; Biaggio, I.; Reekie, T.; Chiu, M.; Diederich, F. Two-Photon Absorption and Spectroscopy of the Lowest Two-Photon Transition in Small Donor-Acceptor–substituted Organic Molecules. *Phys. Rev. A* **2015**, 91, 43818.

(82) Qian, H.; Sfeir, M. Y.; Jin, R. Ultrafast Relaxation Dynamics of [Au25(SR)18]q Nanoclusters: Effects of Charge State. *J. Phys. Chem. C* **2010**, 114, 19935–19940.

(83) Varnavski, O.; Goodson III, T.; Mohamed, M.; El-Sayed, M. Femtosecond Excitation Dynamics in Gold Nanospheres and Nanorods. *Phys. Rev. B* **2005**, 72, 235405.

(84) Sakat, E.; Bargigia, I.; Celebrano, M.; Cattoni, A.; Collin, S.; Brida, D.; Finazzi, M.; D'Andrea, C.; Biagioni, P. Time-Resolved Photoluminescence in Gold Nanoantennas. *ACS Photonics* **2016**, 3, 1489–1493.

(85) Chung, P.-H.; Tregidgo, C.; Suhling, K. Determining a Fluorophore's Transition Dipole Moment from Fluorescence Lifetime Measurements in Solvents of Varying Refractive Index. *Methods Appl. Fluoresc.* **2016**, 4, 45001.

(86) Strickler, S. J.; Berg, R. A. Relationship between Absorption Intensity and Fluorescence Lifetime of Molecules. *J. Chem. Phys.* **1962**, 37, 814–822.

(87) Hirayama, S.; Phillips, D. Correction for Refractive Index in the Comparison of Radiative Lifetimes in Vapour and Solution Phases. *J. Photochem.* **1980**, 12, 139–145.

(88) Breffke, J.; Williams, B. W.; Maroncelli, M. The Photophysics of Three Naphthylmethylene Malononitriles. *J. Phys. Chem. B* **2015**, 119, 9254–9267.

(89) Li, J.; Krasavin, A. V.; Webster, L.; Segovia, P.; Zayats, A. V.; Richards, D. Spectral Variation of Fluorescence Lifetime near Single Metal Nanoparticles. *Sci. Rep.* **2016**, 6, 21349.

(90) Oh, E.; Huston, A. L.; Shabaev, A.; Efros, A.; Currie, M.; Susumu, K.; Bussmann, K.; Goswami, R.; Fatemi, F. K.; Medintz, I. L. Energy Transfer Sensitization of Luminescent Gold Nanoclusters: More than Just the Classical Förster Mechanism. *Sci. Rep.* **2016**, 6, 1–7.

(91) Wu, Z.; Wang, M.; Yang, J.; Zheng, X.; Cai, W.; Meng, G.; Qian, H.; Wang, H.; Jin, R. Well-Defined Nanoclusters as Fluorescent Nanosensors: A Case Study on $Au_{25}(SG)_{18}$. *Small* **2012**, 8, 2028–2035.

(92) Miller, S. A.; Womick, J. M.; Parker, J. F.; Murray, R. W.; Moran, A. M. Femtosecond Relaxation Dynamics of $Au_{25}L_{18}^{-}$ Monolayer-Protected Clusters. *J. Phys. Chem. C* **2009**, 113, 9440–9444.

(93) Zhang, J.; Tu, L.; Zhao, S.; Liu, G.; Wang, Y.; Wang, Y.; Yue, Z. Fluorescent Gold Nanoclusters Based Photoelectrochemical Sensors for Detection of H_2O_2 and Glucose. *Biosens. Bioelectron.* **2015**, 67, 296–302.

(94) Kawasaki, H.; Kumar, S.; Li, G.; Zeng, C.; Kauffman, D. R.; Yoshimoto, J.; Iwasaki, Y.; Jin, R. Generation of Singlet Oxygen by Photoexcited $Au_{25}(SR)_{18}$ Clusters. *Chem. Mater.* **2014**, 26, 2777–2788.

Chapter 5

Efficient Singlet Oxygen Generation in Metal Nanoclusters for Two-Photon Photodynamic Therapy Applications

5.1 Original Publication Information

This chapter was published as the following document:

Ho-Wu, R.; Yau, S. H.; Goodson III, T. "Efficient Singlet Oxygen Generation in Metal Nanoclusters for Two-Photon Photodynamic Therapy Applications" *Journal of Physical Chemistry B*, **2017**, 121, 10073-10080.

5.2 Abstract

The generation of singlet oxygen ($^1O_2$) has been established as the principal mechanism of photodynamic therapy (PDT). Various dyes, metal nanoparticles and clusters have been shown to sensitize $^1O_2$. However, metal nanoclusters are even more promising candidates as photosensitizers for this purpose. By understanding the optical properties that lead to efficient $^1O_2$ generation, one can fully realize their potential as PDT photosensitizers. Three different metal nanoclusters, Au_{25}, Ag_{32}, and Au_{144}, are investigated for $^1O_2$ their generation efficiency. The Au_{144} showed $^1O_2$ generation rate that is two orders of magnitude higher than Au_{25} and Ag_{32}, and several orders of magnitude higher than nanoparticles (>5 nm) due to Au_{144}'s high absorption cross

section-to-volume ratio. The effectiveness of PDT in live cells with nanoclusters was demonstrated by two-photon excitation compared to one-photon excitation. The implication of these results points towards new efficient two-photon $^1O_2$ sensitizers for photodynamic therapy.

5.3 Introduction

Nanoscale materials have shown great potential in medicine and will play a significant role in treatments and medical devices, such as drug delivery and bio-imaging agents.[1–4] Existing nanomaterials that are used for biomedicine are complex systems, requiring multiple components for practical applications and many have shown to be toxic by triggering auto immune response.[5–8] Therefore, exploring alternative nanomaterials for medicinal application is of great interest. One particular application of nanomaterials in medicine is photodynamic therapy.

Photodynamic therapy (PDT) is a procedure in which tumor cells are loaded with photosensitizers which triggers the generation of reactive oxygen species (ROS) upon light excitation (Figure 5.1).[9] The precise targeting of the photosensitizer makes PDT a spatially resolved and selective method for cancer treatment. There are two pathways in which ROS are generated. The photosensitizer is first excited from the ground state to a triplet excited state. The triplet excited state can transfer electrons to molecular oxygen to generate free radicals (type I) or it can transfer its energy to a ground state triplet oxygen to generate excited state singlet oxygen (type II).[9] Detection and quantification of ROS have been usually done with fluorescent probes or ROS scavengers.[10] Photodynamic therapy treatment can result in several pathways of cell death. The major cell death mechanisms are apoptosis, autophagy and necrosis.[9] Selective targeting of

photosensitizers in photodynamic treatment is, therefore, important in order to trigger cell death in tumor cells. The mitochondria, lysosome, and nucleus have been the subcellular targets for photodynamic therapy.[9,11] In general, singlet oxygen is the primary cytotoxic agent in photodynamic therapy, though other reactive oxygen species can also contribute to some extent in triggering cell death.[12] Due to the selective cellular uptake of photosensitizers and light irradiation over a defined area, photodynamic therapy allows a higher degree of control over cell death, thereby protecting healthy tissues from the treatment.

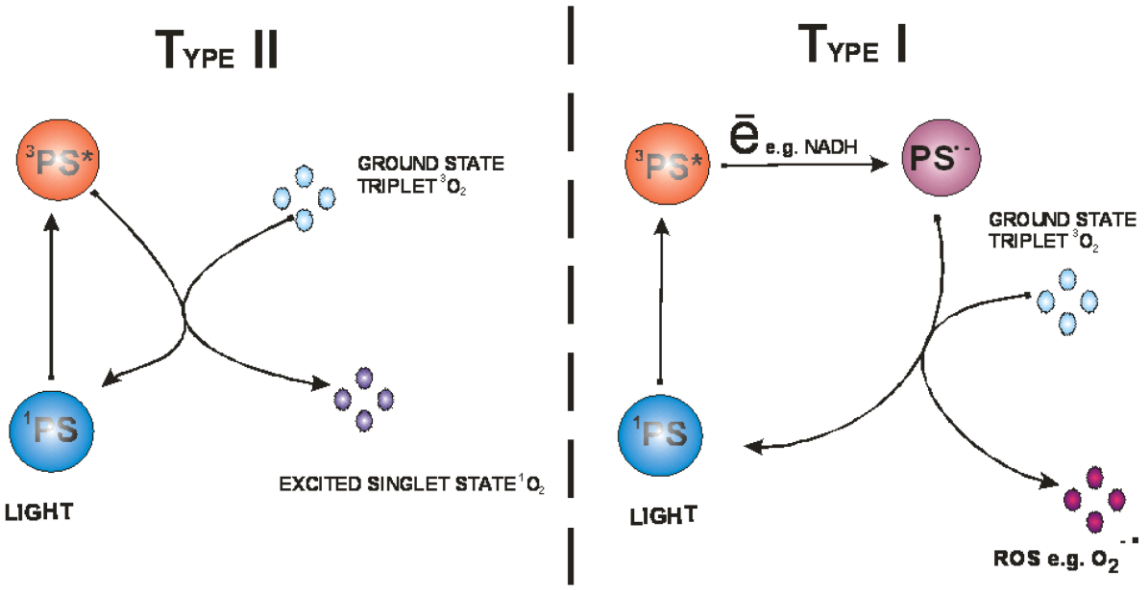

Figure 5.1. Pathways to reactive oxygen species (ROS) generation by excitation of a photosensitizer.[9]

The use of metal nanoparticles for PDT takes advantage of the nanoparticle's surface plasmon resonance (SPR).[2,13,14] Compared to organic dyes, the absorption coefficient of metal nanoparticles is about 5 order of magnitudes larger, which presents the advantage of using lower laser energy to trigger PDT without damaging nearby healthy cells.[15] The SPR of the nanoparticle is usually tailored to ~800 nm wavelength for tissue

penetration.[16] However, the $^1O_2$ yield is very low, and they are best used for enhancing organic dye photosensitizers.[2,15,17] The advantage of using metal nanoparticles tandem with organic dye photosensitizers is to enhance the triplet excited state formation, and more importantly, to act as drug delivery agents due to the poor solubility and tumor cell targeting of organic photosensitizers.[18] Although metal nanoparticles do not photosensitize singlet oxygen in appreciable amounts, an exception has been observed in TiO_2 nanoparticles which can generate radical oxygen species by UV excitation.[19] However, it is more desirable to perform photodynamic therapy with near-IR excitation due to deep tissue penetration. In addition, UV excitation is non-selective which causes damage to healthy tissues as well. These limitations hinder the use of TiO_2 in photodynamic therapy.

Metal nanoclusters, on the other hand, are less than 2 nm in size and do not have SPR, but rather, they exhibit discrete optical transitions.[20–22] Due to the high photo-stability and absorption cross sections, small metal clusters are ideal for deeper penetration in the cells, higher loading without long-term toxicity and precise targeting.[23–25] Unlike nanoparticles, the nanoclusters are emissive which eliminates the use of a dye for imaging.[26,27] More importantly, they have long-lived triplet excited states, which makes them reactive with triplet ground state oxygen to form singlet excited state oxygen.[9,28] $Au_{25}(SR)_{18}$ nanoclusters is the most researched nanocluster due to its high stability.[20,29,30] In addition to its stability, GSH-based Au_{25} nanoclusters have demonstrated to be non-toxic and can be eliminated from the biological system within 28 days, whereas plasmonic gold nanoparticles (~15 nm) can accumulate in the liver and spleen.[31] Therefore, in recent years, metal nanoclusters of different sizes and ligands have been

researched for singlet oxygen generation efficiency.[32–35] However, it is not well understood what makes certain nanoclusters more efficient at singlet oxygen generation than others. In this report, three different nanoclusters, Au_{25}, Ag_{32} and Au_{144}, are examined for their singlet oxygen generation efficiency. The nanoclusters are compared to plasmonic nanoparticles to provide an explanation for their high singlet oxygen generation.

5.4 Experimental

Materials. Chemicals and solvents were used as received. $HAuCl_4 \cdot 3H_2O$, L-glutathione (GSH) reduced, hexanethiol, tetraoctyl ammonium bromide (TOABr) and 1,3-diphenylisobenzofuran (DPBF) were purchased from Sigma-Aldrich. $NaBH_4$ was from Merck Millipore. NIH/3T3 mouse fibroblast cells were from ATCC. Fetal bovine serum (FBS) and streptomycin were from Life Technologies. Dulbecco's Modified Eagle Medium (DMEM) was from Corning.

$Au_{25}(GSH)_{18}$ and $Au_{144}(C_6H_{13}S)_{60}$ nanoclusters synthesis. The synthesis of the gold nanoclusters were performed according to published procedures.[36,37]

To synthesize Au_{25} nanoclusters, a solution of $HAuCl_4 \cdot 3H_2O$ (170 mg, 0.5 mmol) was prepared in 100 mL of methanol and was cooled in an ice bath for 15 min. GSH ($C_{10}H_{17}N_3O_6S$) (614 mg, 2 mmol) was added to the cooled solution and stirred for 30 min. During this time, the solution turned from yellow to colorless, which indicates the formation of Au(I)−SG. A freshly prepared NaBH4 (189 mg, 5 mmol) aqueous solution (25 mL) was then added to the mixture and allowed to stir for 1 h. The final solution turned dark brown. The nanocluster mixture was washed with methanol to remove excess reagents. The mixture was then redissolved in nanopure H_2O and incubated with excess

GSH at 55°C for 3 h. The precipitate from the reaction was discarded. $Au_{25}(GSH)_{18}$ nanoclusters were precipitated from the solution by addition of methanol. Absorption spectrum of the $Au_{25}(GSH)_{18}$ showed absorption at 450, 500, and 670 nm which indicates the purity of the sample.

To synthesize Au_{144} nanoclusters, a solution of $HAuCl_4 \cdot 3H_2O$ (118 mg) and TOABr (190 mg) was prepared in 15 mL of methanol and stirred for 15 min, turning from yellow to red. Then, hexanethiol (0.226 mL) was added to the solution and stirred for 15 min, turning into a colorless solution. A freshly prepared $NaBH_4$ solution (113 mg in 6 mL cold H_2O) was rapidly added to the reaction mixture and stirred overnight. The nanocluster precipitate was collected and washed with methanol. Au_{144} nanocluster was extracted from the mixture with CH_2Cl_2.

Ag_{32} nanocluster synthesis. The Ag_{32} nanoclusters were provided by Prof. Bigioni lab. Briefly, a 1:4 molar ratio of $AgNO_3$ and glutathione solution was allowed to react until a white suspension of Ag-glutathionate is formed. The mixture was then cooled in an ice bath for 30 min and reduced with $NaBH_4$ to yield a dark brown solution. The product was precipitated with methanol and subjected to polyacrylamide gel electrophoresis for size separation. The Ag_{32} nanocluster was extracted from the third band of the gel.[38,39]

Singlet oxygen generation and detection. A cw laser of 532 nm is generated with Millennia Pro (Spectra-Physics) to photo-excite the nanoclusters. The laser intensity was regulated with a neutral density filter. Absorption and emission spectra were recorded after photo-excitation of the nanoclusters. A typical solution used in the experiments contained 1.37×10^{-6} M nanoclusters and 6.15×10^{-5} M DPBF. All solutions are prepared in ethanol. UV-vis absorption spectra were recorded with Agilent 8453

spectrophotometer over 200 – 1200 nm. Fluorescence emission spectra were recorded with Fluoromax-2 spectrophotometer. The samples were loaded in quartz cuvettes and the excitation path length was 1 cm. The concentration of DPBF was calculated from the absorption spectrum.

Cell culture and fluorescence microscopy. NIH/3T3 mouse fibroblast cells were cultured in a working medium consisting of 90% DMEM, 10% FBS and 1% streptomycin. $Au_{25}(GSH)_{18}$ nanoclusters solutions were prepared using the same medium at 400, 200, and 100 μg/mL loading. The nanoclusters were incubated for 24 hours in the cells. The cells were deposited in a 35 mm glass bottom dish from MatTek. The working medium was removed and replaced with tris buffer for imaging experiments. The images were taken with the Leica Inverted SP5X Confocal Microscope System equipped with two-photon fluorescence lifetime imaging (2P-FLIM). Avalanche diode detectors were used to collect the images. For excitation, a 405-nm diode and a Spectra-Physics Mai-Tai two-photon tunable laser (800 nm) was used.

5.5 Results and Discussion

Small metal nanoclusters have a large optical window in the visible wavelengths which eliminates the need to tailor their size to match the excitation wavelength such as the case of plasmonic particles (Figure 5.2). Singlet oxygen generated from PDT can be detected by its emission in the near-IR but this direct method of quantifying singlet oxygen generation by nanoclusters is not ideal due to the spectral overlap with the emission of the nanoclusters.[40] Therefore, an indirect method was used to quantify singlet oxygen generation. Certain fluorescent dyes are reactive towards singlet oxygen, such as 1,3-diphenylisobenzofuran (DPBF), which forms endoperoxides and can be used as

fluorescent organic traps.[10] DPBF has a strong absorption at 412 nm and its absorption change can be used to quantify the singlet oxygen generation (Figure 5.2). DPBF has a strong absorption at 412 nm and its absorption change can be used to quantify the singlet oxygen generation. Both systems can be excited simultaneously to generate and detect singlet oxygen. However, irradiation at 400 nm with femtosecond pulses may result in the photo-degradation of DPBF.[41] Therefore, the generation of singlet oxygen can be triggered by excitation of the nanoclusters at 532 nm or longer wavelengths that correspond to the biological optical window for tissue penetration.

There are several factors that one must consider in using the indirect method for quantifying singlet oxygen generation. The change in the probe DPBF's absorption or emission should be due to the chemical reaction between DPBF and singlet oxygen. DPBF has an affinity towards reacting with singlet oxygen and radical triplet oxygen, $O_2^{\cdot -}$, among the reactive oxygen species.[10,42,43] However, $Au_{25}(Capt)_{18}^-$ nanoclusters have been shown to generate only singlet oxygen as the reactive oxygen species.[40] Additionally, we may assume that the rate of DPBF reacting with singlet oxygen is faster than the rate of singlet oxygen generation by the nanoclusters. Indeed, $Au_{25}(Capt)_{18}^-$ nanoclusters demonstrated higher singlet oxygen generation rate compared to the conventional dye photosensitizer, new methylene blue (NMB), by measuring the concentration change of DPBF upon photo-excitation.[40] Kawasaki *et al* have also demonstrated that the DPBF concentration change is not due to the thermal effects associated with the excited nanoclusters. Therefore, DPBF is used in this study to compare the rate of singlet oxygen generation by three different metal nanoclusters, Au_{25}, Au_{144} and Ag_{32}.

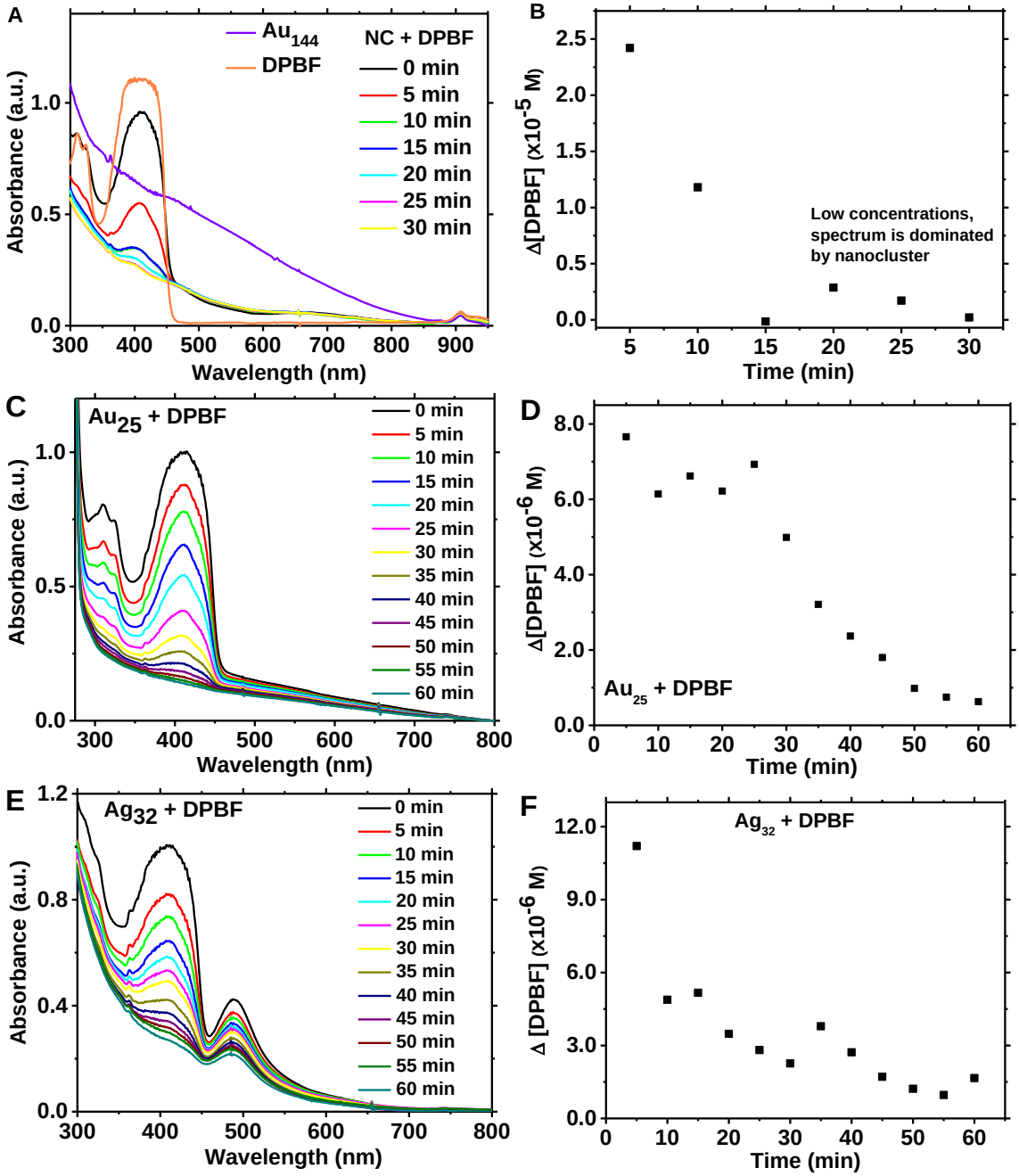

Figure 5.2. Absorption of nanoclusters+DPBF mixture solution excited with a 532 nm cw laser at 4.0×10^3 mW/cm^2 (A, C, E). Change in DPBF concentration over time indicates the rate of $^1O_2$ generation (B, D, F).

It is clear that the Au_{144} nanocluster has a very high $^1O_2$ generation rate (Figure 5.2A, 2B). After just 5 min, the change in the DPBF concentration has become smaller as the amount of $^1O_2$ starts to deplete. At longer exposure time (>15 min), the DPBF

concentration change is small and the absorption spectrum is dominated by the absorption of the nanoclusters, indicating that the concentration of $^1O_2$ and DPBF are too low for a reliable detection. For a more sensitive method to quantify low concentrations of $^1O_2$, one may monitor the fluorescence change of DPBF instead. However, for the purpose of obtaining the $^1O_2$ generation rate and comparing the rate between the different nanoclusters, we probed the initial rate of $^1O_2$ generation.

Table 5.1. Singlet oxygen generation rate by metal nanoclusters and comparison to plasmonic nanoparticle and dye photosensitizer for cw 532 nm irradiation.

photosensitizer type	molar extinction ($M^{-1}cm^{-1}$) / λ (nm)	absorption cross section-to-volume (m^{-1})	$^1O_2$ /cluster/min
Au_{144}	5×10^5 / 390 (46)	$1x10^7$	3.2
Au_{25}	8×10^3 / 670 (47)	$1x10^6$	0.077
Ag_{32}	2.5×10^4 / 480 (48)	$1x10^6$	0.033
NMB	5×10^4 / 630 (49)	$1x10^7$	0.05 ref 36
Au 40-nm	8×10^9 / 506 (50)	$1x10^7$	10^{-6} (quantum yield)[41]

The Au_{25} and Ag_{32} nanoclusters, on the other hand, generated $^1O_2$ at a much slower rate compared to the Au_{144} (Figure 5.2 C-F). The change in the absorption of DPBF was monitored over time at 400 nm ($\log\varepsilon = 4.3\ M^{-1}\ cm^{-1}$).[44] The rate of $^1O_2$ generation was obtained by the initial DPBF concentration change over time (Δ[DPBF]/Δt, which is the initial slope) divided by the concentration of the nanoclusters (Table 5.1). The Au_{144} has a rate of $^1O_2$ generation that is 2 orders of magnitude higher compared to Au_{25} and Ag_{32}. When compared to the conventional dye photosensitizer, NMB, Au_{25} nanoclusters have

been shown to have 1.4x higher $^1O_2$ quantum yield.[40] Although plasmonic nanoparticles have been shown to also sensitize the formation of $^1O_2$, the quantum yield is several orders of magnitude lower compared to photosensitizer dyes and metal nanoclusters.[17,45] Metal nanoparticles are best suited for photothermal therapy, instead, or as an enhancer for organic photosensitizers.[46,47] The high $^1O_2$ yield by metal nanoclusters has been attributed to the existence of a long-lived triplet excited state in metal nanoclusters.[20,21] The Au_{25} and Ag_{32} nanoclusters have very similar excited state lifetimes, which may account for their similar singlet oxygen generation rate.[38] The Au_{144} nanocluster, on the other hand, besides exhibiting quantum confinement characteristics like the smaller nanoclusters, also has core-localized plasmon resonant.[48,49]

Au_{25} has shown to be a better $^1O_2$ photosensitizer than NMB and nanoparticles which is due to the nanocluster's long-lived triplet excited state.[17,40,45,55] However, the triplet excited state lifetime for NMB is longer than those of Au_{25} and Ag_{32} which in turn are longer than that for Au_{144}.[49,55,56] It's been suggested that the higher $^1O_2$ generation rate by Au_{25} compared to NMB is due to the very high triplet formation quantum yield (87%) of Au_{25}.[40,57] In other words, population to the triplet excited states is a more significant factor than the triplet excited state lifetimes. The superior $^1O_2$ generation rate by Au_{144}, therefore, could be an indication that the Au_{144} has higher triplet excited state population. The Au_{144} nanocluster has been shown to have a core-localized plasmon resonance (CLPR) whose excitation frequency is also the same as that for the Au_{144} nanocluster's surface ligand states which are the triplet states.[49,56,58] This is not the case for the smaller nanoclusters whose triplet states are accessed by inter-system crossing when excited at the core.[38,59] Thus, the population to the triplet excited states of Au_{144} is promoted by

direct excitation and CLPR energy transfer within the nanocluster (Figure 5.3). Plasmon-enhanced emission of dyes by resonant energy transfer is a well-known process for dyes at certain distances from plasmonic nanostructures.[60]

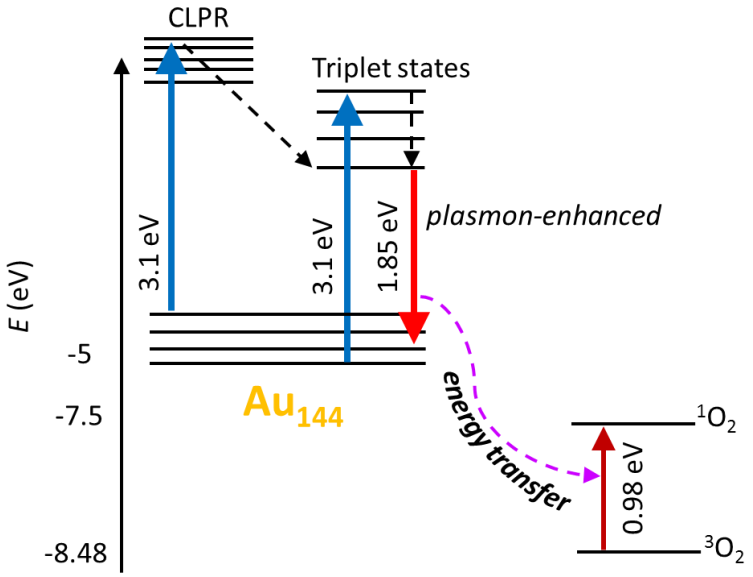

Figure 5.3. Energy diagram of the photosensitization of singlet oxygen by Au_{144} nanocluster.

Besides triplet formation quantum yield, it would be helpful to have an additional parameter that can correlate with the $^1O_2$ production rate. For nanoparticles, it is possible to relate their size or dimension to their optical properties.[61] The SPR of nanoparticles is known to have linear absorption coefficients that are orders of magnitude larger than typical dye photosensitizers and nanoclusters.[15] However, such high absorption cross-sections also come with high thermal effects which may result in non-selective cell damage.[2,62] A nanoparticle's temperature under pulsed laser irradiation can be modelled as a simple heat exchange process as given in equation 5.1, where V is the nanoparticle's volume ($V = 4/3\ \pi r^3$), ρ is the density of gold (19.32×10^3 kg/m^3), c is the heat capacity of gold (129 J/kg·K) and T_{NS} is the maximum temperature for a single excitation pulse

which can be written as equation 5.2, where *I* and *f* are the laser intensity and frequency, respectively.[61] Therefore, the maximum temperature is dependent on the nanoparticles' absorption cross sections and volumes, which are known to follow a linear dependence (Figure 5.4). Using this same analysis for metal nanoclusters, we find that Au_{144} and Ag_{44} have similar absorption cross section-to-volume (A/V) ratio (10^7 m^{-1}) as that of plasmonic nanoparticles and NMB (Figure 5.4). In turn, Au_{25} and Ag_{32} have lower A/V (10^6 m^{-1}). To ensure that the change in DPBF concentration was due to reaction with $^1O_2$, experiments under air-free condition were carried out to rule out thermal effects from the nanoclusters (Figure 5.5).

$$\varepsilon_0 = V\rho_{Au}c_{Au}T_{NS}^0 \tag{5.1}$$

$$T_{NS}^0 = \frac{\sigma_{abs}<I>}{V\rho_{Au}c_{Auf}} \tag{5.2}$$

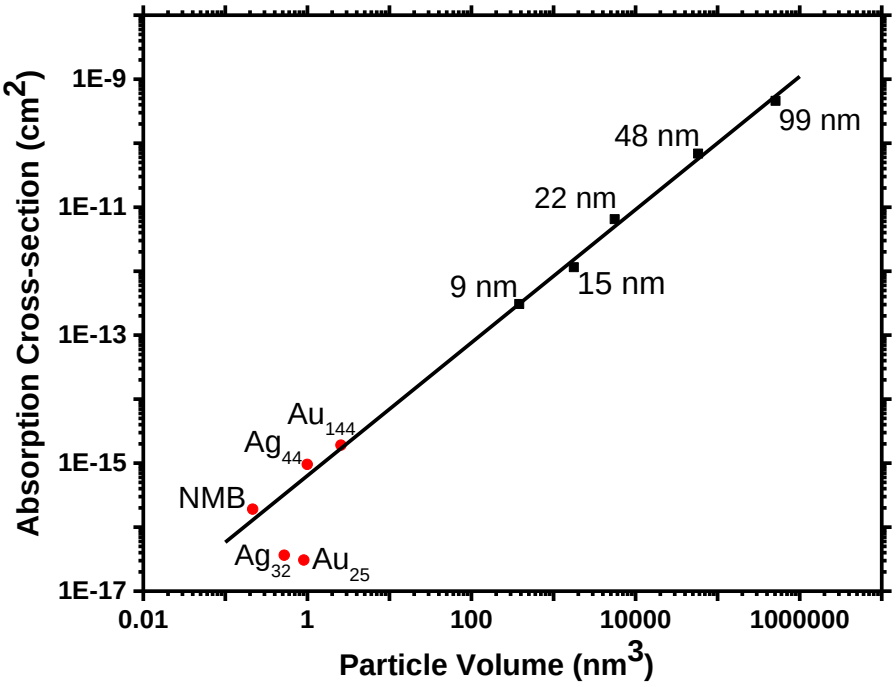

Figure 5.4. Calculated absorption-to-volume ratio for a series of gold plasmonic nanoparticle sizes and 4 selected metal nanoclusters.

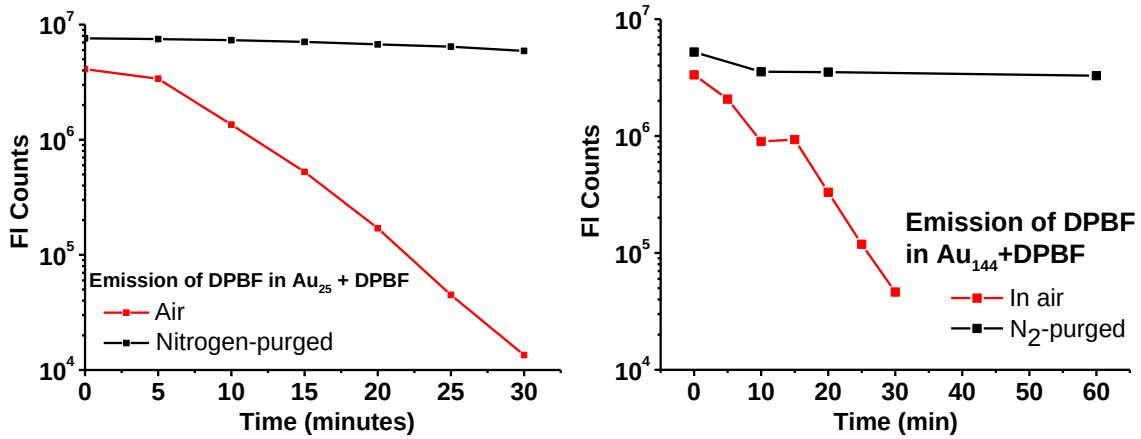

Figure 5.5. Emission of DPBF over time in Au_{25} + DPBF and Au_{144} + DPBF solutions in air and purged with N_2.

A summary of the photosensitizers' properties is presented in Scheme 5.1. As mentioned earlier, the triplet excited state population is a more important factor for $^1O_2$ generation, and we suggest that the Au_{144} nanocluster has a higher triplet excited state population. The high A/V of the Au_{144} indicates that this nanocluster has a higher aspect ratio for photons absorption which promotes the triplet excited state population. Based on the above analysis, we suggest that a combination of properties is necessary for high $^1O_2$ production rate; specifically, high A/V and high triplet excited state population. Silver nanoclusters have been shown to have enhanced optical properties compared to gold nanoclusters, but due to their lower shelf life (colloidal stability), silver nanoclusters have yet to receive the same attention as gold nanoclusters for applications.[38,52,63] It is suggested that a selection of nanoclusters termed high A/V nanoclusters would have high $^1O_2$ generation rate. For example, the Ag_{44} nanocluster is calculated to have the same high A/V as the Au_{144} nanocluster (Figure 5.4) and could be predicted to have a higher $^1O_2$ generation rate than lower A/V nanoclusters.

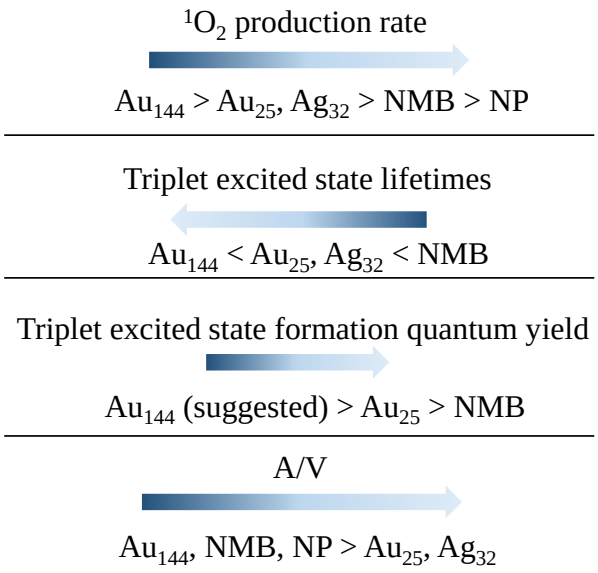

Scheme 5.1. Summary of $^1O_2$ photosensitizers' properties.

Finally, live cell imaging was carried out to explore the viability of metal nanoclusters for PDT in cells by one- and two-photon excitation. The $Au_{25}(GSH)_{18}$ nanocluster was chosen for this demonstration due to their solubility in water. The Au_{144} nanocluster was organic-soluble. The established synthesis of this nanocluster did not involve water-soluble ligands. More importantly, the slower $^1O_2$ generation rate of Au_{25} compared to Au_{144} allows cell imaging in a more reasonable timeframe. In a control experiment, the cells did not show sign of cell death after a 24-hour incubation which indicates the non-toxicity of the nanoclusters (Figure 5.6).

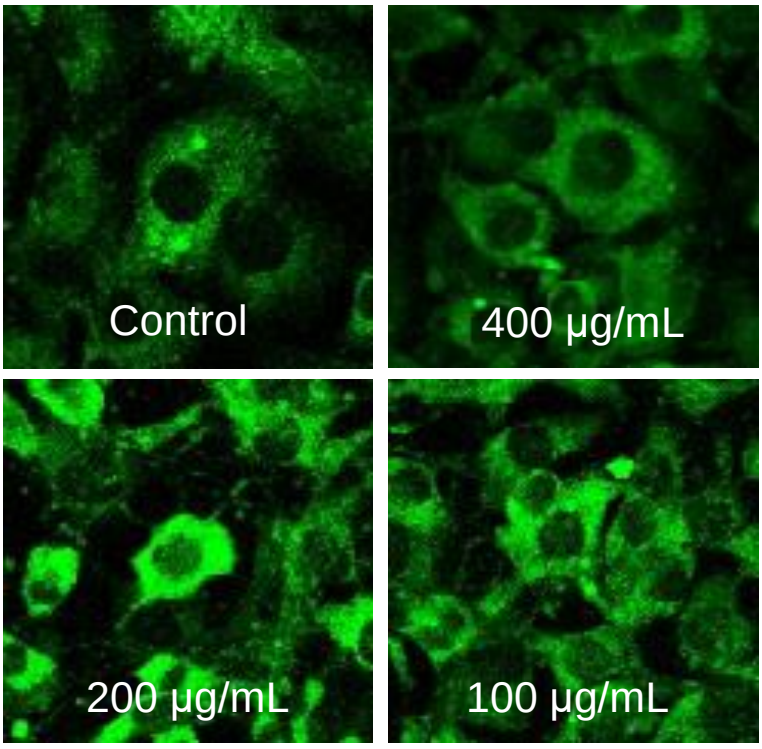

Figure 5.6. Cell viability with $Au_{25}(GSH)_{18}$ nanoclusters at different concentrations, excited at 400 nm (diode) after 24 hour incubation.

Under one-photon excitation (400 nm) by a diode, the energy was not sufficient to trigger PDT within a 20 min timeframe as evidenced by the integrity of the cell after 18 min in figure 5.7. A few examples are highlighted to compare the cells at time 0 and 18 min. The physical shape of the cells did not change after one-photon excitation of the nanoclusters. However, two-photon excitation using a pulsed 800 nm laser triggered cell death in as little as 15 min. The middle panel in figure 5.7 highlights examples of the physical shape of the cells before and after two-photon excitation of the nanoclusters. The deformation and, ultimately, shrinkage of the cells indicate membrane rupture and release of cell contents into the surrounding.[9] The control experiment confirms that cell death is triggered by PDT with the nanoclusters because the cells remain intact after excitation in the absence of the nanoclusters. The effective PDT by two-photon excitation is due to the

high two-photon absorption cross-section of metal nanoclusters (σ = 4 x 10^5 GM) compared to conventional photosensitizers (e.g. NMB, σ = 7 GM).[25,64] Due to the superior spatial resolution and sensitivity of two-photon absorption, and the high $^1O_2$ generation rate of metal nanoclusters, PDT by two-photon excitation with nanoclusters enables deep tissue imaging, fine control over exposure area and efficient treatment.[65–68]

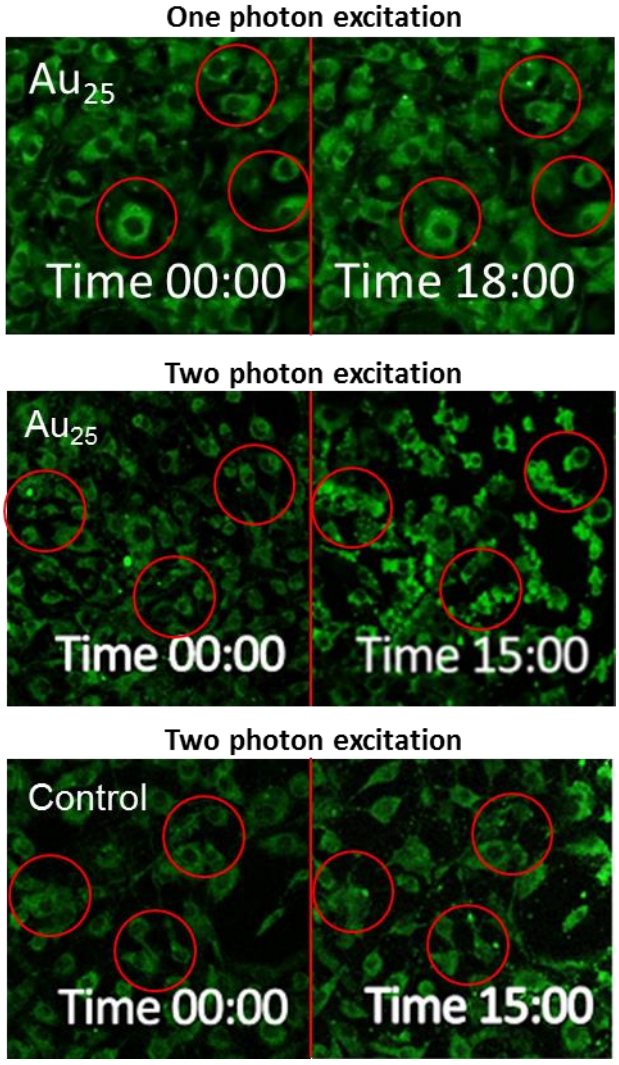

Figure 5.7. Comparison of one- and two-photon excited fluorescence microscopy images of NIH/3T3 mouse fibroblast cells with 400 µg/mL $Au_{25}(GSH)_{18}$. Increase in fluorescence intensity is due to NADH, converted from NAD^+.

5.6 Conclusion

In conclusion, HA/V metal clusters present the superior properties in comparison to conventional dye photosensitizers and plasmonic nanoparticles for $^1O_2$ generation due to their enhanced population in the triplet excited states. Additionally, nanoclusters at the transition between bulk and quantum size exhibit quantum confinement effects that can be enhanced by the localized plasmon resonance within the nanocluster. Effective PDT in cells was illustrated by two-photon excitation of the nanoclusters. Our results indicate that the absorption cross section-to-volume ratio, in other words, the aspect ratio for photons absorption, is an important factor for high $^1O_2$ generation in metal nanoclusters as it means more population to triplet states.

5.7 References

(1) Zhang, G.; Chen, L.; Guo, X.; Khan, A.; Gu, Y.; Gu, N. Nanoparticle-Mediated Drug Delivery Systems (DDS) in the Central Nervous System. *Curr. Org. Chem.* **2016**, *21*, 272–283.

(2) Jain, P. K.; Huang, X.; El-Sayed, I. H.; El-Sayed, M. A. Noble Metals on the Nanoscale: Optical and Photothermal Properties and Some Applications in Imaging, Sensing, Biology, and Medicine. *Acc. Chem. Res.* **2008**, *41*, 1578–1586.

(3) Roy Chowdhury, M.; Schumann, C.; Bhakta-Guha, D.; Guha, G. Cancer Nanotheranostics: Strategies, Promises and Impediments. *Biomed. Pharmacother.* **2016**, *84*, 291–304.

(4) Kravets, V.; Almemar, Z.; Jiang, K.; Culhane, K.; Machado, R.; Hagen, G.; Kotko, A.; Dmytruk, I.; Spendier, K.; Pinchuk, A. Imaging of Biological Cells Using Luminescent Silver Nanoparticles. *Nanoscale Res. Lett.* **2016**, *11*, 30.

(5) Lehman, S. E.; Morris, A. S.; Mueller, P. S.; Salem, A. K.; Grassian, V. H.; Larsen, S. C. Silica Nanoparticle-Generated ROS as a Predictor of Cellular Toxicity: Mechanistic Insights and Safety by Design. *Environ. Sci. Nano* **2016**, *3*, 56–66.

(6) Liu, Z.; Ran, X.; Liu, J.; Du, Y.; Ren, J.; Qu, X. Non-Toxic Lead Sulfide Nanodots as Efficient Contrast Agents for Visualizing Gastrointestinal Tract. *Biomaterials* **2016**, *100*, 17–26.

(7) Yaghini, E.; Turner, H. D.; Le Marois, A. M.; Suhling, K.; Naasani, I.; MacRobert, A. J. In Vivo Biodistribution Studies and Ex Vivo Lymph Node Imaging Using Heavy Metal-Free Quantum Dots. *Biomaterials* **2016**, *104*, 182–191.

(8) Harrington, W. N.; Haji, M. R.; Galanzha, E. I.; Nedosekin, D. A.; Nima, Z. A.; Watanabe, F.; Ghosh, A.; Biris, A. S.; Zharov, V. P. Photoswitchable Non-Fluorescent Thermochromic Dye-Nanoparticle Hybrid Probes. *Sci. Rep.* **2016**, *6*, 36417.

(9) Mroz, P.; Yaroslavsky, A.; Kharkwal, G. B.; Hamblin, M. R. Cell Death Pathways in Photodynamic Therapy of Cancer. *Cancers (Basel).* **2011**, *3*, 2516–2539.

(10) Gomes, A.; Fernandes, E.; Lima, J. L. F. C. Fluorescence Probes Used for Detection of Reactive Oxygen Species. *J. Biochem. Biophys. Methods* **2005**, *65*, 45–80.

(11) Dougherty, T. J.; Gomer, C. J.; Henderson, B. W.; Jori, G.; Kessel, D.; Korbelik, M.; Moan, J.; Peng, Q. Photodynamic Therapy. *JNCI J. Natl. Cancer Inst.* **1998**, *90*, 889–905.

(12) Derosa, M. C.; Crutchley, R. J. Photosensitized Singlet Oxygen and Its Applications. *Coord. Chem. Rev.* **2002**, *233–234*, 351–371.

(13) Sando, G. M.; Berry, A. D.; Owrutsky, J. C. Ultrafast Studies of Gold, Nickel, and Palladium Nanorods. *J. Chem. Phys.* **2007**, *127*, 74705.

(14) Hartland, G. V. Coherent Excitation of Vibrational Modes in Metallic Nanoparticles. *Annu. Rev. Phys. Chem.* **2006**, *57*, 403–430.

(15) Huang, X.; Jain, P. K.; El-Sayed, I. H.; El-Sayed, M. A. Determination of the Minimum Temperature Required for Selective Photothermal Destruction of Cancer Cells with the Use of Immunotargeted Gold Nanoparticles. *Photochem. Photobiol.* **2006**, *82*, 412.

(16) Dreaden, E. C.; El-Sayed, M. A. Detecting and Destroying Cancer Cells in More than One Way with Noble Metals and Different Confinement Properties on the Nanoscale. *Acc. Chem. Res.* **2012**, *45*, 1854–1865.

(17) Vankayala, R.; Sagadevan, A.; Vijayaraghavan, P.; Kuo, C.-L.; Hwang, K. C. Metal Nanoparticles Sensitize the Formation of Singlet Oxygen. *Angew. Chemie Int. Ed.* **2011**, *50*, 10640–10644.

(18) Smith, L.; Kuncic, Z.; Ostrikov, K. (Ken); Kumar, S. Nanoparticles in Cancer Imaging and Therapy. *J. Nanomater.* **2012**, *2012*, 1–7.

(19) Yamaguchi, S.; Kobayashi, H.; Narita, T.; Kanehira, K.; Sonezaki, S.; Kubota, Y.; Terasaka, S.; Iwasaki, Y. Novel Photodynamic Therapy Using Water-Dispersed TiO2-Polyethylene Glycol Compound: Evaluation of Antitumor Effect on Glioma

Cells and Spheroids In Vitro. *Photochem. Photobiol.* **2010**, *86*, 964–971.

(20) Devadas, M. S.; Kim, J.; Sinn, E.; Lee, D.; Goodson III, T.; Ramakrishna, G. Unique Ultrafast Visible Luminescence in Monolayer-Protected Au 25 Clusters. *J. Phys. Chem. C* **2010**, *114*, 22417–22423.

(21) Yau, S. H.; Varnavski, O.; Goodson III, T. An Ultrafast Look at Au Nanoclusters. *Acc. Chem. Res.* **2013**, *46*, 1506–1516.

(22) Varnavski, O.; Ramakrishna, G.; Kim, J.; Lee, D.; Goodson III, T. Critical Size for the Observation of Quantum Confinement in Optically Excited Gold Clusters. *J. Am. Chem. Soc.* **2010**, *132*, 16–17.

(23) Huang, K.; Ma, H.; Liu, J.; Huo, S.; Kumar, A.; Wei, T.; Zhang, X.; Jin, S.; Gan, Y.; Wang, P. C.; *et al.* Size-Dependent Localization and Penetration of Ultrasmall Gold Nanoparticles in Cancer Cells, Multicellular Spheroids, and Tumors *in Vivo*. *ACS Nano* **2012**, *6*, 4483–4493.

(24) Retnakumari, A.; Setua, S.; Menon, D.; Ravindran, P.; Muhammed, H.; Pradeep, T.; Nair, S.; Koyakutty, M. Molecular-Receptor-Specific, Non-Toxic, near-Infrared-Emitting Au Cluster-Protein Nanoconjugates for Targeted Cancer Imaging. *Nanotechnology* **2010**, *21*, 55103.

(25) Ramakrishna, G.; Varnavski, O.; Kim, J.; Lee, D.; Goodson III, T. Quantum-Sized Gold Clusters as Efficient Two-Photon Absorbers. *J. Am. Chem. Soc.* **2008**, *130*, 5032–5033.

(26) Varnavski, O. P.; Ranasinghe, M.; Yan, X.; Bauer, C. A.; Chung, S.-J.; Perry, J. W.; Marder, S. R.; Goodson III, T. Ultrafast Energy Migration in Chromophore Shell-Metal Nanoparticle Assemblies. *J. Am. Chem. Soc.* **2006**, *128*, 10988–10989.

(27) Ding, C.; Tian, Y. Gold Nanocluster-Based Fluorescence Biosensor for Targeted Imaging in Cancer Cells and Ratiometric Determination of Intracellular pH. *Biosens. Bioelectron.* **2015**, *65*, 183–190.

(28) Zheng, J.; Zhou, C.; Yu, M.; Liu, J. Different Sized Luminescent Gold Nanoparticles. *Nanoscale* **2012**, *4*, 4073.

(29) Jin, R. Atomically Precise Metal Nanoclusters: Stable Sizes and Optical Properties. *Nanoscale* **2015**, *7*, 1549–1565.

(30) Brust, M.; Walker, M.; Bethell, D.; Schiffrin, D. J.; Whyman, R. Synthesis of Thiol-Derivatised Gold Nanoparticles in a Two-Phase Liquid-Liquid System. *J. Chem. Soc., Chem. Commun.* **1994**, 801–802.

(31) Zhang, X.-D.; Wu, D.; Shen, X.; Liu, P.-X.; Fan, F.-Y.; Fan, S.-J. In Vivo Renal Clearance, Biodistribution, Toxicity of Gold Nanoclusters. *Biomaterials* **2012**, *33*, 4628–4638.

(32) Yamamoto, M.; Osaka, I.; Yamashita, K.; Hasegawa, H.; Arakawa, R.; Kawasaki, H. Effects of Ligand Species and Cluster Size of Biomolecule-Protected Au Nanoclusters on Efficiency of Singlet-Oxygen Generation. *J. Lumin.* **2016**, *180*, 315–320.

(33) Das, T.; Ghosh, P.; Shanavas, M. S.; Maity, A.; Mondal, S.; Purkayastha, P.; Johnson, B. F. G.; Lambert, R. M.; Jahnen-Dechent, W.; Hsiao, J. K.; *et al.* Protein-Templated Gold Nanoclusters: Size Dependent Inversion of Fluorescence Emission in the Presence of Molecular Oxygen. *Nanoscale* **2012**, *4*, 6018.

(34) Shibu, E. S.; Sugino, S.; Ono, K.; Saito, H.; Nishioka, A.; Yamamura, S.; Sawada, M.; Nosaka, Y.; Biju, V. Singlet-Oxygen-Sensitizing Near-Infrared-Fluorescent Multimodal Nanoparticles. *Angew. Chemie Int. Ed.* **2013**, *52*, 10559–10563.

(35) Lv, R.; Yang, P.; He, F.; Gai, S.; Yang, G.; Dai, Y.; Hou, Z.; Lin, J. An Imaging-Guided Platform for Synergistic Photodynamic/photothermal/chemo-Therapy with pH/temperature-Responsive Drug Release. *Biomaterials* **2015**, *63*, 115–127.

(36) Qian, H.; Jin, R. Ambient Synthesis of Au $_{144}$ (SR) $_{60}$ Nanoclusters in Methanol. *Chem. Mater.* **2011**, *23*, 2209–2217.

(37) Wu, Z.; Suhan, J.; Jin, R. One-Pot Synthesis of Atomically Monodisperse, Thiol-Functionalized Au 25 Nanoclusters. *J. Mater. Chem.* **2009**, *19*, 622–626.

(38) Yau, S. H.; Ashenfelter, B.; Desireddy, A.; Ashwell, A. P.; Varnavski, O.; Schatz, G. C.; Bigioni, T.; Goodson III, T. Optical Properties and Structural Relationships of the Silver Nanoclusters Ag32(SG)19 and Ag15(SG)11. *J. Phys. Chem. C* **2017**, *121*, 1349–1361.

(39) Guo, J.; Kumar, S.; Bolan, M.; Desireddy, A.; Bigioni, T. P.; Griffith, W. P. Mass Spectrometric Identification of Silver Nanoparticles: The Case of Ag $_{32}$ (SG) $_{19}$. *Anal. Chem.* **2012**, *84*, 5304–5308.

(40) Kawasaki, H.; Kumar, S.; Li, G.; Zeng, C.; Kauffman, D. R.; Yoshimoto, J.; Iwasaki, Y.; Jin, R. Generation of Singlet Oxygen by Photoexcited Au 25 (SR) 18 Clusters. *Chem. Mater.* **2014**, *26*, 2777–2788.

(41) Wang, P.; Qin, F.; Zhang, Z.; Cao, W. Quantitative Monitoring of the Level of Singlet Oxygen Using Luminescence Spectra of Phosphorescent Photosensitizer. *Opt. Express* **2015**, *23*, 22991.

(42) Ohyashiki, T.; Nunomura, M.; Katoh, T. Detection of Superoxide Anion Radical in Phospholipid Liposomal Membrane by Fluorescence Quenching Method Using 1,3-Diphenylisobenzofuran. *Biochim. Biophys. Acta - Biomembr.* **1999**, *1421*, 131–139.

(43) Wozniak, M.; Tanfani, F.; Bertoli, E.; Zolese, G.; Antosiewicz, J. A New Fluorescence Method to Detect Singlet Oxygen inside Phospholipid Model

Membranes. *Biochim. Biophys. Acta - Lipids Lipid Metab.* **1991**, *1082*, 94–100.

(44) Zhang, X.-F.; Li, X. The Photostability and Fluorescence Properties of Diphenylisobenzofuran. *J. Lumin.* **2011**, *131*, 2263–2266.

(45) Chadwick, S. J.; Salah, D.; Livesey, P. M.; Brust, M.; Volk, M. Singlet Oxygen Generation by Laser Irradiation of Gold Nanoparticles. *J. Phys. Chem. C* **2016**, *120*, 10647–10657.

(46) Link, S.; El-Sayed, M. A. Shape and Size Dependence of Radiative, Non-Radiative and Photothermal Properties of Gold Nanocrystals. *Int. Rev. Phys. Chem.* **2000**, *19*, 409–453.

(47) Huang, X.; Qian, W.; El-Sayed, I. H.; El-Sayed, M. A. The Potential Use of the Enhanced Nonlinear Properties of Gold Nanospheres in Photothermal Cancer Therapy. *Lasers Surg. Med.* **2007**, *39*, 747–753.

(48) Negishi, Y.; Nakazaki, T.; Malola, S.; Takano, S.; Niihori, Y.; Kurashige, W.; Yamazoe, S.; Tsukuda, T.; Häkkinen, H. A Critical Size for Emergence of Nonbulk Electronic and Geometric Structures in Dodecanethiolate-Protected Au Clusters. *J. Am. Chem. Soc.* **2015**, *137*, 1206–1212.

(49) Yi, C.; Tofanelli, M. A.; Ackerson, C. J.; Knappenberger, K. L. Optical Properties and Electronic Energy Relaxation of Metallic Au $_{144}$ (SR) $_{60}$ Nanoclusters. *J. Am. Chem. Soc.* **2013**, *135*, 18222–18228.

(50) Mustalahti, S.; Myllyperkiö, P.; Lahtinen, T.; Salorinne, K.; Malola, S.; Koivisto, J.; Häkkinen, H.; Pettersson, M. Ultrafast Electronic Relaxation and Vibrational Cooling Dynamics of Au $_{144}$ (SC $_{2}$ H $_{4}$ Ph) $_{60}$ Nanocluster Probed by Transient Mid-IR Spectroscopy. *J. Phys. Chem. C* **2014**, *118*, 18233–18239.

(51) Negishi, Y.; Nobusada, K.; Tsukuda, T. Glutathione-Protected Gold Clusters Revisited: Bridging the Gap between gold(I)-Thiolate Complexes and Thiolate-Protected Gold Nanocrystals. *J. Am. Chem. Soc.* **2005**, *127*, 5261–5270.

(52) Ashenfelter, B. A.; Desireddy, A.; Yau, S. H.; Goodson III, T.; Bigioni, T. P. Fluorescence from Molecular Silver Nanoparticles. *J. Phys. Chem. C* **2015**, *119*, 20728–20734.

(53) Paul, P.; Mati, S. S.; Bhattacharya, S. C.; Suresh Kumar, G. Exploring the Interaction of Phenothiazinium Dyes Methylene Blue, New Methylene Blue, Azure A and Azure B with tRNA Phe : Spectroscopic, Thermodynamic, Voltammetric and Molecular Modeling Approach. *Phys. Chem. Chem. Phys.* **2017**, *19*, 6636–6653.

(54) Extinction Coefficient of Gold Nanoparticles with Different Sizes and Different Capping Ligands. *Colloids Surfaces B Biointerfaces* **2007**, *58*, 3–7.

(55) Ronzani, F.; Trivella, A.; Arzoumanian, E.; Blanc, S.; Sarakha, M.; Richard, C.; Oliveros, E.; Lacombe, S.; Richard, C.; Lacombe, S. Comparison of the Photophysical Properties of Three Phenothiazine Derivatives: Transient Detection and Singlet Oxygen Production. *Photochem. Photobiol. Sci.* **2013**, *12*, 2160.

(56) Link, S.; Beeby, A.; FitzGerald, S.; El-Sayed, M. A.; Schaaff, T. G.; Whetten, R. Visible to Infrared Luminescence from a 28-Atom Gold Cluster. *J. Phys. Chem. B* **2002**, *106*, 3410–3415.

(57) Wen, X.; Yu, P.; Toh, Y.-R.; Hsu, A.-C.; Lee, Y.-C.; Tang, J. Fluorescence Dynamics in BSA-Protected Au $_{25}$ Nanoclusters. *J. Phys. Chem. C* **2012**, *116*, 19032–19038.

(58) Koivisto, J.; Malola, S.; Kumara, C.; Dass, A.; Häkkinen, H.; Pettersson, M. Experimental and Theoretical Determination of the Optical Gap of the Au $_{144}$ (SC $_{2}$ H $_{4}$ Ph) $_{60}$ Cluster and the (Au/Ag) $_{144}$ (SC $_{2}$ H $_{4}$ Ph) $_{60}$ Nanoalloys. *J. Phys. Chem. Lett.* **2012**, *3*, 3076–3080.

(59) Miller, S. A.; Womick, J. M.; Parker, J. F.; Murray, R. W.; Moran, A. M. Femtosecond Relaxation Dynamics of Au 25 L 18 − Monolayer-Protected Clusters. *J. Phys. Chem. C* **2009**, *113*, 9440–9444.

(60) Thomas, M.; Greffet, J.-J.; Carminati, R.; Arias-Gonzalez, J. R. Single-Molecule Spontaneous Emission close to Absorbing Nanostructures. *Appl. Phys. Lett.* **2004**, *85*, 3863.

(61) Baffou, G.; Rigneault, H. Femtosecond-Pulsed Optical Heating of Gold Nanoparticles. *Phys. Rev. B* **2011**, *84*, 35415.

(62) Huang, X.; El-Sayed, M. A. Plasmonic Photo-Thermal Therapy (PPTT). *Alexandria J. Med.* **2011**, *47*, 1–9.

(63) Yau, S. H.; Abeyasinghe, N.; Orr, M.; Upton, L.; Varnavski, O.; Werner, J. H.; Yeh, H.-C.; Sharma, J.; Shreve, A. P.; Martinez, J. S.; *et al.* Bright Two-Photon Emission and Ultra-Fast Relaxation Dynamics in a DNA-Templated Nanocluster Investigated by Ultra-Fast Spectroscopy. *Nanoscale* **2012**, *4*, 4247–4254.

(64) He, F.; Yang, G.; Yang, P.; Yu, Y.; Lv, R.; Li, C.; Dai, Y.; Gai, S.; Lin, J. A New Single 808 Nm NIR Light-Induced Imaging-Guided Multifunctional Cancer Therapy Platform. *Adv. Funct. Mater.* **2015**, *25*, 3966–3976.

(65) Abeyasinghe, N.; Kumar, S.; Sun, K.; Mansfield, J. F.; Jin, R.; Goodson III, T. Enhanced Emission from Single Isolated Gold Quantum Dots Investigated Using Two-Photon-Excited Fluorescence Near-Field Scanning Optical Microscopy. *J. Am. Chem. Soc.* **2016**, *138*, 16299–16307.

(66) Ding, Y.; Li, C. Dual-Color Multiple-Particle Tracking at 50-Nm Localization and over 100-Mm Range in 3D with Temporal Focusing Two-Photon Microscopy.

Biomed. Opt. Express **2016**, *7*, 4187–4197.

(67) Griesbeck, S.; Zhang, Z.; Gutmann, M.; Lühmann, T.; Edkins, R. M.; Clermont, G.; Lazar, A. N.; Haehnel, M.; Edkins, K.; Eichhorn, A.; *et al.* Water-Soluble Triarylborane Chromophores for One- and Two-Photon Excited Fluorescence Imaging of Mitochondria in Cells. *Chem. - A Eur. J.* **2016**, *22*, 14701–14706.

(68) Doan, P.; Pitter, D. R. G.; Kocher, A.; Wilson, J. N.; Goodson, T. A New Design Strategy and Diagnostic to Tailor the DNA-Binding Mechanism of Small Organic Molecules and Drugs. *ACS Chem. Biol.* **2016**, *11*, 3202–3213.

Chapter 6

Summary and Future Direction

6.1 Optical characterization of solid state metal nanoclusters

As a result of their strong quantum confinement effects, metal nanoclusters show unusual optical, electronic, magnetic and catalytic properties. Our group and several others have previously focused on the investigation of the optical properties of metal nanoclusters in the solution phase by ultrafast spectroscopy.[1–9] In this chapter, the optical properties of a series of metal nanocluster films of varying inter-cluster distances are presented. Emphasis was given on the effect of decreasing the inter-cluster distance on the solid state photoluminescence and two-photon absorption. The Au_{25} was used as the model nanocluster for the solid state optical investigations because it is a well-studied nanocluster.[6,8,10]

Optical quality films were produced with the $Au_{25}(SC_6H_{13})_{18}$ nanocluster in a polystyrene matrix at different inter-cluster distances. The metal nanocluster retains its core's electronic structure as evidenced in the absorption spectra. Furthermore, the optical spectrum of the nanocluster film indicates that solid state nanoclusters do not form aggregation. The photoluminescence and two-photon absorption cross sections of solid state nanoclusters are enhanced with respect to the solution phase nanoclusters due to a strong dipole coupling between the nanoclusters in the solid state. The enhanced

optical properties of metal nanoclusters indicate that they can be potentially used as materials for the fabrication of small optoelectronic and magnetic devices. They may also be used as fine protective coatings for optical limiting applications due to the two-photon absorption enhancement.

6.2 The synthesis and optical characterization of chromophore-nanocluster oligomers

As the interest in small metal topologies increases, the use of these materials continues to grow as well. It is now clear that metal nanocluster have unique optical properties due to the quantum confinement effect. There is a great interest in the possibility of collective nanocluster properties in oligomers and larger networks.[11–14] Theoretical insights into the metal cluster assemblies indicate that they would exhibit collective properties and novel properties.[15,16]

There are two ways to achieve nanocluster assemblies: one by direct linkage between the metal nanoclusters through metal-metal bonds, two by using an external linker. The advantage of using an external linker is the ability to add functionality to the metal nanoclusters. In the work presented in this thesis, a chromophore, 4,4'-thiodibenzenedithiol (TBT), was used as the linker to link and to functionalize the Au_{25} nanoclusters. An emphasis was given on the correlation of chromophore-Au_{25} nanocluster oligomer size and molecular geometry with their linear and non-linear optical properties compared to single Au_{25} nanoclusters.

The optical absorption of the chromophore-Au_{25} nanocluster oligomers suggests an increase in the transition dipole moment compared to single Au_{25} nanoclusters. The chromophore-Au_{25} nanocluster oligomers also showed two-photon absorption cross

section enhancement of up to 68 times due to the strong dipole coupling between the nanoclusters. An analysis on the molecular geometry between Au_{25}-chromophore-Au_{25} revealed that it has a bent molecular geometry around a central electronegative sulfur atom. Due to this geometry, the chromophore-Au_{25} nanocluster oligomers have higher polarizability compared to a monomer Au_{25}.

Furthermore, the chromophore-nanocluster oligomers show strong dipole coupling between the chromophore and the nanocluster. Such functionality is not found in cluster assemblies with fused metal cores as the linkage type. The nanoclusters in the chromophore-Au_{25} nanocluster oligomers have a common energy state due to the shared chromophore – a common surface state. Excited state dynamics of the oligomers show long excited state lifetimes compared to single Au_{25}. The long excited state lifetime is due to the contribution by each cluster in the oligomer. The nanocluster's core energy transfer to a common surface state. Thus it is expected that the near-IR emission of the oligomers should enhance but due to the mix ligands distribution on the oligomers, fluorescence enhancement was not observed. The effect of nanocluster's core energy transfer to the surface states and the effect of ligands on the emission quantum yield are well documented.[4,17,18]

Overall, the collective properties of nanoclusters in an assembly can be used in a wide variety of applications. For instance, long triplet excited state lifetimes can be employed in photodynamic therapy. If large networks or crystals of nanoclusters can be made, they can be used as optics elements or devices, or they may be used as fluorescent coatings for imaging or as protective coatings for optical limiting.

6.3 Metal nanoclusters as two-photon photodynamic therapy agents

The creation of nanomaterials has led to new applications in biology and medicine such as photodynamic therapy (PDT).[19-22] Metal nanoclusters have emerged as new candidates for PDT to replace existing PDT agents due to their excellent photostability, precise targeting, low toxicity and quantum confinement effects.[6,23–25] Furthermore, they have been shown to be effective PDT photosensitizers for singlet oxygen generation.[26–29] Chapter 5 aimed to understand the singlet oxygen generation rate of metal nanoclusters of different sizes and correlate the rate to their electronic properties. It is also the aim of this work to demonstrate the efficiency and viability of using metal nanoclusters for two-photon PDT in live cells.

Three different metal nanoclusters were investigated, Au_{25}, Ag_{32} and Au_{144}. The Au_{144} showed a singlet oxygen generation rate that was twice as high as the other clusters. An analysis on the electronic properties of the Au_{144} indicates that the core-localized plasmon resonance enhances the triplet excited state population in Au_{144}. Additionally, the Au_{144} show higher absorption-to-volume ratio, comparable to that of plasmonic nanoparticles, but due to the presence of triplet states, the Au_{144} possesses both properties which enhances the singlet oxygen generation rate.

Finally, due to the high two-photon absorption cross sections of metal nanoclusters, two-photon excitation can be used as a safer alternative to PDT. Additionally, using near-IR excitation will allow deep tissue penetration. Live cells imaging of metal nanoclusters in action reveals that two-photon excitation resulted in fast PDT as evidenced by the rapid cell death. One-photon excitation, on the other hand, did not show PDT within the

monitored time frame. Thus this work highlight that high absorption-to-volume ratio metal nanoclusters are new promising candidates for effective two-photon PDT.

6.4 Future direction: Non-linear optical investigation of highly fluorescent bimetallic Au@Ag nanoclusters

Metal nanoclusters are quantum sized (< 2 nm) nanoparticles which show molecular-like properties.[6,30,31] Over the years, research effort has been devoted to the understanding of the fundamental science behind these nanoclusters due the importance of this size regime which bridge between the molecular and metallic systems.[32–35] In particular, the structure-function relationship has been a question of scientific importance.[1,8,31,36] However, it is only partially clear the relationship between size evolution and electronic properties. Since there are large differences in the structure between metal nanoclusters, understanding the size-property correlation is challenging.[8] Jin et al discovered recently that a series of gold nanoclusters exhibit periodicity in both their structure and optical properties.[31] Although this is the first step in the direction to understanding size-property evolution, the challenge still remains to encompass all the known stable sizes nanoclusters into a clear size-property picture.

On the other hand, the structure-property relationship is now better understood due to the successful crystallization of metal nanoclusters and structural determination, and the combined experimental and theoretical studies of their electronic properties.[1,6,37,38] It is known, for example, that the electronic transitions in $Au_{25}(SR)_{18}$ nanoclusters are due to the intra-bands and inter-bands transition of the Au_{13} icosahedral core.[37,39,40] Ultrafast spectroscopic techniques allowed us to understand the intra-molecular energy transfer property and origin of fluorescence of metal nanoclusters.[1,4–7,41]

The molecular-like properties of metal nanoclusters that are most interesting for applications are fluorescence and two-photon absorption (TPA).[42–46] They have found applications in biomedical fields such as sensing and imaging which rely on the fluorescence property of the nanoclusters.[47,48] However, the fluorescence quantum yields of most metal nanoclusters are low.[49–51,17] Motivated by the useful applications of nanocluster's fluorescence, synthetic efforts have been focused on preparing highly fluorescent metal nanoclusters.[9,36,49–53] One interesting discovery is the phenomenon of aggregation-induced emission (AIE) of the precursors of gold nanoclusters, Au(I)-thiolates.[49] Later, Xie et al expanded this discovery to bimetallic gold-silver nanoclusters.[51] Silver nanoclusters are known to show enhanced optical properties when compared to gold nanoclusters but due to their lower colloidal stability, silver nanoclusters have yet to receive the same research interest as gold nanoclusters.[1,36] Nevertheless, silver has been used as a dopant in gold nanoclusters and the resulting bimetallic nanoclusters have shown synergistic effects from the two metal atoms.[54]

With the collaboration of professor Jianping Xie, we aim to explore the TPA property of the highly fluorescent $Au_x@Ag_{(1-7)}$ nanoclusters and compare them to the parental Au_x nanoclusters. Gold nanoclusters have shown to be efficient two-photon absorbers compared to larger particles which makes them good candidates for two-photon imaging.[2] On the other hand, silver nanoclusters, although they have higher emission quantum yields than gold nanoclusters, have very low TPA cross sections.[1] Unlike traditional Au-Ag alloy nanoclusters, where the Ag atom is usually a dopant in the Au nanocluster's structure, the Au@Ag nanoclusters synthesized by our collaborators

maintain an intact Au nanocluster structure with Ag^{1+} ions coordinating the sulfur atoms on the Au nanocluster's staple motifs.[51]

Shown in Figure 6.1. is the steady state absorption of the Au@Ag nanoclusters compared to the monometallic Au nanoclusters. The Au@Ag nanoclusters show higher absorption coefficients, which indicate that they have higher transition dipole moments compared to the monometallic Au nanoclusters. It is therefore expected that the Au@Ag nanoclusters would have enhanced two-photon absorption. The two-photon absorption cross section can be approximated by equation 6.1, where C is a constant; μ are the transition dipole moment from the ground state to the intermediate state, and from the intermediate state to a final state; E is the energy gap between the ground state and intermediate state and Γ is the HWHM of the two-photon absorption band.[55]

$$\sigma \approx C \frac{\mu_{gi}^2 \mu_{if}^2}{\left(\frac{E_{gi}}{h\nu} - 1\right)^2 \Gamma} \tag{6.1}$$

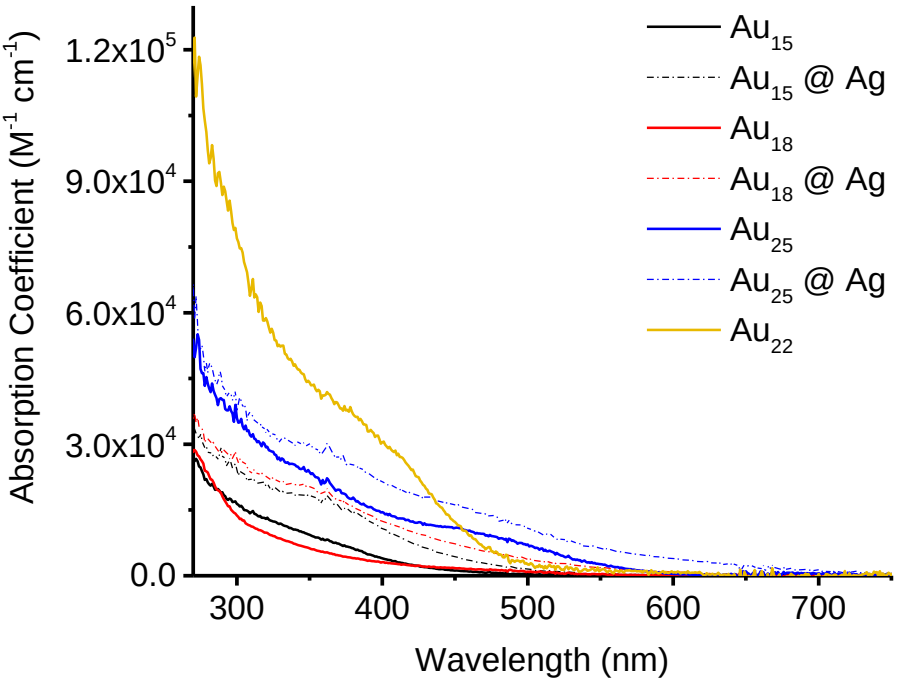

Figure 6.1. Steady state absorption of Au@Ag nanoclusters compared to their parental Au nanoclusters and the highly luminescent monometallic Au_{22} nanocluster.

The two-photon absorption cross sections of Au@Ag and parental Au nanoclusters were obtained by the two-photon excited fluorescence method. The cross sections were normalized by dividing them by the number of metal atoms in the cluster (Figure 6.2). Since the Au@Ag nanoclusters contain a distribution of 1 to 7 Ag^{1+} atoms, the cross sections are displayed as a range. The median of the range is displayed in the figure. Taking into account the standard deviation of the median, the Au_{15}@Ag and Au_{18}@Ag appear to have comparable TPA cross sections. The larger cluster, Au_{25}@Ag has a lower TPA cross section per atom by 2 orders of magnitude. This observation is in line with our previous observations that the TPA cross section per atom of metal nanoclusters increases with decreasing cluster size due to the strong quantum confinement effect.[2]

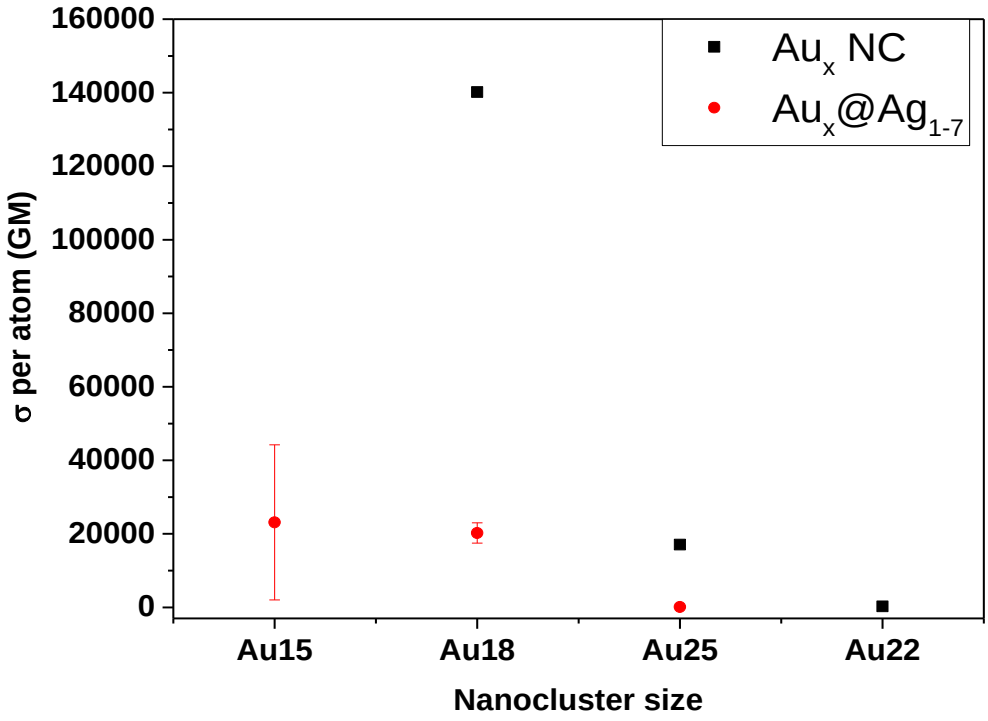

Figure 6.2. Two-photon absorption cross section per atom of the bimetallic Au@Ag nanoclusters compared to the parental Au nanoclusters at 800 nm.

However, the TPA cross sections of the Au@Ag nanoclusters are lower compared to the parental Au nanoclusters despite the higher transition dipole moment of the Au@Ag nanoclusters. It may be due to the fact that Ag has lower electron count than Au, which results in Ag nanoclusters having lower TPA cross sections than Au nanoclusters.[1] However, the Au atoms are not replaced by the Ag^{1+} ions in Au@Ag nanoclusters. It is not clear how the Ag^{1+} ions are distributed on the surface of the Au nanoclusters, therefore, it is likely that there is symmetry breaking which may affect the TPA cross sections (Figure 6.3). In fact, the effects of molecular symmetry on the TPA cross sections have been demonstrated previously in our group in multi-annulene molecules.[56] The molecules exhibiting the highest symmetry were shown to have larger TPA cross sections by a factor of 10-100. According to equation 6.1, the TPA cross section is also influenced by the two-photon absorption spectral width. A future direction on this project is to analyze the two-photon absorption of these clusters at different excitation wavelengths. Two-photon absorption spectra can be obtained in this manner by plotting the TPA cross sections against the absorption wavelengths. Our group has an Opal – femtosecond synchronously pumped optical parametric oscillator (SPPO) by Spectra Physics which can be used for two-photon excited fluorescence measurements at different visible to IR wavelengths of excitation. By analyzing the two-photon absorption spectral width between Au@Ag and Au nanoclusters, we will be able to provide a more complete explanation to the observed TPA cross section trend. Lastly, a highly fluorescent Au_{22} nanocluster was also used to compare to the Au@Ag nanoclusters. The Au_{22} nanocluster have a TPA cross section per atom similar to that of Au_{25}@Ag. The

Au_{22} nanocluster is non-spherical, but is symmetric on one axis.[9] It is therefore a non-centrosymmetric molecule.

Additionally, the excited state dynamics of the bimetallic nanoclusters will be analyzed by time-correlated single photon counting and transient absorption spectroscopy. As seen in equation 6.1, the TPA cross section is strongly influenced by the transition dipole moments between the ground state and the intermediate state, and the transition dipole moment between the intermediate state and final excited state (Figure 6.3). Analysis of the excited state dynamics of the bimetallic nanoclusters will reveal information regarding the excited-state transition dipole moment.[56] Together with the transition dipole moment of the ground state (Figure 6.1), the μ_{gi} and μ_{if} terms can be compared to understand the effect of symmetry of the bimetallic nanoclusters on their TPA cross sections.

This work is already in progress. Two undergraduate researchers in our group will be collaborating on the optical investigations of these materials as well. This work encompasses five different optical characterization techniques and is an excellent opportunity to introduce the students to ultrafast spectroscopy. A manuscript is in preparation for this work.

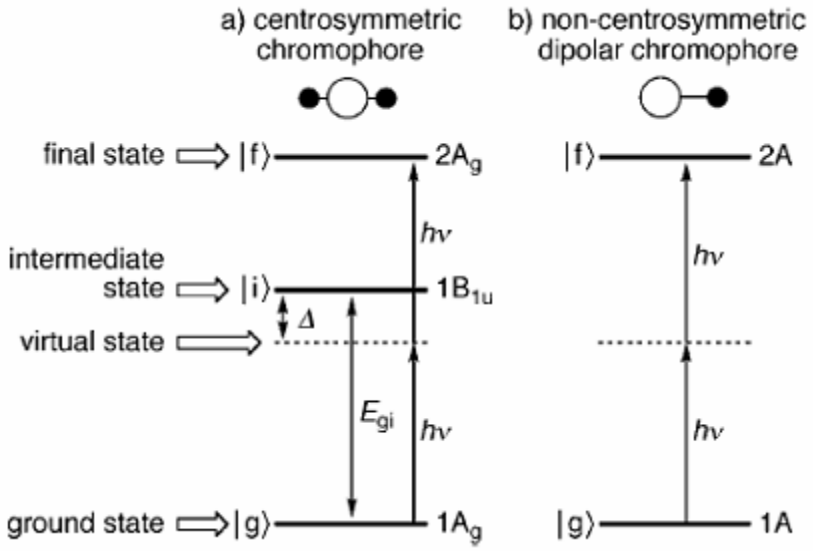

Figure 6.3. Energy level diagram of two-photon absorption for centrosymmetric and non-centrosymmetric molecules.[57,58]

6.5 Functionalized metal nanocluster-conjugated polymer films

As a continuation to the work on solid state metal nanoclusters embedded in polymer host, one particular direction that is worthy of pursuit is the fabrication of metal nanoclusters-conjugated polymer films and their optical characterization. For practical applications, metal nanoclusters are used in conjunction with other functional materials for the construction of devices.[59–62] Metal nanoclusters have been shown to couple strongly with organic chromophores and fluorescent proteins.[63–67] Non-radiative energy transfer and electron transfer between a metal nanocluster and a chromophore have been observed. As shown in chapter 3, the fluorescence and two-photon absorption of metal nanoclusters in the solid state are significantly enhanced compared to the solution phase, further demonstrating that metal nanoclusters are promising materials for the fabrication of miniature devices. In particular, the fluorescence of metal nanoclusters is of interest for both the fundamental science (e.g. origin of fluorescence) and applications. It's been shown that the fluorescence of the metal nanoclusters is influenced by the ligand-to-metal

charge transfer (LMCT), metal core and staple motifs electron-phonon coupling, cluster-cluster coupling if the inter-cluster distance is within the resonance energy transfer distance, and aggregation-induced emission.[17,50,68,69] Therefore, a systematic study on the modulation of the optical properties of metal nanoclusters and conjugated polymer in a nanocluster-polymer film will allow us to understand the photophysical properties of these coupled materials for applications in devices. This project is currently lead by a graduate student in the group. As a first step in this direction, the optical properties of a series of benzodifuran (BDF) and diketopyrrolopyrrole (DPP) polymer films are currently being investigated.

6.6 References

(1) Yau, S. H.; Ashenfelter, B.; Desireddy, A.; Ashwell, A. P.; Varnavski, O.; Schatz, G. C.; Bigioni, T.; Goodson III, T. Optical Properties and Structural Relationships of the Silver Nanoclusters Ag32(SG)19 and Ag15(SG)11. *J. Phys. Chem. C* **2017**, *121*, 1349–1361.

(2) Ramakrishna, G.; Varnavski, O.; Kim, J.; Lee, D.; Goodson III, T. Quantum-Sized Gold Clusters as Efficient Two-Photon Absorbers. *J. Am. Chem. Soc.* **2008**, *130*, 5032–5033.

(3) Varnavski, O.; Ramakrishna, G.; Kim, J.; Lee, D.; Goodson III, T. Optically Excited Acoustic Vibrations in Quantum-Sized Monolayer-Protected Gold Clusters. *ACS Nano* **2010**, *4*, 3406–3412.

(4) Devadas, M. S.; Kim, J.; Sinn, E.; Lee, D.; Goodson III, T.; Ramakrishna, G. Unique Ultrafast Visible Luminescence in Monolayer-Protected Au 25 Clusters. *J. Phys. Chem. C* **2010**, *114*, 22417–22423.

(5) Yau, S. H.; Abeyasinghe, N.; Orr, M.; Upton, L.; Varnavski, O.; Werner, J. H.; Yeh, H.-C.; Sharma, J.; Shreve, A. P.; Martinez, J. S.; *et al.* Bright Two-Photon Emission and Ultra-Fast Relaxation Dynamics in a DNA-Templated Nanocluster Investigated by Ultra-Fast Spectroscopy. *Nanoscale* **2012**, *4*, 4247–4254.

(6) Yau, S. H.; Varnavski, O.; Goodson III, T. An Ultrafast Look at Au Nanoclusters. *Acc. Chem. Res.* **2013**, *46*, 1506–1516.

(7) Yau, S. H.; Varnavski, O.; Gilbertson, J. D.; Chandler, B.; Ramakrishna, G.;

Goodson III, T. Ultrafast Optical Study of Small Gold Monolayer Protected Clusters: A Closer Look at Emission. *J. Phys. Chem. C* **2010**, *114*, 15979–15985.

(8) Jin, R. Atomically Precise Metal Nanoclusters: Stable Sizes and Optical Properties. *Nanoscale* **2015**, *7*, 1549–1565.

(9) Yu, Y.; Luo, Z.; Chevrier, D. M.; Leong, D. T.; Zhang, P.; Jiang, D.; Xie, J. Identification of a Highly Luminescent Au22(SG)18 Nanocluster. *J. Am. Chem. Soc.* **2014**, *136*, 1246–1249.

(10) Parker, J. F.; Fields-Zinna, C. A.; Murray, R. W. The Story of a Monodisperse Gold Nanoparticle: Au25L18. *Acc. Chem. Res.* **2010**, *43*, 1289–1296.

(11) Khanna, S. N.; Jena, P. Assembling Crystals from Clusters. *Phys. Rev. Lett.* **1992**, *69*, 1664–1667.

(12) Khanna, S. N.; Jena, P. Atomic Clusters: Building Blocks for a Class of Solids. *Phys. Rev. B* **1995**, *51*, 13705–13716.

(13) Castleman, A. W.; Khanna, S. N. Clusters, Superatoms, and Building Blocks of New Materials. *J. Phys. Chem. C* **2009**, *113*, 2664–2675.

(14) Claridge, S. A.; Castleman, A. W.; Khanna, S. N.; Murray, C. B.; Sen, A.; Weiss, P. S. Cluster-Assembled Materials. *ACS Nano* **2009**, *3*, 244–255.

(15) Liu, L.; Li, P.; Yuan, L.-F.; Cheng, L.; Yang, J. From Isosuperatoms to Isosupermolecules: New Concepts in Cluster Science. *Nanoscale* **2016**, *8*, 12787–12792.

(16) Reber, A. C.; Khanna, S. N.; Castleman, A. W. Superatom Compounds, Clusters, and Assemblies: Ultra Alkali Motifs and Architectures. *J. Phys. Chem. C* **2009**, *113*, 2664–2675.

(17) Wu, Z.; Jin, R. On the Ligand's Role in the Fluorescence of Gold Nanoclusters. *Nano Lett.* **2010**, *10*, 2568–2573.

(18) Wang, S.; Zhu, X.; Cao, T.; Zhu, M. A Simple Model for Understanding the Fluorescence Behavior of Au25 Nanoclusters. *Nanoscale* **2014**, *6*, 5777–5781.

(19) Roy Chowdhury, M.; Schumann, C.; Bhakta-Guha, D.; Guha, G. Cancer Nanotheranostics: Strategies, Promises and Impediments. *Biomed. Pharmacother.* **2016**, *84*, 291–304.

(20) Lucky, S. S.; Soo, K. C.; Zhang, Y. Nanoparticles in Photodynamic Therapy. *Chem. Rev.* **2015**, *115*, 1990–2042.

(21) Mroz, P.; Yaroslavsky, A.; Kharkwal, G. B.; Hamblin, M. R. Cell Death Pathways in Photodynamic Therapy of Cancer. *Cancers (Basel).* **2011**, *3*, 2516–2539.

(22) Lv, R.; Yang, P.; He, F.; Gai, S.; Yang, G.; Dai, Y.; Hou, Z.; Lin, J. An Imaging-Guided Platform for Synergistic Photodynamic/photothermal/chemo-Therapy with pH/temperature-Responsive Drug Release. *Biomaterials* **2015**, *63*, 115–127.

(23) Zhang, X.-D.; Wu, D.; Shen, X.; Liu, P.-X.; Fan, F.-Y.; Fan, S.-J. In Vivo Renal Clearance, Biodistribution, Toxicity of Gold Nanoclusters. *Biomaterials* **2012**, *33*, 4628–4638.

(24) Huang, K.; Ma, H.; Liu, J.; Huo, S.; Kumar, A.; Wei, T.; Zhang, X.; Jin, S.; Gan, Y.; Wang, P. C.; *et al.* Size-Dependent Localization and Penetration of Ultrasmall Gold Nanoparticles in Cancer Cells, Multicellular Spheroids, and Tumors *in Vivo*. *ACS Nano* **2012**, *6*, 4483–4493.

(25) Retnakumari, A.; Setua, S.; Menon, D.; Ravindran, P.; Muhammed, H.; Pradeep, T.; Nair, S.; Koyakutty, M. Molecular-Receptor-Specific, Non-Toxic, near-Infrared-Emitting Au Cluster-Protein Nanoconjugates for Targeted Cancer Imaging. *Nanotechnology* **2010**, *21*, 55103.

(26) Yamamoto, M.; Osaka, I.; Yamashita, K.; Hasegawa, H.; Arakawa, R.; Kawasaki, H. Effects of Ligand Species and Cluster Size of Biomolecule-Protected Au Nanoclusters on Efficiency of Singlet-Oxygen Generation. *J. Lumin.* **2016**, *180*, 315–320.

(27) Das, T.; Ghosh, P.; Shanavas, M. S.; Maity, A.; Mondal, S.; Purkayastha, P.; Johnson, B. F. G.; Lambert, R. M.; Jahnen-Dechent, W.; Hsiao, J. K.; *et al.* Protein-Templated Gold Nanoclusters: Size Dependent Inversion of Fluorescence Emission in the Presence of Molecular Oxygen. *Nanoscale* **2012**, *4*, 6018.

(28) Shibu, E. S.; Sugino, S.; Ono, K.; Saito, H.; Nishioka, A.; Yamamura, S.; Sawada, M.; Nosaka, Y.; Biju, V. Singlet-Oxygen-Sensitizing Near-Infrared-Fluorescent Multimodal Nanoparticles. *Angew. Chemie Int. Ed.* **2013**, *52*, 10559–10563.

(29) Kawasaki, H.; Kumar, S.; Li, G.; Zeng, C.; Kauffman, D. R.; Yoshimoto, J.; Iwasaki, Y.; Jin, R. Generation of Singlet Oxygen by Photoexcited Au 25 (SR) 18 Clusters. *Chem. Mater.* **2014**, *26*, 2777–2788.

(30) Qian, H.; Zhu, M.; Wu, Z.; Jin, R. Quantum Sized Gold Nanoclusters with Atomic Precision. *Acc. Chem. Res.* **2012**, *45*, 1470–1479.

(31) Zeng, C.; Chen, Y.; Iida, K.; Nobusada, K.; Kirschbaum, K.; Lambright, K. J.; Jin, R. Gold Quantum Boxes: On the Periodicities and the Quantum Confinement in the Au_{28}, Au_{36}, Au_{44}, and Au_{52} Magic Series. *J. Am. Chem. Soc.* **2016**, *138*, 3950–3953.

(32) Negishi, Y.; Nakazaki, T.; Malola, S.; Takano, S.; Niihori, Y.; Kurashige, W.; Yamazoe, S.; Tsukuda, T.; Häkkinen, H. A Critical Size for Emergence of Nonbulk Electronic and Geometric Structures in Dodecanethiolate-Protected Au Clusters. *J. Am. Chem. Soc.* **2015**, *137*, 1206–1212.

(33) Russier-Antoine, I.; Bertorelle, F.; Vojkovic, M.; Rayane, D.; Salmon, E.; Jonin, C.; Dugourd, P.; Antoine, R.; Brevet, P.-F. Non-Linear Optical Properties of Gold Quantum Clusters. The Smaller the Better. *Nanoscale* **2014**, *6*, 13572–13578.

(34) Philip, R.; Chantharasupawong, P.; Qian, H.; Jin, R.; Thomas, J. Evolution of Nonlinear Optical Properties: From Gold Atomic Clusters to Plasmonic Nanocrystals. *Nano Lett.* **2012**, *12*, 4661–4667.

(35) Varnavski, O.; Ramakrishna, G.; Kim, J.; Lee, D.; Goodson III, T. Critical Size for the Observation of Quantum Confinement in Optically Excited Gold Clusters. *J. Am. Chem. Soc.* **2010**, *132*, 16–17.

(36) Ashenfelter, B. A.; Desireddy, A.; Yau, S. H.; Goodson III, T.; Bigioni, T. P. Fluorescence from Molecular Silver Nanoparticles. *J. Phys. Chem. C* **2015**, *119*, 20728–20734.

(37) Zhu, M.; Aikens, C. M.; Hollander, F. J.; Schatz, G. C.; Jin, R. Correlating the Crystal Structure of a Thiol-Protected Au25 Cluster and Optical Properties. *J. Am. Chem. Soc.* **2008**, *130*, 5883–5885.

(38) Aikens, C. M. Origin of Discrete Optical Absorption Spectra of M 25(SH) 18 - Nanoparticles (M = Au, Ag). *J. Phys. Chem. C* **2008**, *112*, 19797–19800.

(39) Heaven, M. W.; Dass, A.; White, P. S.; Holt, K. M.; Murray, R. W. Crystal Structure of the Gold Nanoparticle [N(C8H17)4][Au25(SCH2CH2Ph)18]. *J. Am. Chem. Soc.* **2008**, *130*, 3754–3755.

(40) Akola, J.; Walter, M.; Whetten, R. L.; Häkkinen, H.; Grönbeck, H. On the Structure of Thiolate-Protected Au25. *J. Am. Chem. Soc.* **2008**, *130*, 3756–3757.

(41) Link, S.; Beeby, A.; FitzGerald, S.; El-Sayed, M. A.; Schaaff, T. G.; Whetten, R. Visible to Infrared Luminescence from a 28-Atom Gold Cluster. *J. Phys. Chem. B* **2002**, *106*, 3410–3415.

(42) Wu, Z.; Wang, M.; Yang, J.; Zheng, X.; Cai, W.; Meng, G.; Qian, H.; Wang, H.; Jin, R. Well-Defined Nanoclusters as Fluorescent Nanosensors: A Case Study on Au(25) (SG)(18). *Small* **2012**, *8*, 2028–2035.

(43) Abeyasinghe, N.; Kumar, S.; Sun, K.; Mansfield, J. F.; Jin, R.; Goodson III, T. Enhanced Emission from Single Isolated Gold Quantum Dots Investigated Using

Two-Photon-Excited Fluorescence Near-Field Scanning Optical Microscopy. *J. Am. Chem. Soc.* **2016**, *138*, 16299–16307.

(44) Polavarapu, L.; Manna, M.; Xu, Q.-H. Biocompatible Glutathione Capped Gold Clusters as One- and Two-Photon Excitation Fluorescence Contrast Agents for Live Cells Imaging. *Nanoscale* **2011**, *3*, 429–434.

(45) Shang, L.; Dong, S.; Nienhaus, G. U. Ultra-Small Fluorescent Metal Nanoclusters: Synthesis and Biological Applications. *Nano Today* **2011**, *6*, 401–418.

(46) Ho-Wu, R.; Yau, S. H.; Goodson III, T. Efficient Singlet Oxygen Generation in Metal Nanoclusters for Two-Photon Photodynamic Therapy Applications. *J. Phys. Chem. B* **2017**, *121*, 10073–10080.

(47) Ding, C.; Tian, Y. Gold Nanocluster-Based Fluorescence Biosensor for Targeted Imaging in Cancer Cells and Ratiometric Determination of Intracellular pH. *Biosens. Bioelectron.* **2015**, *65*, 183–190.

(48) Biswas, A.; Banerjee, S.; Gart, E. V.; Nagaraja, A. T.; McShane, M. J. Gold Nanocluster Containing Polymeric Microcapsules for Intracellular Ratiometric Fluorescence Biosensing. *ACS Omega* **2017**, *2*, 2499–2506.

(49) Luo, Z.; Yuan, X.; Yu, Y.; Zhang, Q.; Leong, D. T.; Lee, J. Y.; Xie, J. From Aggregation-Induced Emission of Au(I)-Thiolate Complexes to Ultrabright Au(0)@Au(I)-Thiolate Core-Shell Nanoclusters. *J. Am. Chem. Soc.* **2012**, *134*, 16662–16670.

(50) Li, B.; Wang, X.; Shen, X.; Zhu, W.; Xu, L.; Zhou, X. Aggregation-Induced Emission from Gold Nanoclusters for Use as a Luminescence-Enhanced Nanosensor to Detect Trace Amounts of Silver Ions. *J. Colloid Interface Sci.* **2016**, *467*, 90–96.

(51) Dou, X.; Yuan, X.; Yu, Y.; Luo, Z.; Yao, Q.; Leong, D. T.; Xie, J. Lighting up Thiolated Au@Ag Nanoclusters via Aggregation-Induced Emission. *Nanoscale* **2014**, *6*, 157–161.

(52) Zhou, Q.; Lin, Y.; Xu, M.; Gao, Z.; Yang, H.; Tang, D. Facile Synthesis of Enhanced Fluorescent Gold–Silver Bimetallic Nanocluster and Its Application for Highly Sensitive Detection of Inorganic Pyrophosphatase Activity. *Anal. Chem.* **2016**, *88*, 8886–8892.

(53) Wang, S.; Meng, X.; Das, A.; Li, T.; Song, Y.; Cao, T.; Zhu, X.; Zhu, M.; Jin, R. A 200-Fold Quantum Yield Boost in the Photoluminescence of Silver-Doped Ag(x)Au(25-X) Nanoclusters: The 13th Silver Atom Matters. *Angew. Chem. Int. Ed. Engl.* **2014**, *53*, 2376–2380.

(54) Negishi, Y.; Iwai, T.; Ide, M. Continuous Modulation of Electronic Structure of Stable Thiolate-Protected Au25 Cluster by Ag Doping. *Chem. Commun.* **2010**, *46*, 4713–4715.

(55) Pawlicki, M.; Collins, H. A.; Denning, R. G.; Anderson, H. L. Two-Photon Absorption and the Design of Two-Photon Dyes. *Angew. Chem. Int. Ed. Engl.* **2009**, *48*, 3244–3266.

(56) Bhaskar, A.; Guda, R.; Haley, M. M.; Goodson, T. Building Symmetric Two-Dimensional Two-Photon Materials. *J. Am. Chem. Soc.* **2006**, *128*, 13972–13973.

(57) Heflin, J. R.; Wong, K. Y.; Zamani-Khamiri, O.; Garito, A. F. Nonlinear Optical Properties of Linear Chains and Electron-Correlation Effects. *Phys. Rev. B* **1988**, *38*, 1573–1576.

(58) Dixit, S. N.; Guo, D.; Mazumdar, S. Essential-States Mechanism of Optical Nonlinearity in π-Conjugated Polymers. *Phys. Rev. B* **1991**, *43*, 6781–6784.

(59) Venugopalan, V.; Lamboll, R.; Joshi, D.; Narayan, K. S. Facile Fabrication of Ultra-Stretchable Metallic Nanocluster Films for Wearable Electronics. *ACS Appl. Mater. Interfaces* **2017**, *9*, 28010–28018.

(60) Nakaya, M.; Iwasa, T.; Tsunoyama, H.; Eguchi, T.; Nakajima, A. Formation and Control of Ultrasharp Metal/Molecule Interfaces by Controlled Immobilization of Size-Selected Metal Nanoclusters onto Organic Molecular Films. *Adv. Funct. Mater.* **2014**, *24*, 1202–1210.

(61) Karimi, N.; Kunwar, P.; Hassinen, J.; Ras, R. H. A.; Toivonen, J. Micropatterning of Silver Nanoclusters Embedded in Polyvinyl Alcohol Films. *Opt. Lett.* **2016**, *41*, 3627.

(62) Kunwar, P.; Turquet, L.; Hassinen, J.; Ras, R. H. A.; Toivonen, J.; Bautista, G. Holographic Patterning of Fluorescent Microstructures Comprising Silver Nanoclusters. *Opt. Mater. Express* **2016**, *6*, 946.

(63) Devadas, M. S.; Kwak, K.; Park, J.-W.; Choi, J.-H.; Jun, C.-H.; Sinn, E.; Ramakrishna, G.; Lee, D. Directional Electron Transfer in Chromophore-Labeled Quantum-Sized Au 25 Clusters: Au 25 as an Electron Donor. *J. Phys. Chem. Lett.* **2010**, *1*, 1497–1503.

(64) Raut, S.; Chib, R.; Butler, S.; Borejdo, J.; Gryczynski, Z.; Gryczynski, I. Evidence of Energy Transfer from Tryptophan to BSA/HSA Protected Gold Nanoclusters. *Methods Appl. Fluoresc.* **2014**, *2*, 35004.

(65) Pu, K.-Y.; Luo, Z.; Li, K.; Xie, J.; Liu, B. Energy Transfer between Conjugated-Oligoelectrolyte-Substituted POSS and Gold Nanocluster for Multicolor

Intracellular Detection of Mercury Ion. *J. Phys. Chem. C* **2011**, *115*, 13069–13075.

(66) Oh, E.; Huston, A. L.; Shabaev, A.; Efros, A.; Currie, M.; Susumu, K.; Bussmann, K.; Goswami, R.; Fatemi, F. K.; Medintz, I. L. Energy Transfer Sensitization of Luminescent Gold Nanoclusters: More than Just the Classical Förster Mechanism. *Sci. Rep.* **2016**, *6*, 35538.

(67) Bogh, S. A.; Cerretani, C.; Kacenauskaite, L.; Carro-Temboury, M. R.; Vosch, T. Excited-State Relaxation and Förster Resonance Energy Transfer in an Organic Fluorophore/Silver Nanocluster Dyad. *ACS Omega* **2017**, *2*, 4657–4664.

(68) Green, T. D.; Yi, C.; Zeng, C.; Jin, R.; McGill, S.; Knappenberger Jr, K. L. Temperature-Dependent Photoluminescence of Structurally-Precise Quantum-Confined Au25(SC8H9)18 and Au38(SC12H25)24 Metal Nanoparticles. *J. Phys. Chem. A* **2014**, *118*, 10611–10621.

(69) Ho-Wu, R.; Yau, S. H.; Goodson III, T. Linear and Nonlinear Optical Properties of Monolayer-Protected Gold Nanocluster Films. *ACS Nano* **2016**, *10*, 562–572.